

University of Strathclyde

Department of Electrical and Electronic Engineering



University of  
**Strathclyde**  
**Glasgow**

**The Development of Microfluidic Assays for  
Functional Neural Network Communication  
Studies & CNS Drug Discovery**

**Christopher MacKerron**

This thesis is presented in partial fulfilment of the requirements for  
attaining Doctor of Philosophy

September 2019

## **Declaration of Authorship**

This thesis was composed by the author, and the results obtained from scientific experimentation are from the author's original research. The findings presented within have not been previously submitted for examination which has led to the award of a degree.

The copyright of this thesis belongs to the author under the terms of the United Kingdom Copyright Acts as qualified by University of Strathclyde Regulations 3.50. Due acknowledgement must always be made for the use of any materials contained, or derived, in this thesis.

Signed:

Date:

## Acknowledgements

First, I would like to thank the National Centre for the Replacement, Refinement & Reduction of Animals in Research for the funding of this research. I would also like to thank the department of Electronic and Electrical Engineering for providing me with the opportunity to conduct my own research.

This work would not have been possible without the continued support of my supervisors, Dr Michele Zagnoni & Trevor Bushell. Both have made every effort to guide and motivate me during my research and have demonstrated near endless patience with me over the course of this long journey. I am deeply grateful for learning new techniques under their tutelage, meanwhile their constructive criticism, and encouragement to reflect on the data obtained, has made me a more objective scientist, and a better person.

I would also like to thank Dr Graham Robertson who laid the groundwork for the microfluidic assay development and taught me how to perform primary hippocampal cultures and  $\text{Ca}^{2+}$  imaging assays. As a source of immediate guidance, he was always available if I had immediate questions on data interpretation, and I frequently enjoyed discussing ideas with him concerning assay designs, and unrelated topics. Additionally, I would like to thank Dr Louise Ritchie for her valued friendship and lending me support with the performance of electrophysiological assessments. I was very fortunate to work with excellent colleagues from both EEE and SIPBS departments, and very much appreciate their valuable inputs, constant support, and regular outings that made for fond memories.

I would like to acknowledge my parents for their endless support and advice during my studies, and the culmination of my efforts, contained in this thesis, would not have been achieved without them. Finally, I thank my brother, sisters, friends and my partner Emily for their continued encouragement, comradery and love which has helped me remain grounded and sane after all this time.

## Thesis Abstract

The study of neuroscience and the research tools used to perform this research is fundamental to the understanding of the human brain under physiological and pathophysiological conditions. Indeed, the prevalence of CNS disorders in the global population has sharply increased over the last two decades, and new techniques are required to dissect the complexities of the underlying mechanisms.

Whilst *in vivo* research presents the closest means of replicating human CNS disorders, there are significant translational challenges in replicating these diseases using animal models. Breaking down the complexities present within the brain to assess single cellular mechanisms sequentially may be facilitated by *in vitro* methodologies, which provide invaluable information on neural network function under controlled conditions. A surge in microfluidic technology over the last 15 years has enabled considerable advances in the development of new *in vitro* research tools for neuroscientific research, offering greater control over experimental conditions including neural network patterning and fluid handling. Microfluidic devices are often transparent and thus can be readily interfaced with microscopy for optical imaging assays following chemical stimulation of neuronal cultures.

This thesis explores novel avenues for microfluidic assay development using dual chamber microfluidic devices containing environmentally isolated, but synaptically connected neural networks. First, voltage imaging assays are considered as an alternative to  $\text{Ca}^{2+}$  imaging assays to improve upon the temporal resolutions of standard optical imaging, whilst maintaining a higher data throughput when compared to electrophysiological whole cell patch clamp recordings. Then, the need for manual drug applications are resolved by means of developing a microfluidic perfusion system for early CNS drug discovery. Finally, chemogenetic assays are employed in combination with  $\text{Ca}^{2+}$  imaging and microfluidic perfusion to selectively stimulate a sub-population of transfected neurons whilst monitoring the subsequent cascade of activity in the surrounding neural network. In conclusion, the microfluidic assays developed can be used for studying neurophysiological mechanisms of synaptic communication, are capable of screening CNS acting drugs, and lay the groundwork for alternative methods to manipulate the activity of neural networks.



# Contents

List of Figures.....	VIII
List of Abbreviations.....	XI
1. The Emerging Role of Microfluidics in Neuroscientific Research.....	1
1.1. Chapter Overview.....	1
1.2. The Hippocampal Neural Network.....	2
1.2.1. Hippocampal Pyramidal Neurons.....	4
1.2.2. Hippocampal Interneurons.....	5
1.2.3. Glial Cells.....	7
1.2.4. Synaptic Communication within the Hippocampus.....	9
1.2.5. Pathophysiological Neural Network Activity.....	17
1.3. Tools for Investigating Neural Network Activity.....	25
1.3.1. Electrophysiological Research Tools.....	25
1.3.2. Optical Imaging Techniques.....	28
1.3.3. Genetic Manipulation.....	32
1.4. The Current Challenges of Neuroscientific Research.....	36
1.5. An Introduction to Microfluidics.....	37
1.5.1. Microfluidic Devices for Neural Network Culture.....	39
1.5.2. Investigating Neuronal Projection Development and Pathogenesis.....	41
1.5.3. Manipulation of Microfluidic Neural Network Activity.....	44
1.5.4. CNS Pathologies: From Microfluidic Devices to <i>In Vivo</i> Models.....	46
1.6. Thesis Objectives and Outline.....	48
2. Methods & Materials.....	50
2.1. Fabrication and Device Production.....	50
2.1.1. Designing Microfluidic Systems.....	50
2.1.2. Two-layer Photolithography Fabrication.....	52
2.1.3. Silanisation of the Master Silicon Wafer.....	54
2.1.4. PDMS Casting and Microfluidic Device Creation.....	54
2.1.5. Spatio-Temporal Profiling of <i>In Situ</i> Drug Application.....	55
2.2. Hippocampal Cultures for <i>In Vitro</i> Studies.....	55
2.2.1. Device Preparation.....	56
2.2.2. Preparation of Coverslips and 4-Well Plate.....	56
2.2.3. Solution Preparation for Hippocampal Cultures.....	56
2.2.4. Procedures for Hippocampal Dissection.....	57
2.2.5. Hippocampal Tissue Dissociation.....	57
2.2.6. Mixed Primary Hippocampal Culture Plating and Maintenance.....	57

2.3. Immunocytochemistry for Primary Hippocampal Cultures.....	58
2.3.1. Antibodies for Neural Network Populations and Synaptic Connectivity.....	58
2.3.2. Immunocytochemical Staining of Neural Networks.....	59
2.3.3. Immunocytochemistry - Epifluorescent Imaging .....	59
2.4 Calcium Imaging in Microfluidic Neural Networks .....	60
2.4.1. Setup for Calcium Imaging Assays .....	60
2.4.2. Experimental Protocol for Microfluidic Calcium Imaging Assays .....	61
2.4.3 Signal Processing and Analysis post Calcium Imaging Assays .....	63
2.5. Neuronal Experiments for Improved Temporal Resolutions .....	64
2.5.1. Voltage Sensitive Dye Imaging .....	64
2.5.2. Whole Cell Patch Clamp Experiments on Neuronal Networks.....	67
2.6. Assay Development using the Microfluidic Drug Discovery Platform.....	68
2.6.1. Solution Preparation for Microfluidic Perfusion .....	68
2.6.2. Microfluidic Perfusion System Setup.....	68
2.6.3. Experimental Protocols for the Microfluidic Drug Discovery Platform .....	71
2.7. Chemogenetics for Microfluidic Communication Assays.....	77
2.7.1. DREADD Transfection of Hippocampal Cultures. ....	77
2.7.2. Pharmacological Agent Preparation for Chemogenetic Assays .....	77
2.7.3. Transfection Protocols for Chemogenetic Assays .....	77
2.7.4. Imaging Plate based Transfected Neural Networks .....	78
2.7.5. Imaging Transfected Microfluidic Neural Networks.....	80
2.7.6. Analysis of Chemogenetic Assays.....	81
2.8. Statistical Analysis .....	81
3. Investigating Voltage Imaging Techniques .....	82
3.1. Chapter Overview .....	82
3.2. Introduction and Chapter Objectives .....	82
3.3. Immunocytochemical Staining of Microfluidic Hippocampal Cultures .....	85
3.3.1. $\beta$ III-Tubulin and Glial Fibrillary Protein.....	85
3.3.2. $\beta$ III-Tubulin & Synaptophysin .....	87
3.4. Confirmation of Synaptic Activity in Microfluidic Neuronal Networks .....	88
3.4.1. Theoretical Model of <i>In Situ</i> Microfluidic Applications .....	88
3.4.2. Experimental Validation of Environmentally Isolated Culture Chambers.....	90
3.4.3. Detection of Synaptic Connectivity between Environmentally Isolated Neural Networks Using $\text{Ca}^{2+}$ Imaging. ....	92
3.4.4. Direct Stimulation of a Neuronal Network Indirectly Stimulates an Adjacent Naïve Neural Network .....	94

3.4.5. Ca <sup>2+</sup> Imaging is Unable to Resolve Action Potential Firing in the Microfluidic Setup.....	96
3.5. Optimising Voltage Sensitive Dye Imaging using Di-3-ANEPPDHQ .....	98
3.5.1. Preliminary VSDI Assessments with D3AD .....	100
3.5.2. Electrophysiological Recordings of Neuronal Activity.....	102
3.5.3. Spatial Averaging Improves SNR in VSD Recordings .....	104
3.5.4. Improved Temporal Resolutions Fail to Identify Action Potential Firing .....	105
3.5.5. Signal Processing Unable to Resolve Action Potentials in Fluorescent Readouts.....	106
3.6. Discussion .....	109
3.6.1. Immunocytochemistry in Microfluidic Hippocampal Cultures.....	109
3.6.2. <i>In Situ</i> Microfluidic Assays for Functional Communication Studies .....	109
3.6.3 Considerations for Voltage Sensitive Dye Imaging when Recording Neuronal Activity.....	113
3.6.4. Chapter 3 Summary .....	116
4. Development of the Microfluidic Perfusion System for Early CNS Drug Discovery & Communication Studies .....	118
4.1. Chapter Overview .....	118
4.2. Introduction and Chapter Objectives .....	119
4.3. Optimising Microfluidic Perfusion for Neuropharmacological Assays .....	121
4.3.1. Considerations for Microfluidic Perfusion in Assay Design .....	121
4.3.2. Investigating Steady Flow Rate Perfusion on Neural Network Health.....	122
4.3.3. Characterising the Temporal Kinetics of Microfluidic Drug Perfusion .....	125
4.4. Neuropharmacological Assays using the Microfluidic Perfusion Platform .....	127
4.4.1. Concentration Response Curve generated using Glutamate Microfluidic Perfusion. ....	127
4.4.2. Assessment of Functional Changes in Neural Network Activity in Response to Repeated Glutamate Application.....	128
4.4.3. Assessment of Functional Changes in Neural Network Activity during Glutamatergic Competitive Antagonism Assays .....	132
4.4.4. Assessment of Synaptic Transmission via Neuronal Networks during the Co-Perfusion of Glutamate and TTX.....	135
4.4.5. Assessment of Mechanical Stimulation on the Activation of Perfused and Naive Neural Networks .....	138
4.4.6. Assessment of Retrograde Signalling on Axons Repeatedly Stimulated by Glutamate .....	142
4.5. Chapter 4 Discussion .....	144
4.5.1. Optimisation of the Microfluidic Perfusion System .....	144
4.5.2. Neuropharmacological Profiling of Glutamate in Neural Networks with Microfluidic Perfusion. ....	147
4.5.3. Dynamic Activation of Naïve Neural Networks During Neuropharmacological Assays are Synaptically Driven .....	149
4.6. Chapter 4 Summary.....	152

5. Assessing Network Activity via DREADD Activation .....	153
5.1. Chapter Overview .....	153
5.2. Introduction and Chapter Objectives .....	154
5.3. Preliminary Assessment of DREADD Transfected Primary Hippocampal Networks .....	157
5.3.1. Assessing Impact of Transfection on Neural Network Viability in 4-well Assay Plates .....	157
5.3.2. Direct Application of CNO Activates Chemogenetic Transfected Neural Networks .....	159
5.3. Preliminary Development of Chemogenetic Microfluidic Perfusion Assays .....	164
5.3.1. Assessing Impact of Transfection on Neural Network Viability in Microfluidic Devices .....	165
5.3.2. Changes in Local Network Activity following Direct CNO Perfusions.....	167
5.3.3. Changes in Naïve Network Activity following Direct CNO Perfusions.....	170
5.4. Chapter 5 Discussion .....	172
5.4.1. Transfection Efficiencies Within 4-Well Assay Plates & Microfluidic Devices.....	172
5.4.2. Impact of Transfection on Neural Network Viability.....	173
5.4.3 Assessing CNO Induced Changes in Neural Network Activity .....	174
5.5. Chapter 5 Summary .....	177
6. Thesis Discussion .....	179
6.1. Chapter Overview .....	179
6.2. Chapter 3 Outcomes.....	180
6.3. Chapter 4 Outcomes.....	181
6.4. Chapter 5 Outcomes.....	182
6.5. Future Studies.....	184
6.6. Thesis Conclusions.....	185
References .....	186
Appendix.....	233
Microfluidic Protocol for Calcium Imaging Assays .....	233
Reagents, Equipment & Software .....	233
Experimental Setup .....	234
Calcium Imaging Assay Procedure.....	237
Supplementary Figure 2 .....	238
Supplementary Figure 3 .....	238
Supplementary Figure 4 .....	239
Publication.....	240

## **List of Figures**

Figure 1.1: Image of the Hippocampal Formation.....	3
Figure 1.2: Adapted Images of Pyramidal Neurons from the CA1 and CA3 Sub-Regions of the Hippocampus.....	5
Figure 1.3: Reconstructed Image of Interneurons within the CA1 Hippocampal Sub-Region.....	6
Figure 1.4: Adapted Image of Glial Trophic Support to a Pyramidal Neuron.....	8
Figure 1.5: Changes in Neuronal Membrane Potential during Action Potential Propagation.....	10
Figure 1.6: Models of Synaptic Activity.....	13
Figure 1.7: Adapted Image of Alzheimer’s Induced Neurodegeneration.....	19
Figure 1.8: Whole-Cell Patch Clamping Technique.....	26
Figure 1.9: Multi-Electrode Arrays.....	28
Figure 1.10: Voltage Sensitive Dye Mechanisms of Action.....	31
Figure 1.11: Liposomal Gene Delivery.....	35
Figure 1.12: Microfluidic Neural Networks.....	40
Figure 1.13: Microfluidic Axonal Isolation.....	43
Figure 1.14: Stimulation of Microfluidic Networks.....	45
Figure 1.15: Microfluidic & In Vivo Model of Tau Pathology.....	47
Figure 2.1: Microfluidic Device Designs.....	51
Figure 2.2: Microfluidic Device Fabrication.....	53
Figure 2.3: Schematic of the Microfluidic Calcium Imaging Protocol.....	62
Figure 2.4: Identification of Neurons and Glial Cells during Calcium Imaging.....	64
Figure 2.5: Syringe Driven Pump Setup for Microfluidic Perfusion.....	70
Figure 2.6: Fluid Flow Path for Microfluidic Perfusion.....	71
Figure 2.7: Analysis of Individual Readouts.....	75

Figure 2.8: Automated Detection of Calcium Events.....	76
Figure 2.9: DREADD Transfected Hippocampal Network Assay Setup.....	79
Figure 3.1: Representative Immunofluorescent Images of Neurons and Astrocytes present in Primary Hippocampal Cultures.....	86
Figure 3.2: Representative Fluorescent Images of Synaptic Protein in Neuronal Networks.....	87
Figure 3.3: The Microfluidic Dynamics of In Situ Calcein Applications.....	91
Figure 3.4: Activation of Neural Networks Identified by Ca <sup>2+</sup> Imaging.....	93
Figure 3.5: Direct Activation of a Neural Network following Glutamate Applications.....	95
Figure 3.6: Indirect Activation of a Naïve Neural Network.....	96
Figure 3.7: Ca <sup>2+</sup> Imaging with Improved Temporal Resolution Fails to Resolve AP Firing.....	97
Figure 3.8: Fluorescent Signals Obtained by Di-3-ANEPPDHQ during Blue-Shifts.....	99
Figure 3.9: Preliminary Assessments with the VSD Di-3-ANEPPDHQ.....	101
Figure 3.10: The Application of KCl Depolarises Neuronal Membrane Potential.....	103
Figure 3.11: Spatial Averaging Improves SNR During VSD Recordings.....	105
Figure 3.12: Inability to Identify sAPs with Further Improvements to Temporal Resolutions.....	106
Figure 3.13: Minimal Differences between +/-ve Peak Response Observed in Recordings.....	108
Figure 4.1: Live/Dead Imaging Assay following Microfluidic Perfusion.....	124
Figure 4.2: Microfluidic Perfusion preserves Neural Network Viability.....	125
Figure 4.3: Calcein Delivery Demonstrates Robustness of the Microfluidic Perfusion Model.....	126
Figure 4.4: Concentration Response Curves following Direct Glutamate Perfusions.....	128
Figure 4.5: Robust Increases in Intracellular Ca <sup>2+</sup> with Repeated Glutamate Applications.....	130
Figure 4.6: Synaptic Activation of Naïve Neural Network during Glutamate Perfusions.....	131
Figure 4.7: Competitive Antagonism Reveals Cell Type-Dependent Responses to Perfusates.....	133
Figure 4.8: Competitive Antagonism of Glutamate Synaptic Activation of Neurons.....	134

Figure 4.9: Co-perfusion of Glutamate and TTX does not Significantly Reduce Neural Network Response to Glutamate.....	136
Figure 4.10: Synaptic Activation of Astrocytes but not Neurons, occur during Co-Perfusion of TTX and Glutamate.....	137
Figure 4.11: Steady Vehicle Perfusion Induces Subtle Changes to Neural Network Activity.....	140
Figure 4.12: Repeated Syringe Pump Alternation Induces Increased Neuronal Network Activity...	141
Figure 4.13: Naïve Neural Network Activation is Dependent on Synaptic Communication from Perfused Neural Networks.....	143
Figure 5.1: hM3Dq Transfection does not Impact Neural Network Viability in 4-Well Assay Plates.....	158
Figure 5.2: CNO Application Exclusively Activates hM3Dq Transfected Cells.....	160
Figure 5.3: CNO Application Activates Local Neurons in mCherry-hMD3q Transfected Neural Networks.....	162
Figure 5.4: CNO Application Activates Local Astrocytes in mCherry-hMD3q Transfected Neural Networks.....	163
Figure 5.5: Liposomal Transfection Reduces Viability of Microfluidic Neural Networks.....	166
Figure 5.6: hMD3q Transfected Cells Respond to Vehicle and CNO Perfusions.....	168
Figure 5.7: Vehicle and CNO Perfusions Significantly Increase Activity of hMD3q Transfected Microfluidic Networks.....	169
Figure 5.8: CNO Perfusions Increase Naïve Neuronal Network Activity.....	171
Supplementary Figure 1: Syringe Driven Pump Setup for Microfluidic Perfusion.....	236
Supplementary Figure 2: Direct Activation of a Neural Network following Glutamate Applications.....	238
Supplementary Figure 3: Indirect Activation of a Naïve Neuronal Network .....	238
Supplementary Figure 4: Transfection Efficiency in 4-well Assay Plates and Microfluidic Devices .....	239

## **List of Abbreviations**

AAV	Adeno associated virus
AM	Acetoxymethyl ester
AMPA	Alpha-amino-3-hydroxy-5-methyl-4-isoxazolepropionic acid
sAP	Spontaneous action potential
AraC	Cytosine $\beta$ -D-arabinofuranoside
ATP	Adenosine triphosphate
AU	Arbitrary units
A $\beta$	Amyloid beta
BBB	Blood brain barrier
BSA	Bovine serum albumin
CA	Cornu ammonis
Ca <sup>2+</sup>	Calcium
Ca <sub>i</sub> <sup>2+</sup>	Intracellular calcium
CaCl <sup>-2</sup>	Calcium chloride
Cl <sup>-</sup>	Chloride
CamKIIa	Ca <sup>2+</sup> /calmodulin-dependent protein kinase II
CCD	Charge-coupled device
CMV	Cytomegalovirus
CNO	Clozapine-N-oxide
CNS	Central nervous system
DAPI	4',6-diamidino-2-phenylindole
D3AD	Di-3-ANEPP DHQ
DG	Dentate gyrus
DI	De-ionised
DIV	Days in vitro
DL-AP5	DL-2-amino-5-phosphonovaleric acid
DMSO	Dimethyl sulfoxide
DNA	Deoxyribonucleic acid



DRG	Dorsal root ganglion
DREADD	Designed receptors exclusively activated by designed drugs
EAM	Events per astrocyte per minute
EC	Entorhinal cortex
EEG	Electroencephalogram
EM	Electron multiplier
ENM	Events per neuron per minute
ePSCs	Excitatory postsynaptic currents
mEPSC	Miniature excitatory post synaptic current
FBS	Foetal bovine serum
FOV	Field of view
GABA	Gamma-aminobutyric acid
GEVI	Genetically Encoded Voltage Indicator
GFAP	Glial fibrillary acidic protein
GPCR	G-protein coupled receptors
GTC	Generalised tonic-clonic
HBS	HEPES based external solution
HEPES	4-(2-hydroxyethyl)-1-piperazineethanesulfonic acid
iGluR	Ionotropic glutamate receptor
IP3	Inositol trisphosphate
iPSCs	Inhibitory postsynaptic currents
K <sup>+</sup>	Potassium
KCC2	Potassium chloride co-transporter
KCl	Potassium chloride
KO	Knock-out
LTD	Long term depression
LTP	Long term potentiation
MAP-2	Microtubule-associated protein 2
MCPG	(R, S)- $\alpha$ -Methyl-4-carboxyphenylglycine

MEA	Multielectrode array
mV	Milli volt
Opti-MEM	Optimal minimum essential medium
MgSO <sub>4</sub>	Magnesium sulphate
MCA	Middle cerebral artery
Na <sup>+</sup>	Sodium
NaCl	Sodium chloride
NaHCO <sub>3</sub>	Sodium hydrogen carbonate
NaH <sub>2</sub> PO <sub>4</sub>	Sodium dihydrogen phosphate
NBQX	2,3-dihydroxy-6-nitro-7-sulfamoyl-benzo[f]quinoxaline-2,3-dione
NIHSS	National Institute of Health Stroke Scale
NFU	Normalised fluorescence units
NFG	Nerve growth factor
NMDA	N-methyl-D-aspartate receptors
NO	Nitric oxide
Par	Parasubiculum
PBS	Phosphate buffered saline
PDMS	Polydimethylsiloxane
PFA	Paraformaldehyde
PI	Propidium iodide
PKC	Protein kinase C
PLC	Phospholipase C
PLL	Poly(l-lysine)
PNS	Peripheral nervous system
Pre	Presubiculum
RNA	Ribonucleic acid
ROI	Region of interest
SNARE	Soluble NSF attachment receptor
TA	Temporoammonic

TTX	Tetrodotoxin
UV	Ultraviolet
VSD	Voltage sensitive dye
VSDI	Voltage sensitive dye imaging
LIGA	Lithographie, galvanoförmung, abförmung; Lithography, electroplating, moulding

# **1. The Emerging Role of Microfluidics in Neuroscientific Research**

## **1.1. Chapter Overview**

The Edwin Smith Papyrus, transcribed in the 17<sup>th</sup> century B.C. is the oldest medical text to detail the organ we know is responsible for consciousness, thought, speech, movement and a vast number of functions in the human body. It was in this text that the term 'brain' was first described, and gives a description of the protective meninges, the brain's external features and the cerebrospinal fluid in the context of head trauma<sup>1</sup>. A great deal of research has been performed since by surgeons and researchers alike, such as Thomas Willis who published the medical textbook 'Anatomy of the Brain' concerning the different regions of the organ and neuropathologies including epilepsy and paralysis<sup>2</sup>, to the combined efforts of Renshaw, Forbes & Morrison in their study of pyramidal cell activity using microelectrodes in cats<sup>3</sup> to name a few. Scientific progress in the field of neuroscience has since allowed the characterisation of physiological neural network activity and correlated changes in this activity to neuropathologies such as epilepsy<sup>4</sup> and Parkinson's disease<sup>5</sup>.

This research would be for naught without the development of tools with which neural network activity can be investigated. Indeed, it was the early published works of Richard Caton<sup>6</sup> and Adolf Beck<sup>7</sup> using electrodes to map spontaneous activity of different network regions across multiple species (rabbits, dogs, monkeys), before Hans Berger developed and tested the electroencephalogram (EEG) on humans for the first time in 1924<sup>8</sup>. The EEG is still used to this day to determine and diagnose conditions such as epilepsy, tumours and brain death. Elsewhere, from the early use of the glass electrode for detecting single neuron activity units by Renshaw et al 1939<sup>3</sup> came the development of multi-electrode arrays in the 1950's, used to record electrical activity in cells for the first time by C.A Thomas et al in 1972<sup>9</sup> and has since been heavily used to record activity in cultured neural networks.

With the medical advances brought to bear over the last few decades, the ageing population has reached levels not observed previously, and with it, the increasing emergence of age-related disorders such as dementia. However, our understanding of these neuropathologies is still limited, with no definitive cure for CNS disorders such as Alzheimer's disease, Parkinson's disease or epilepsy in sight, and so there is a clear need to expand and develop the research tools for neuropharmacological research. Microfluidic techniques have seen increasing use in the field of neuroscience, granting a range of benefits to assess neural networks including customisable

patterned networks, precise drug application, integration of electrical and optical recording techniques, and *in vitro* modelling of neuropathologies. Importantly, such techniques have been used to demonstrate functional communication between neural networks *in vitro* which would be impossible otherwise using standard approaches to cell culture.

This chapter describes in brief the function of cell types within the hippocampus primarily responsible for synaptic communication in physiological and pathological states, and the methods used for investigating neural network activity. Additionally, a range of microfluidic applications for neuroscientific research will be discussed. Finally, some of the limitations in the field of neuroscience will be highlighted, and the objectives of this thesis defined.

## **1.2. The Hippocampal Neural Network**

The hippocampus is a sub-region within the well-defined hippocampal formation alongside the dentate gyrus (DG), subiculum (Sub), presubiculum (Pre), parasubiculum (Par) and the entorhinal cortex (EC), and plays an integral role in emotional regulation, spatial processing and importantly, long-term memory formation<sup>10–12</sup>. The hippocampus can be divided into three compartments, specifically, Cornu Ammonis 1, 2 and 3 (CA1, CA2 & CA3 respectively) and each section plays an integral role in relaying major excitatory inputs or providing negative feedback in processing memory<sup>13–15</sup>. The hippocampal formation itself is one of the few regions of the brain to receive multi-modal, highly processed information from neighbouring regions such as the neocortex, and within its neuroanatomy underlies a unique circuitry for this signal processing (Figure 1.1).

To provide a summary of the hippocampal circuitry, neocortical signals are received at the EC and thus can be considered the initiating step of the activated hippocampal formation. Axonal projections from the EC primarily travel to the DG via the perforant pathway (major hippocampal input pathway) and are unidirectional<sup>16</sup>. From the DG, the mossy fibers of granule cells provide unidirectional synaptic input to the pyramidal neurons in CA3 which in turn provide unidirectional stimulation of the CA1 hippocampal field Schaffer collateral axons<sup>17,18</sup>. Additionally, EC layer III neurons may stimulate the CA3 sub-region directly via the temporoammonic (TA) pathway prior to stimulation from the perforant pathway<sup>19,20</sup>. Thus, the EC may operate under two distinct phases of feedforward excitation of pyramidal neurons.

From the CA1, axonal projections traverse to both the Sub for further spatial signal processing (via Pre and Para sub-regions)<sup>21,22</sup>, and to the EC where a variety of feedforward and feedback signal modulation takes places<sup>23–25</sup>, thus closing the hippocampal circuitry loop. It would be impossible to detail the true complexity of the intrinsic connections within this region in full, whilst maintaining relevancy to the purpose of this thesis. Instead, the cells primarily responsible for communication and indeed, the basis of synaptic activity within the hippocampus will be discussed.

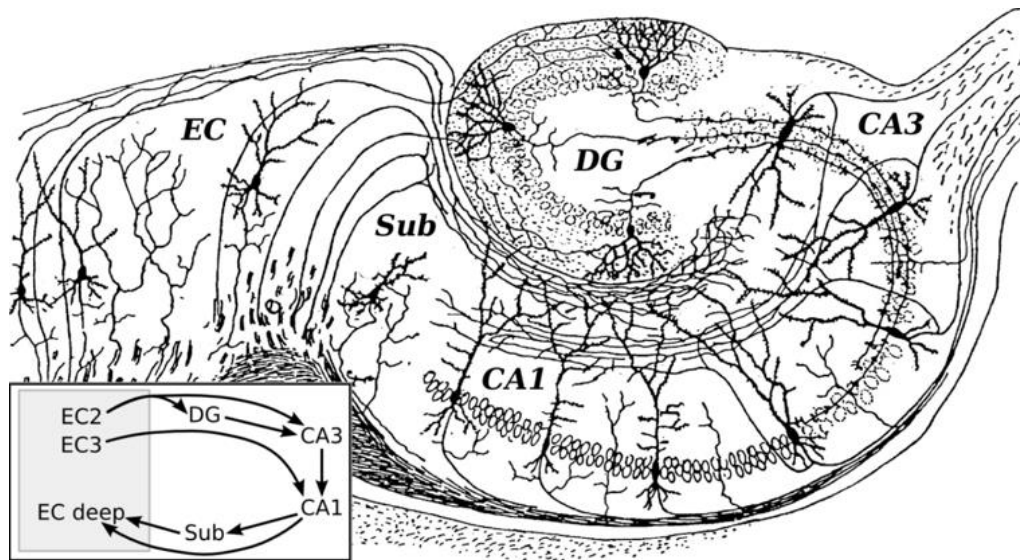


**Figure 1.1: Image of the Hippocampal Formation, as drawn by Santiago Ramón y Cajal (1911)<sup>26</sup>.** The hippocampal formation depicted illustrates the perforant projection pathway from the EC through to the CA3 via axonal projection traces, followed by CA3-CA1 schaffer collaterals. The inset provides an overview of the hippocampal formation circuitry.

### 1.2.1. Hippocampal Pyramidal Neurons

Pyramidal neurons derived of the CA1 & CA3 sub-regions are cells that specialise in the delivery of excitatory signals and within the context of mixed, primary hippocampal cultures, are primarily responsible for hippocampal network communication. To permit the constant signal processing of electrochemical impulses over varied frequencies and strength of stimulus, the pyramidal neuron structure is complex and is composed of different regions, each with their own properties which plays a fundamental role in signal processing (Figure 1.2). The cell soma forms the central body of the neuron, which contains the nucleus and other organelles such as the mitochondria responsible for metabolic activity and homeostatic regulation of the cell. Meanwhile, the cytoskeleton of the neuron is supported by the combined presence of neurotubules and neurofilaments which form neurofibril bundles to facilitate the transport of proteins and ions through the cell membrane, in addition to the extension of processes projecting forth from the cell soma<sup>27</sup>. These processes are defined as either basal dendrites or apical axonal dendrites. Basal dendrites branch out considerably around the soma, are shorter in length by comparison to apical dendrites and are covered with dendritic spines which protrude from the membrane to receive either an excitatory or inhibitory signal input<sup>28,29</sup>. From the axonal hillock of the cell soma comes the primary apical dendrite, where up to 30 oblique dendrites emerge as branches which extend out considerably<sup>30</sup>. The oblique dendrites will only branch a few times more, however each will produce up to 15 terminal branches in close proximity, which are regarded as the apical tuft<sup>30,31</sup>. The terminal axonal branches from pyramidal neurons are responsible for the release of the excitatory neurotransmitter glutamate to the dendritic spines of the basal dendrite branches from another neuron<sup>32</sup>. In doing so, a synapse is established from which neuronal communication is enabled. An alternative to axo-dendritic synapses is the formation of axo-axonal synapses, whereby axonal segments of interneurons form synapses with the axonal initial segment of pyramidal neurons, and the release of GABA inhibits action potential generation<sup>33</sup>. Whilst similar, pyramidal neurons from the CA3 sub-region differ from those in the CA1 sub-region in that the primary apical dendrite bifurcates into branches closer to the axonal hillock and the basal dendrites have a lower order of complexity.

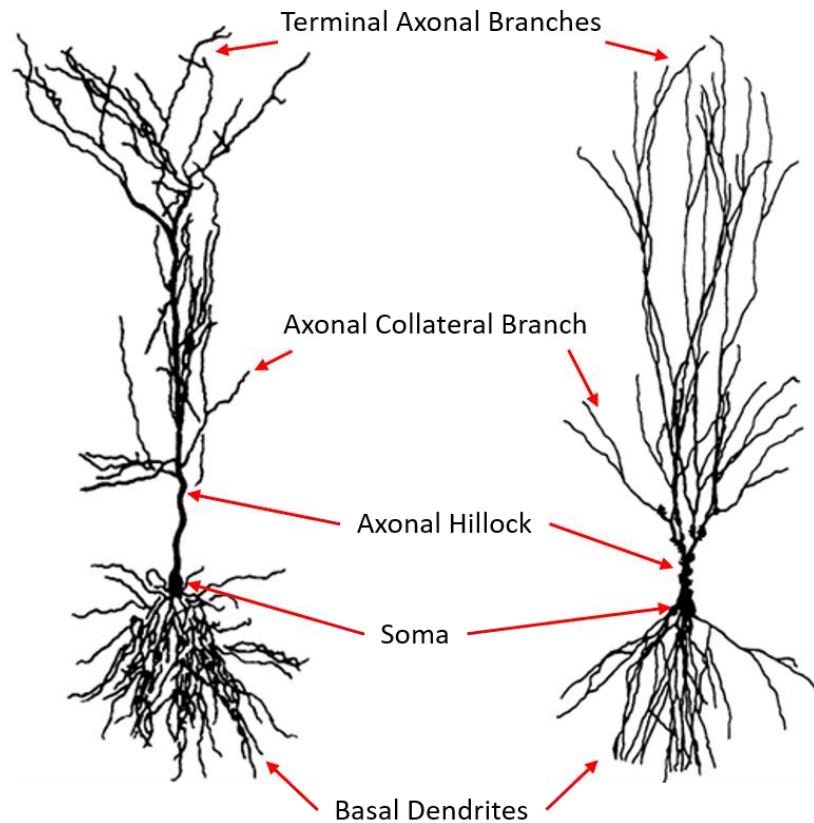


**Figure 1.2: Adapted Images of Pyramidal Neurons from the CA1 and CA3 Sub-Regions of the Hippocampus, by Bannister et al <sup>30</sup> & Gonzalez et al <sup>34</sup> (respectively).**

### 1.2.2. Hippocampal Interneurons

Whilst pyramidal neurons display a highly organised structure throughout the laminae of the hippocampus, interneurons display no such pattern and are instead interspersed throughout the sub-regions of the hippocampal formation (Figure 1.3). The interneuron displays a varied cell structure, however their axon branches typically present as short-ranged projections and release the inhibitory neurotransmitter GABA on dendritic spines across the synapse. The composition of the interneuron is similar to that of pyramidal neurons, whereby the cytoskeletal membrane of the soma and dendritic processes is supported by neurofibril bundles, and organelles such as the mitochondria are located within the soma and dendrites to provide the energy to maintain homeostatic function. Accounting for only 10 - 15 % of the total hippocampal neuronal population <sup>35</sup> whilst considering their dendritic organisation and inhibitory tone on signal processing, interneurons can be described as regulators of local neural network activity at first glance. However, studies have demonstrated that local interneuron networks are also able to fine tune and control the excitatory activity of glutamatergic pyramidal neuronal populations across multiple networks <sup>35,36</sup>. There is a surprising



diversity in the interneuron population present within the hippocampus, with as many as 20 sub-types identified in early studies <sup>37,38</sup>. Attempts have been made to distinguish different interneurons based on their neurochemical composition and physiological function. The expression of parvalbumin for example is present throughout inter-neuronal basket and axo-axonic cells <sup>39,40</sup>, meanwhile oriens-lacunosum moleculare cells have comparatively lower levels of parvalbumin expression and is absent from synaptic terminals <sup>41,42</sup>. Understanding inter-neuronal presentation is of importance to understanding synaptic communication in neural networks, as differences in the expression of proteins such as parvalbumin can impact the dynamics of GABAergic synaptic activity <sup>43</sup>.

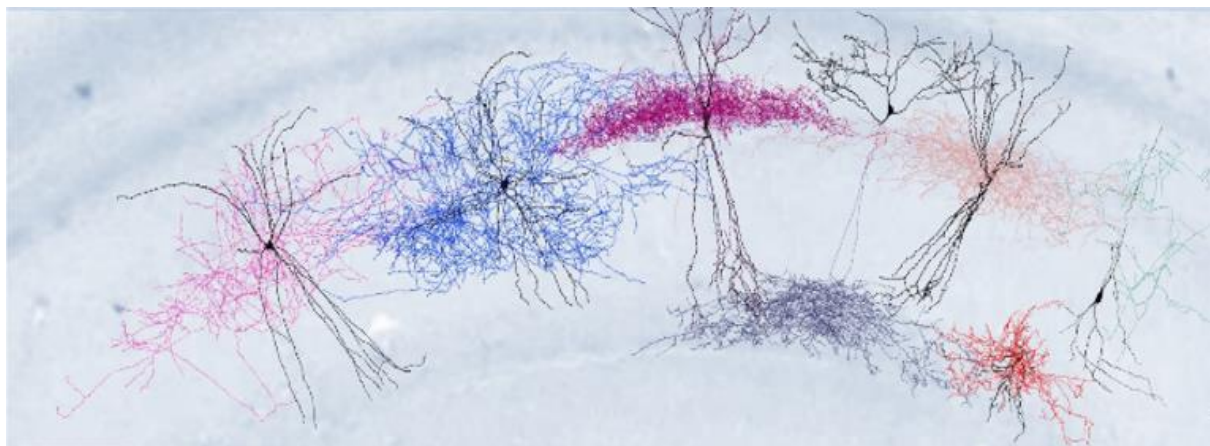


**Figure 1.3: Reconstructed Image of Interneurons within the CA1 Hippocampal Sub-Region.** Axons of each interneuron are depicted black. Dendrites of different interneuron sub-types from left to right: Basket cell (pink); Bistratified cell (blue); Axo-axonic cell (purple); Oriens-lacunosum moleculare cell (dark blue); Ivy cell (light pink); Perforant path associated interneuron (red); Schaffer collateral associated interneuron (green). Image adapted from Migliore et al <sup>44</sup>.

### 1.2.3. Glial Cells

Glial cells within the CNS are specialised for the modulation of the neural microenvironment, in contrast to the neurons, which are almost exclusively tailored to network communication. There are three primary glial cell types that can be located within the hippocampus, namely the microglia, oligodendrocytes and astrocytes. Astrocytes (as the name implies) have a structure similar to that of stars and as the most abundant glial cell, are primarily responsible for maintaining the homeostasis of the CNS. Indeed, they are interspersed throughout brain tissue and envelop blood vessels to promote/modulate the integrity and permeability of the blood brain barrier (BBB)<sup>45</sup>. Where the density of neurons are greater, the astrocyte/neuron ratio increases to account for the increased metabolic requirements of neuronal network activity via the regulation of metabolic and ionotropic systems whilst recycling neurotransmitters in the extracellular space<sup>46</sup>. These glial cells are now considered full participants in the electrochemical activity of hippocampal neural networks as they express a range of ion channels and are capable of glutamate and GABA by way of gliotransmission<sup>47-49</sup>. Astrocytic bodies and processes can be observed to envelop neurons and dendritic spines respectively (Figure 1.4) and by doing so, are able to perform a variety of critical functions. These include but are not limited to the regulation of extracellular space volume, synaptogenesis, modulation and elimination of synapses, recycling neurotransmitters and ion transport<sup>50-53</sup>. The coverage of neurons provided by astrocytes is brought about by intracellular changes in the cytoskeleton. The cytoskeleton of the astrocyte membrane is supported by actin filaments and microtubules, with the re-arrangement of actin filaments in the cytoskeleton critical for cell motility<sup>54</sup> whilst depolymerisation of microtubules facilitate the trafficking of neuroactive vesicles<sup>55</sup>.

The microglia were previously considered to be no more than motile phagocytotic cells that cleared waste and cell debris as part of the innate CNS immune system, however increasing evidence over the last decade suggests they may play a role in synaptic communication by a mechanism called synaptic pruning. This mechanism suggests that microglia remove damaged or unnecessary synaptic protein, which facilitates efficient synaptic transmission and modulation of synaptic plasticity<sup>56-58</sup>. Meanwhile oligodendrocytes support synaptic transmission of neurons specifically by wrapping their glial processes around the apical axonal projections to form the myelin sheath, which provides insulation to the propagating electrical signal of a neuron. Perhaps unsurprisingly, evidence suggests that the electrical activity of neurons promotes oligodendrocyte proliferation and promotes the formation of myelin sheaths<sup>59-61</sup>.

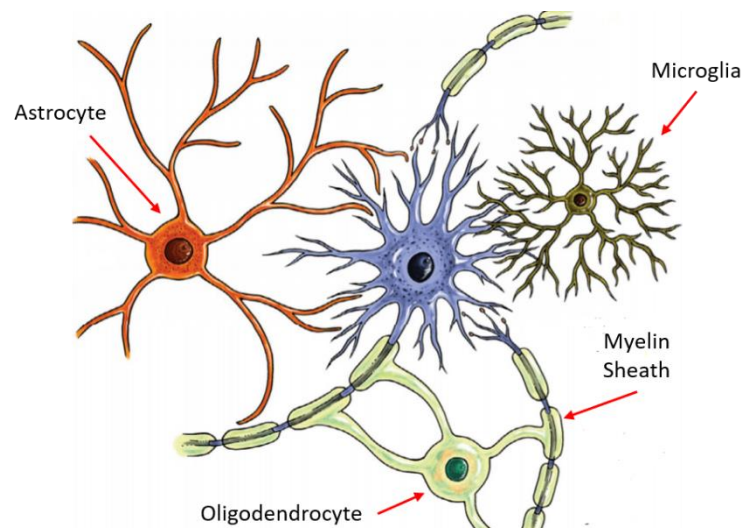


**Figure 1.4: Adapted Image of Glial Trophic Support to a Pyramidal Neuron. Image taken from by Souza et al<sup>62</sup>.**

#### 1.2.4. Synaptic Communication within the Hippocampus

The electrochemical transmission of a signal across a synapse from one neuron to another is the basic premise of functional communication across neural networks. Rhythmic fluctuations in network activity arise from the precise control and release of neurotransmitters within defined sub-regions of the hippocampus and CNS. Synaptic communication begins with the generation of action potentials in neurons, which should first be discussed before detailing synaptic plasticity within the hippocampus.

##### 1.2.4.1. Action Potentials

Neurons are sensitive to changes in their microenvironment, and so the ionic composition of neurons are tightly regulated to prevent aberrant activity by gated ion channels. Indeed, it is the expression and activity of these channels allow the passage of ions across the cell membrane. The intracellular space will typically contain, with respect to the extracellular space, a high concentration of potassium ( $K^+$ ) ions ( $\sim 140$  mM), and low concentrations of chloride ( $Cl^-$ ;  $\sim 5$  mM), sodium ( $Na^+$ ; 10 mM) and calcium ( $Ca^{2+}$ ;  $< 0.0002$  mM) ions<sup>63</sup>, resulting in a resting membrane potential between -60 to -70 mV (Figure 1.5). To ensure the neuron is capable of receiving and propagating signals, the  $Na^+/K^+$  pump will actively transport  $Na^+$  out of the cell and  $K^+$  inside, across the membrane<sup>64</sup>. A single neuron within the hippocampus can receive hundreds of signals of either excitatory or inhibitory origin from connected cells along a single basal dendritic branch. Where these are excitatory,  $Na^+$  ions from the extracellular space rapidly enter the membrane via glutamatergic ligand gated  $Na^+$  channels. As the local membrane potential increases above  $\sim -55$  mV, voltage gated  $Na^+$  channels begin to open<sup>65</sup>, followed by voltage gated  $Ca^{2+}$  channels above a membrane potential of -40 mV<sup>66</sup>. Once the local membrane potential reaches a threshold of +30 mV,  $Na^+$  &  $Ca^{2+}$  voltage gated channels begin to close whilst  $K^+$  channel open to allow the efflux of  $K^+$  ions leave the neuron and permit the repolarisation of the cell. The membrane potential further repolarises beyond -70 mV to  $\sim -90$  mV in what is called the refractory period where the membrane is effectively immune to excitatory stimuli. The  $Na^+/K^+$  pump becomes activated during this period to re-attain a resting state and ensure the membrane is capable of responding to subsequent signals. During the repolarisation of the local membrane, the surrounding membrane becomes positively charged and depolarises, and this repeated action results in a propagating wave of depolarisation, travelling from the basal dendrites to the soma, and beyond via the apical axonal projection to the terminating apical branches. This mechanism is given the term

action potential and is the primary requirement for synaptic communication to occur. In between the insulated coverage of the myelinated sheath provided by oligodendrocytes lies regions of axonal membrane called the Nodes of Ranvier that express voltage-gated  $\text{Na}^+$  channels at a high density<sup>67</sup>. As the myelin sheath prevents local membrane conductance, the propagating action potential effectively hops from one node of Ranvier to the next with minimal loss to signal strength. It is the combination of nodes of Ranvier and the myelin sheath that permit the propagation of action potential to travel up to  $\sim 150 \text{ m s}^{-1}$ <sup>68</sup>, which is why highly specialised tools with superior temporal resolutions are required to monitor action potential firing.

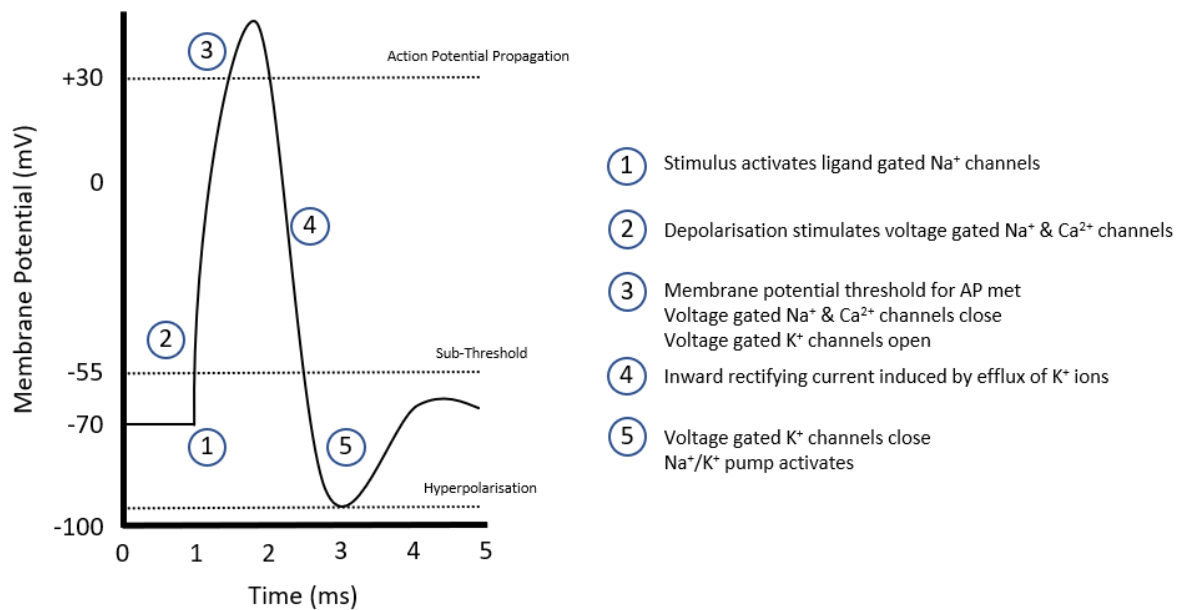


**Figure 1.5: Changes in Neuronal Membrane Potential during Action Potential Propagation.**

#### 1.2.4.2. Formation of Synapses in Hippocampal Networks

The classic bipartite synapse considers synapse formation by the exocytosis of neurotransmitters from the axonal terminal branches (pre-synaptic) of one neuron to the dendritic spine (post-synaptic) of another across a micro-domain of the extracellular space known as the synaptic cleft (Figure 1.6). Neurotransmitter release from the pre-synaptic neuron is only possible through the increase in intracellular  $\text{Ca}^{2+}$  ( $\text{Ca}_i^{2+}$ ) ions in response to the activation of voltage gated  $\text{Ca}^{2+}$  channels<sup>69–71</sup>. The translocation of the synaptic vesicles to the membrane occurs independently to that of somal activity as part of the synaptic vesicle cycle<sup>72</sup>, and vesicles effectively dock against the membrane via complexin and SNARE protein complex formation. During an action potential, the  $\text{Ca}^{2+}$  ions bind to the synaptotagmin protein, and interaction with the surrounding phospholipids effectively displace complexin to create a pore in the membrane through which exocytosis of neurotransmitters occurs<sup>73</sup>. Freely diffusive neurotransmitters in the synaptic cleft are then capable of binding to ligand gated ionotropic and metabotropic channels present at the synapse to influence post-synaptic membrane potential.

Since the bipartite model was introduced, a more accurate model has been presented to describe synaptic activity between two neurons, known as the tripartite synapse, that includes the presence of astrocytic input (Figure 1.6). Following the pre-synaptic release of glutamate, the concentration of unbound glutamate can exceed that taken up by glutamate transporters at the pre-synaptic terminal. To prevent extensive post-synaptic excitation and subsequent excitotoxicity, astrocytes provide support by the internalisation of glutamate via glutamate re-uptake transporter proteins<sup>74</sup>. The glutamate molecules are then recycled into glutamine, released into the micro-domain by the astrocyte, and subsequently used by pre-synaptic neurons to synthesis and replenish glutamate stores<sup>75</sup>.

As neuronal increases in  $\text{Ca}_i^{2+}$  gives rise to synaptic activity, it is important to consider how the changes in astrocytic  $\text{Ca}_i^{2+}$  can modulate synaptic activity via gliotransmission. Astrocytes are capable of spontaneous  $\text{Ca}_i^{2+}$  elevation via  $\text{IP}_3$  mediated activity and whilst the exact mechanisms for this remain unknown, the oscillations may be attributed to constitutively active metabotropic receptors<sup>76</sup>. They also demonstrate increases in  $\text{Ca}_i^{2+}$  following synaptic activity induced by local neurotransmission<sup>52,77</sup>, as these cells express glutamatergic<sup>78</sup>, GABAergic<sup>48,52</sup> and metabotropic receptors<sup>79</sup> similarly expressed on post-synaptic neuronal dendritic spines. Indeed, a recent study

demonstrated that increases in extracellular GABA concentration results in the activation of the astrocytic GABA transporter protein, GAT-3 pathway, leading to the gliotransmission of ATP/adenosine which inhibits the pre-synaptic release of glutamate<sup>80</sup>. Additionally, numerous studies have demonstrated astrocyte release of glutamate via mechanisms including the reversal of glutamate uptake transporters<sup>81</sup>, diffusion of glutamate stores via ionotropic purinergic receptors<sup>82</sup>, and  $Ca_i^{2+}$  dependent prostaglandin mediated exocytosis<sup>83</sup>. There is contrary evidence to the belief that astrocytes are involved in neurotransmitter release in response to synaptic dependent  $Ca^{2+}$  signalling. Astrocytes are known to express  $Ca^{2+}$  release channel  $IP_3$  receptors<sup>84</sup> and pharmacological inhibition prevents gliotransmission *in vitro*<sup>85,86</sup>. However,  $IP_3R_2$  knockout mice display no behavioural changes, no impact to memory and learning tests, and electrophysiological assessments reveal no abnormal changes in evoked neuronal activity<sup>87,88</sup>. A recent study also demonstrated that astrocytes don't actively express RNA for  $Ca^{2+}$  sensitive synaptotagmin protein or vesicular glutamate transporters<sup>89</sup>. Thus, whilst evidence exists for astrocyte function in neuron-neuron synaptic activity, it is yet unclear as to whether they play a role in neurotransmitter release.

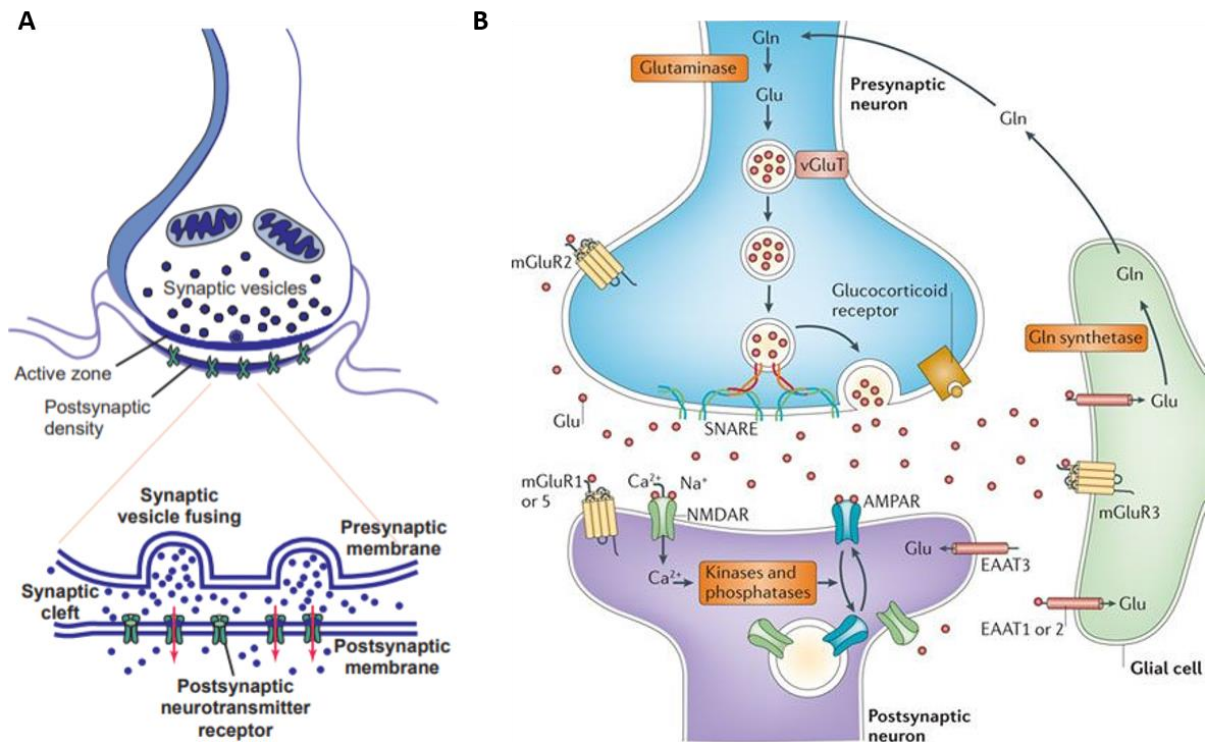


**Figure 1.6: Models of Synaptic Activity.** (A) Image of the bipartite synapse depicting the exocytosis of neurotransmitters from the pre-synaptic terminal to the post-synaptic dendritic branch, as illustrated by Cohen-Cory S<sup>90</sup>. (B) Image of the tripartite synapse revealing glial input whereby excess glutamate in the extracellular space is converted by astrocytes via de novo glutamine synthesis and transferred to presynaptic neurons to replenish glutamate stores, as illustrated by Popoli et al<sup>91</sup>.

#### 1.2.4.2.1. Glutamatergic Synaptic Transmission

Pyramidal neurons of the hippocampus are excitatory in nature and typically release glutamate to stimulate and further propagate action potential firing. There are two families of glutamatergic receptors on the post-synaptic dendritic spine, namely ligand gated ionotropic receptors, which permit the flow of extracellular ions through the post-synaptic membrane. Glutamate may also act on three different groups of metabotropic receptors (Groups I, II & III), each with their own distinct function.



The primary glutamatergic ionotropic receptors include  $\alpha$ -amino-3-hydroxy-5-methyl-4-isoxazolepropionic acid (AMPA) and N-methyl-D-aspartate (NMDA), both of which are expressed on the post-synaptic neuronal membrane. AMPA receptors have a weaker affinity to glutamate when compared to NMDA receptors which facilitates fast receptor activation/deactivation during the initial high concentrations of synaptic glutamate<sup>92</sup>. They are relatively impermeable to  $\text{Ca}^{2+}$  influx due to the polarity of its subunit GluA2, and upon activation by glutamate, the rapid influx of  $\text{Na}^+$  &  $\text{K}^+$  ions depolarises the local membrane, which is critical for NMDA receptor activity. The expression of AMPA receptors is modulated by synaptic activity via the trafficking of AMPA receptors which in turn shapes synaptic plasticity<sup>93</sup>. This appears to be controlled by the frequency of excitatory stimulation received by the post-synaptic membrane, whereby high frequencies tend to favour AMPA receptor recruitment<sup>93,94</sup> to facilitate efficient transmission of propagating signals. The slight increase in membrane potential following activation of either NMDA or AMPA receptors are described as excitatory post-synaptic potentials (EPSPs) and it is by receiving multiple EPSPs within a microsecond timescale that a post-synaptic neuron is able to propagate action potentials. NMDA receptors have a strong affinity to glutamate but are limited by slow activation kinetics, first due to the presence of the NR2B receptor subunit blockade by  $\text{Mg}^{2+}$  ions<sup>95</sup>, followed by the binding of co-agonists glycine or D-Serine<sup>96</sup>. Following AMPA receptor activation and increasing membrane depolarisation, the  $\text{Mg}^{2+}$  block is removed, and a large influx of  $\text{Na}^+$  &  $\text{Ca}^{2+}$  enters the post-synaptic dendrite. The NMDA receptor is typically expressed at high densities at mature dendritic spines and considering their affinity to glutamate, self-regulating synaptic control are critical to neural network stability in the prevention of excitotoxicity. Low levels of stimulation frequency favours NMDA expression<sup>97</sup> however this can result in the down-regulation of AMPA receptor expression<sup>98</sup>. As such, the levels of NMDA and AMPA receptor expression may vary considerably overtime in response to the frequency of presynaptic activity. Kainate receptors are similarly expressed on the pre-synaptic and post-synaptic membrane and are composed of subunits GluK<sub>1-5</sub> (GluK<sub>4</sub> & GluK<sub>5</sub> were formerly known as GluK<sub>6</sub> and GluK<sub>7</sub> respectively)<sup>99</sup>. These receptors are permeable for  $\text{Na}^+$  and  $\text{K}^+$  ions, but less so for  $\text{Ca}^{2+}$  ions<sup>100</sup> and may display weak or strong affinities for glutamate, depending on the subunit composition. The homomeric kainite receptors composed of GluK<sub>1</sub> to GluK<sub>3</sub> for example express relatively low sensitivity to glutamate and produce rapid depolarisation and desensitisation of the post-synaptic membrane<sup>101-103</sup>. Meanwhile, mGluK<sub>4</sub> and mGluK<sub>5</sub> are obligatory heterodimers that must assemble to one of the mGluK<sub>1-3</sub> subunits to form functional receptors, and are typically more sensitive to glutamate than their homomeric equivalents<sup>104,105</sup>. In contrast to the excitatory function

of post-synaptic kainate receptors, pre-synaptic receptors display inhibitory function where their activation can increase GABA release from interneurons by increasing the frequency of miniature inhibitory post-synaptic currents (mIPSCs), however only when mGluK5 subunits are absent <sup>106</sup>.

In contrast to the ionotropic NMDA, AMPA and Kainate receptors that permit the flow of ions in and out the cell, the family of metabotropic glutamate receptors (mGluRs groups I-III) activate cascades of activity. This activity is dependent on the type of G-protein signalling mechanism involved, may be excitatory or inhibitory in nature, and can be located at either pre-synaptic or post-synaptic membranes. The Gq coupled receptors mGluR1 & mGluR5, once activated, results in the hydrolysis of phosphatidylinositol by phospholipase C with an associated formation of IP<sub>3</sub> and elevated Ca<sub>i</sub><sup>2+</sup>. Both mGluR1 & mGluR5 are generally observed at the post-synaptic membrane <sup>107</sup>, and their activation increases the conductance of NMDA receptors, promotes receptor recruitment at the dendritic membrane whilst promoting LTP <sup>108,109</sup>. Meanwhile, metabotropic glutamate receptors such as mGluR2 or mGluR4 are Gi/Go coupled and are mainly associated with the inhibition of adenylate cyclase activity through which reductions in ATP & cAMP production and subsequent cAMP-dependent protein kinase activity are observed. Located at the presynaptic membrane, this Gi/Go receptor mediated activity is primarily responsible for depressing synaptic activity to prevent excitotoxicity. Examples include the high frequency stimulation dependent, glutamate induced activation of pre-synaptic mGluR2 at mossy fibre synapses within hippocampal slice cultures, which results in negative feedback on pre-synaptic glutamate release <sup>110</sup>. Additionally, cortical neurons from mGluR4 knockout mice demonstrated significantly greater levels of basal glutamate concentration in the extracellular space and were more susceptible to NMDA induced neurotoxicity <sup>111</sup>.

#### **1.2.4.2.2. GABAergic Synaptic Activity**

Inhibitory neurotransmission across hippocampal synapses can be observed by the pre-synaptic release of  $\gamma$ -aminobutyric acid (GABA) from interneurons. There are two sub-groups of GABAergic receptors, namely the ligand gated, ionotropic receptors, which include GABA<sub>A</sub> & GABA<sub>C</sub> <sup>112,113</sup>, and the metabotropic GABA<sub>B</sub> receptor <sup>114</sup>. GABA receptors display a heterogenous functionality throughout the hippocampus whereby their presence on pre-synaptic terminals may display autocrine or heterosynaptic activity to prevent Ca<sup>2+</sup> signalling and consequently reducing neurotransmitter release <sup>115-117</sup>. Meanwhile, post-synaptic paracrine activity can prevent membrane depolarisation by increased Cl<sup>-</sup> influx, thus preventing action potential propagation <sup>112</sup>. This

reduction in post-synaptic membrane potential following paracrine GABAergic activity is given the term, inhibitory post-synaptic membrane potential (IPSP).

Within the CA3, post-synaptic GABA<sub>A</sub> activation results in hyperpolarisation of the post-synaptic membrane by the large increase in intracellular Cl<sup>-</sup> (Cl<sub>i</sub><sup>-</sup>) which directly negates the positive increases in membrane potential exerted by EPSPs. A further mechanism which post-synaptic GABA<sub>A</sub> receptors are known for is shunting glutamatergic receptor activity. As NMDA activity is largely dependent on positive inward currents, the hyperpolarising effect of Cl<sup>-</sup> via GABAergic activity effectively diminishes NMDA receptor sensitivity to glutamate stimulation<sup>118,119</sup>. Similarly, to the GABA<sub>A</sub> receptor, GABA<sub>C</sub> receptor activation results in large increases in intracellular Cl<sup>-</sup> however studies have also revealed this sub-receptor to remain active over a longer period of time (150 -200 ms), does not readily desensitise and is significantly more sensitive to GABA concentration by comparison, with an EC<sub>50</sub> value range as low as 0.8 - 2 μM<sup>120-123</sup>. The GABA<sub>p</sub> receptor may also be expressed extrasynaptically in the CA1 sub-region, where small concentrations of endogenous GABA<sub>p</sub> escaping the synaptic cleft bind to the receptor to induce extended reductions to post-synaptic excitability<sup>124</sup>.

The GABA<sub>B</sub> metabotropic receptor has a dual function, as it is coupled to G<sub>i/o</sub> receptor proteins, as well as inward rectifying K<sup>+</sup> channels<sup>125</sup>. Through G<sub>i/o</sub> signalling, the suppressed cAMP protein kinase activity reduces endoplasmic release of Ca<sub>i</sub><sup>2+</sup> stores, whilst K<sup>+</sup> channel activation leads to hyperpolarisation and through these combined mechanisms can modulate neuronal excitability. Alternatively, large scale post-synaptic inhibition of pyramidal neurons by interneuron activity may be regulated by the negative feedback of GABA<sub>B</sub> autoreceptors located on the pre-synaptic terminal, which subsequently prevents further GABA release<sup>126</sup>. Similar to GABA<sub>A</sub>, the GABA<sub>B</sub> receptor is expressed at both presynaptic and post-synaptic membranes and thus serves a dual role in the inhibition of interneurons and pyramidal neurons. Post-synaptic GABA<sub>B</sub> receptors in the hippocampus are typically less sensitive to GABA concentrations when compared to GABA<sub>A</sub> and GABA<sub>p</sub>, requiring persistent and synchronous firing of pre-synaptic, GABAergic activity before the inhibitory response is achieved, and is therefore strongly implicated in synaptic plasticity<sup>127-129</sup>.

### 1.2.5. Pathophysiological Neural Network Activity

The interconnectivity of networks comprising the CNS presents an extraordinary challenge in dissecting the underlying mechanisms and subsequent treatment of CNS disorders, which often affect multiple networks and present with behavioural abnormalities in the subject. There is often poor translation of findings from animal models to clinical trials, primarily due to disease models mimicking one aspect of the conditions investigated but not all. An additional difficulty presented by CNS disorders is the BBB, which tightly regulates the trafficking of molecules back and forth between the circulatory system and the CNS. Whilst there are a considerable number of CNS disorders, for the purpose of this thesis, Alzheimer's disease, epilepsy and ischaemic stroke will be used as examples of neuropathologies that impact neurophysiological function within the hippocampus.

#### 1.2.5.1 Alzheimer's Disease

The hippocampus is one of the main focus of Alzheimer's research due to the region's critical involvement in the formation and retention of memories, and the observed degradation during the progression of the disease. This is characterised symptomatically as initial short-term memory loss, with changes in behaviour, loss of spatial awareness, long term memory loss and eventual vegetative state in the final stages<sup>130,131</sup>. Whilst neurodegeneration and shrinkage of the brain are well documented during the disease progression, the primary mechanisms responsible for this disease have eluded researchers to date.

The amyloid  $\beta$  ( $A\beta$ ) hypothesis initially proposed by John Hardy & Gerald Higgins<sup>132</sup> suggested that the extracellular build-up of  $A\beta_{42}$  and related proteins (created by  $\beta$ -secretase and  $\gamma$ -secretase pathways) resulted in the formation of plaques, which were neurotoxic to those neurons immediately adjacent<sup>133,134</sup> (Figure 1.7). Neurotoxicity may present as induced excitotoxicity via the formation of  $Ca^{2+}$  permeable pores in the cell membrane<sup>135,136</sup> and modulating NMDA receptor activity<sup>137,138</sup> such that glutamate-mediated excitotoxicity cascades result in the death of surrounding neurons. This is further exacerbated by the reduced expression of neuronal vesicular glutamate transporter protein and disease specific variants of astrocytic excitatory amino acid transporter 2 protein, preventing the recycling of excessive glutamate which accumulates in the synaptic cleft<sup>139,140</sup>. Additionally, the ability to regulate neurotransmitter release becomes compromised, with Jang In et al (2014) demonstrating rapid dysregulation of presynaptic neuron function and reduced expression of pre-synaptic proteins including synaptotagmin and synaptophysin in response to  $A\beta$  applications. This

would suggest glutamate availability is reduced at the synaptic cleft which contradicts the established evidence of glutamate induced post-synaptic excitotoxicity. This mechanism is nonetheless consistent with synaptic loss in Alzheimer's disease and could be observed during later stages of the disease. For these reasons, the formation of A $\beta$  plaques is still used diagnostically as the early signs of Alzheimer's disease, and it is considered that the inability to clear these protein aggregates through the BBB promotes this pathogenesis<sup>141</sup>. However, there are instances where A $\beta$  plaques do not correlate with cognitive decline in otherwise non-demented patients<sup>142</sup> which may partially explain why pharmaceutical endeavours have proved relatively fruitless, with an excess of 400 failed clinical trials since the last symptomatic therapies were approved<sup>143</sup>. These clinical trials are performed on symptomatic patients and so the disease may have progressed to far for these drugs to take effect. Thus, A $\beta$  hypothesis is losing traction as the leading cause of Alzheimer's.

An alternative hypothesis surrounding Alzheimer's disease is tauopathy. The tau protein is one of many neuronal microtubules that are essential to the integrity of the neuronal membrane. However, site-specific phosphorylation caused by mutations at sites such as Thr231, Ser396 and Ser422, promotes aggregation and the formation of intracellular tau neurofibrillary tangles(NFT)<sup>144</sup>. Through the formation of tau aggregates and NFTs, the integrity of the membrane gradually becomes compromised, and this is the potential cause of axonal transport defects, elevated Ca $_i^{2+}$ , mitochondrial dysfunction and synapse death<sup>145,146</sup>. As this protein is not only internalised but excreted, tauopathy may spread throughout the brain as the disease progresses. The presence of tauopathy in the human brain is positively correlated with cognitive decline<sup>147</sup>, with higher densities in the CA1 and Brodmann's areas (7 & 23) strongly associated with spatiotemporal disorientation<sup>148</sup>. Evidence also suggests there is interplay between both A $\beta$  plaques and tau protein in the progression of Alzheimer's disease, such as the reduction in A $\beta$  synaptic degradation in response to reduced endogenous tau protein<sup>149</sup>, or the role of dendritic tau on A $\beta$  synaptotoxicity<sup>150</sup>. There are tau antibodies and vaccines currently undergoing clinical trials which may show promise in due time<sup>143</sup>

and given the lack of success with solely A $\beta$  driven therapeutics, pharmaceutical research aimed at treating tauopathy is likely to become the next focus of Alzheimer's research.

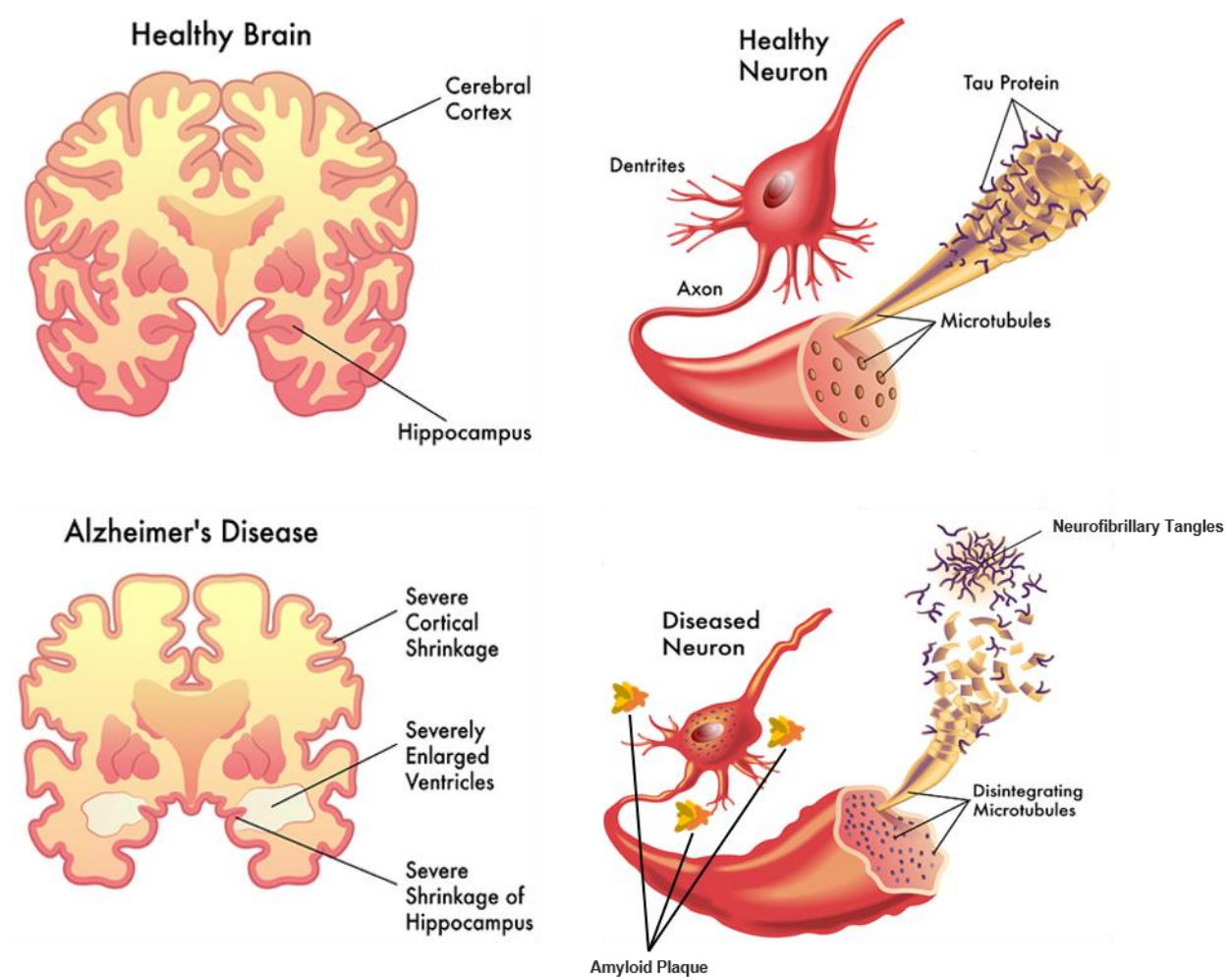


**Figure 1.7: Adapted Image of Alzheimer's Induced Neurodegeneration; original image illustrated by Mariel Corinne Tai Sander (2017) <sup>151</sup>.** As Alzheimer's disease progresses, the brain gradually shrinks in volume and mass, with amyloid plaques and neurofibrillary tangles spreading neurotoxicity out from the hippocampus to other neighbouring brain regions.

### 1.2.5.2 Epilepsy

As a common and disabling disease, epilepsy is well known for the seizures that occur as a result of neuronal dysfunction. There are multiple forms of seizures associated with this condition, some more subtle than others. Indeed, there are three primary categories of seizures; generalised (includes absence, generalised tonic-clonic (GTC), myoclonic & atonic sub forms), focal and epileptic spasms <sup>152,153</sup>. Generalised seizures involve the loss of neurophysiological activity across networks that are connected bi-laterally. Within this category, absence seizures typically present with a silent stare and unresponsiveness to verbal stimulation, meanwhile GTC involves the convulsive gestures typically associated with epilepsy. Myoclonic seizures occur rapidly with a brief jerk in motion without loss of consciousness, and atonic seizure are associated with the temporary loss of muscle tone, where individuals may collapse. Focal seizures tend to originate within a neural network confined to a specific cerebral hemisphere, and the symptoms depend on the network afflicted. Focal seizures within the occipital lobe (responsible for visual processing) for example results in visual disturbances, including reduced perception, hallucinations, scotomas and amaurosis <sup>154</sup>. Less is known about epileptic spasm seizures due to their rarity in presentation, however present as a series of flexes and extensions as a result of involuntary muscle contraction.

The underlying cause of epilepsy is often poorly understood, with the term genetic generalised epilepsies used to describe cases that are largely unaccounted but present with a suspected genetic mutation or inherited genetic defect <sup>155</sup>. Meanwhile, the known risk factors for acquiring epilepsy include strokes, brain tumours, infection (meningitis) and head injuries. A diagnosis requires at least two to three occurrences of seizures, with an EEG used to confirm abnormal brain activity. Hippocampal sclerosis, whereby a significant loss of neurons is identified within the CA1 and subiculum sub-regions, are strongly associated with recurring epilepsy, however it is yet unknown if this is a symptom or the underlying cause of epilepsy. Thus, the hippocampus serves as a crucial network at the heart of epilepsy research.

As described previously, there is fine control over excitatory and inhibitory tone associated with healthy neurophysiological activity. Epilepsy on the other hand represents an imbalance between excitation and inhibition and characterised by excessive hyper-synchronised activity within local network circuits. Whilst there are multiple cell types implicated in the continuity and resurgence of seizures, the GABAergic interneuron is the common denominator in the initiation of discharge from local neural network circuitry. Mutation of the GABA<sub>A</sub> receptor subunit is considered to predispose

individuals to generalised and idiopathic epilepsy in some cases; mutations of  $\gamma 2(R82Q)$  are associated with febrile seizures and presents with reduced surface protein expression and reduced GABAergic currents<sup>156</sup>. Other mutations implicated include  $\gamma 2(K328M)$  associated with generalised epilepsy with reductions in the single channel mean opening times<sup>157</sup>. GABAergic signalling is strongly mediated by  $Cl^-$  currents and the inability to regulate this is considered to pre-dispose GABAergic neurons to irregular activity following insult or change in the extracellular environment. In a previous study, Rivera et al (1999) demonstrated that the inhibition of potassium-chloride co-transporter (KCC2) function, via antisense oligonucleotide therapy, resulted in hyperpolarising GABA<sub>A</sub> signalling in hippocampal neurons<sup>158</sup>. Furthermore, a recent study performed by Moore et al (2018) demonstrated that knock-in mouse model of a KCC2 (T906A/T1007A), which prevents phosphorylation dependent receptor inactivation, was resistant to 4-aminopyridine ( $K_v^+$  channel blocker) induced epileptiform seizures when compared to wild types<sup>159</sup>.

Whilst dysfunctional GABAergic signalling is often the trigger of epileptic seizures, the excitatory neurotransmitter glutamate plays a pivotal role in the perpetuation of excessive synchronous activity and seizure induced brain damage. Pharmacological induction of status epilepticus (SE) for example results in excessive glutamate release which overstimulates NMDA receptors and increases the recruitment of GluN1 subunits to the post-synaptic membrane to enhance NMDA dependent synaptic activity<sup>160</sup>. The increased NMDA dependent synaptic activity can then enhance AMPA receptor mediated activity, arising from increased NMDA driven post-synaptic surface expression of GluA1 subunit, as well as a diminished expression of GluA2 subunits<sup>161,162</sup>. This chain of events can be attenuated however with the NMDA antagonist MK-801 which has demonstrated success in protecting against epileptogenesis in electrical stimulation SE and lithium-pilocarpine epilepsy models<sup>163,164</sup>. Meanwhile, ketamine demonstrates anti-convulsant effects in multi-drug resistant SE and prevents refractory SE in over 50% of paediatric and adult cases<sup>165,166</sup>. This relief to epileptic seizures is due to the prevention of ERK1/2 activation following NMDA activation which otherwise leads to the down regulation of the GABA<sub>A</sub>  $\delta$ -subunit, resulting in diminished GABAergic activity which predisposes neural networks to seizures<sup>167,168</sup>.

Remission rates in patients with epilepsy were found to be ~60% following treatment in an early study performed by Kwan P & Brodie MJ (2000)<sup>169</sup>. However, the latest pharmaceutical therapies aimed at reversing epilepsy have struggled to significantly improve upon these statistics when compared to the earliest antiepileptic drugs<sup>170</sup>. Perampanel for example is a novel competitive



AMPA antagonist and prevents seizure induction by inhibiting the synchronous firing of neurons following AMPA mediated activity<sup>171</sup>; in three phase III clinical trials, perampanel demonstrated a reduction in seizure frequency in 26.3 – 37.6% of patients with an 8mg daily dose<sup>172–174</sup>. Gabapentin on the other hand is a structural analogue of GABA however does not directly bind to GABA receptors, instead inhibiting  $\alpha 2\delta$ -1 and  $\alpha 2\delta$ -2 auxiliary subunits of voltage-gated calcium channels which attenuates calcium currents in the brain required for seizure generation<sup>175</sup>. It has also been shown to significantly increase levels of GABA *in vivo* by stimulation of GAD<sup>176,177</sup>, and the inhibition of GABA transaminase<sup>177</sup>. A meta-analysis demonstrated gabapentin reduced seizure frequency in 19.3 - 32.3% of patients<sup>178</sup>, which is comparable to that observed with the use of perampanel. Due to the multi-factorial nature of epilepsy and the number of co-morbidities associated with this disease, limited improvement in clinical outcome following further drug development is understandable. Alternative avenues of research are likely required before beneficial therapies can be realised and implemented. This may include the use of epileptic zebrafish due to the relatively high-throughput *in vivo* assays and genetic manipulation that may be performed<sup>179</sup>. Alternatively, exploring metabolic pathways through biochemical signalling, such as the use of 2-deoxyglucose (induces glycolytic restriction)<sup>180</sup>, are becoming increasingly considered as potent modulators of epileptic activity.

### 1.2.5.3 Ischaemic Stroke

Stroke can be generally described as impaired blood flow to the brain, with ischaemia typically presenting as the occlusion of the middle cerebral artery (MCA) due to atherosclerosis and/or embolism, and accounts for approximately 71% of stroke cases<sup>181</sup>. Alternative incidents of stroke present as haemorrhagic whereby weak arterial blood vessels burst and blood seeps into the surrounding tissue, and transient ischaemic attacks which are usually shorter and precede an ischaemic stroke. There are many risk factors that can predispose an individual to ischaemic stroke, some associated with life-style including diet, low level of physical activity smoking and high alcohol consumption, often resulting in atherosclerosis and/or diabetes mellitus<sup>182</sup>.

During ischaemic strokes, an ischaemic core forms around the MCA, whereby the loss of oxygen and glucose to the surrounding tissue depletes energy stores to cause irreversible damage, with potentially salvageable tissue surrounding the core regarded as the penumbra. Ischaemia triggers calcium sequestration in the immediate surrounding area in an effort to maintain  $Ca_i^{2+}$  and limit the risk of cell death, however this relies on using ATP stores which inevitably exhaust. This rapid reduction in neuroglial ATP leads to impaired functioning of the ion transporters  $Na^+ / K^+$  ATPase and

$\text{Ca}^{2+}$  ATPase, resulting in cations to accumulate within cells<sup>183,184</sup>. Then, the BBB becomes compromised following an increase in endothelial ion transporter (Na-K-Cl cotransporter; Na/H exchanger) activity resulting in  $\text{Na}^+$ ,  $\text{Cl}^-$  and water into the adjacent neuroglial tissue to cause cytotoxic edema<sup>185</sup>. The uptake of  $\text{Na}^+$  results in neuronal depolarisation, and the additional increase in  $\text{Ca}_i^{2+}$  leads to the excessive release of neurotransmitters such as dopamine and glutamate. Glutamate becomes particularly damaging to the cells within the ischaemic core due to overstimulation of metabotropic, AMPA and NMDA receptors, all of which leads to adverse signalling throughout the brain circuitry prior to ischaemic cell necrosis and development of infarction. Following cell death, cytotoxic elements such as glutamate, ROS, TNF- $\alpha$  and IL-1 $\beta$  are released into the interstitial space that can seep into immediately adjacent tissue to propagate the ischaemic cascade via over-stimulation, mitochondrial degradation and the induction of necroptotic elements such as caspase 8<sup>186,187</sup>.

In most ischaemic stroke cases affecting the MCA, patients are often treated before the ischaemic core and penumbra are able to expand into the hippocampal area, with the notable exception of stroke occurring in the posterior cerebral artery. In this instance, infarction of the adjacent hippocampus results in transient global amnesia, with symptoms ranging in severity from confusion and an inability to retain new information, to irreversible amnesia and epilepsy<sup>188-190</sup>. Even in standard cases however patients will often present with persistent episodic memory loss that can develop into vascular cognitive impairment and dementia, suggesting that local damage to cerebral tissue surrounding the MCA is sufficient to alter hippocampal function<sup>191</sup>. A recent *in vivo* study in Sprague-Dawley rats has provided some evidence of this by occlusion of the MCA (MCAO) and injection of the tracer  $\text{Mg}^{2+}$  into the entorhinal cortex to visualise hippocampal-thalamic communication post stroke via transport of  $\text{Mg}^{2+}$  through axons<sup>192</sup>. Cognitive deficits were first observed using a novel object recognition test within 28 days post-stroke, in the presence/absence of hippocampal lesions, meanwhile the  $\text{Mg}^{2+}$  signal was found to accumulate within the ipsilesional thalamus. This data suggests that whilst hippocampal projections may be preserved following MCA stroke, the retrograde projections from the thalamus are compromised, the damage is sufficient to induce memory deficits, and is supported by thalamic lesion studies<sup>193,194</sup>. The MCAO model is not a true representative of ischaemic stroke however due to the extent of damage to cerebral tissue caused by this approach and thus excludes the potential for recovery of tissue following reperfusion. Further research is therefore required to develop more precise models both *in vitro* and *in vivo*, to

elucidate the pathological changes and subtle alterations to brain circuitry following ischaemic stroke.

In 2016, reports from the GBD (2016) Stroke Collaborators revealed stroke as the 2<sup>nd</sup> most leading cause of global deaths <sup>181</sup>, in addition to the 2<sup>nd</sup> leading cause of disability adjusted life-years, highlighting the great need for treatment strategies and drug development <sup>195</sup>. Despite this, it has been well over 20 years since the last novel treatment, recombinant tissue plasminogen activator (tPA), was approved for use, with much research through 1990 into the early 2000's confounded by poor study design, both in preclinical and clinical trials <sup>196</sup>. Not all patients meet the criteria for receiving tPA due to the risks associated with haemorrhagic stroke and internal bleeding, with the remaining therapeutic options involving anti-coagulant/platelet drugs, however these do not necessarily prevent cognitive disability following treatment. Recent work on neuroprotective methods have given some success, with Riboflavin (Vitamin B<sub>2</sub>) being used to remove excess glutamate from the blood in a phase IIb clinical trial <sup>197</sup>. Intravenous administration of Riboflavin at a concentration of 5 mg/mL significantly reduced blood-glutamate levels relative to the placebo control group, with improved clinical outcome indicated by significantly reduced score in the assessed national institute of health stroke scale (NIHSS). Another approach is the use of peptide nerinetide which specifically disrupts NMDAR-PSD-95-nNOS signalling complex to prevent the neurotoxic cascade whilst permitting synaptic activity <sup>198</sup>. A recent phase III trial revealed reductions in infarct volume and mortality following ischaemic stroke following administration of nerinetide relative to the placebo group, but only when administered in the absence of tPA <sup>199</sup>. It is thought that this diminished outcome arises from plasmin (activated by tPA) cleaving the amino acid sequence of nerinetide. Whilst this requires further testing to confirm, the results suggest neuroprotection may become a viable therapeutic option in ischaemic stroke patients.

### 1.3. Tools for Investigating Neural Network Activity

Studying neural physiology typically involves investigating networks in one of three states: *in vivo*, whereby the network involved functions within a living organism, *ex vivo* which involves the isolation and study of specific brain region or hemisphere of interest) or *in vitro*, where the network has been isolated, dissociated and grown under conditions that mimic their natural microenvironment. Whilst *in vivo* research permits the most physiologically relevant microenvironment with which to study neural activity, it can be difficult to isolate specific mechanisms and interpret results due to the incredible complexity of intact neural network connectivity and functionality. Where animal models are required without the constraints of high costs and ethical barriers, *ex-vivo* models offer a good compromise by permitting research on intact cerebral tissue but with post-mortem cells displaying electrophysiological measurements quite different from that pre-mortem<sup>200</sup>. *In vitro* approaches meanwhile are less indicative of typical neural network function however permit far greater control over experimental conditions for elucidating mechanisms involved in neurophysiological and pathophysiological behaviour, and multiple tools have been developed to investigate this.

#### 1.3.1. Electrophysiological Research Tools

Neural network communication is electrochemical in nature, and so tools that can detect changes in the electrical activity of neurons can therefore be used to determine neural network function. Two common methods are used for this, namely, whole-cell patch clamping which records the activity from single cells, or multi-electrode arrays which networks are patterned on.

##### 1.3.1.1. Whole-Cell Patch Clamping

The gold standard of neuroscientific research tools is the patch clamp technique, which records electrical activity of neurons by detecting changes in membrane potential brought about by ion movement (Figure 1.8). A glass micropipette is filled with physiologically relevant solution, and a silver/silver chloride electrode is placed within<sup>201,202</sup>. This permits the exchange of chloride ions between the interface of the electrode and solution, thus currents flow through the electrode<sup>203</sup>. The membrane is effectively broken into by placing the electrode tip against the cell and exerting an inward pressure to form a giga seal. By inserting a grounding electrode in separate extracellular solution as a reference, the primary electrode can detect changes in the membrane potential that correspond to neuronal activity. The patch clamp setup can be used to interrogate neuron

electrophysiology by fixing the current flowing through the membrane (current clamp mode) and action potential firing is detected via changes in transmembrane potential. Alternatively, the voltage can be fixed to monitor changes in the current (voltage clamp mode).

Whilst whole-cell patch clamping provides neuronal activity with great temporal resolutions in the kHz range, it has a few significant drawbacks. Specifically, it requires specialist training and equipment, and most setups are limited to single cell recordings therefore can be considered low throughput.

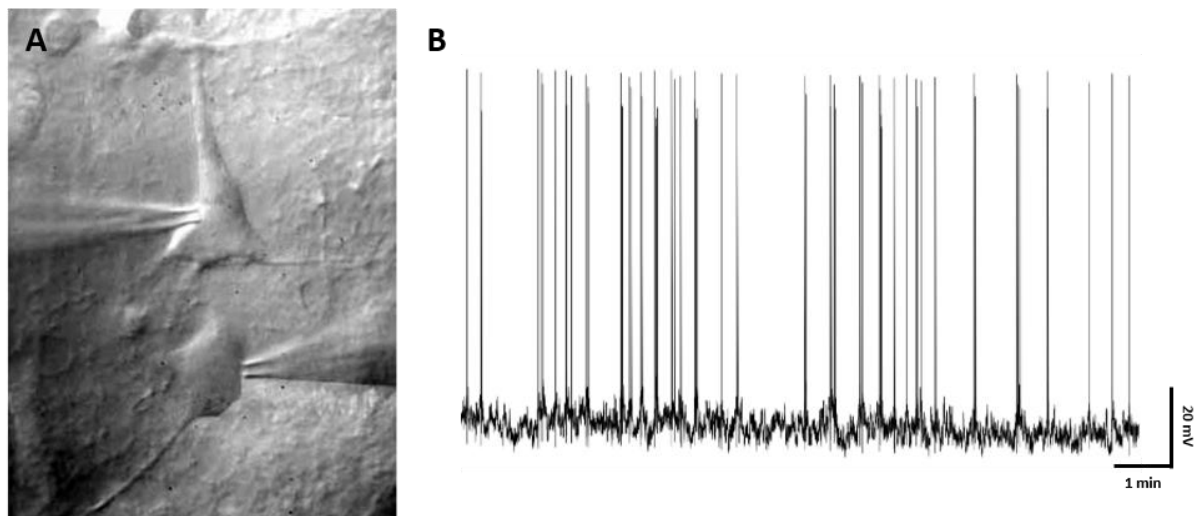


**Figure 1.8: Whole-Cell Patch Clamping Technique.** (A) An adapted brightfield image depicts glass electrodes being placed over adjacent neurons *in vitro* (Cowan A., Stricker Ch. Institute for Neuroinformatics). (B) Representative electrophysiological data obtained from a neuron during whole-cell patch clamping where baseline membrane potential rapidly fluctuates and corresponds to action potential firing (Gunhanlar N. et al (2018))<sup>204</sup>.

### 1.3.1.2. Multi-Electrode Array

A high-throughput alternative for recording electrophysiological activity in neurons is the use of multi-electrode arrays (MEAs; Figure 1.9). This is typically achieved by patterning neuronal cultures across the planar surface of the electrodes *in vitro* but may also be used with *ex vivo* brain slices or can be inserted onto the periphery of the brain *in vivo*. Assuming membranous tissue overlaps an electrode, electrochemical changes will be detected which are associated with neuronal action potentials. The polarity of the electrodes will naturally attract and repel respectively charged ions, giving rise to high electrical impedance for low-frequency signals, and low impedance for high frequency signals. Neuronal activity is brought about by action potentials that fire within milliseconds, and so MEAs are ideal for detecting these high frequency signals<sup>205</sup>.

An entire network can potentially be recorded simultaneously, and therefore offers improved spatiotemporal resolutions for neuroscientific research, as propagation of signals can be traced throughout the network. Despite their usefulness, the means by which MEAs record activity contrarily leads to some disadvantages. First, a great deal of data generated is potentially unusable, as the proximity of neural membranes to an electrode will vary considerably and may not interface at all. The electric field potential surrounding the cell typically varies with synaptic activity, however in the presence of electrodes, is diminished by the presence of the electrodes, resulting in a strong reliance on detecting high frequency signals. Consequently, it is incredibly difficult to detect sub-threshold potentials (EPSPs/IPSPs) and the researcher will therefore struggle to determine the nature of the neurons in question (Glutamatergic/GABAergic). Finally, these instruments have limited re-use, as repeated culturing and exposure to extracellular solution degrades the electrodes, making this a particularly expensive approach to neuroscientific research.

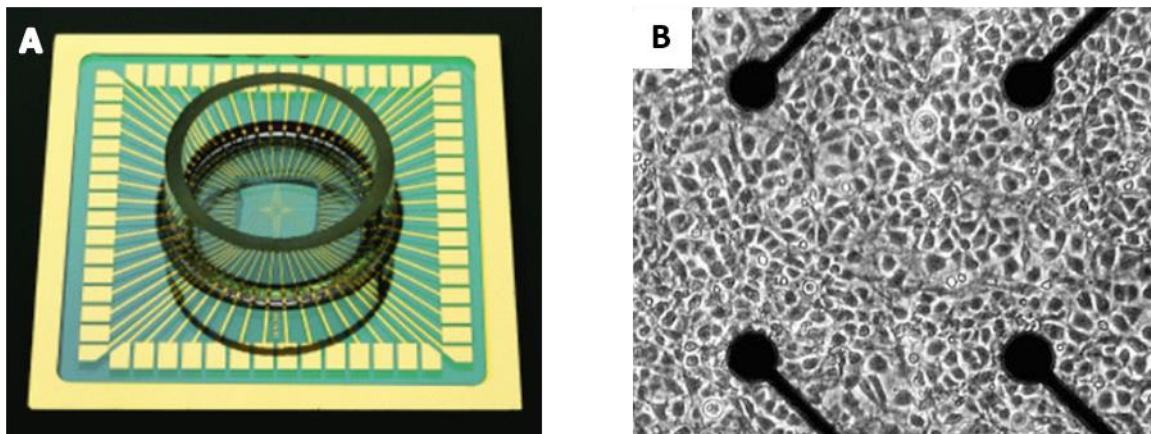


**Figure 1.9: Multi-Electrode Arrays.** (A) Adapted image of a multi-electrode array composed of 60 fabricated electrodes on glass substrate and glass ring, used for monitoring the activity of neural networks (Feber J et al (2010) )<sup>206</sup>. (B) Adapted image of cortical neurons cultured over an MEA (Potter et al (2006))<sup>207</sup>.

### 1.3.2. Optical Imaging Techniques

Fluorescent chemical dyes are designed to bind to either ions or proteins that are directly involved in cell activation and a wide variety have been developed. In principal, fluorescent dyes are versatile research tools, as they can be applied both *in vitro*, *ex vivo* and *in vivo* do not require previous extensive specialist training to use, and are relatively cheap. An alternative to the use of fluorescent dyes is the genetic manipulation of the neural network for the expression of fluorescent indicator proteins through transgenic or viral gene transfer, which permits imaging for the study of *In Vivo* models<sup>208</sup>.

#### 1.3.2.1. Calcium Imaging

Neural network activity can be monitored with the use of fluorescent probes that are sensitive to changes in the concentration of  $Ca_i^{2+}$ , otherwise regarded as calcium sensitive fluorescent dyes. As described previously,  $Ca^{2+}$  ions are prevalent during synaptic activity, caused by the large influx through voltage gated  $Ca^{2+}$  channels for action potential propagation.

There are different  $Ca^{2+}$  probes commercially available, such as the ratiometric Fura-2 which, upon binding to  $Ca^{2+}$  changes its excitation wavelength. This requires imaging to be performed using multiple wavelengths, however in turn provides a very accurate measurement of  $Ca_i^{2+}$  concentrations<sup>209</sup>. Where multiple fluorochromes are desired during calcium imaging, a long wavelength fluorochrome such as Rhod-2 may be useful, as it permits the use of GFP and lower

wavelength fluorochromes during assessments whilst providing increases to fluorescent intensity during  $\text{Ca}^{2+}$  binding. Perhaps the most commonly used however, are the Fluo-X dyes such as Fluo-4, which have been designed to provide minimal background noise, and generate large increases in fluorescent intensity upon  $\text{Ca}^{2+}$  binding.

Each calcium dye can typically be prepared as an ester or a salt. When prepared as an acetoxymethyl ester (AM), there is enhanced cell membrane permeability due to its organic nature, however this reduces its solubility in extracellular preparations. Upon entering the cell, the AM ester is cleaved by plasma esterases to reveal the charged Fluo-4 (reduces leakage from cells) which subsequently binds to freely available  $\text{Ca}^{2+}$  ions. If the dye is particularly insoluble due to its hydrophobic, organic nature, a solution is to prepare the dye as a salt (Fura-2 pentapotassium); caution should be taken when using these particular preparations in neuron cultures, as the neural network is particularly sensitive to changes in extracellular  $\text{K}^+$  concentrations.

As the fluctuation of fluorescent intensity corresponds calcium activity within the cell, calcium imaging can therefore be used to monitor the activity of individual neurons and neuronal networks *in vitro* & *In vivo* <sup>210–213</sup>. The temporal resolution offered by these dyes is limited, primarily due to a combination of fast  $\text{Ca}_i^{2+}$  dynamics, and slow dissociative constants of bound fluorochrome  $\text{Ca}^{2+}$  ion. Nonetheless, the spatial resolutions offered by this technique, in addition to permitting the activity of multiple cell types to be monitored simultaneously, makes calcium imaging an attractive, low cost neuroscientific research tool.

### 1.3.2.2. Voltage Imaging

Conventional electrophysiological techniques used to monitor synaptic activity via changes in membrane potentials are technically difficult and can be low throughput. Voltage sensitive dye imaging (VSDIs) offer a non-invasive alternative, allowing the researcher to monitor changes in the membrane potential, with the potential of a greater throughput through improved spatial resolutions, as multiple cells can be monitored simultaneously. Whilst this dye has obvious applications for proof of concept using CHO cells <sup>214,215</sup>, and investigating changes in membrane potentials within cardiac cells <sup>216,217</sup>, its use as a high-throughput tool in primary neuroscientific research is less well documented, with only several cells monitored simultaneously at any given time <sup>218–221</sup>. Where changes in membrane potentials are observed over an entire network using VSDI, a global, on/off response is typically obtained, rather than precise, high SNR action potentials visualised



for multiple cells<sup>222–225</sup>. Thus, there is scope for further investigation into using VSDIs in primary hippocampal cultures to establish high-throughput assays.

For the design of VSDs, the primary objective is to induce an altered fluorescent characteristic in response to changes in the membrane potential that the fluorochrome is bound to. This may include on/off active/resting states at voltage thresholds, re-orientation of the dye within the plasma membrane or electrochromism (Figure 1.10).

Dyes that are composed of cyanine and oxonol chromophores typically display this mechanism<sup>226,227</sup>, in which the dye moves from the extracellular space to the cell membrane during cell activation. As the dyes are charged, changes in the membrane potential will change the excitation/emission spectra, with an increase in fluorescent intensity generally observed where the dye has partitioned into the cell membrane. The mechanism of re-orientation meanwhile can be described as microscopic changes to the position of the bound fluorescent dye with respect to the plasma membrane during changes in membrane potential. This effect observed in styryl dyes such as RH421<sup>228</sup>, and the change in the electrical field results in the membrane bound dye flipping from a perpendicular orientation, to one where the dipole of the dye is parallel with the plasma membrane surface. This results in altered spectral properties and the quantity of light that is available for excitation and subsequent emission. Whilst the temporal resolutions with these dyes are favourable for monitoring action potentials (< 0.5 ms), the signal generated is quite low, (2 - 6% change in fluorescent intensity) which may influence its suitability for VSDI assessments<sup>229</sup>.

The more robust method of performing VSDI utilises dyes that exert electrochromic mechanisms of action, such as the Di-X-ANEPPS family (Di-4-ANEPP, Di-3-ANEPPDHQ etc). In this instance, the structure of the dye is composed of two sections, an electron rich aminonaphthyl moiety, and an electron deficient pyridinium moiety, separated by a series of double bonds. In the presence of a depolarised membrane potential and photons, the bound dye switches the distribution of free electrons to an excited state, whereby the aminonaphthyl moiety is positively charged<sup>227,230,231</sup>. As the dye molecules are amphiphilic in nature, they are anchored perpendicular to the plasma membrane, thus, the direction of electron transfer of the dye is parallel with the exchange of ions through the plasma membrane. As the grounded and excited states of the dye are relative to changes in membrane potential, the spectral properties of these dyes respond in kind to membrane depolarisation & hyperpolarisation.

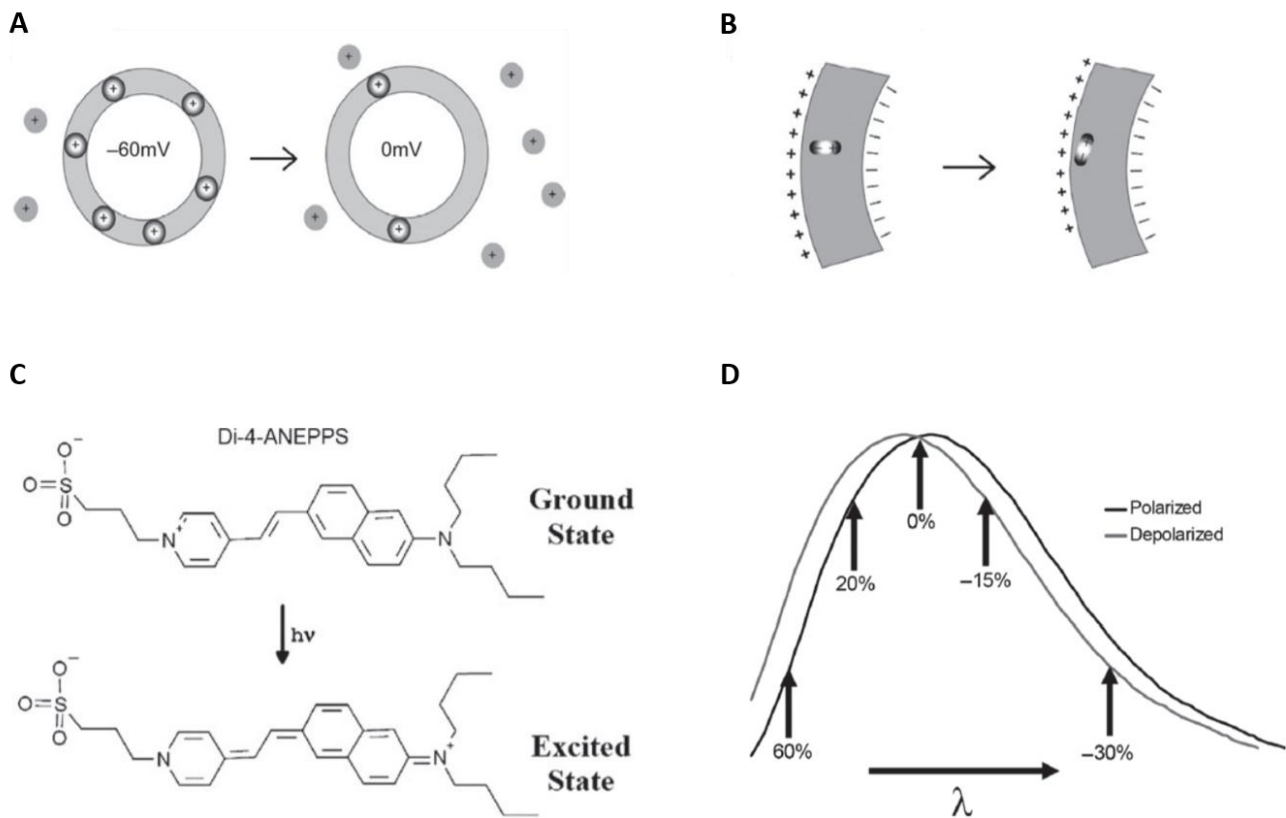


**Figure 1.10: Voltage Sensitive Dye Mechanisms of Action; images adapted from L. Loew (2010) <sup>227</sup>.**

(A) The On-Off mechanism demonstrates the movement of the VSD between the extracellular space and plasma membrane during resting and excited membrane potentials. (B) The re-orientation mechanism demonstrates the change in alignment of the fluorescent dye, relative to the membrane during membrane potential change. (C) The VSD Di-4-ANEPPS is used to demonstrate the electrochromic effect, whereby electrons are re-distributed between the aminonaphthyl and pyridinium groups during changes in membrane potential. (D) The spectral properties of the dye are subsequently affected, whereby a shift in the excitation/emission spectra (typically 5-15 nm) are observed. The changes in fluorescent intensity are expressed as a percentage relative to a specific wavelength range used between polarised and depolarised states.

### 1.3.3. Genetic Manipulation

An additional avenue of neuroscientific research is genetically manipulating proteins of interest within sub-populations, or across entire networks, an approach which is typically undertaken during proof of concept or mimicking disease models. This introduction of foreign protein, or indeed their removal, can be facilitated by different methods, transgenic, viral transduction and liposomal delivery as the most common examples. One specific example of genetic manipulation is chemogenetics, a relatively new neuroscientific tool undergoing development. Whilst this is further discussed in Chapter 5, chemogenetics demonstrates usefulness because it can be used in addition to the traditional methods of electrophysiology and optical imaging techniques to gain further insight into physiological and pathological signalling mechanisms.

#### 1.3.3.1. Viral Transduction

Viral vectors may also be used to infect/transfer foreign DNA into mammalian cells, a process regarded as viral transduction, and is currently the primary research tool for gene therapy. First, a plasmid is constructed in which the gene of interest is flanked by viral sequences that are recognised by viral proteins and packaged into virions. Then, the virions adhere to the cell surface and are drawn into the cell by endocytosis where the outer capsid is broken down to release the plasmid DNA which is delivered to the nucleus for transcription.

Whilst plasmids containing DNA for the formation of new infectious virions may be delivered to the cell, the responsible sequence is modified by the removal of gene segments to prevent the virion population growing exponentially. One common virus used in neuroscientific research is the lentivirus, which expresses reverse transcriptase (viral RNA to DNA conversion), integrase (insertion of viral DNA into host genome) and establishes stable transgenic expression. Unlike other retroviruses, lentiviruses do not discriminate between post/mitotic cells, thus make an obvious candidate for the infection of neurons<sup>232</sup>. In contrast, adeno-associated viruses (AAV) contain a single strand of DNA and are not pathogenic in nature as it is a contaminant of the adenovirus, rather than a derived pathogen<sup>233</sup>. However, the DNA will only integrate at a specific location on the genome, the AAVS1 locus of chromosome 19, which permits transgene insertion without harming cells<sup>234</sup>.

Additionally, it requires helper plasmid genes from adenoviruses to package the transgene of interest. The AAV used in assessments contain modified genes termed Rep and Cap which are required for integration and replication, but are otherwise deleted for the most part to prevent the helper plasmid promoting further replication of new virions, significantly limits AAV integration into the genome, whilst permitting gene insertions up to 4 kb long <sup>235</sup>.

There are numerous advantages of using lentiviral and AAV transduction as methods of genetic manipulation; high levels of transduction efficiency can be achieved both *in vivo* & *in vitro* <sup>236,237</sup>, they can transfect both mitotic glial cells and post-mitotic neuronal bodies, and can target sub-population from particular pathways specifically <sup>238</sup>. Disadvantages of this approach include the relative lack of experimental control over the virus once it has infected the tissue/culture, they are expensive to perform due to the inherent inability to replicate and replenish stocks, and immunogenicity can develop *in vivo* <sup>239</sup> which potentially invalidates results obtained.

### 1.3.3.2. Liposomal Transfection

There are numerous non-viral means by which one can introduce foreign genetic material into a cell, including electroporation (use of electric pulses to deliver DNA to cells), calcium phosphate transfection (direct cellular uptake of DNA trapped within the precipitate of  $\text{Ca}^{2+}/\text{K}^{+}$  ions in solution). Liposomal transfection (Lipofection) involves the use of lipid complexes for the delivery of DNA, and is considered to be the most routine, non-viral method of gene delivery due to its general simplicity and use across a broad range of cell types.

Liposomes are composed of cholesterol and phospholipids, and the type of lipid has a large impact on its integrity and solubility. The use of dipalmitoylphosphatidylcholine for example is a saturated phospholipid and increases the impermeability of the liposome bilayer <sup>240</sup>; increasing the complexity of the acyl chain has been shown to improve the stability and phase transition temperature of liposomes, as the hydrophobic chains are densely packed at the exterior surface <sup>241</sup>. Due to their amphiphilic nature, in the presence of an aqueous solution, the self-assembly of lipids and their thermodynamic phase properties results in the formation of spherical bilayers, known as lamellae. Ranging in size from about ~30 nm to several  $\mu\text{m}$ ., the hydrophilic phosphate headgroups are arranged to face the interior and exterior aqueous phase (Figure 1.11).

Liposome-DNA complexes are formed passively by the formation of liposomes in the presence of the DNA in solution; the negatively charged DNA interacts with the phosphate head group of the lipids and become effectively trapped within the centre of the liposome sphere <sup>242,243</sup>.

When the liposome-DNA complex is applied to cells, one of two reactions typically occur; direct fusion with the cell membrane or endocytosis. Liposomes may directly fuse with the cell membrane using certain compositions, for example where charged lipids (negatively charged phosphatidylserine) are used, application of the complex in a liquid-crystalline state, or reduced molar ratios of cholesterol used in the preparation of liposomes <sup>244</sup>. One means by which fusion interaction is considered to occur is fluid phase endocytosis, where adhesion at the surface between adjacent cells creates a bridging effect which enlarges during interactions between the lipid membranes until complete fusion occurs and the contents of the liposome are released into the cytoplasm <sup>244,245</sup>. Receptor mediated endocytosis is considered to be the more common interaction between liposome-DNA complexes and the cell membrane, which relies on regions of the membrane where small pits or indents are lined with clathrin proteins. These areas permit the assembly of intracellular vesicles composed of adaptin, dynamin and rab proteins, which facilitate the binding of the liposome to the cell membrane, followed by internalisation within an endosome. It is considered that the liposome trapped within the endosome is degraded under enzymatic processes regulated by lysosome activity, and those that escape this fate interact with anionic lipids present in the cell membrane <sup>246,247</sup>. This results in the degradation and loss of liposome integrity, and the DNA is released into the cytoplasm.

Liposomal delivery of foreign DNA/RNA has been used to investigate a variety of signalling pathways and mechanisms within neural circuitry. Pellegrino et al (2011) for example assessed the neuroprotective effects of potassium chloride co-transporter (KCC2) during toxic insults of NMDA in hippocampal cultures, using lipofectamine to silence KCC2 with shRNAs <sup>248</sup>. Other uses of liposomal delivery includes the investigation of potential treatments in Alzheimer's <sup>249-251</sup> and Parkinson's disease <sup>251,252</sup>, dendritic growth during suppressed network activity <sup>253</sup>, and development of gene delivery strategies through the BBB <sup>254</sup>.

The advantages of liposomal gene delivery are that it can be used to deliver both genetic material or therapeutic agents to a variety of different cell types and is comparatively cheaper when compared to viral and transgenic approaches. Additionally, one has near full control over the experimental conditions when using liposomes, typically presents with low toxicity and does not induce an immune response<sup>255,256</sup>. The primary disadvantage with this approach is the highly variable transfection efficiency, with mitotic cells displaying greater transfection efficiencies than post-mitotic cells. Other disadvantages include low solubility, a short half-life, and may be degraded completely by endolysosomal pathway.

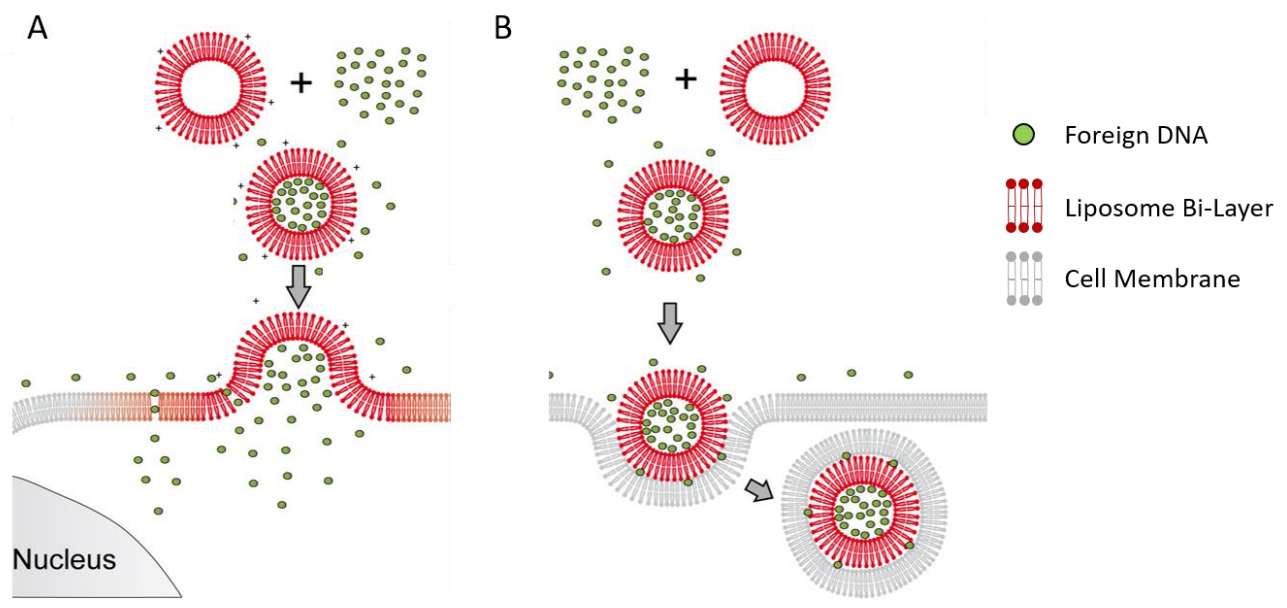


**Figure 1.11: Liposomal Gene Delivery; images adapted from S. Kube et al (2017)<sup>257</sup>.** Liposomes form complexes with DNA in solution which, upon application to cell culture, can either: (A) directly fuse with the cell membrane, releasing the foreign DNA into the cytoplasm immediately; (B) adheres to surface proteins on the cell surface membrane where it is internalised within an endosome where degradation by interactions with anionic lipids degrades the liposome to release DNA.

## 1.4. The Current Challenges of Neuroscientific Research

The prevalence of CNS disorders is on the rise, due to a combination of an ever-increasing elderly population, hereditary acquisition through an increasing population, diet and awareness programs. In 2017, a retrospective review performed by the GBD 2015 Neurological Disorders Collaborator Group revealed CNS disorders as currently the leading cause of disability adjusted life-years, and the second most common cause of leading global death (9.4 million) <sup>258</sup>. This is an increase of ~36.7% over rates observed in 1990, which is a stark contrast to reductions in CNS related deaths when standardised against age (-26.1%). To put this problem in the perspective of economic burden, a previous report indicated that dementia alone was costing the UK an estimated £26 billion in 2014 <sup>259</sup>, whilst common CNS disease (dementia, epilepsy, stroke etc) costing the USA nearly \$800 billion in the same year <sup>260</sup>. There is a clear need to address this growing issue, which is only exacerbated by larger pharmaceutical companies such as Pfizer, GSK and Merck reducing the number of CNS drug development programs in excess of 65% between 2009 and 2014 alone <sup>261</sup>.

The brain could be described as the most complex object in the known universe; weighing a mere ~ 1.4 Kg, it contains an estimated 100 billion interconnected neurons across multiple networks, each of which holds a distinct physiological function and susceptibility to disease. Researching the brain, even in the absence of CNS disorders, presents a major challenge. *In vivo* studies offer fantastic opportunities to observe function under neuro/pathophysiological conditions, however interpretation of the data observed and translation into clinical trials is often confounded by either the complexity of the neural microenvironment, or the inability to perfectly encompass the human CNS disease using animal models. In contrast, *in vitro* studies, whilst considered to have diminished translational value, have allowed the study of specific cellular mechanisms and systems under controlled experimental conditions. Standardised methods of neuronal culture and research tools such the patch clamp technique, Ca<sup>2+</sup> imaging and water bath perfusion systems, whilst providing the foundations of neuroscientific research over the last century, face their own limitations. This may include low data through-put, suboptimal spatiotemporal resolutions, low drug perfusion precision and the inability to investigate neurophysiological systems over multiple networks.

Microfluidic technology, initially developed for molecular analysis using systems such as capillary electrophoresis and gas-phase chromatography, has emerged as an ideal platform for conducting *in vitro* neuroscientific research over the last two decades. Its rise has been attributed to the integration and improvement upon the traditional research tools within these microsystems, in

addition to improving experimental control and the architecture of increasingly complex cultures. In the following sections, I will discuss examples of its current application in neuroscientific research, and outline avenues of further development relevant to this thesis.

## **1.5. An Introduction to Microfluidics**

The field of microfluidics pertains to the study of fluid manipulation within the microenvironment (and its lower dimensions), typically working in the range of 1  $\mu\text{m}$  to 1000  $\mu\text{m}$  and has observed steady advances in this field over the last few decades. The origin of microfluidics first began with the improvement of microelectronics, specifically the development of photoengraving (photolithography) to allow for finer details when patterning printed circuit boards for the purpose of telecommunication and through this, permitted semiconductors to be fabricated from silicon <sup>262</sup>. Further developments would see its use in the emergence of inkjet printing where photolithography was used to fabricate an array of inkjet nozzles on a single silicon wafer, illustrating the use of silicon wafers to mass produce microfluidic devices <sup>263</sup>. The LIGA (Lithographie, Galvanoformung, Abformung; Lithography, Electroplating, Moulding) process would later add an electroplating step after photolithography to create moulds that could produce multiple replicate devices from the original master. This involved depositing a thin layer of nickel-vanadium (NiV) onto the master wafer via sputter coating, followed by a thicker layer by electroplating, an approach which is used for injection moulding biomimetic surfaces <sup>264</sup>. Soft lithography <sup>265</sup> was a family of techniques such as micromoulding capillaries <sup>266</sup>, replica moulding <sup>267</sup> and microcontact printing <sup>268</sup>, developed to permit fabricated replicates of microfluidic devices with well-defined geometries using 'soft' elastomeric materials such as polydimethylsiloxane (PDMS), cross-linked Novolac<sup>TM</sup> resin, polyamides and polyurethanes.

Additional developments that have had a large impact on sample processing, cell biology and pharmacology studies include the incorporation of valves and pumps. In 1979, Terry et al introduced sample injection valves into their silicon wafer fabrication to permit molecular analysis using gas chromatography <sup>269</sup>, and those that followed were of a similar diaphragm design. These early designs required large pressures to actuate the parts and control air flow, and was improved upon by Jerman whereby the valve was controlled by electrostatic forces via heated bimetallic contacts, with the inlet pressure applied through the topside of the actuator <sup>270</sup>. Through this, the valve was resistant to the effects of inlet pressure pulses when closed, as observed in earlier electrostatic valve designs, and provided stable flow control amenable for micro-electromechanical applications. Building upon valve



designs, researchers sought to miniaturise pump systems that could be incorporated into a single device for greater control over fluid applications. One of the first to be created was the piezoelectric micropump created by Smits that could achieve steady flow rates of up to 100  $\mu\text{l}/\text{min}$  which had immediate applications in the medical device industry (diabetes mellitus/cancer drug delivery) <sup>271</sup>. Fluid handling was further improved with the introduction of peristaltic pumps which can be used to induce net flows through phasing of actuators with great precision, with Berg et al demonstrating a two stage peristaltic micropump that could deliver a steady, small flow of 0.1  $\mu\text{l}/\text{s}$  with negligible backflow (hydrostatic backpressure relative to the actuator source pressure) <sup>272</sup>. With the rapid advances in microfluidic technology over the last few years and indeed, the speed at which different systems may be prototyped, microfluidic devices offer distinct advantages to neuroscientific research over traditional methods. A standardised approach to performing microfluidic assays is through the use of PDMS based microfluidic devices, which are typically fabricated by soft lithography techniques. Their popularity stems from their low toxicity, translucence and gas-permeable nature, permitting the maintenance of cultures over extended periods of time and the performance of optimal imaging assessments <sup>273</sup>. Additionally, the composition of PDMS, whilst relatively firm to stabilise the microfluidic compartments contained within, is relatively malleable, allowing the research to manually create inlets and outlets throughout the structure to permit additional manipulation of the cultured microenvironment. PDMS based device usage does come with caveats, for example the hydrophobicity and protein adsorption can limit their applications in molecular biology and pharmacology, meanwhile the high cell number to volume ratio in the culture chambers results in frequent re-feeding of cultures. Examples of PDMS based devices include the dual microfluidic chamber device, first conceptualised by Taylor et al in 2003 <sup>274</sup>, to permit the assessment of multiple cultured neural networks within isolated compartments that are connected across an array of microchannels. The compartments were spacious enough to visualise thousands of cells in each chamber, and the microfluidic array dimensions restricted enough such that neuronal/glial projections may enter exclusively. This could therefore be considered as the first step towards mimicking the compartmentalised nature that the sub-regions comprising the brain display. Since then, a vast number of studies have taken advantage of this simple approach, either modifying the design slightly to suit experimental requirements <sup>275,276</sup>, or expanding upon the approach further, such as Honegger T et al (2016) that patterned four separate networks across MEAs <sup>277</sup>.

### 1.5.1. Microfluidic Devices for Neural Network Culture

Using microfluidic devices, it is possible to assess the interactions between a combination of different cell types, which may include custom artificial networks for the sake of demonstrating proof of concepts, or those that more closely resemble the *in vivo* microenvironment for assessing specific activity. This may be as simple as assessing the connectivity between two single cell types; Gao et al (2016) for example grew isolated neuron and glial cells within separate, adjacent compartments<sup>278</sup>. The frequency and amplitude of glial calcium transients significantly increased in the presence of neuronal bodies (co-culture), and more so when exposed to neuronal projections (separate cultures) alone (Figure 1.12). An alternative approach by Shi et al (2013) demonstrated the importance of glial-neuron co-cultures on synaptic integrity using three distinct methods; neuronal cultures exposed to glial conditioned media, independent neuron/glial cultures within a sandwich microfluidic culture chamber, and independent neuron/glial cultures in adjacent culture chambers<sup>279</sup>. Using Ca<sup>2+</sup> imaging techniques, the presence of glial cells significantly increased the presence of synaptic contacts and dendritic spines (as identified by neurons selectively stained for mCherry/GFP synaptophysin), when compared to neurons treated with glial conditioned media alone. Additionally, a 1.5-fold increase in synaptic contact preservation was observed over time in the co-culture groups when compared to the conditioned media treatment group, further revealing the importance of glial presence in the formation of stable synapses between neural networks.

Other methods of neuronal culture within microfluidic devices may include organotypic slice preparations and 3-D cultures. As proof of concept, Berdichevsky et al (2009) took advantage of the environmentally isolated chambers to culture hippocampal slices on either side of a microfluidic array, whereupon synchronous activity between slices was detected beyond 16 days *in vitro* (DIV), identified using microelectrodes inserted within the CA1 subregion<sup>280</sup>. In the attempt to create realistic models of the functional brain, researchers have turned to the formation of 3-D neural networks. When neurons are grown within matrigel, they naturally form 3-dimensional circuits, however without stimulus, neurite growth can often appear disorganised, even with the aid of micropillars and microchannel arrays. By applying a volumetric gradient on either side of a compartment containing the 3-D network grown in deformed Matrigel, Bang et al (2016) demonstrated the formation of highly organised neurite bundles, with directed growth in line with the gradient<sup>281</sup>.

Developing culturing techniques at higher degrees of organisation are an important step towards bridging the gap between *in vitro* and *in vivo* studies. However, there are still many mechanisms that are yet to be fully understood using monolayer culture techniques, and the increasing complexity of neural networks may result in misinterpretation of results obtained prematurely.

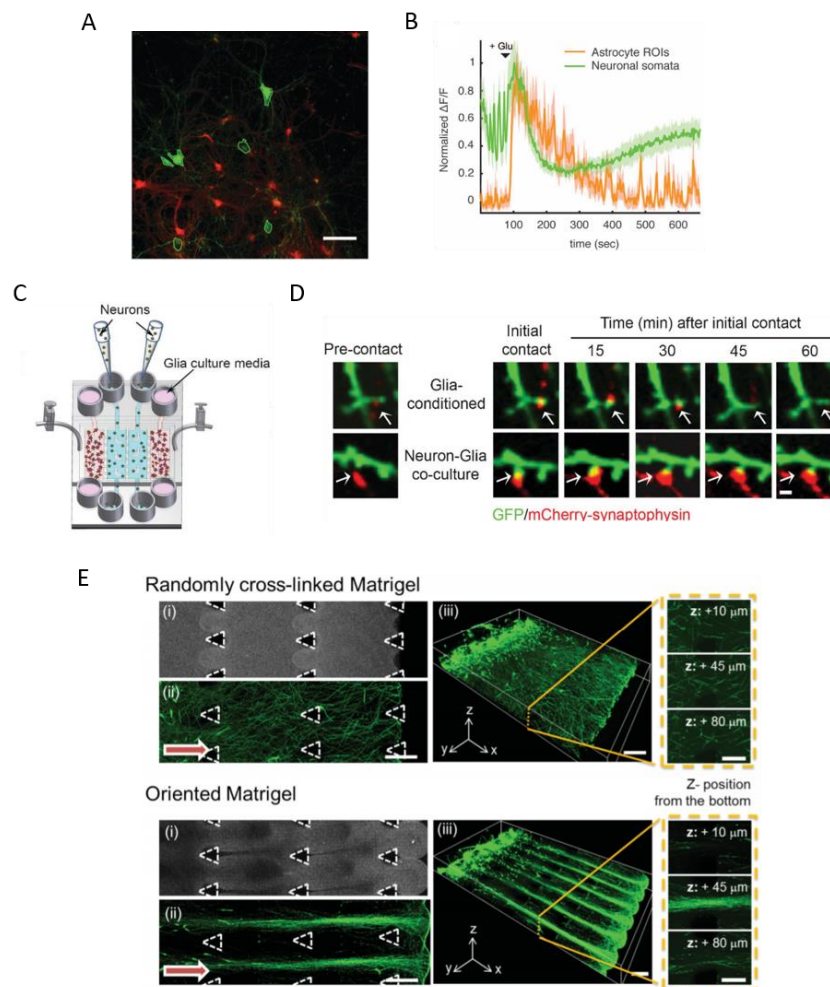


**Figure 1.12: Microfluidic Neural Networks.** (A, B) Microfluidic neuron-glia co-cultures reveal rapid calcium transients in response to glutamate during  $Ca^{2+}$ , followed by spontaneous glial activity. (C, D) Adjacent cultures of neurons and glial cells in a quad-chamber microfluidic device results in the preservation of synaptic contact between neuronal networks. (E) Axonal projections grown within a matrigel may be manipulated by volumetric gradients to establish oriented, highly structured neurite bundles. (A) Scale Bars = 100  $\mu\text{m}$ ; (E) Scale Bars = 200  $\mu\text{m}$  (ii, iii) & 100  $\mu\text{m}$  (i-iii, dashed box). (A, B) Images taken from Gao et al (2016)<sup>278</sup>; (C, D) Adapted images taken from Shi et al (2013)<sup>279</sup>; (E) Image taken from Bang et al (2016)<sup>281</sup>.

### 1.5.2. Investigating Neuronal Projection Development and Pathogenesis

Axons present a major focus for neuroscience research because of their integral role in communication. Whilst the peripheral nervous system can recover from insults with modest degrees of regeneration, axonal projections within the CNS are can become damaged and unable to restore functional communication across the original synapses. Microfluidic devices present as ideal tools for the isolation and investigation of neuronal projections, because of the ease at which networks may be patterned and manipulated according to the device design.

The first device used to examine neurites was the Campenot chamber, developed in 1977 by Robert B. Campenot whereby an array of channels was constructed using a series of insect pins to guide neurite growth of neurons grown on a collagen-coated coverslip, with a Teflon divider used to environmentally isolate three independent sections. With neuronal cultures grown in the central chamber in the presence of nerve growth factor (NGF), neurite growth could be manipulated to traverse into an adjacent chamber, but only following application of NGF, and withdrawal of NGF from the chamber resulted in gradual neurite degeneration<sup>282</sup>. Since then, researchers have taken advantage of soft lithography to study and manipulate neuron projection growth in microfluidic devices. The original two compartment PDMS-based device by Taylor et al (2003) demonstrated, as proof of concept, the ability to culture viable neurons within a single chamber and observe neuronal projections across the microfluidic array (75  $\mu\text{m}$  wide), within the adjacent, non-cultured chamber<sup>274</sup>. A similar device was then used to demonstrate axonal guided growth via the establishment and maintenance of a volumetric gradient across the somal-neurite compartments<sup>283</sup>. The microfluidic array was also extended, such that lengths greater than 450  $\mu\text{m}$  excluded dendrite, but not axonal growth beyond the array and into the non-cultured compartment (Figure 1.13). This would be of importance to future microfluidic-neuroscience research, as this simple modification to device design ensures that inducible communication between two neural networks is axonal dependent, and not the consequence of retrograde activation via dendritic stimulation<sup>276,284</sup>. Using this device, axotomy was performed via vacuum aspiration applied to the axonal compartment, which resulted in the transcription of GADPH associated with pro-apoptotic mitochondrial activity<sup>285</sup>. This device was then further modified to include microfluidic perfusion across the microarray to manipulate synaptic protein expression<sup>286</sup>. During glutamate perfusions,  $\text{Ca}^{2+}$  imaging revealed sharp increases in projection fluorescence and a gradual increase in somal fluorescence (due to dendrite stimulation). Spaced glutamate perfusions revealed a

significant increase in pCREB expression, demonstrating that modest activation encourages neurons to express additional glutamatergic receptors which is fundamental to long-term potentiation in neural networks<sup>287</sup>. This is further verified by other studies demonstrating reductions in pCREB are observed in Alzheimers disease, in which synaptic plasticity and long-term potentiation is lost during disease progression<sup>288</sup>.

A very novel approach of manipulating axonal development was demonstrated by Honnegar et al (2016) in the absence of chemotaxis or volumetric gradients, instead using voltage applied electric fields to stimulate unidirectional axon growth. Neural networks were patterned across MEAs, with collagen used not only as an environmental barrier to separate the two adjacent chambers, but as a matrix for 3-D neurite growth. By increasing the voltage applied to the electric field (1-3 V), the speed at which neurites were observed to grow towards the field increased. Further investigation revealed the strength of the electric field had a repellent effect on neurite growth, where neurite growth rises in height (z). Increases in the number of neurites produced by networks, and the speed at which they grow had already been established previously, and the effects abolished with the treatment of lectin Concanavalin A<sup>289</sup>. Applying voltage across the electric field was then used to manipulate and focus neurite growth across four neural networks. This approach could be expanded upon in the future to assess activity in response to stimuli across multiple interconnected, different networks, which more closely resemble the functional brain.

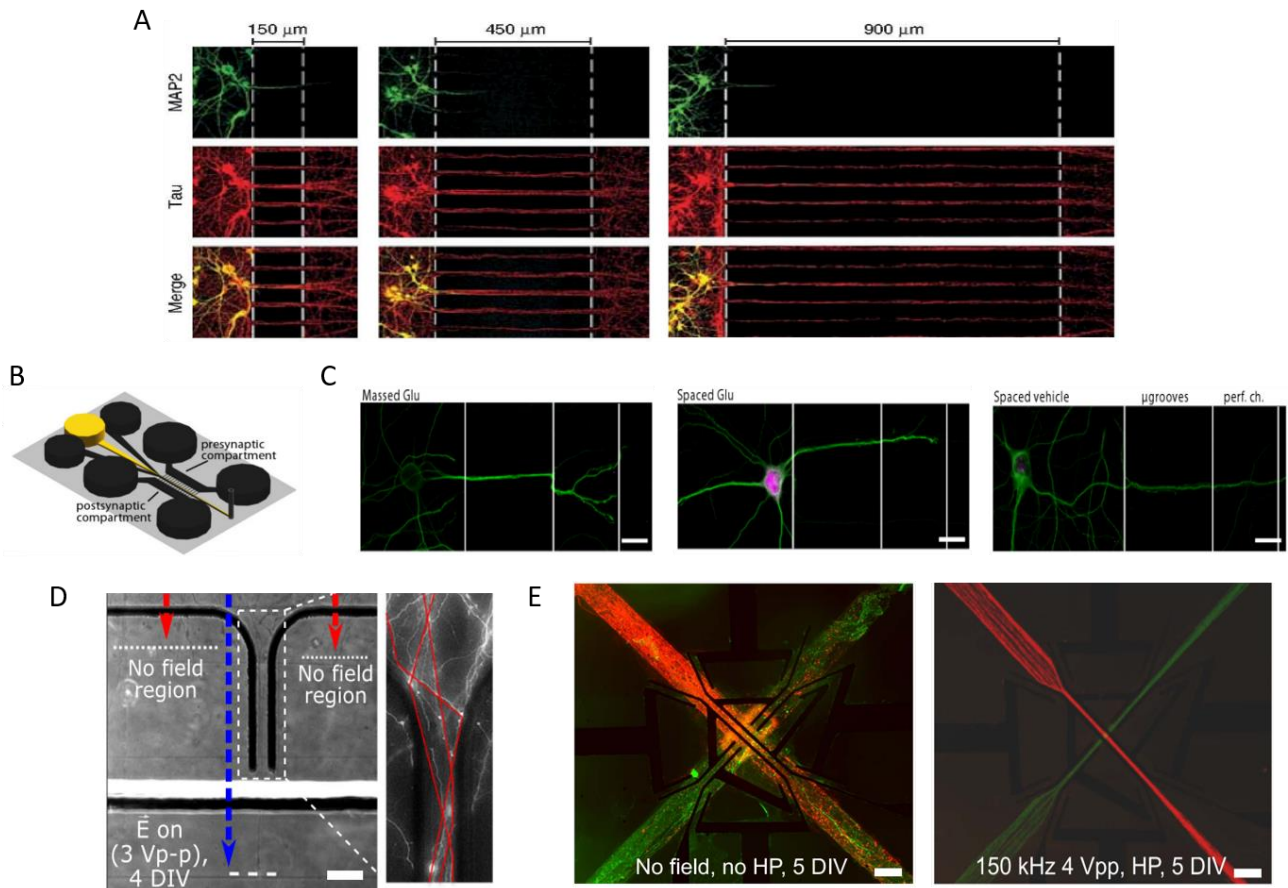


**Figure 1.13: Microfluidic Axonal Isolation.** (A) When the microfluidic array width is within 200  $\mu\text{m}$ , neuronal dendrites (identified by MAP2; green) can traverse through to the non-cultured, adjacent chamber alongside axonal projections (identified by Tau; red). When the width is increased beyond 450  $\mu\text{m}$ , only axons are present within the adjacent chamber. (B, C) The microfluidic perfusion device developed by Taylor et al (2010) is used to deliver glutamate perfusions through the microfluidic array. Spacing glutamate perfusions results in an increase in pCREB expression (purple) within the neuronal soma (identified by MAP; green); (D) Directed growth of neurites is induced by the application of an electric field when networks are patterned across MEAs. (E) Application of electric fields can stimulate randomised neurite growth patterns into highly organised neurite bridges from multiple neural networks (Network A – red; Network B – green). (C) Scale Bars = 20  $\mu\text{m}$ ; (D) Scale Bars = 50  $\mu\text{m}$ ; (E) Scale Bars = 100  $\mu\text{m}$ . (A) Image taken from Taylor et al (2005)<sup>283</sup>; (B, C) Images taken from Taylor et al (2010)<sup>286</sup>; (D, E) Images taken from Honegger et al (2016)<sup>277</sup>.

### 1.5.3. Manipulation of Microfluidic Neural Network Activity

Assessing network activity within microfluidic devices is typically performed by the *in situ* application of a stimulus, with readouts obtained using  $\text{Ca}^{2+}$  imaging or electrophysiological techniques. Such assessments are fundamental in determining the mechanisms by which neural networks communicate with each other in complex systems, which is otherwise impossible to achieve using traditional *in vitro* methods. Small changes in volumes confined to a given chamber can induce significant effects on microflows within the device however, and so care should be taken adjusting volumes during experimental setup. Fluidic Isolation was initially demonstrated by Taylor et al (2003) using the dual chamber by establishing volumetric gradients across the microfluidic array, such that fluorescein applied to the neurite chamber was unable to traverse the array against the flow of PBS <sup>274</sup>. This approach was later adapted by Graham et al (2014), who demonstrated functional communication between two environmentally isolated networks within dual chamber microfluidic devices(Figure 1.14) <sup>275</sup>. In this instance, glutamate application was restricted to the stimulated network which resulted in the indirect, synaptic activation of the naïve, adjacent neural network.

Alternatively, valves and lasers may be incorporated into the microfluidic assay design to manipulate network activity. The use of solenoid valves for example was employed by Kamudzandu et al (2019) to enable the controlled delivery of TTX solutions to specific networks within a multi-compartment device <sup>290</sup>. By alternating TTX application between cortical, striatal and globus pallidal networks, different patterns of waveform between interconnected neurons were observed (as measured by  $\text{Ca}^{2+}$  imaging). TTX application in the globus pallidus for example attenuated oscillations within the substantia nigra, whilst this was less evident with TTX application in the cortical network. Another study, performed by Renault et al (2015), combined  $\text{Ca}^{2+}$  imaging with optogenetics to induce network activation in the absence of a chemical stimulus, thereby negating the need for volumetric gradients and fluidic isolation <sup>291</sup>. By exposing Channelrhodopsin transfected neurons to brief pulses of blue light, bursts of activity through the activation of light-gated  $\text{Na}^+$  channels, as revealed by increases in calcium dependent fluorescence, were observed. When this stimulus was applied to a single neural network, increases in fluorescence were observed in the adjacent network, thereby demonstrating functional synaptic communication between the microfluidic networks.

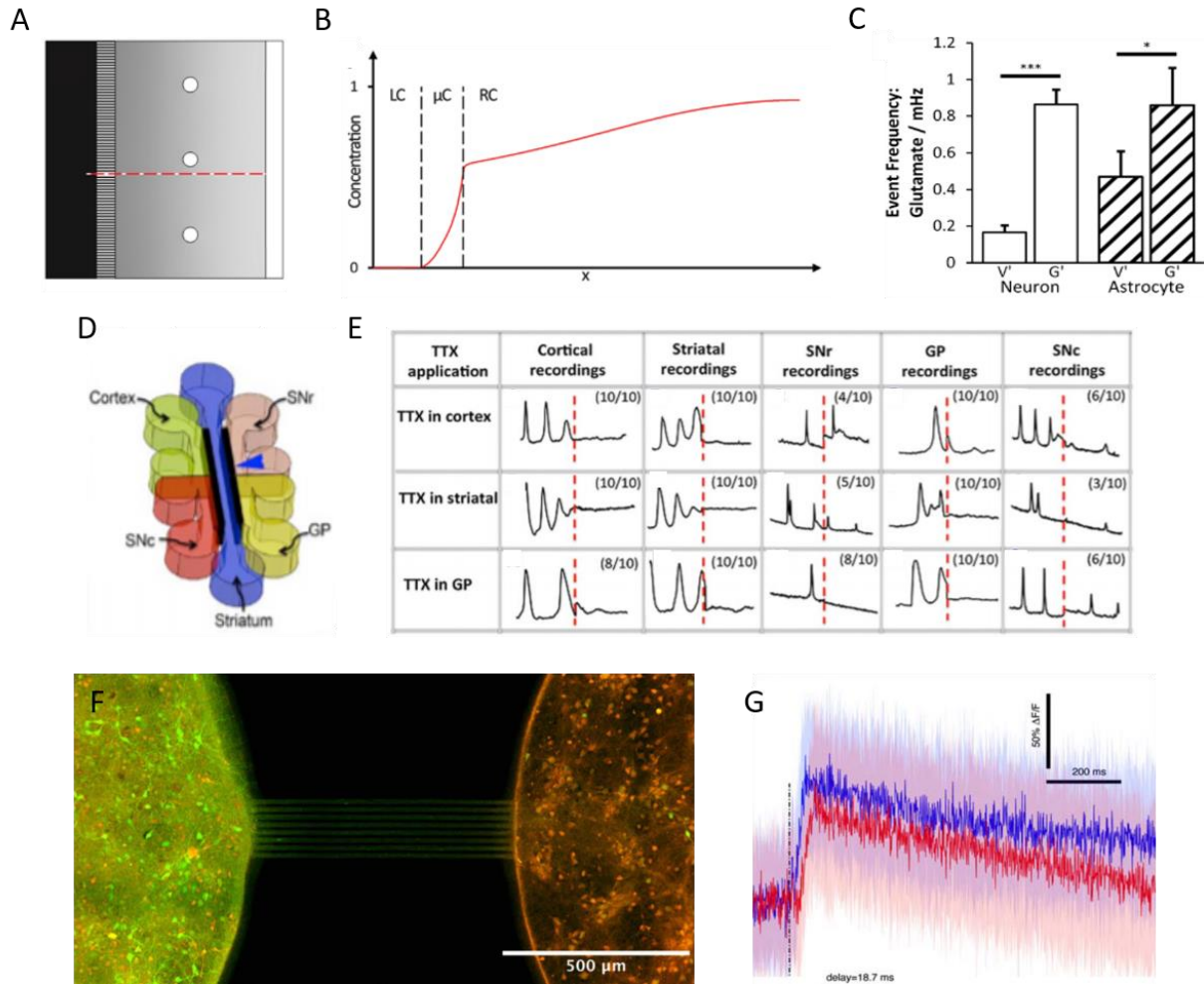


**Figure 1.14: Stimulation of Microfluidic Networks.** (A, B) Fluidic isolation, established by volumetric gradients, is demonstrated by the absence of fluorescein within the left culture chamber (LC). (C) Direct stimulation of a neural network with glutamate application results in significant increases in neural network activity within the adjacent network, relative to vehicle controls. (D) A representative image of the multi-compartment microfluidic device depicts the positions of different, interconnected primary networks. Differences in representative calcium oscillations are identified following attenuation of activity by TTX application (red dashed line), dependent on the targeted neural network. (E) An image depicting two connected neural networks stained with calcium orange indicator (orange cells), the left network of which is transfected with Channelrhodopsin (ChR2-YFP; yellow cells). (F) Representative traces depict activation of a transfected neuron (blue trace) in response to blue light stimulation (dashed line), and the subsequent activation of cell within the adjacent neural network. (A-C) Images were taken from Robertson et al (2014)<sup>275</sup>; (D, E) Images were taken from Kamudzandu et al (2019)<sup>290</sup>; (F, G) Images were taken from Renault et al (2015)<sup>291</sup>.



#### 1.5.4. CNS Pathologies: From Microfluidic Devices to *In Vivo* Models

The ultimate goal of neuroscientific research with microfluidic technology is to better understand CNS pathologies, with the potential of developing therapeutic strategies that may be assessed *In Vivo*. Whilst modelling certain diseases such as Epilepsy<sup>292</sup>, Parkinson's<sup>293,294</sup> and Multiple Sclerosis<sup>295</sup> on microfluidic devices are still in their infancy, Alzheimer's disease has received significant attention, with numerous methods developed to characterise this condition<sup>296–301</sup>.

In line with the focus on tau propagation as the suspected predominant factor responsible for Alzheimer's disease, Wu et al (2016) undertook a multi-stage approach by first, assessing tau pathologies in microfluidic devices, then, replicating these findings *in vivo*<sup>300</sup> (Figure 1.15). In brief, mixed primary hippocampal and cortical neurons from mouse lines encoding YFP labelled tau protein, were cultured in bi/tri compartment microfluidic devices and formed connections across the separating microfluidic arrays. Treatment of the first network (fluidically isolated) with tau clone 9 seeded lysate induced perinuclear aggregate formation, and accumulation of tau then observed within the cytoplasm of neurons, followed by aggregation, then observed in the subsequent, adjacent compartments over time. It was then demonstrated that hyperactivity of neurons, induced by picrotoxin application, significantly increases the extracellular release of tau in networks derived from wild type mouse lines, over-expressing human tau (rTg4510) mouse lines, and human iPSC neurons. Extracellular tau contained within conditioned media was also confirmed to propagate tau aggregation in donor neurons. Finally, tau propagation was assessed in rTg4510 & MAPT<sup>-/-</sup> (tau knockout) mouse lines transfected with Channelrhodopsin, following optogenetic stimulation of the hippocampus within a single hemisphere. Neuronal activation was confirmed via implanted electrodes and after 20 days of stimulation, the brain was dissected and stained with tau antibodies. Tau pathology and hippocampal atrophy, particularly within the stimulated hemisphere, was identified, and otherwise absent within the tau knock-out brain. These observations were replicated using chemogenetics as an additional approach to stimulation, however the rate of hippocampal degradation was lower when compared to optogenetic approaches. The model presented in this study demonstrates many of the cellular hallmarks and proposed mechanisms associated with Alzheimer's disease and importantly, how microfluidic technology can be used to develop proof-of-concepts, prior to successful translation in *in vivo* studies. Additional research to include behavioural assessments would be required however to further validate this model as appropriate for drug screening against Alzheimer's disease.

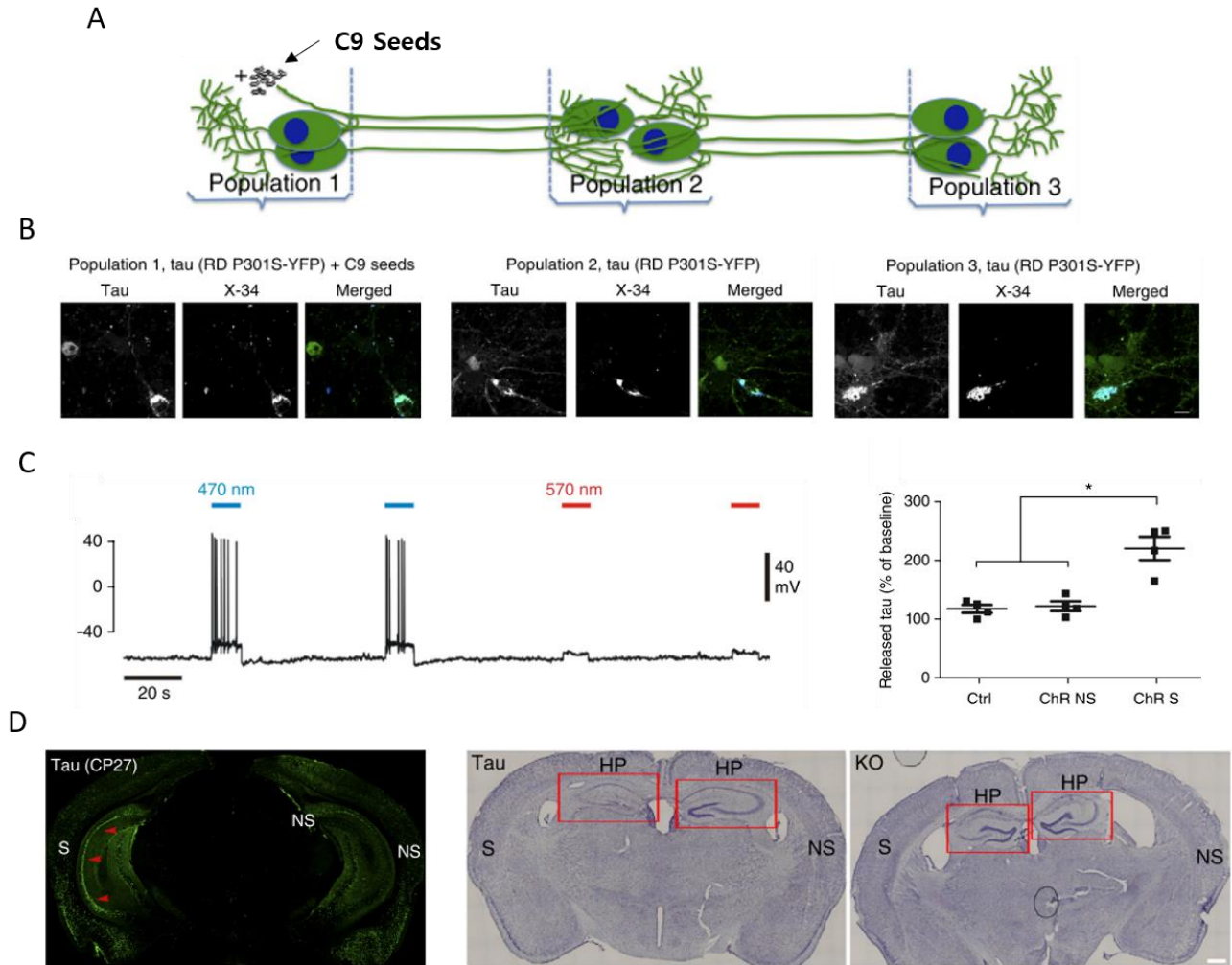


**Figure 1.15: Microfluidic & *In Vivo* Model of Tau Pathology.** (A) A schematic design of the tri-partite microfluidic device cultured with hippocampal & cortical neurons, the first network of which is treated with tau clone 9 seed lysate (C9 Seeds). (B) Representative images of neurons from each network stained with X34 (tau aggregate dye) reveals the propagation of tau throughout the naïve networks of the microfluidic device. (C) Transduced neurons expressing human tau and channelrhodopsin are activated in response to blue light (470 nm), resulting in significant increases in extracellular release of tau protein, relative to controls. (D, E) Representative image of posterior tissue (from rTg4510 tau expressing mouse line) stained with fluorescently tagged tau antibody (CP27) reveals significant tau pathology in the optogenetically stimulated hemisphere. Stimulation of this hemisphere also revealed significant reductions of cell bodies as revealed by Nissl staining, indicative of atrophy, relative to controls. (B, D & E) Scale Bars = 500  $\mu$ m. (A – E) Adapted images obtained from Wu et al (2016)<sup>300</sup>.

## 1.6. Thesis Objectives and Outline

Whilst current *in vitro* research tools and methodologies are used to perform assays that demonstrate important mechanisms underlying neural network activity, they are primarily limited to the assessment of a single network. Consequently, neurophysiological mechanisms across multiple networks cannot be realised, nor the indirect activation of synaptically connected neurons following drug applications. Over the last 15 years however, microfluidic technology has taken significant steps towards resolving these issues by permitting the design of interconnected neural networks in greater complexity, whilst integrating many neuroscientific tools into assay development.

Microfluidic assays for neuroscientific research are not without their limitations however. The use of  $\text{Ca}^{2+}$  imaging for example, has been used to assess hundreds of cells from multiple neural networks simultaneously. The slow  $\text{Ca}_i^{2+}$  dynamics, coupled with poor dissociative kinetics typical of  $\text{Ca}^{2+}$  sensitive dyes prevents researchers from identifying synaptic activity in detail when compared to electrophysiological techniques. Meanwhile, drug application often requires user interference, with limited control over induced flow rates which may have adverse effects on experimental outcome. Neuronal cultures are particularly sensitive to changes in their microenvironment and sudden, large changes in flow rates could activate the networks, thus biasing the results obtained from drug applications. Additionally, many studies using microfluidic techniques are limited to single drug applications; multiple wash steps would need to be performed manually without further disturbance to the neural network which is time-consuming and risks compromising the assay. Finally, the spatial resolution of imaging studies struggles to allow the visualisation of neurons that are responsible for the indirect activation of synaptically connected neurons, information which can only be gleaned through the use of MEAs.

This thesis details novel microfluidic assay development for investigating functional synaptic communication and neuropharmacological drug discovery. Initially, functional communication between neural networks was demonstrated by a simple assay design using  $\text{Ca}^{2+}$  imaging, and the temporal limitations of  $\text{Ca}^{2+}$  imaging highlighted. Whilst VSDs were considered as a potential alternative to patch clamping techniques at higher throughput, preliminary experiments and data analysis revealed sophisticated imaging equipment would be required to reveal synaptic transmission. Development of a microfluidic perfusion platform was performed which permitted a multi-stage assay design for repeated stimulation of a single network, and simultaneous readouts of a synaptically activated, naïve neural network obtained. Taking advantage of microfluidic perfusion,

preliminary work with chemogenetic assays was carried out, where neural networks were transfected with the metabolic DREADD hM3Dq, and transfected cells activated by the perfusion of the otherwise inert compound, CNO. Thus, the methods described in this thesis for early microfluidic assay development in neural networks can be applied to the research of neurophysiological mechanisms and early CNS drug discovery in the study of neuropathologies.

To summarise, the objective of this thesis is to develop novel microfluidic assays for the study of neural network communication and CNS drug discovery, with the following assay formats assessed:

1. Development of voltage imaging assays
2. Development and optimisation of a microfluidic perfusion platform
3. Development of chemogenetic assays in the microfluidic perfusion platform

## **2. Methods & Materials**

### **2.1. Fabrication and Device Production**

Two separate microfluidic systems were used during this study, expanding on earlier concepts of studying functional communication between environmentally isolated neural networks<sup>274,275</sup> to include a perfusion system amenable to drug discovery. The procedural guidelines for producing microfluidic devices are outlined below.

#### **2.1.1. Designing Microfluidic Systems**

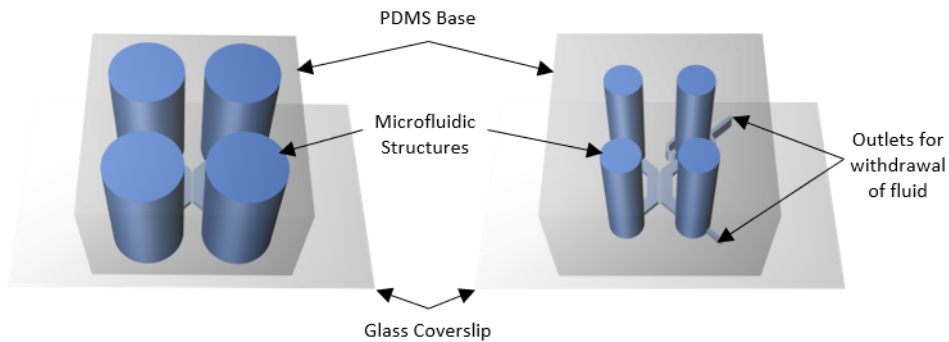
Microfluidic device layouts were designed using the drawing software package CorelDrawX5. Devices consisted of dual culture chamber designs, each chamber connected to an inlet and outlet well and separated by an array of microchannels (Figure 2.1). The large well (8 mm diameter; ~4 mm height) microfluidic devices were initially used to demonstrate functional connectivity between independent, environmentally isolated neuronal networks via *in situ* drug applications. Meanwhile, small well devices (4 mm diameter; 4 mm height) were used for the integration of a semi-automated microfluidic perfusion system. The dimensions of the devices on the x and y axis were designed on CorelDrawX5, and the thickness (z-axis) of the device features was determined by the fabrication process. By carrying out two-layer fabrication, the final thickness of the microchannel array (composed of 200 microchannels) was significantly smaller than that of the culture chambers, resulting in a greater hydraulic resistance by an order of 2 magnitudes. The calculations used to determine this are provided later in Section 3.4.1. (Theoretical Model of In Situ Microfluidic Application).

A fluidic barrier may be established by careful control of volumes in the inlet/outlet wells, such that one microfluidic channel contains a greater hydrostatic pressure than the other. By doing so, a microflow of solution acts through the microchannel array, effectively isolating the chamber with the smaller volume in the open wells.

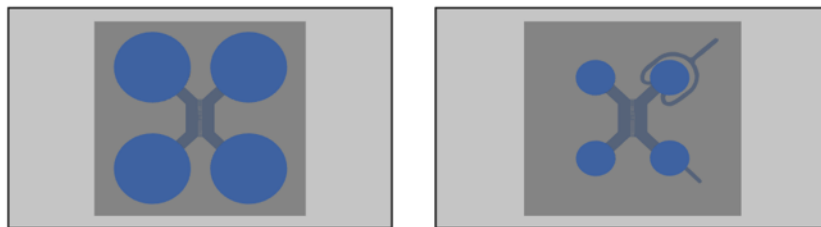
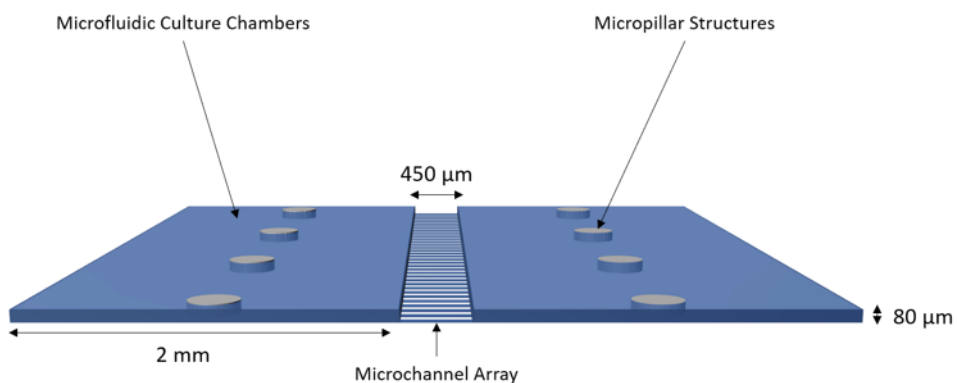
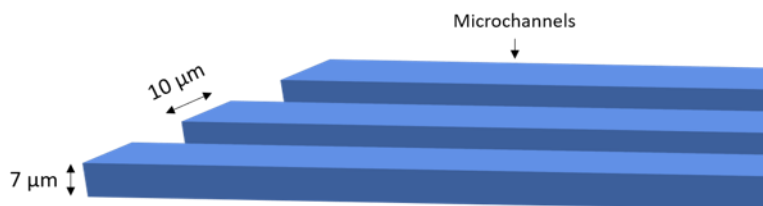
**A****Microfluidic Devices**

Large well (8 mm diameter) device  
*In-Situ* pharmacological applications

Small well (4 mm diameter) device  
 Microfluidic perfusion applications



Top-down Perspective

**B****C**

**Figure 2.1: Microfluidic Device Designs.** (A) Microfluidic devices with large (*in situ* drug applications) and small wells (microfluidic perfusions) were used to characterise functional communication between fluidically isolated, independent neural networks. (B + C) Both devices share the same internal structure of the culture chambers and microchannel array.

### 2.1.2. Two-layer Photolithography Fabrication

The microfluidic devices used for the culturing of neurons were fabricated from master silicon wafers, following two-layer, standard photo-lithography procedures (Figure 2.2) with SU8 photoresist (3000 series, MicroChem, US). Transparent photomasks were obtained from JD Photo Tool, UK. Briefly, the first layer of microchannels were obtained by spinning photo-resist SU8 3010 at 500 rpm for 10 seconds, then 4000 rpm for 30 seconds and pre-baked at 110 °C (final thickness of 7 μm), followed by exposure to collimated UV light ( $> 10 \text{ J}\cdot\text{cm}^{-1}$  for 20 s) after positioning of the first photomask. Then, the silicon wafer was post-baked at 65 °C for 1 minute, then 95 °C for 5 minutes, before allowing to cool to room temperature, thereby reducing internal stress within the resist. Microchannel features were developed for ~ 6 minutes in MicroPosit EC solvent (Rohm & Haas, US), with minor agitation applied via pipetting, to reveal distinct microchannel array patterns. The wafer was then washed gently with Isopropanol (100 %), dried with N<sub>2</sub> gas and hard baked at 200 °C for 20 minutes to evaporate residual solvent prior to the fabrication of an additional.

To fabricate the second layer, the previously developed wafer was spun with a layer of SU8 3035 at 500 rpm for 10 seconds, followed by 1000 rpm for 30 seconds and pre-baked at 110 °C for 5 minutes (final thickness of ~80 μm). A second photomask was aligned around the microchannels and the wafer then exposed to collimated UV light ( $> 10 \text{ J}\cdot\text{cm}^{-1}$  for 80 s). The exposed wafer was then post-baked at 65 °C for 5 minutes, then 110 °C for 20 minutes and allowed to cool down to room temperature. Development, washing and drying of the culture chamber features was carried out as described previously to reveal two-layer fabricated features, validated by eye using an upright microscope with a filter corrected lens to confirm correct alignment and developed features. Finally, the wafer was hard baked by ramping up temperature on the hotplate to exceed 180 °C for 30 minutes then allowed to cool back to room temperature. Once cooled, the fabricated features were then confirmed using an Alpha Stylus profilometer (KLA-Corp, US).

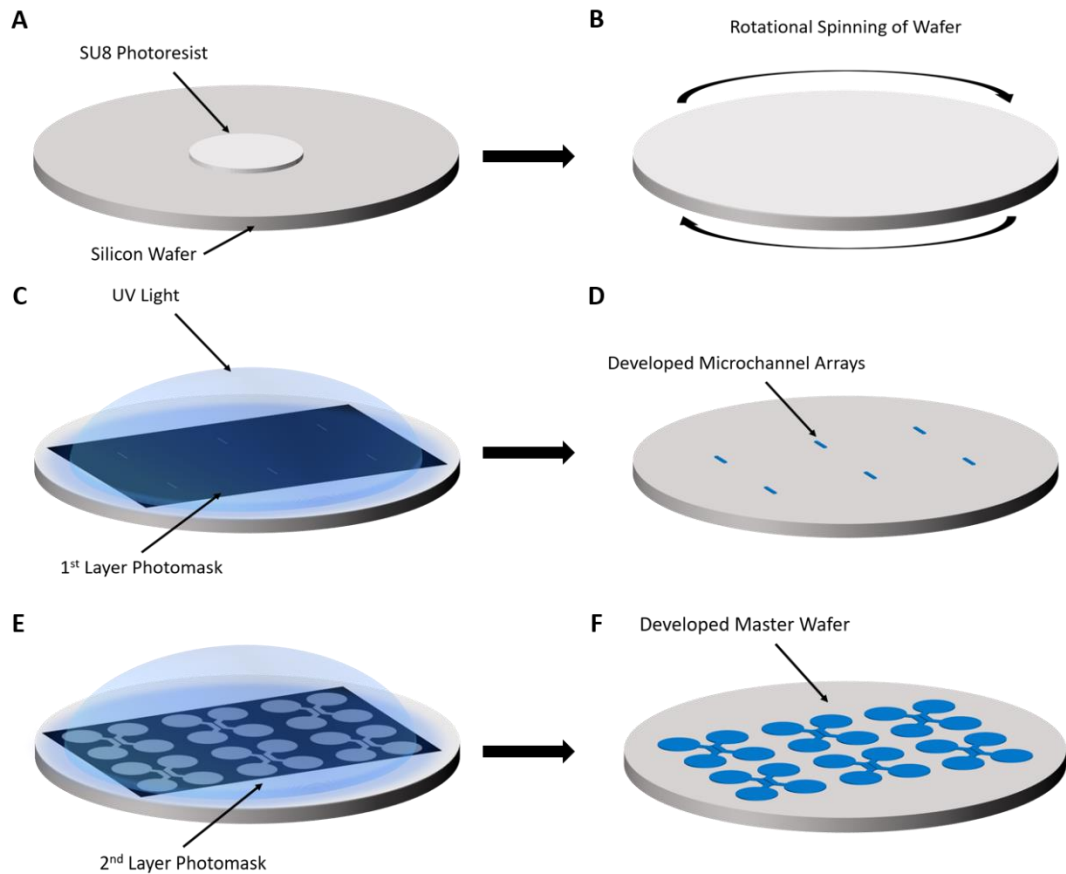


**Figure 2.2: Microfluidic Device Fabrication.** (A, B) The first layer of the master wafer was created by applying a small volume of SU8 photo-resist to the centre of the silicon wafer and spinning down to the desired thickness. (C, D) After baking, the first photomask is placed over the wafer, which is exposed briefly to UV light and development in Microposit solvent reveals microchannel array features. (E) Steps A-D are repeated, with the thickness of SU-8 photo-resist adjusted and the second photomask placed over the microchannel array features prior to UV exposure. (F) Applications of Microposit solvent reveal the complete features of microfluidic devices on the master wafer.



### 2.1.3. Silanisation of the Master Silicon Wafer

The surface of the master wafer was initially exposed to oxygen plasma (0.28 mbar, 99 %, 2 minutes) using a plasma etcher (Pico A, Diener Electronic, Germany) and transferred to a vacuum sealed desiccator which contained a weighing boat with 50  $\mu\text{L}$  of 1H,1H,2H,2H-perfluorooctyl-trichlorosilane (Sigma Aldrich, UK). Silanisation was subsequently performed for 1 hour via vapour deposition, thereby preventing PDMS adhesion to the wafer. The silanised wafer was finally transferred to a glass dish internally lined with tin foil.

### 2.1.4. PDMS Casting and Microfluidic Device Creation

Within a ventilated hood, PDMS was poured onto the wafer at a 10:1 w/w ratio of base to curing agent and degassed within a vacuum desiccator chamber for 30 minutes. The PDMS was then cured for 3 hours at 80 °C. The first cast of PDMS using the master wafer was discarded to remove residual silane groups from the wafer surface, and the volume of base PDMS/curing agent used for the wafer was maintained throughout this study to ensure consistent microfluidic device height of approximately 4 mm. Devices from subsequent casts were cut from the slab of PDMS, and wells punched out on both sides of each chamber using 2/4 mm diameter biopsy punches for small/large well devices respectively. Additionally, horizontal and vertical needle inlets (0.723 mm diameter) were created in the wells connecting to the right chamber of small well devices, which would later be used to connect to syringe pumps (AL-1000, World Precision Instruments) Polytetrafluoroethylene (PTFE) tubing (0.255 mm inner diameter, ~ 700 mm length; Cole-Parmer, UK) on the day of experimentation. Individual microfluidic devices were cleaned with scotch tape<sup>1</sup> three times to ensure residual dust was removed which may interfere with the formation of a clean bond to glass. Glass coverslips (Borosilicate glass, 25x40 mm, VWR, Germany) were washed via sonication for 5 minutes (37 kHz, 100 %) with separate solvents (Acetone, 100 % Methanol then 100 % Isopropan-2-ol) and blow dried with  $\text{N}_2$  gas.

Exposure of PDMS and borosilicate glass to plasma oxygen replaces methyl ( $-\text{CH}_3$ ) structural groups with polar structural groups, such as  $\text{SiOH}$ , to the exposed surface. This serves two functions: 1) The exposed surface becomes more readily hydrophilic; 2) Bringing into contact the exposed PDMS and glass surfaces together results in the formation of strong, cross linked covalent bonds ( $-\text{Si-O-Si}-$ ). To this end, PDMS devices were permanently bonded to glass coverslips using oxygen plasma (0.28 mbar, 45 %, 0.1 min; Pico plasma system, Diener Electronic, Germany). Bonded devices were

left to rest for 15 minutes prior to further plasma oxygen exposure (0.28 mbar, 99 %, 2 min). Deionised (DI) water was applied to the top two wells of each device and allowed to flow through the chambers.

### 2.1.5. Spatio-Temporal Profiling of *In Situ* Drug Application

To characterise fluid flow in response to *in situ* drug application within a single culture chamber and demonstrate the absence of cross contamination across the microchannel array, non-cultured devices containing DI water were first transferred to an inverted microscope (Axio Observer A1). Then, volumetric conditions were established such that a fluid pressure gradient originating in the left (naïve) chamber was acting across the microchannel array and against the right (treated) chamber. This was achieved by ensuring all connecting wells initially contained 50 µL of DI water, and an additional 100 µL of DI water applied to both wells connecting to the naïve chamber. Images were acquired at 2 Hz, 0.4 ms exposure with 2x2 binning, using a cooled EM-CCD camera (1004x1004 pixels; Luca R; Andor Technologies), a 2.5x objective and filter set 46HE (in nm: BP 500/25, FT 515 HE, BP 535/30; Carl Zeiss, AG). The electron multiplier (EM) gain was adjusted to 150x to provide a clear signal to noise ratio. The field of view (FOV) was adjusted until the full width of the treated chamber, the microchannel array and the immediately adjacent area of the naïve chamber were visible. A baseline flow was established over the course of 5 minutes and recordings were initiated within the last 30 seconds of this period. After 30 seconds of recorded baseline, 50 µl of calcein solution (50 µM) was applied to both wells connecting to the treated chamber, separated by 20 seconds. The recording was stopped after 5 minutes and a region of interest (ROI) was selected for the chambers on either side of the microchannel array. Greyscale images obtained from the recording were processed using Andor SOLIS (DL-01339) and Excel (Microsoft Office, 2013).

## 2.2. Hippocampal Cultures for *In Vitro* Studies

Primary mixed hippocampal networks have been used extensively in neuroscientific research as an *in vitro* model for synaptic communication, and methods for their routine culture on coverslips standardised over the last few decades. It was therefore logical to culture primary mixed hippocampal networks for the purpose of demonstrating synaptic communication in the microfluidic environment instead of using human induced pluripotent stem cell derived neural networks, the methods for culturing of which are still in the process of development and characterisation. Through the development of microfluidic cell culture techniques and optimisation of cell culture protocols

over the course of this PhD, healthy and confluent neural networks were formed with single cell resolution. Using the procedural guidelines below, one rat pup (1-2 days old) provides enough cells to seed 10-12 devices, up to 15 coverslips or one 4-well plate.

### 2.2.1. Device Preparation

To maintain internal hydrophilicity of the device, the chambers remained wet throughout device preparation and cell culture. Microfluidic devices containing DI water were transferred to plastic trays and sterilised by UV exposure (DaRo UV Systems, UK) for 30 minutes, and kept under sterile conditions until the day of experimentation. This UV exposure was later reduced to 15 minutes after the first year of this PhD, which minimised cell aggregation during cell culture. Prolonged exposure to UV, similar to oxygen plasma treatment, increases the presence of free radicals and a silica crust in the PDMS device<sup>303,304</sup>, both of which have been demonstrated toxic to neurons<sup>305,306</sup>. The DI water was removed from each well and 1X poly-L-lysine (10  $\mu\text{g mL}^{-1}$  in DI water; PLL; Sigma Aldrich, UK) was applied to the top two wells of each device, allowed to flow through the culture chambers, then left at room temperature for 1.5 hours. This was followed by a washing step repeated three times, whereby the volume of fluid in all wells was replaced by fresh, filter sterilised supplemented Neurobasal A media supplemented with L-glutamine (2 mM; Tocris Bioscience, UK) and B27 (2 % w/v; Life Technologies, UK). Devices containing supplemented media were transferred to the fridge for 5-7 days, followed by an additional 1X PLL (10  $\mu\text{g mL}^{-1}$  in DI water) treatment, and three-step washout with supplemented media prior to cell culture that day.

### 2.2.2. Preparation of Coverslips and 4-Well Plate

Autoclaved glass coverslips (13 mm; VWR, US) and sterile 4-well plates (Nunc; ThermoFisher, UK) were treated with 100/500  $\mu\text{l}$  of 1X PLL (10  $\mu\text{g mL}^{-1}$  in DI water) respectively for 1.5 hours at room temperature. Coverslips were rinsed in filter sterilised DI water and left to air dry on sterile paper before being transferred to petri dishes (33 mm diameter; 3 coverslips per dish). The 4-well plates were washed similarly as coverslips, whereby the volume of fluid in each well was replaced by fresh sterile DI water three times, prior to plating cell solution.

### 2.2.3. Solution Preparation for Hippocampal Cultures

In advance of hippocampal dissections, papain (1.5 mM; Sigma Aldrich, UK) and bovine serum albumin solutions (BSA; 10mg  $\text{mL}^{-1}$ ; Sigma Aldrich, UK) were prepared in buffered hippocampal

enzyme solution (H-enzyme) containing in mM: NaCl 6.78, KCl 0.402, NaHCO<sub>3</sub> 2.184, NaH<sub>2</sub>PO<sub>4</sub> 0.156, MgSO<sub>4</sub> 0.146, glucose 4.504, CaCl<sub>2</sub> 0.22; then filter sterilised and transferred to a water bath (37 °C) until required. The remaining H-enzyme solution was also filter sterilised into a sterile petri dish and left at room temperature until further required.

#### 2.2.4. Procedures for Hippocampal Dissection

In accordance with the UK Home Office guidelines, Sprague Dawley rat pups (1-2 days old) were obtained from in-house colonies maintained in the Biological Procedures Unit at the University of Strathclyde. Cervical dislocation was carried out on pups, immediately followed by decapitation. A small pair of scissors were then used to cut from the spinal cord, along the fused sagittal suture to the point of bregma, and forceps used to expose the brain. The brain was removed, and a sagittal incision was made with a scalpel blade to separate the two hemispheres. The hindbrain of each hemisphere was turned over to reveal the hippocampi, which was then excised and placed in cool H-enzyme solution.

#### 2.2.5. Hippocampal Tissue Dissociation

Excised hippocampi were chopped several times with a scalpel blade and incubated in papain solution for 20 minutes at 37 °C before transferral to BSA solution to inhibit the papain digestion. The tips of three glass pipettes were tapered in decreasing diameter using an open bunsen flame and the hippocampal tissue in BSA was gradually dissociated via trituration. Following this, the single cell solution was spun down at 2000 rpm for 135 seconds, the supernatant discarded, and the cell pellet re-suspended in 1 mL of supplemented media. Of this solution, 10 µL was mixed with 10 µL of Trypan blue (0.4%; Sigma Aldrich, UK) and applied to a haemocytometer (Marienfield Superior, AG) to determine cell density. The cell solution was spun down again and re-suspended to  $5 \times 10^6$  cells mL<sup>-1</sup> in fresh, sterile supplemented media.

#### 2.2.6. Mixed Primary Hippocampal Culture Plating and Maintenance

*Microfluidic devices:* In initial cultures, 10 µL ( $50 \times 10^3$  cells) were pipetted into the chambers of each device via the top two wells and incubated (37 °C/5 % CO<sub>2</sub>) for 10 minutes, followed by the application of supplemented media to the device wells (200/50 µL per well; large/small well devices respectively). This procedure was later updated, whereby 5 µL of cell solution was first pipetted into the top two wells, followed by 5 µL into the bottom two wells of each device. The device was then

incubated (37 °C/5 % CO<sub>2</sub>) for 10 minutes following each application, which ensured an even distribution of cells throughout the culture chamber. Following cell adhesion in the culture chambers, all wells were filled with warm, sterile supplemented media and devices maintained in a humidified incubator (37 °C/5 % CO<sub>2</sub>).

*Coverslips and 4-well assay plates:* The cell solution remaining after seeding devices was diluted 1:10 with fresh supplemented media (final density of  $5 \times 10^5$  cells mL<sup>-1</sup>), and 100 µL of this cell solution was used to plate individual coverslips (1X PLL pre-treatment). Plated coverslips were incubated for 1 hour at 37 °C/5% CO<sub>2</sub>, the remaining solution then removed, and the petri dish gently flooded with 2 mLs of warm, sterile supplemented media. Alternatively, 200 µL of the cell solution was used to plate individual wells of the 4-well assay plate, and a further 300 µL of warm, sterile supplemented media was immediately added to each well. This ensured an even cell distribution across the bottom of the well.

Microfluidic devices, coverslips and 4-well plates were transferred to and maintained in a humidified (90 %) incubator at 37.5 °C/5 % CO<sub>2</sub> after plating. Neural networks were grown for 10-14 days *in vitro* (DIV) before experiments were carried out. At DIV 5, cytosine β-D-arabinofuranoside (AraC; 1 µM final concentration) was added to petri dishes and individual wells of 4-well plates to inhibit further glial proliferation. Media replenishment was performed every 2-3 days by replacing 50 % of the media with fresh supplemented media.

### **2.3. Immunocytochemistry for Primary Hippocampal Cultures**

Hippocampal cultures were stained for the identification of neurons, astrocytes and synapses to ensure similar distribution was observed under different culturing conditions.

#### **2.3.1. Antibodies for Neural Network Populations and Synaptic Connectivity**

Antibodies were prepared by dilution with blocking buffer (5 % v/v foetal bovine serum (FBS) and 1 % w/v BSA in phosphate buffered saline (PBS)) to prevent non-specific binding. Primary antibodies for βIII-Tubulin (neuronal specific cytoskeleton marker; Life Technologies, UK), glial fibrillary acidic protein (GFAP; intermediate filament marker; Sigma Aldrich, UK), microtubule associated protein-2 (MAP2; somatodendritic marker; Millipore, UK) and synaptophysin (pre-synaptic vesicle marker; Millipore, UK) were used to identify neurons, glial cells, neuronal dendrites, and synaptic vesicles respectively. Secondary antibodies (Alexa Fluor 488/555/633nm for anti-chicken, mouse, and rabbit) were prepared at 1:200 dilutions, species corrected for primary antibody used.

### 2.3.2. Immunocytochemical Staining of Neural Networks

Cultures in devices, coverslips (within petri dishes) and 4-well plates were washed as previously described three times with (PBS) prior to fixing with ice cold paraformaldehyde (4 % w/v) on an ice block for 10 minutes. The washing step was repeated and ice-cold methanol (100 %) was washed over the cultures for a further 10 minutes. The cultures were then washed with PBS, removed from the ice block and permeabilised with Triton X100 solution (0.01% in PBS; Fluka Biochemika, UK) for 10 minutes. The cultures were washed again prior to the treatment with blocking solution at room temperature for 1 hour to prevent non-specific binding of primary antibodies. Following blocking, primary antibodies diluted in blocking solution, were applied and incubated for at least 18 hours at 4°C. For devices, 50/100 µL of primary antibody solution was applied to each of the top two wells for small/large well devices respectively, whilst 100 µL applied to each coverslip, and 200 µL to each well of a 4-well plate. Following this, the cultures were washed to remove unbound primary antibodies and cultures were then stained with the appropriate fluorescently labelled secondary antibodies in the absence or presence of DAPI (nucleic acid marker; 350 nm; 1 mM) for 1 hour in darkness at room temperature. The washing step was repeated a final time prior to imaging.

### 2.3.3. Immunocytochemistry - Epifluorescent Imaging

Epifluorescent imaging was carried out initially using an inverted microscope (Axio Observer A1, Carl Zeiss, AG) with a cooled EM-CCD camera (LucaR, Andor Technologies). Greyscale images obtained were processed using Andor SOLIS (DL-01339), then coloured and merged using GIMP (v 2.8.14). Further into the study, an alternative setup was used, which included an automated inverted microscope (Axio Observer Z1, Carl Zeiss, AG) with a cooled EM-CCD camera (AxioCam mRM, Carl Zeiss, AG; later replaced by Orca Flash 4.0, Hamamatsu Photonics, JPN) and the colour images obtained were processed using Zen 2012 (Blue edition; Carl Zeiss, AG). Epifluorescent images were captured with 5/10/20/40/63X dry objective lenses as required, performed on either setup described above. Devices, coverslips, and 4-well plates were maintained in PBS between protocol steps and throughout imaging.

## 2.4 Calcium Imaging in Microfluidic Neural Networks

To demonstrate functional synaptic communication between environmentally isolated neuronal networks,  $\text{Ca}^{2+}$  imaging assays were carried out following previously published protocols<sup>275</sup>. These assays initially involved the use of large well devices for direct drug application, before being used for small well devices with microfluidic perfusion. The recording setup would also be adjusted to demonstrate the temporal limitations of calcium imaging.

To monitor neural activity during  $\text{Ca}^{2+}$  imaging assays, a physiologically relevant solution is required for neural network maintenance throughout recordings. A HEPES based external solution (HBS) containing in mM: NaCl 140, KCl 5,  $\text{MgCl}_2$  2, HEPES 10, D-glucose 10,  $\text{CaCl}_2$  2 was used, pH adjusted to  $7.4 \pm 0.1$  with NaOH and the osmolarity adjusted to  $310 \text{ mOsm} \pm 0.1$  using sucrose. The calcium sensitive dye Fluo-4 AM (Life Technologies, UK) was used to detect intracellular calcium levels, with changes in  $\text{Ca}_i^{2+}$  levels being used as an assay to identify changes in cellular activity. Stock solutions were prepared by diluting 50  $\mu\text{g}$  of Fluo-4 AM with 50  $\mu\text{L}$  dimethyl sulfoxide (DMSO) and aliquoted into 1  $\mu\text{L}$  samples. Working solutions were then prepared by diluting stock solutions to 1:300 with HBS (final concentration of 5  $\mu\text{M}$ ).

### 2.4.1. Setup for Calcium Imaging Assays

Following 10-14 DIV, mixed hippocampal cultures in each device were washed 3 times with freshly prepared HBS before the wells were emptied and 100  $\mu\text{l}$  of the Fluo-4 AM (5  $\mu\text{M}$ ) was applied to each culture chamber and incubated for 1 hour at room temperature in darkness. Excess dye was removed following three washes with HBS and individual devices were transferred to the Axio Observer (A1) for monitoring neural activity. Typically, a 5x objective was used for ideal spatial resolutions during recordings, allowing 100s of cells to be monitored simultaneously. Meanwhile, a 10x objective was used during assays which required a greater sensitivity of the signal to be obtained, at a loss of spatial resolution. Images were acquired at 2 Hz, 0.4 ms exposure, using the Luca R EM-CCD camera, a 2.5x objective and filter set 46HE. The intensity of light was typically reduced to  $\leq 20\%$  with a neutral density filter (FI attenuator, position 5/6), otherwise cellular excitotoxicity and fluorophore photobleaching occurred during continuous live cell recording. Recordings lasted between 16-20 minutes in duration, performed without binning and the FOV centred across a segment of the microchannel array.



A faster rate of frame acquisition was required to demonstrate the temporal limitations of calcium imaging, which does not permit an optical measure of individual action potential (AP) generation. A frame rate of 250Hz was achieved by reducing the time-lapsed exposure to 3.11 ms, applying 4x4 binning, and reducing the field of view to 800x100 pixels. Due to the limited field of view, the likelihood of detecting indirect activation of cells taking place within the naïve neural network is significantly reduced. As such, the FOV was centred over cells in the treated chamber where increases in fluorescence in response to drug application are guaranteed. The duration of recording for this experiment was therefore limited to 4 minutes. To compensate for pixel binning and maintain spatial resolution, the magnification was then increased by using a 20x objective. Increasing the magnification generally increases the numerical aperture of the optical system, permitting more light to be gathered and thereby eliminating the need to increase the intensity of excitatory light during recordings.

#### 2.4.2. Experimental Protocol for Microfluidic Calcium Imaging Assays

To identify synaptically driven neuronal network communication in response to direct drug applications, I used compounds that stimulate neurons, including glutamate and KCl for direct stimulation and identification of neurons from glial cells respectively. Working solutions of the pharmacological agents were prepared from frozen, pre-made 1000X stock solutions on the day of experimentation by dilution with HBS.

The volume present in the microfluidic device was adjusted, such that wells connecting to the naïve culture chamber contained 150  $\mu$ L of HBS, whilst those connecting to the treatment chamber contained 100  $\mu$ L, with neural networks left to equilibrate for five minutes prior to recording (Figure 2.3). This establishes a fluidic barrier across the microchannel array, whilst ensuring that any cells activated by vehicle manipulation would recover back to basal levels of activity and not influence the outcome of the assay. After 4 minutes of baseline recording, 50  $\mu$ L HBS was removed from wells connecting to the treatment chamber and replaced with 50  $\mu$ L HBS (vehicle control) at the inlet well, followed by 50  $\mu$ L of HBS at the outlet well 30 seconds later. This permits the solution applied at the inlet well to traverse the culture chamber and stimulate cells before the second application (at the outlet well) equilibrating volumetric conditions. This approach was repeated after another 4 minutes with glutamate (100  $\mu$ M). Following glutamate application, 50  $\mu$ L HBS was removed from the inlet/outlet wells connecting to the non-stimulated chamber, and KCl (25 mM) was applied to both inlet wells for the identification of neuronal and non-neuronal signals.



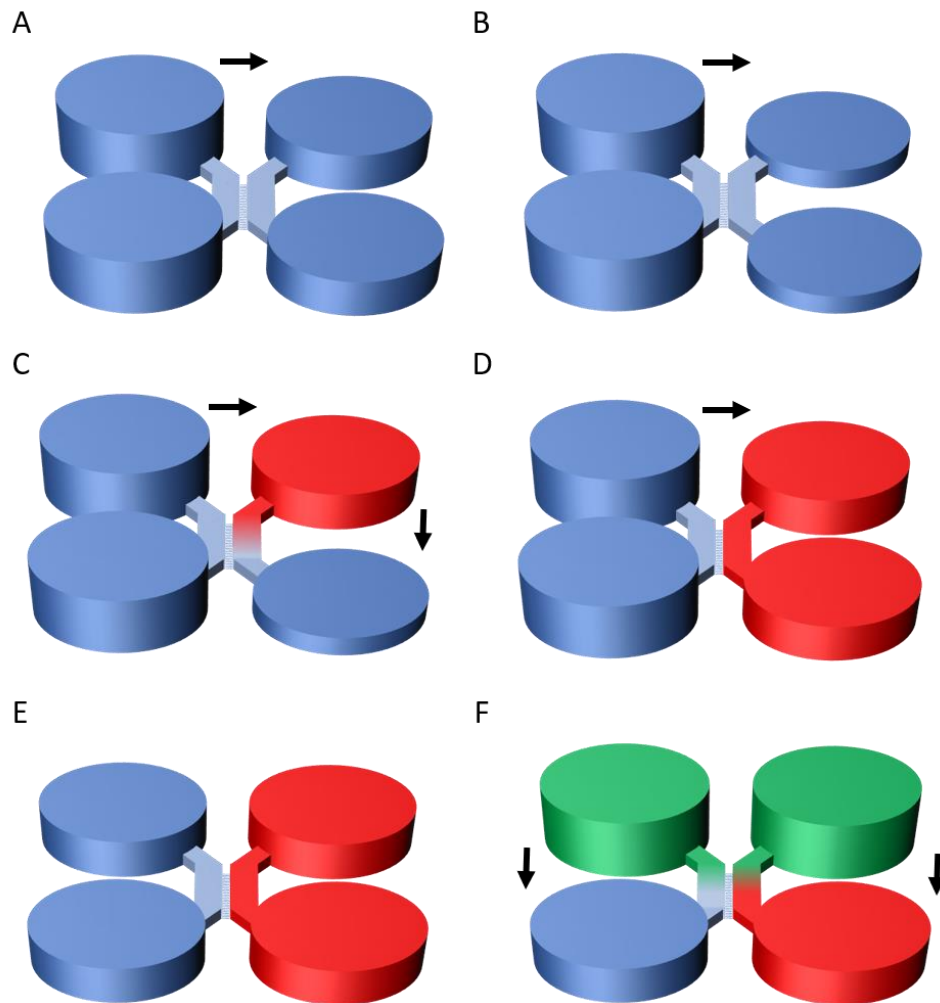


**Figure 2.3: Schematic of the Microfluidic Calcium Imaging Protocol.** (A) A volumetric barrier exists across the microchannel array between the non/stimulated microfluidic chambers due to differences in volume within the respective inlet/outlet wells. (B) Immediately prior to drug application, solution is withdrawn from the inlet/outlet wells of the stimulated chamber. (C, D) Glutamate (Red) is applied to the inlet well of the stimulated chamber and allowed to flow across the hippocampal culture prior to a second glutamate application (100  $\mu$ M final concentration) at the outlet well. (E, F) Volume is withdrawn from the wells of the non-stimulated chamber, prior to the application of KCl (25 mM final concentration; Green) at the inlet wells of both chambers. (A – F) Black arrows represent volumetric gradients established across the microchannel array and culture chambers over the course of the assay.

### 2.4.3 Signal Processing and Analysis post Calcium Imaging Assays

Following the assay, cells were highlighted on Andor SOLIS as ROIs, with an additional ROI of the same size placed in a non-fluorescent area of the microchannel array, used to determine background fluorescence levels during recordings. The raw mean intensity of the ROIs were exported to MATLAB (2013a), converted into time variant signals and each trace normalised to the average of the first 100 values. Filtering was then applied using a moving window filter (11 frames averaged) to eliminate noise from traces and produce a clean signal from which synaptically driven calcium events could be identified. The manual analysis of traces involved firstly, determining the type of signal for each trace sequentially. Neurons presented with a sharp and sustained increase in fluorescence following KCl application, whilst a smaller fluorescent increase prior to recovering baseline fluorescence was observed in non-neuronal cells due to neuronal-induced activation (Figure 2.4). Calcium events, which were defined as uninterrupted increases in the fluorescent signal  $\geq 0.5$  normalised fluorescent units (NFU) over baseline fluorescence, were manually counted and stored for statistical analysis. Increases in calcium events were attributed to specific treatments during the recordings and could therefore be separated into specific analytical groups for comparison e.g. Baseline vs Vehicle. To determine changes in activity in response to treatment, calcium events from multiple devices were pooled into the same population for each analytical group and expressed as events per neuron per minute (ENM). Statistical analysis was performed using paired t-tests because frequencies of cell activity across groups were derived from a single cell, as part of a larger sample population.

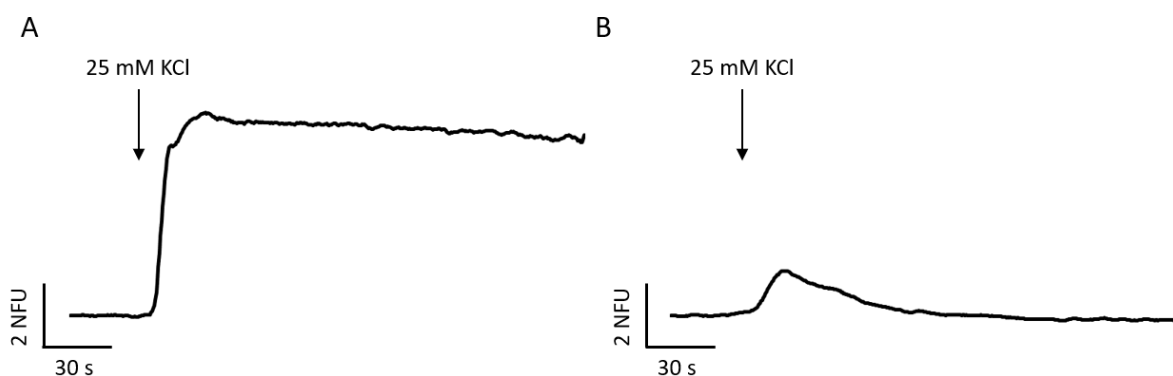


**Figure 2.4: Identification of Neurons and Glial Cells during Calcium Imaging.** (A, B) Representative traces depicting the neuronal and non-neuronal (B) fluorescent response to direct KCl application, used for the identification of cells during  $\text{Ca}^{2+}$  imaging. Neurons typically display sharp increases in fluorescence which remains elevated over the course of minutes, whereas non-neuronal cells such as astrocytes will display brief increases in fluorescence however remain largely unaffected by KCl application.

## 2.5. Neuronal Experiments for Improved Temporal Resolutions

To overcome the temporal limitation of  $\text{Ca}^{2+}$  imaging, I attempted to perform voltage-sensitive dye imaging (VSDI) assays over a sequence of optimisation steps. Electrophysiological experiments were carried out separately as controls, designed by myself and kindly performed by Dr Louise Ritchie. All in-house MATLAB routines used for VSD signal analysis and electrophysiological simulations were written by Dr Michele Zagnoni.

### 2.5.1. Voltage Sensitive Dye Imaging

Before experiments with VSDs were performed on microfluidic devices, experimental conditions were optimised for recording cellular activity on coverslip cultures. Similar to calcium imaging experiments, HBS was used throughout the experimental procedure. The voltage sensitive dye used for VSDI experiments was Di-3-ANEPPDHQ (D3AD; ThermoFisher Scientific, USA), which interlocks within the neuronal phospholipid membrane and displays a blue-shift in its excitation/emission spectra during membrane depolarisation. As with many VSDIs, it is proposed that it can be used to identify changes in neuronal activity with greater temporal precision than calcium sensitive dyes. Stock solutions were prepared by diluting 1 mg of D3AD with 1 mL of DMSO (final concentration 1.57 mM) and aliquoted into 100  $\mu\text{L}$  samples. Stock solutions of Pluronic F-127 (ThermoFisher Scientific, USA), used to improve D3AD staining, were prepared by dissolving 2 g in 10 mL of DMSO

(final concentration 20 % w/v) and aliquoted into 1 mL samples. Working solutions of D3AD (1.57  $\mu$ M) were then prepared by diluting stock solutions to 1:1000 in HBS in the absence/presence of Pluronic F-127 (0.1% w/v).

#### 2.5.1.1. Voltage Sensitive Dye Imaging Setup

Following 10-14 DIV, mixed hippocampal cultures grown on coverslips were transferred to a clean petri dish and washed 3 times with freshly prepared HBS. Residual HBS was aspirated and 100  $\mu$ L of D3AD working solution (in the absence/presence of Pluronic F-127), was applied to the coverslip and incubated in the dark, at room temperature between 30-60 minutes. Excess dye was removed via three HBS washes to eliminate background fluorescence and individual coverslips were transferred to a custom made, PDMS based reservoir (3.5 x 1.5 x 1.5mm (l x w x h)) bonded to coverslip glass, containing 1 mL of HBS. The reservoir was transferred to the Axio Observer (A1), and 10/20/40X objectives were used for monitoring neuronal activity. The intensity of light from the mercury arc lamp ranged from 20 - 100% by alternating the filter attenuator position of the neutral density filter during separate recordings (position 5 - 1 respectively). This was performed to determine the optimum intensity required to obtain the maximum signal during the blue - shift of the dye following membrane depolarisation. Preliminary experiments employed an EM-CCD Luca R camera and filter cube set 16 (in nm: BP 485/20, FT 510, LP 515; Carl Zeiss, AG), both of which were later replaced by a cooled sCMOS camera (2560x2160 pixels; Zyla 5.5; Andor Technologies), with a custom filter cube set (in nm: BP 525/35, FT 570, LP:580 Chroma Technology Corp, US). Replacement of the camera used permitted increased temporal resolutions for capturing synaptic activity. By changing the filter set, the band capturing the dyes excitation spectra was reduced, and so the difference in signal detected between membrane resting and depolarisation states (brought about by the spectra blue shift) was enhanced to produce a theoretically improved signal to noise ratio.

The EM gain was adjusted between 0 - 150x prior to recordings, depending on the level of background fluorescence and recordings lasted between 30 seconds and 10 minutes, depending on the intensity of excitatory light used, in order to minimise photobleaching/phototoxicity. The FOV was reduced as appropriate (described previously in section **2.4.1**) and binning (8 x 8 to 32 x 32) applied to achieve a frame rate between 200 Hz, to a maximum of 1 kHz. The reduced FOV obtained when recording at faster frame rates and using greater objective magnitudes led to a significant reduction in the number of cells that could be spatially monitored during the VSDI assays. Recordings from single cells required narrowing the cone of excitatory light with a shutter to eliminate debris

and artefacts that contributed to background noise. Neuronal cells were identified by a 'halo' outline following staining with D3AD, whilst internalisation of the dye would indicate an unhealthy cell with a leaky membrane.

#### 2.5.1.2. Experimental Protocol for Voltage Sensitive Dye Imaging Assays

Following baseline recording periods of up to 5 minutes, performed in the attempt to detect spontaneous firing of APs, the reservoir was gently flooded with 1 mL of KCl (20 mM) to produce global depolarisation and a reduction in fluorescence, recordings continuing up to 5 minutes. Additional experiments involved multiple recordings of single cells, performed at increasing acquisition rates and in turn, greater intensities. To reduce the impact of phototoxicity/bleaching, these recordings were kept to a duration of 30 seconds, separated by 5 minutes of recovery.

#### 2.5.1.3 Data Analysis post Voltage Sensitive Dye Imaging Assays

During preliminary experiments, cell somas, selected as separate ROIs (1x1 to 2x2 pixels) using Andor SOLIS, were represented as a single pixel because of the lower magnifications (10X) and binning used, with a separate ROI (2x2 pixels) placed in a non-fluorescent area to determine background levels of noise during recordings. Following single cell experiments, performed at greater temporal resolutions and magnification, multiple ROIs (1x1 pixels) were highlighted on the cell membrane. Raw intensity values from the selected ROIs were then exported to MatLab (v2014a) and converted into time variant signals. Signals obtained following KCl applications were then processed similarly to signals from Ca<sup>2+</sup> imaging assays (described previously in section **2.4.3**) to reduce the level of noise and determine the change in fluorescent magnitude. Neuronal depolarisation in the presence of KCl was considered as a reduction in NFU signal of >10% from the baseline recording, occurring within 15 seconds of pharmacological insult, followed by a signal plateau (non-recovery). Noise was determined by the standard deviation of each individual trace and results for each cell were pooled into the same population and expressed as mean  $\pm$  S.E.M. The signal to noise ratio was then determined and expressed as Units. Traces were excluded from analysis if there was complete absence of fluorescence change following KCl application. Where appropriate, signals obtained from multiple ROIs on the neuronal membrane were averaged and compared against background fluorescence.

The averaged trace was then filtered and a fixed +/- threshold was manually applied to the average fluorescent value determined over the duration of the recording. This was then used to detect and compare the number of positive and negative fluorescent peaks, indicating if the imaging setup could detect APs beyond the background noise.

## 2.5.2. Whole Cell Patch Clamp Experiments on Neuronal Networks

To determine if my cultured neuronal networks were spontaneously active, whole cell patch clamping was performed. This would also indicate if I was observing the correct fluorescence change with respect to KCl application, under the VSDI experimental conditions with D3AD.

Whole cell patch clamp recordings were setup using in-house methods previously established<sup>307</sup>, with experiments performed on neuronal networks at 10-14 DIV. Data was analysed by Dr Louise Ritchie using MiniAnalysis software to determine the number of spontaneous AP firing, and final membrane potential achieved following KCl perfusion. Data is expressed as mean  $\pm$  S.E.M.

### 2.5.2.1. Processing Simulated Electrophysiological Signals.

The raw values obtained from electrophysiological readouts of neuronal activity were processed through simulations on MATLAB via an in-house program. First, a clean, single AP was simulated, using known AP duration and basal/peak membrane potentials. Then the signal was distorted by the manual adjustment of sampling frequency and the signal to noise ratio. Readouts of neuronal activity obtained experimentally were then processed by simulating the raw values from bursts of APs across a range of sampling frequencies (0.3 – 5 kHz) to generate a series of alternative, theoretical electrophysiological readouts. Using a separate program, the electrophysiological signal was inverted to mimic the theoretical shape of a clean AP signal obtained using VSD imaging. Manual manipulation of the sampling frequency and parameters that influence noise when imaging (exposure time, data transfer time, noise amplitude before/after acquisition) was performed to distort the original signal and obtain readouts that closely resembled experimental VSDI traces.

## 2.6. Assay Development using the Microfluidic Drug Discovery Platform

The preliminary design of a microfluidic perfusion system was first produced and later improved upon by Dr Graham Robertson and used for the purpose of developing microfluidic perfusion assays in this thesis. The current microfluidic setup is primarily limited by a lack of flexibility during pharmacological assays due to the repeated performance of manual fluid application and removal. The aim of developing a microfluidic perfusion system in the current open-well microfluidic setup was to bypass the need for manual drug application, improve experimental control over drug delivery, and maximise the data throughput per device via multiple drug applications. MATLAB routines were designed by Dr Graham Robertson and Dr Michele Zagnoni and used for semi-automatic communication with syringe driven pumps via RS232 ports. Meanwhile, microfluidic perfusion assays were designed by myself and Dr Trevor Bushell.

### 2.6.1. Solution Preparation for Microfluidic Perfusion

To characterise the temporal kinetics of the perfusion system experimentally, calcein (25 - 75  $\mu\text{M}$  in DI water) was used to visualise fluid perfusion in the microfluidic device. Working solutions of the pharmacological agents, glutamate (0.0-1  $\mu\text{M}$ ), glutamatergic antagonists (2,3-dihydroxy-6-nitro-7-sulfamoyl-benzo[f]quinoxaline (NBQX), DL-2-Amino-5-Phosphonovalerate (DL-AP5) & (R,S)- $\alpha$ -methyl-4-carboxyphenylglycine ((R,S)-MCPG); Abcam, UK) and the  $\text{Na}^+$  channel blocker tetrodotoxin (TTX; TTX Citrate; Abcam, UK) were used to demonstrate the perfusion systems drug discovery capabilities and were prepared from frozen, pre-made stock solutions on the day of experimentation by dilution with HBS.

### 2.6.2. Microfluidic Perfusion System Setup

To ensure a drug solution flows through the perfused microfluidic chamber with precise temporal control, multiple syringe driven pumps were prepared prior to experimentation. Solutions previously prepared were loaded into glass syringes (5 mL, 10.3 mm diameter; SGE, UK), and air bubbles ejected before connecting to PTFE tubing (0.255 mm diameter, ~70 cm; Cole-Parmer, UK) via a blunted needle tip (0.4 mm diameter, ~20 mm length) and Tygon tubing ( ~20 mm). To permit continuous, undisturbed flow in the culture chamber, two syringe pumps were designated for the withdrawal of fluid, containing either DI water or vehicle (HBS) as appropriate. The tubing was primed with 1 mL of solution to eject air and ensure the inner diameter of the tubing was pre-loaded with fluid. Loaded syringes were placed into syringe pumps (AL-1000; WPI, UK), then locked into position to minimise

lag in fluid perfusion (Figure 2.5). Semi-automated perfusion was achieved using the programmable syringe pumps via MATLAB (2015a), which permitted user control of flow direction and flow rate for individual syringes. The tubing was then connected to needle ports previously created through the PDMS wall of the small well microfluidic device, via another piece of Tygon tubing and a needle tip (both ends blunted, 0.723 mm diameter, ~20 mm length). Silicone grease was applied to the connections responsible for fluid withdrawal to prevent leaking caused by the exerted negative pressure.

Rapid alternation between pumps is ideal to prevent changes to the pressure driving a constant steady flow, which would otherwise lead to delays in perfusate delivery and removal. Semi-automated control of up to four syringes (as required) ensured sharp transition periods between different perfusates, all set to the same constant flow rate ( $Q_{I-P}$ ), and only a single pump activated at any given time. Two pumps were set to withdraw fluid at a constant rate for the entirety of the experimental procedure, one syringe connected to the inlet well ( $Q_{I-W}$ ) and one to the outlet ( $Q_{O-W}$ ) well respectively (Figure 2.6). The following conditions for syringe driven perfusion were set prior to recording:

$$Q_{I-P} > Q_{I-W} \gg Q_{O-W} \quad \text{Equation 1}$$

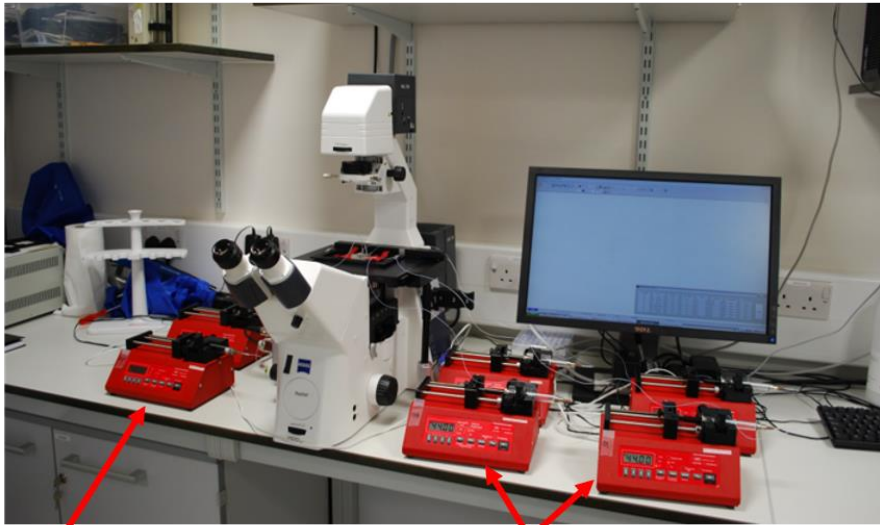
$$Q_{I-P} - Q_{I-W} = Q_{O-W} = Q_{Ch} \quad \text{Equation 2}$$

Prior to performing the experimental protocol, it is important to consider the time it takes for a perfusate to reach the microfluidic culture chamber, and, the area to be recorded. It is therefore necessary, to consider the hydraulic retention time (**HRT**) of the microfluidic inlet well, which is directly proportional to the transition time of perfusate delivery between different syringes. Under a steady constant flow rate ( $Q_{I-P}$ ), and a known defined volume ( $V_{I-well}$ ), it is possible to determine the time taken to completely exchange fluid in the inlet well ( $HRT \sim V_{I-well} / Q_{I-P}$ ). It is then possible to estimate the time ( $T_{ex}$ ) taken for drug solution to arrive at specific distance ( $L$ ) from the inlet well, assuming flow is travelling through a well-defined cross-section ( $S_{Ch}$ ), given by the following equation:

$$T_{ex} \sim HRT + \frac{S_{Ch} * L}{Q_{Ch}} \quad \text{Equation 3}$$



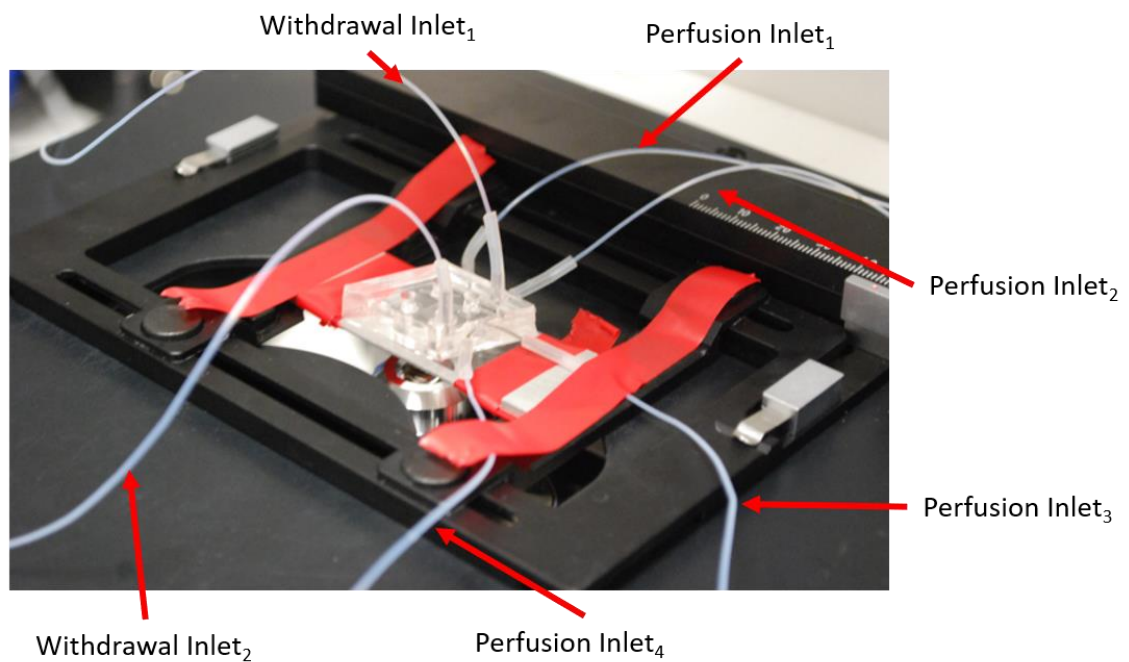
A



Syringe driven pumps  
(Withdrawal)

Syringe driven pumps  
(Perfusion)

B



Withdrawal Inlet<sub>1</sub>

Perfusion Inlet<sub>1</sub>

Perfusion Inlet<sub>2</sub>

Perfusion Inlet<sub>3</sub>

Withdrawal Inlet<sub>2</sub>

Perfusion Inlet<sub>4</sub>

**Figure 2.5: Syringe Driven Pump Setup for Microfluidic Perfusion.** (A) Semi-automated syringe driven pumps are positioned around the inverted microscope; two are used for the withdrawal of fluid from the microfluidic device, whilst 4 are used for the perfusion of fluid. (B) The microfluidic device and tubing are secured to the inverted microscope using red tape. Needle ports are used to connect tubing between the syringe pumps and the device via horizontal (perfusion) and vertical (withdrawal) inlets.

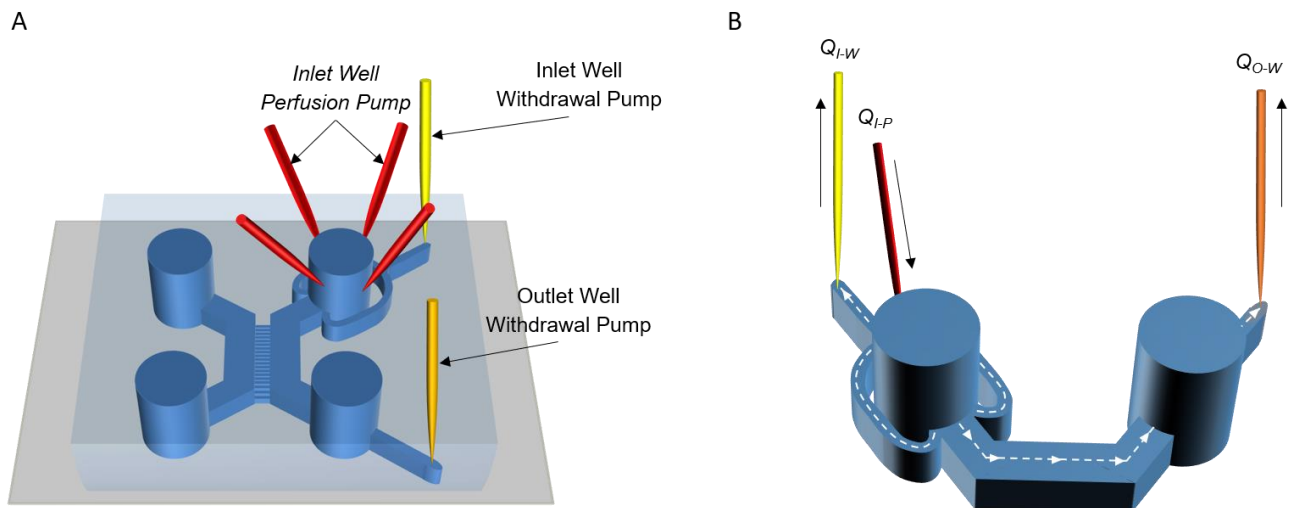


**Figure 2.6: Fluid Flow Path for Microfluidic Perfusion.** (A) A schematic of the microfluidic device shows syringe needles connected via ports to facilitate a steady flow rate and delivery of drug compounds to a single neural network. (B) By adjusting the flow rates of the syringe pumps responsible for perfusing fluid ( $Q_{I-P}$ ) and withdrawal of fluid at the inlet/outlet wells ( $Q_{I-W}$  &  $Q_{O-W}$  respectively), a positive net flow will pass through the culture chamber, highlighted by the white arrow paths.

### 2.6.3. Experimental Protocols for the Microfluidic Drug Discovery Platform

A variety of assays were developed to ensure the microfluidic perfusion system is not only a robust, reliable neuroscience research tool, but one that is also amenable to drug discovery. Recordings were performed on the Axio observer (A1) using the Luca R EM-CCD camera, with cultured/non-cultured devices used as appropriate for the assay performed. The devices were secured in place to minimise potential drift during recordings. Cultured microfluidic devices were washed three times with HBS to remove residual Neurobasal media. This washing step was repeated for devices after incubation with Fluo-4 AM ( $5 \mu\text{M}$  in HBS) for 1 hour at room temperature in the dark, whereupon devices were transferred to the inverted microscope and connected to the perfusion system. Similar to microfluidic assays described earlier (see section 2.4.), the fluidic conditions within small well microfluidic devices were adjusted such that the volume of fluid in wells connecting to the naïve chamber ( $50 \mu\text{L}$  each) was greater than that present in wells connecting to the perfused chamber ( $10 \mu\text{L}$  each), establishing a hydrostatic pressure gradient across the microchannel array. Due to the differences in hydraulic resistance between the microchannels and culture chambers, there is an inherent, negligible flow of vehicle from the naïve to the perfused culture chamber.

### 2.6.3.1. Live/Dead Imaging Assays

To determine the optimal flow rate for carrying out pharmacological assays, live/dead imaging assays were performed on microfluidic, primary hippocampal cultures at 12 - 14 DV. Separate devices were subjected to different single flow rates of HBS (ranging from 0.4 - 10  $\mu\text{l min}^{-1}$ ) through the perfusion chamber for an hour, followed by staining to assess the impact of shear stress on neuronal health. Controls included cultured devices that were left under static conditions at room temperature or stained immediately following removal from the incubator. Microfluidic devices were disconnected from the perfusion setup, HBS removed from the inlet/outlet wells and replaced with propidium iodide (necrotic cell stain; PI, 20  $\mu\text{M}$ ) and Hoescht (DNA stain 4.5  $\mu\text{M}$ ) in HBS solution. The hippocampal cultures were washed with HBS three times after a 30-minute incubation period in the dark at room temperature, followed by a 15 minutes recovery period before transferral to the Axio Observer (Z1).

Signal from PI and Hoescht was obtained using filter set 63 HE (BP 572/25, FT 590, BP 629/62; Carl Zeiss, AG) and filter set 44 (BP 475/40, FT 500, BP 530/50; Carl Zeiss, AG) respectively. Brightfield and fluorescent images were taken at three fixed locations in culture chambers, namely the top, middle and bottom, centred over the internal micropillar structures, using a 10X objective and the AxioCam MRm. For a set of images taken at any given location in the culture chamber, the bright field image was used as a reference, the two fluorescent images were combined, and cells manually counted on ZEN 2012 (blue edition). Cells were identified from debris by the presence of projections, dead cells were identified by the co-staining of Hoescht and PI, and living cells were identified by the staining of the former.

### 2.6.3.2. Validation of the Microfluidic Perfusion Protocol

Non-cultured microfluidic devices were connected to the perfusion set up and syringe pumps set to perfuse DI water at a steady flow rate of 4  $\mu\text{l min}^{-1}$  (as detailed in **Equation 1 & 2**), determined during live/dead imaging assays to be the optimal flow rate to maintain neural network health. The FOV for the experimental protocol was set to span an area encompassing the full width of the perfused chamber, the microchannel array and the immediately adjacent segment of the naïve chamber, using a 2.5X objective. Recordings were sampled at 2 Hz, no binning applied, EM gain set to 150x, and the filter set 46HE (with FI attenuator at position 6) used to excite the calcein dye. A steady flow rate was allowed to establish over the course of 8-10 minutes prior to 4 minute recordings that were

separated by 8-10 minutes without signal acquisition. This would minimise residual calcein solution that may still have been present in the perfused chamber of the microfluidic device.

Syringe pumps containing calcein solution were activated individually during separate recordings for a minute after 30 seconds of background readings with DI water perfusion, semi-automated control of the perfusion setup permitting the near simultaneous transition between different active pumps. Recordings were first processed on Andor SOLIS and two ROIs were selected opposite each other across the microchannel array, positioned along the horizontal centre line of the recording. To account for differences in the onset of calcein perfusate reaching the FOV between recordings and devices, the mean raw data obtained from the ROIs of each device was scaled using the following equation:

$$f(x) = \frac{(x-\min)}{(max-\min)} \quad \text{Equation 4}$$

In this instance, “x” can be defined as the raw fluorescent data obtained per trace, per ROI, and the “min/max” value is defined as the absolute minimal and maximal fluorescent values obtained.

### 2.6.3.3. Development of Pharmacological Assays

The pharmacological characterisation of glutamate was performed on hippocampal cultures (10-14 DIV) within microfluidic devices and additional assays were performed to highlight changes in neuronal communication between perfused and naïve neural networks following multiple drug applications. The FOV was centred over the microchannel array to provide readouts of up to 400 cells in either culture chamber using a 5X objective. An exception to this was during assays performed to generate a glutamate concentration curve, which involved the use of a 10X objective to improve upon the sensitivity of readouts. The recording setup is as described previously (see section **2.6.3.2.**) with the exception that a greater intensity of excitatory light was used (FI attenuator position 5) to increase the magnitude of fluorescent response obtained.

The perfusion system was set to a steady flow rate of 4  $\mu\text{l min}^{-1}$ , the perfusion of HBS rapidly switched to a pharmacological agent for 1 minute during recordings, following 30 seconds of baseline readings. Recordings lasted for 4 minutes each, separated by 8-10 minutes in darkness to ensure pharmacological agents were completely washed out of the chamber prior to the next recording. The first recording was obtained to observe basal levels of activity in the absence of perfusing syringe pump alternation. Three subsequent recordings examined perfused and naïve neural network activity under different stimulatory conditions before the continuous steady flow was stopped and a

final recording performed to identify neurons from glial cells with the application of KCl (25 mM final concentration) to each culture chamber. One of the four syringes contained HBS, and three syringes contained experimental solutions as required.

Additional assays performed to demonstrate the absence of retrograde activation of the naïve neuronal network by perfused glutamate, involved the use of microfluidic devices cultured with a single neural network in the naïve, non-perfused chamber. Using the same perfusion protocol described above, axonal projections traversing the microchannel array from the naïve chamber into the adjacent chamber were exposed to repeated glutamate perfusions.

#### 2.6.3.4. Data Processing for Pharmacological Assays

Recordings were processed on Andor SOLIS similarly to that described previously (see section 2.4.3.), converted to time variant signals on Matlab (2015a). The traces obtained from each cell were manually identified as neuronal or glial in origin (see section 2.4.3.). Depending on the perfusate used during recordings, and the network analysed, one of two methods were employed to process data qualitatively and quantitatively.

##### 2.6.3.4.1. Determining Fluorescent Magnitude in Response to Stimuli

Fluorescent readouts per recording were temporally averaged to determine the fluorescent response per cell population following drug perfusion used in the experiment. Then, 10 frames were averaged from highlighted segments of the basal plateau before drug perfusion, and at the fluorescent peak response (Figure 2.7). All traces were normalised to their respective basal fluorescent values, with the difference between baseline and peak response reporting a peak fluorescent magnitude. The peak magnitude values for each cell are pooled with respect to recording/drug perfusion and each peak magnitude value is divided by the mean peak fluorescent response, thereby providing individual cell peak magnitude response with respect to the average response to pharmacological treatment.

To generate a glutamate concentration response curve, individual peak magnitude response per recording/treatment was averaged, then normalised to the mean peak magnitude of the maximal glutamate concentration (1 mM). The results were plotted using the Hill-Langmuir equation using BioGraph:

$$y = \frac{R_{Max}}{1 + \left(\frac{x}{EC_{50}}\right)^n} \quad \text{Equation 5}$$

$R_{Max}$  in this instance is the maximum response observed, the  $EC_{50}$  is the effective concentration at which 50 % of the maximum response is obtained. The Hill co-efficient,  $n$ , is used to describe the saturation of a ligand with respect to ligand concentration when competing for a finite population of receptors.

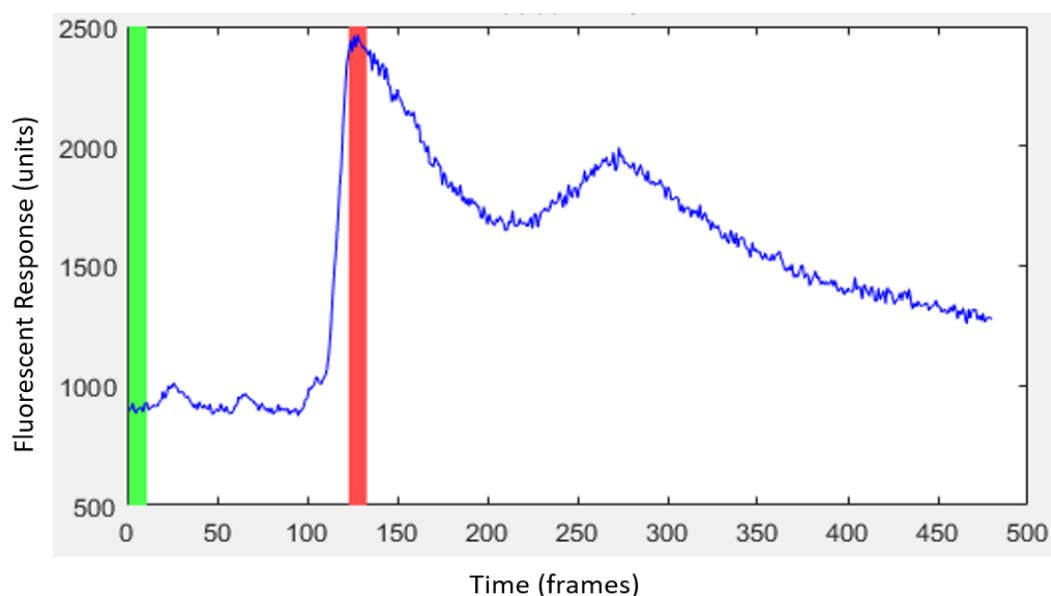


**Figure 2.7: Analysis of Individual Readouts.** A Representative trace is shown of the averaged neuronal response to 1 mM Glutamate perfusion from a single device. The green bar highlights 10 frames used to determine the average basal fluorescence at the start of the recording, whilst the red bar highlights the 10 frames at which the peak fluorescent response to 1 mM Glutamate is observed.

#### 2.6.3.4.2. Determining Neuronal Network Activity

Changes in network activity, with respect to the delivery of CNS acting compounds to the perfused culture chamber, were assessed by the automated counting of calcium events for each recording before and during perfusate delivery. This allowed the determination of the causal relationship between direct neuronal stimulation and the indirect stimulation of the adjacent naïve neuronal network. An in-house program developed in Matlab was used to stitch traces obtained from multiple recordings together, displaying cellular activity during the recorded segments of the assay. Then, the signals were filtered with a moving window filter (11 frames averaged) and normalised to the first 24 frames of the baseline recording. A threshold was applied to minimise the detection of superficial events above background noise. Additionally, specific values for parameters applied were varied slightly between devices depending on the level of background noise, or if a noticeable amount of activity was present at the sub-region used for baseline. Generally, an event was identified when

significant increases in fluorescence value exceeded 7 standard deviations of the median baseline fluorescence, occurring within a moving window of 10 seconds (Figure 2.8).

Due to the fluidic protocol of 30 seconds baseline recording prior to a minute of perfusate delivery, the output of data processing provides the number of events taking place per cell, per minute, expressed as ENM (events/neuron/minute). Results obtained across multiple devices were pooled with respect to the type of recording/perfusate and averaged. Finally, the data obtained during each recording for basal activity and during perfusate delivery were compared using the appropriate statistical analysis.

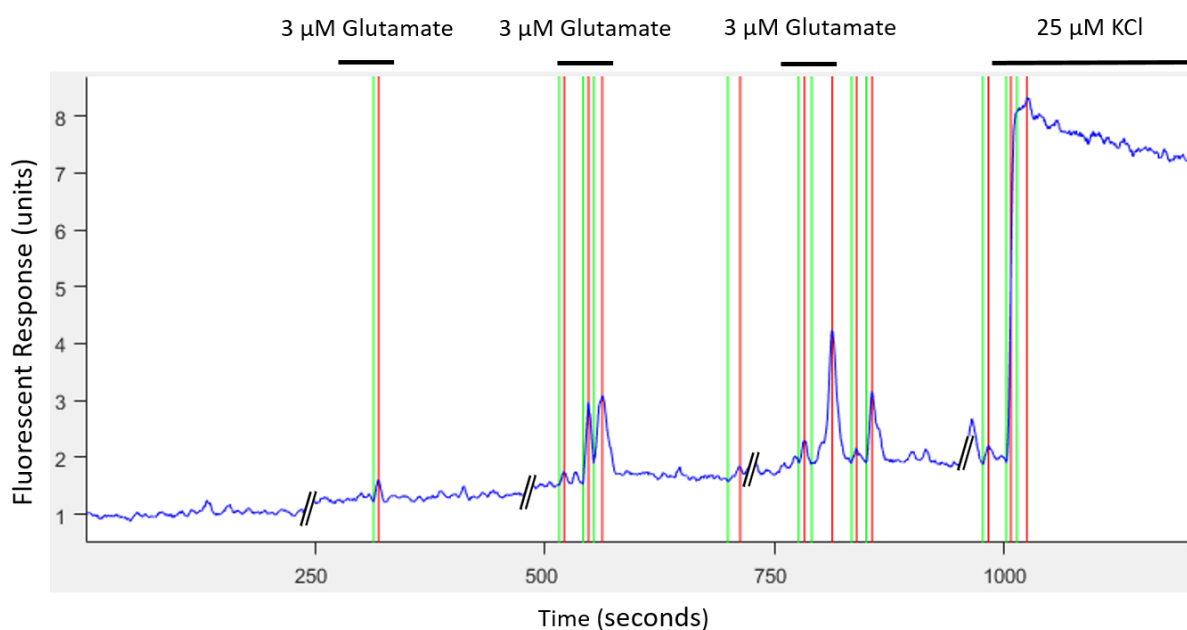


**Figure 2.8: Automated Detection of Calcium Events.** Fluorescent traces obtained from recordings were stitched together (highlighted by black/white dashes) and processed on MATLAB. The image depicts a naïve neuron indirectly activated by the directly perfused neural network, calcium events (red bars) detected where an increase in fluorescence was greater than 7 standard deviations of the basal fluorescence (green bars).



## 2.7. Chemogenetics for Microfluidic Communication Assays

Following development of microfluidic perfusion assays for CNS drug discovery, chemogenetic assays using DREADDs (designed receptors exclusively activated by designed drugs) were developed using standard hippocampal culturing techniques. A combined approach utilising chemogenetics and the microfluidic perfusion system previously described would then permit the performance of novel assay design.

### 2.7.1. DREADD Transfection of Hippocampal Cultures.

The DREADD containing plasmid used during assays was pAAV-CaMKIIa-hM3D(Gq)-mCherry, and was obtained from Addgene (USA), whilst empty, fluorescently tagged plasmids used were pAAV-CMV-mCherry/GFP. All plasmids used during assays were prepared by Dr Rothwell Tate (University of Strathclyde, UK) to a concentration ranging between 3 - 3.5  $\mu\text{g mL}^{-1}$  in sterile, RNase free water, aliquoted and stored at -20 °C.

### 2.7.2. Pharmacological Agent Preparation for Chemogenetic Assays

To activate the Gq coupled DREADDs, working solutions of the otherwise inert compound, clozapine-n-oxide (CNO; Tocris, UK) were prepared on the day of experimentation to a final concentration of either 10  $\mu\text{M}$  or 20  $\mu\text{M}$ , diluted from frozen stock concentrations (20 mM in DMSO).

### 2.7.3. Transfection Protocols for Chemogenetic Assays

Cultures were grown in 4 well plates and microfluidic devices and transfected between 8 - 10 DIV using the Lipofectamine 3000 kit (ThermoFisher, UK), with differing transfection protocols. Briefly, for every 1  $\mu\text{g}$  of plasmid DNA required, 2  $\mu\text{L}$  of P3000, and 1.5  $\mu\text{L}$  of Lipofectamine 3000 was required. The plasmid DNA was mixed with P3000 and diluted to 50  $\mu\text{L}$  in Opti - MEM I (ThermoFisher, UK), whilst Lipofectamine 3000 was diluted separately to 50  $\mu\text{L}$  in Opti - MEM I; both solutions were mixed separately and allowed to rest for 5 minutes. The solutions were then pooled together, mixed and left to rest for approximately 30 minutes before dilution in 400  $\mu\text{L}$  solution containing a 1:1 ratio of Opti - MEM I and conditioned culture media. Culture media was completely withdrawn from the 4 well plates, and 500  $\mu\text{L}$  of transfection solution (containing 1  $\mu\text{g}$  plasmid DNA) was transferred to each well, and transfection taking place for 3 hours under static conditions. To compensate for the smaller volume present in microfluidic devices (~102  $\mu\text{L}$  per culture chamber and connecting wells), 50  $\mu\text{L}$  of transfection solution containing either 5 or 10  $\mu\text{g}$  of plasmid DNA was



transferred to emptied inlet/outlet wells (1  $\mu\text{g}$  plasmid DNA per culture chamber). Transfection occurred under either static conditions (3 hours or overnight) or under a gentle flow rate, induced by withdrawing 5  $\mu\text{L}$  of solution from the lower outlet wells connecting to each chamber, and 5  $\mu\text{L}$  of fresh transfection solution re-applied to the top, inlet wells every 30 minutes for 3 hours. Following the transfection procedure, cultures were gently washed with warm, supplemented Neurobasal media, which was then completely replaced with a solution containing a 1:1 ratio of fresh Neurobasal media and conditioned culture media. Cultures were then transferred back to the incubator for 2 - 3 days prior to experimentation.

#### 2.7.4. Imaging Plate based Transfected Neural Networks

Each 4 well plate underwent live/dead imaging and calcium imaging, two wells transfected with a single, mCherry tagged plasmid, and the remaining two wells served as internal negative controls (Figure 2.9). First, each well was washed three times with HBS and the plate transferred to the Axio Observer (A1), images taken at random locations of the well with the EM CCD to determine transfection efficiency. A 10X objective was used with the custom filter cube set and FI attenuator (position 4) to identify transfected cells, and bright field images taken to identify cell somas. Images were with an EM Gain of 150x applied to increase the signal of fluorescently labelled cells. Then, solution was removed from all wells and two wells (one non/transfected) were treated with PI (20  $\mu\text{M}$ ) and Hoescht (4.5  $\mu\text{M}$ ) in HBS solution for 30 minutes, whilst the remaining two wells were treated with Fluo-4-AM (5  $\mu\text{M}$ ) in HBS for an hour, incubated in the dark at room temperature.

The wells used for live/dead imaging were subjected to the washing step again and the plate transferred back to the inverted microscope and camera setup. Brightfield and fluorescent images were taken at random locations within the wells, obtained with a 10X objective, processed using Andor SOLIS and assessed following the criteria outlined in section **2.6.3.1**.

Following 1 hour incubation with Fluo-4 AM, wells were washed and left to rest for 5 minutes with 500  $\mu$ L of fresh HBS. A random area was selected as the FOV for recording activity in the non-transfected well, whilst at least one transfected cell would be located within the FOV for the transfected well. Using a 10X objective and the recording setup described previously (see section 2.6.3.2.), changes in activity were monitored over the course of 4 minutes in response to drug applications. After a 30 second baseline period 250  $\mu$ L of HBS was withdrawn and immediately replaced with 250  $\mu$ L of fresh HBS (vehicle control). After 1 minute, 250  $\mu$ L of HBS was replaced with CNO (10  $\mu$ M), followed by KCl (25 mM) a minute later.

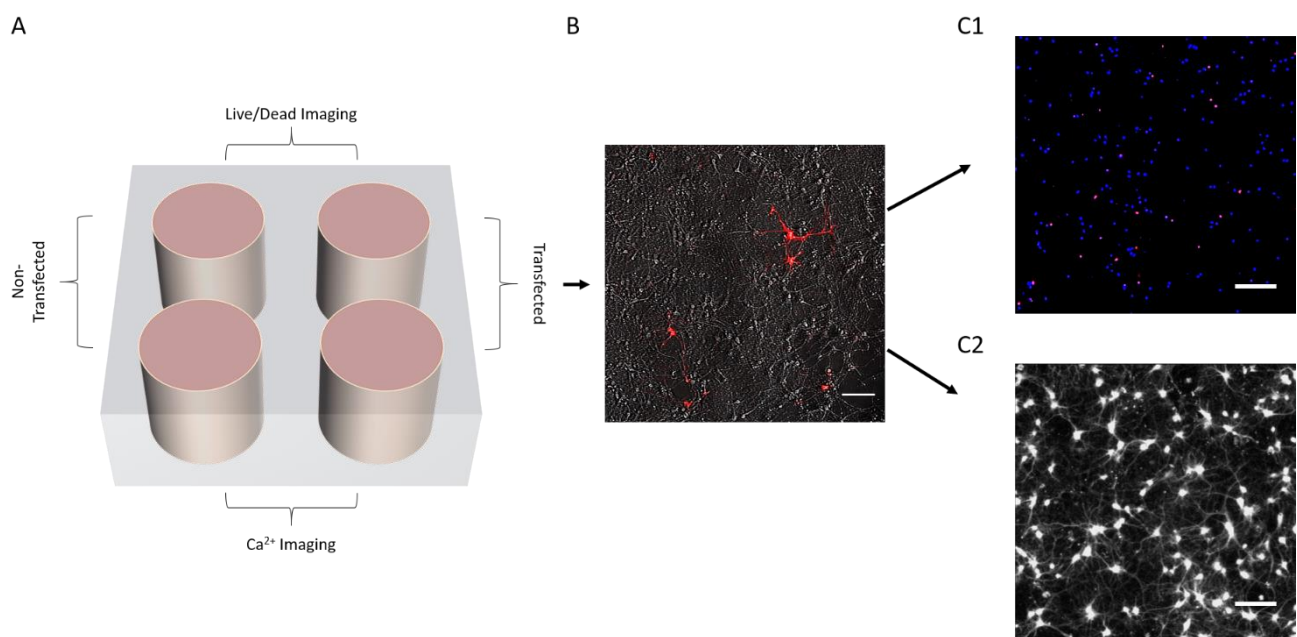


**Figure 2.9: DREADD Transfected Hippocampal Network Assay Setup.** (A) Two wells of the cultured 4-well assay plate were transfected with the DREADD hM3Dq. This permitted live/dead imaging and  $\text{Ca}^{2+}$  imaging to be performed on transfected neural networks alongside their respective, non-transfected control wells. (B) A representative image merging brightfield and red emitting fluorescent channels reveals DREADD transfected cells which co-express the mCherry gene. (C) Following imaging of transfected cells, live/dead imaging (C1) and  $\text{Ca}^{2+}$  imaging (C2) was performed to assess neural network health and activity. Scale Bars = 100  $\mu$ m.

### 2.7.5. Imaging Transfected Microfluidic Neural Networks

The impact of transfection on neural network viability and transfection efficiency was first determined in microfluidic devices prior to chemogenetic perfusion experiments. Devices were washed with HBS solution, fluorescent and bright field images then taken from both culture chambers of individual devices to determine transfection efficiency. Immediately after this, live/dead assays were performed, images captured, processed and assess following the protocols outlined in section **2.6.3.1**.

Separate transfected devices were stained with Fluo-4 AM (5  $\mu$ M in HBS) for 1 hour in the dark at room temperature, washed with HBS, transferred to the Axio Observer (A1) and connected to the perfusion set up described previously (see section **2.6.2**). The flow rate was adjusted to a steady flow rate of 4  $\mu$ l  $\text{min}^{-1}$ , and a 5X objective used to identify non/transfected cells with the recording setup described previously (section **2.6.3.2**; FI attenuator position 5). Still fluorescent images were taken immediately prior to chemogenetic assays to ensure transfected cells were indeed present in the directly perfused culture chamber. Thus, any changes in the activity of the naïve neuronal network observed during CNO perfusions were attributed to the excitation of transfected cells in the perfused chamber, and the subsequent activation of local and adjacent neural networks. Chemogenetic assays were similar to previous perfusion-based assays in duration of recordings and perfusate delivery during recordings (see section **2.6.3.3**). The exception to this was that there was only a single recording in which the pharmacological agent of interest (CNO) was perfused, instead of multiple times over separate recordings. After washout, the perfusion was stopped, and networks were exposed to the application of KCl (25 mM).

### 2.7.6. Analysis of Chemogenetic Assays

Following calcium imaging based chemogenetic assays in 4-well plates and microfluidic devices, the recordings obtained were processed on Andor SOLIS as described previously (see section **2.4.3.**). Intracellular calcium increases observed as a direct response to fluidic applications and the changes in activity of local/indirect networks were processed on MATLAB (2015a) as appropriate, using methods described previously (see section **2.6.3.4.**).

## 2.8. Statistical Analysis

The data obtained from experimental procedures were expressed as mean  $\pm$  S.E.M. and compared using paired t-tests, unpaired t-tests, or one-way ANOVA with Tukey's post-hoc comparison where appropriate. When assessing neural network activity, either as a measurement of basal activity or in response to pharmacological assessments, neuronal and astrocyte mean  $\pm$  S.E.M. and n numbers represent (respectively) populations pooled from multiple devices/coverslips/4-well plates, unless otherwise stated. Differences between sample groups were determined as significant when  $P < 0.05$ .

## **3. Investigating Voltage Imaging Techniques**

### **3.1. Chapter Overview**

PDMS based microfluidic devices offers numerous advantages over standard platforms for assay performance, as the gas permeable PDMS facilitates the maintenance of most forms of microscopic biological life including 2D & 3D non/primary cell cultures and pathogens when combined with fluid exchange via open reservoirs. Additionally, microfluidic device prototyping is a cost-effective approach in academic environments, the ability to custom design microfluidic layouts allow user influence over cell patterning, and high-throughput fluorescent assays can be performed by taking advantage of the transparent PDMS structure. Using established microfluidic methodologies in neural network culture, this chapter explores the potential of VSDI to be used as a low-cost, higher-throughput alternative to patch clamp techniques for recording neuronal network activity, at a cost of a lower temporal resolutions.

There are numerous studies that have shown functional communication between environmentally isolated functional neuronal networks in microfluidic devices, using either microscopy<sup>275,276,278,291,308</sup>, MEA techniques<sup>277,309,310</sup> or a combination thereof<sup>311,312</sup>. The use of VSDs in neuroscience meanwhile has permitted the visualisation of synaptic activity with similar resolutions as whole cell patch clamp recordings<sup>219,313,314</sup>, and as an optical imaging tool, offers a potential increase in spatial resolutions for numerous cells to be recorded simultaneously. In this work, building upon previously established Ca<sup>2+</sup> imaging techniques for monitoring neuronal network activity, the optimisation of a VSDI assay was performed in the attempt to optically monitor the activity of multiple neurons simultaneously.

### **3.2. Introduction and Chapter Objectives**

Over the last century, the observation of synaptic activity within hippocampal neural networks both *in vitro* and *in vivo* has played a vital role in our understanding of the functional brain under physiological conditions<sup>211,315–317</sup>. It is through this understanding that we have identified the basis for neurological disorders, such as the complete degradation of synapses in Alzheimer's disease<sup>134,135,146</sup> and thus there is a clear need to further investigate the changes in synaptic activity under pathophysiological conditions. Restoring synaptic function by targeting the suspected underlying pathways has been the primary focus of neuropharmacological research in many CNS related

disorders<sup>144,180,318</sup>. Animal models of neurological disease such as Alzheimer's or Parkinson's disease are crucial for understanding the impact of disease on normal neurophysiological behaviour<sup>319,320</sup>. Their translational value has been poor however, and the success rate of new pharmaceutical therapies based on these early studies have been to date, relatively fruitless<sup>321–323</sup>. Thus, the development of novel research tools is required to investigate, model, and better understand CNS disorders for neuropharmacological development to be a success.

Microfluidic systems are particularly beneficial for neuroscience studies in this regard because of the greater control and design over neural network patterning and fluid manipulation<sup>324</sup>. Such systems have been used to demonstrate functional communication between environmentally isolated networks<sup>275</sup>, the spread of neurotoxicity<sup>276</sup>, and modelling disorders such as Alzheimer's disease<sup>300</sup>. An additional benefit of this research tool is the integration of standard neuroscientific techniques such as MEA recordings and Ca<sup>2+</sup> imaging. Patterning neural networks across an MEA chip permits high-throughput electrophysiological readouts of network activity<sup>325</sup>, however the associated equipment and consumables are expensive, a low likelihood typically exists for a neuron-electrode interface and recordings do not necessarily detect subthreshold membrane potentials used to identify excitatory/inhibitory signal inputs<sup>326</sup>. Ca<sup>2+</sup> imaging on the other hand is comparatively cheaper and requires significantly less expertise to use, and similarly provides high data-throughput with single cell spatial resolutions<sup>210</sup>. However, the temporal resolutions are lacking, primarily due to slow Ca<sub>i</sub><sup>2+</sup> dynamics. This can be overcome with VSDs, which are reported to offer temporal resolutions on par with electrophysiology techniques<sup>313</sup>. Indeed, these dyes have been used to optically monitor the synaptic activity across cultured neural networks, with fluorescent responses provided following dynamic changes in membrane potential<sup>225,314</sup>. This approach of imaging neuronal activity with fast temporal resolution therefore presents a potential for greater spatial resolutions during recordings with respect to techniques such as the whole cell patch clamp. A caveat to this approach however is that spatial resolution is often required to be sacrificed in order to achieve greater temporal resolutions. Developing this tool for use in dual chamber microfluidic devices therefore presents a challenging opportunity for investigating synaptic communication between environmentally isolated neuronal networks in greater detail than current approaches.

The purpose of this chapter is to develop VSDI in a microfluidic setup and demonstrate fit for purpose in the measurement of synaptic activity between isolated neuronal networks. This assumes first, that synaptic communication exists between hippocampal networks cultured in dual chamber microfluidic devices, and that current  $\text{Ca}^{2+}$  imaging techniques employed are insufficient to record synaptic activity. Additionally, the spatio/temporal resolution trade-off when using VSDs must allow the observation of synaptic activity whilst permitting the recording of multiple neurons simultaneously.

I first attempted to replicate previous findings of functional synaptic activity present between environmental isolated neuronal networks. This was achieved by investigating neuronal projections for synaptic proteins via immunocytochemical staining. The protocol for drug application in the microfluidic system was then validated by demonstrating the absence of cross-contamination between the two culture chambers which would otherwise confound results obtained from pharmacological assessments. The aim was then to assess synaptic communication between the two networks by the direct stimulation of a single network whilst simultaneously observing the adjacent network for indirect activation.

The temporal limitations of  $\text{Ca}^{2+}$  imaging was experimentally assessed to demonstrate the need for VSDI assay development. By stimulating cells using improved temporal resolutions, individual cell readouts can be evaluated to assess the evidence for synaptic activity detection.

Whilst the final objective is to perform VSDI assays in a microfluidic format, it is important to first demonstrate that VSDs are functionally active and produce a signal, both spontaneously and evoked following neuronal stimulation. To this end, a variety of optimisation steps were performed, with the findings presented and discussed.

### **3.3. Immunocytochemical Staining of Microfluidic Hippocampal Cultures**

Immunocytochemistry was performed to confirm that the microfluidic array does not impede the growth of axonal projections between neuronal populations of one network to the other, and that synapses are indeed present within the microchannels. Primary hippocampal cultures were maintained for 10-14 DIV before staining for neuronal, glial and synaptic markers, with coverslips serving as controls for networks grown in microfluidic devices.

#### **3.3.1. $\beta$ III-Tubulin and Glial Fibrillary Protein**

Standard markers for neuronal and glial cell bodies are  $\beta$ III-tubulin and glial fibrillary acidic protein (GFAP) and thus used to assess neural network growth in the dual chamber microfluidic device. Immunocytochemical staining revealed highly confluent hippocampal neural networks on both coverslips and in microfluidic devices (Figure 3.1). From the fluorescent signal obtained in the microchannel array, axonal projections are seen traversing the microchannels without hindrance to the adjacent network. In contrast, glial projections are significantly shorter than their neuronal counterparts and are unable to fully traverse the width of the microchannel array. Whilst the presence of axonal projections through the microchannels suggests the environmentally isolated networks are connected to each other, these images alone do not prove that synaptic communication between the two networks exists.



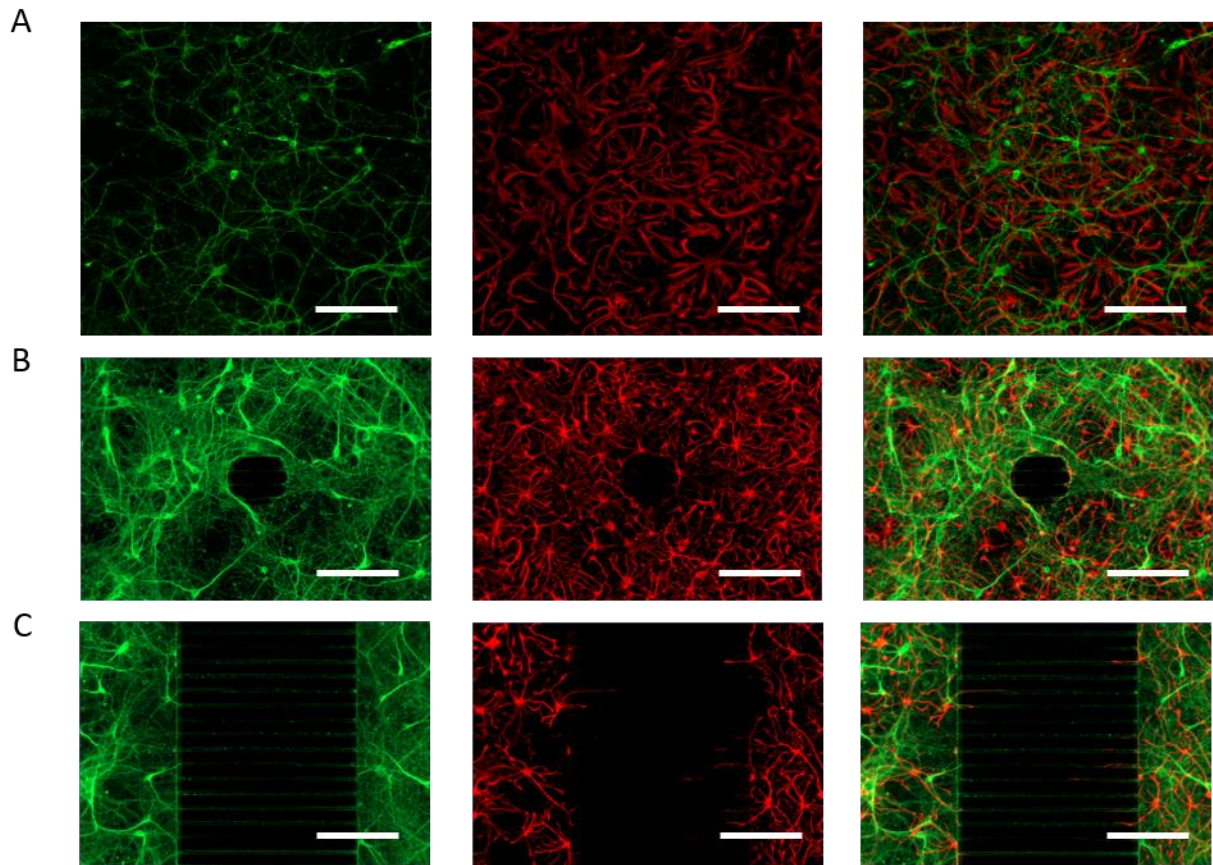


**Figure 3.1: Representative Immunofluorescent Images of Neurons and Astrocytes present in Primary Hippocampal Cultures.** (A) Images highlighting the presence of neurons ( $\beta$ III-tubulin positive, green) and astrocytes (GFAP positive, red) grown on glass coverslips. (B) Images conforming to an identical cellular composition when cultures are grown in microfluidic devices. (C) Images revealing that neurons, but not astrocytes, traverse the microchannel array and into the opposing culture chamber. (A-C) 10X magnification was used to acquire images; Scale Bars: 200  $\mu$ m.

### 3.3.2. $\beta$ III-Tubulin & Synaptophysin

Synaptophysin is a synaptic vesicle protein that is implicated in the development of immature synapses between neurons and modulates activity dependent synapse formation during the maturation of neural network circuits<sup>327,328</sup>. As a commonly used marker for the detection of synapses, hippocampal cultures were stained for synaptophysin and  $\beta$ III-Tubulin (Figure 3.2). Synaptophysin staining reveals synapses are present throughout the network and images taken of the microchannel arrays show clearly defined synaptophysin staining indicative of synapse formation. Nonetheless, immunocytochemistry is unable to determine whether the synapses present between the two neuronal networks are functionally active.

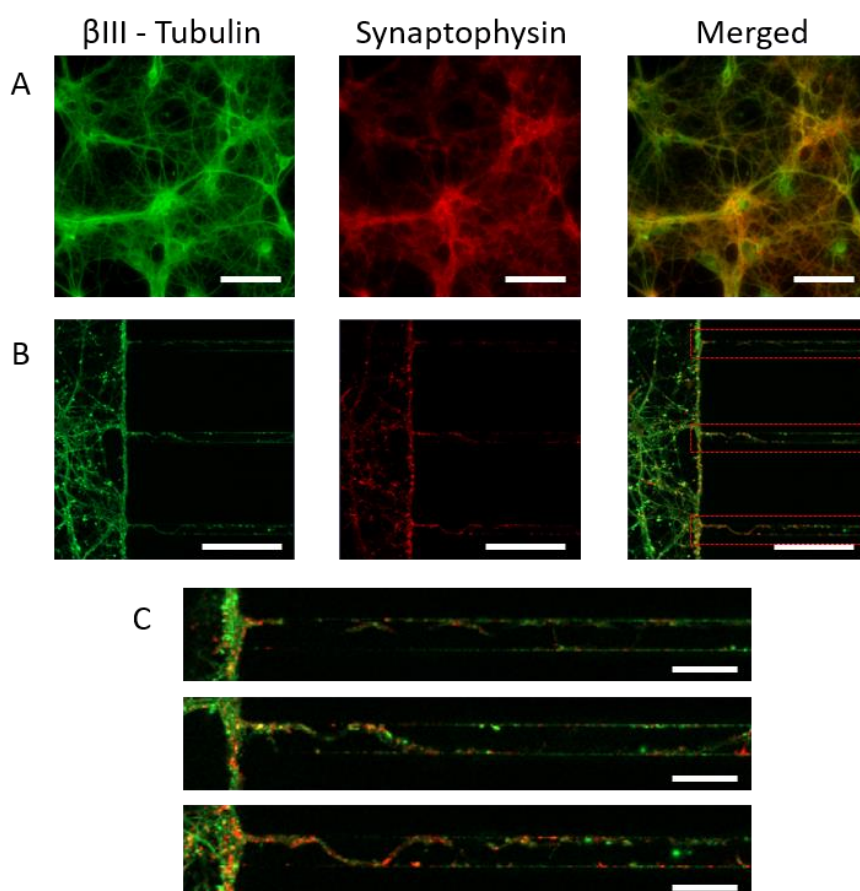


**Figure 3.2: Representative Fluorescent Images of Synaptic Protein in Neuronal Networks.**

(A, B) Neuronal networks grown on coverslips and microfluidic devices (20X images) reveals the co-localisation of synaptic vesicle protein synaptophysin (red) with  $\beta$ -III-Tubulin (green) on neuronal somas and projections. (B, C) Higher magnification (63X images) of the microfluidic array (obtained at the request of Scientific Reports) reveals synaptic vesicles at greater spatial resolutions, with synaptic boutons, highlighted by synaptophysin, present on neuronal projection bundles within and outwith the microchannel array. (A, B) Scale Bars: 100  $\mu$ m; (C) Scale Bars: 25  $\mu$ m.

### 3.4. Confirmation of Synaptic Activity in Microfluidic Neuronal Networks

The fluidic conditions of a microfluidic assay setup were tested to ensure that directly applied samples to a single chamber do not contaminate the adjacent chamber during  $\text{Ca}^{2+}$  imaging, which would otherwise bias results. Then the functionality of synapses observed from immunocytochemical imaging would be determined via pharmacological assessments during  $\text{Ca}^{2+}$  imaging assays, in microfluidic cultures at 10-14 DIV.

#### 3.4.1. Theoretical Model of *In Situ* Microfluidic Applications

The direction of fluid flow from one chamber to another is reliant on a hydrostatic pressure difference amongst all chambers, which can be determined mathematically by calculating the internal pressure of each chamber. By applying a set volume in each reservoir ( $V = \pi r^2 h$ ), a pressure ( $P = \rho g h$ ) is created by gravity ( $g$ ) acting upon the resulting height ( $h$ ) of the fluid with a known density ( $\rho$ ), which can be resolved using the simplified Equation 6

$$P = \frac{\rho g}{\pi r^2} V \quad \text{Equation 6}$$

In the microfluidic device, fluid will flow through a channel when a pressure difference is present across its ends. The fluidic resistance of a channel is defined by its geometry (width,  $w$ , height,  $h$  & length,  $l$ ) and the dynamic viscosity ( $\mu$ ) of fluid used. In this case, the culture chamber between connecting inlet-outlet wells, and the array of microchannels separating the two culture chambers, have separate, distinct hydraulic resistance ( $R_h$ ). The channels used have rectangular geometries, where width,  $w$ , is greater than height,  $h$ , and so hydraulic resistance ( $R_h$ ) for the culture chamber can be defined using Equation 7, whilst the resistance of the microchannel array ( $R_{Par}$ ), obtained from the resistance of the microchannels ( $R_i$ ) running in parallel can be solved using Equation 8.

$$R_h = \frac{12\mu l}{wh^3 \left(1 - 0.630 \frac{h}{w}\right)} \quad \text{Equation 7}$$

$$R_{Par}^{-1} = \sum_1^N R_i^{-1} \quad \text{Equation 8}$$

Using Equations 7 & 8, it is possible to verify that the fluidic resistance present across the microchannel array is indeed at least two orders of magnitude greater than that of the culture chamber, thereby demonstrating negligible flow across the array when a pressure gradient has been established:

Culture Chamber Hydraulic Resistance:

$$R_h \approx \frac{12\mu L}{wh^3\left(1-0.63\left(\frac{h}{w}\right)\right)} = \frac{12 \times 8.9 \times 10^{-4} \text{ Pa.s} \times 9.0 \times 10^{-3} \text{ m}}{2 \times 10^{-3} \text{ m} \times 5.12 \times 10^{-13} \text{ m}^3 \times \left(1-0.63 \times \left(\frac{0.08 \times 10^{-3}}{2 \times 10^{-3}}\right)\right)} = \frac{0.9612 \times 10^{-4}}{1.024 \times 10^{-15} \times 0.9748} = 9.629 \times 10^{10} \text{ Pa.s m}^{-3}$$

Individual Microchannel Hydraulic Resistance:

$$R_h \approx \frac{12\mu L}{wh^3\left(1-0.67\left(\frac{h}{w}\right)\right)} = \frac{12 \times 8.9 \times 10^{-4} \text{ Pa.s} \times 0.45 \times 10^{-3} \text{ m}}{0.01 \times 10^{-3} \text{ m} \times 3.43 \times 10^{-16} \text{ m}^3 \times \left(1-0.63 \times \left(\frac{0.007 \times 10^{-3}}{0.01 \times 10^{-3}}\right)\right)} = \frac{4.806 \times 10^{-6}}{3.43 \times 10^{-21} \text{ m} \times 0.559} = 2.506 \times 10^{15} \text{ Pa.s m}^{-3}$$

Microchannel Array Hydraulic Resistance:

$$R_{par}^{-1} = \sum_{i=1}^N R_i^{-1} = \frac{2.506 \times 10^{15}}{200} = 1.253 \times 10^{13} \text{ Pa.s m}^{-3}$$

Volumes present within the inlet/outlet wells of a dual chamber microfluidic device give rise to pressure; If the pressure in one well is greater than another connected well, then a pressure gradient will form across the microchannel network. The flow rate of a fluid established between two sources of pressure (open wells;  $\Delta P = P_2 - P_1$ ) through a channel presenting resistance ( $R_h$ ) to flow, can be determined using the following equation:

$$Q = \frac{\Delta P}{R_h} \quad \text{Equation 9}$$

Using a combination of Equation 6 & Equation 9, it is possible to approximate the initial flow rate in the culture chamber when the volume present in the inlet well is double that present in the outlet well.

Pressure at Inlet Well:

$$P = \frac{\rho g}{\pi r^2} V = \frac{1000 \text{ kg m}^{-3} * 9.8 \text{ N kg}^{-1}}{3.1416 * (0.004 \text{ m})^2} 1 \times 10^{-7} \text{ m}^3 = \frac{9800 \text{ N m}^{-3}}{5.02656 \times 10^{-5} \text{ m}^2} 1 \times 10^{-7} \text{ m}^3 = 19.5 \text{ N m}^{-2}$$

Pressure at Outlet Well:

$$P = \frac{\rho g}{\pi r^2} V = \frac{1000 \text{ kg mm}^{-3} * 9.8 \text{ N kg}^{-1}}{3.1416 * (0.004 \text{ m})^2} 5 \times 10^{-8} \text{ m}^3 = \frac{9800 \text{ N mm}^{-3}}{5.02656 \times 10^{-5} \text{ m}^2} 5 \times 10^{-8} \text{ m}^3 = 9.75 \text{ N m}^{-2}$$

Solve for Flow Rate ( $U$ ):

$$U = \frac{\Delta P}{R_h} = \frac{9.75 \text{ N m}^{-2}}{9.62910 \times 10^{10} \text{ Pa s m}^{-3}} = \frac{9.75 \text{ N m}^{-2}}{9.62910 \times 10^{10} \text{ Pa s m}^{-3}} = 1.01 \times 10^{-10} \text{ m}^3 \text{ s}^{-1} = 0.101 \text{ } \mu\text{L s}^{-1}$$
$$= 6.06 \text{ } \mu\text{L min}^{-1}$$

Changes to pressure are dynamic and fluctuate in response to fluid manipulations. It is therefore necessary to ensure that all applications to the chamber of interest do not disrupt the volumetric gradient acting across the microchannel array that would otherwise result in undesirable cross-contamination.

### 3.4.2. Experimental Validation of Environmentally Isolated Culture Chambers

The fluorescent molecule calcein can be used as a visual aid to experimentally validate the absence of cross-contamination between the treated and naïve culture chambers (Figure 3.3) and the theoretical conditions imposed by the microfluidic system were used in the design of the experimental setup. Laminar flow in the treated chamber during fluidic manipulations was obtained with a Reynolds number of approximately 0.2. Following calcein applications *in situ*, a sharp increase in fluorescence was observed within the directly treated chamber, adjacent to the microchannel array achieving a plateau approximately 90 seconds after the initial application. Importantly, fluorescent signal was completely absent in the adjacent, naïve chamber throughout recordings, demonstrating that the volumetric gradient established across the microchannel array effectively prevents cross-contamination. The data obtained using this microfluidic assay protocol is comparable to experimental and computational models previously determined by Robertson et al (2014)<sup>275</sup> and thus suitable for use in microfluidic Ca<sup>2+</sup> imaging assays. As such, an increase in neuronal network activity in the naïve culture chamber must be an indirect response to CNS acting stimulants applied directly to the treated chamber.

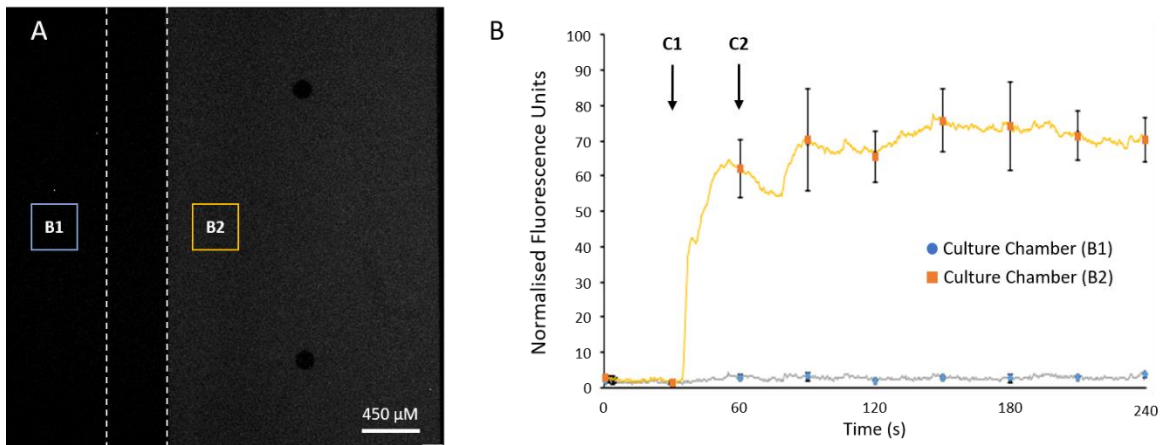


**Figure 3.3: The Microfluidic Dynamics of *In Situ* Calcein Applications.** Non-cultured devices containing water (150/100 μl per well connected to naïve/treated chambers respectively) were used to validate the absence of cross-contamination between the treated and naïve chambers. (A) A representative image (2.5X magnification) shows calcein solution (50 μM) flowing through the treated culture chamber. A single ROI is used to obtain fluorescent readouts from naïve (B1) and treated (B2) culture chambers, adjacent to the microchannel array. (B) A sharp increase in fluorescence, followed by signal plateau, was observed in the treated chamber during calcein applications (C1 & C2), meanwhile no fluorescence was observed in the adjacent, naïve chamber. N = 3 devices; Data expressed as mean ± S.E.M. for every 30 seconds of recording.

### 3.4.3. Detection of Synaptic Connectivity between Environmentally Isolated Neural Networks Using Ca<sup>2+</sup> Imaging.

To determine the functionality of synapses observed by immunocytochemical staining, pharmacological assays using Ca<sup>2+</sup> imaging were performed on environmentally isolated primary hippocampal cultures. Glutamate was used as the pharmacological stimulant of choice because of its physiological relevance in neuronal activation and synaptic communication. Shear stress is induced by fluidic manipulations, and has been previously demonstrated to modulate neural network activity<sup>329</sup>, thus the application of vehicle preceded glutamate stimulations as a control. The preliminary results obtained demonstrate that the activity of hundreds of cells can be monitored simultaneously across two environmentally isolated hippocampal networks and suggest that glutamate, but not vehicle applications, induce indirect activation of the naïve, un-treated neural network (Figure 3.4).



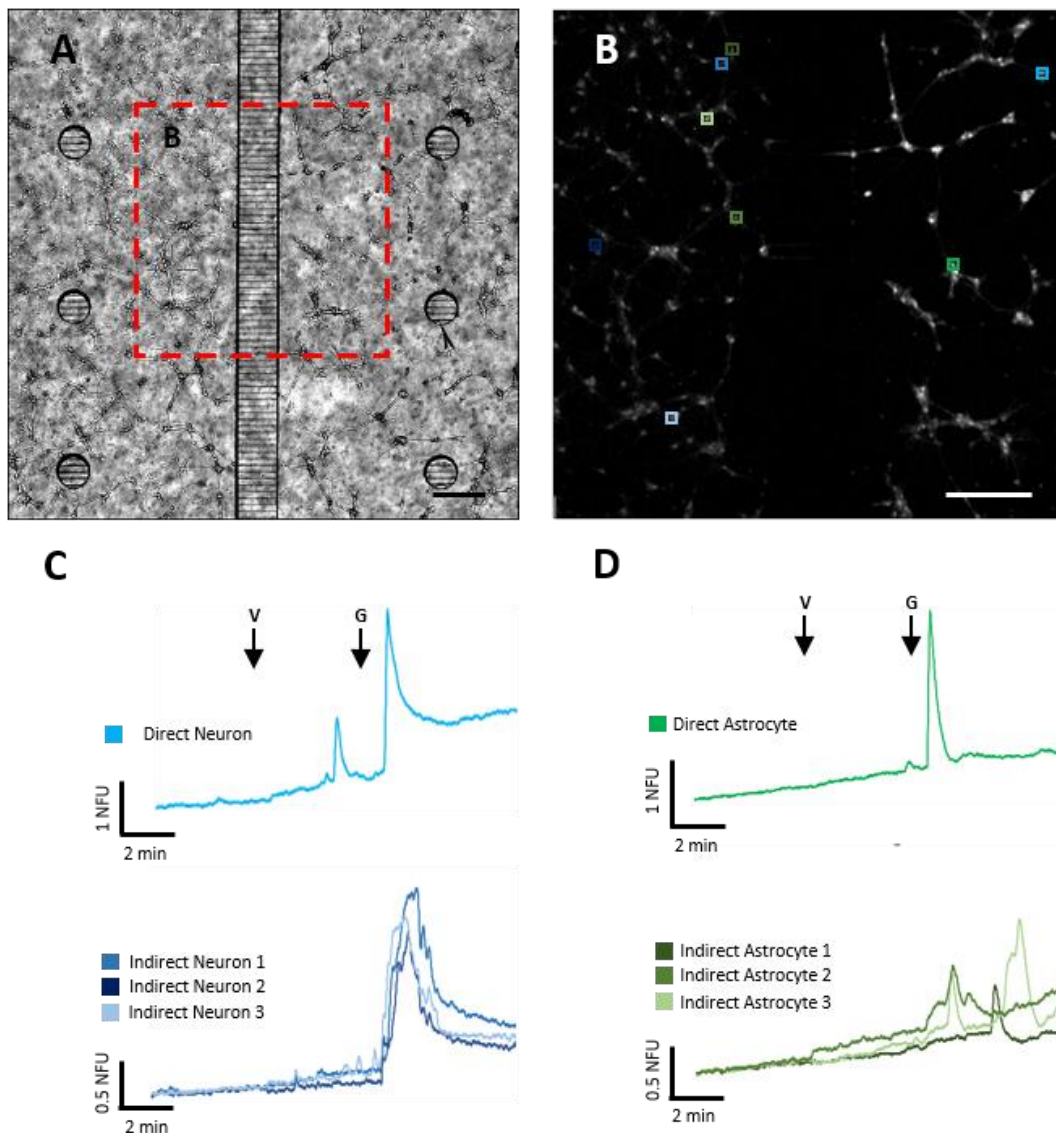


**Figure 3.4: Activation of Neural Networks Identified by  $\text{Ca}^{2+}$  Imaging.** (A) Representative brightfield image (2.5X magnification) of cultures present within the microfluidic device. (B) The FOV is placed over the centre of the microchannel array at 5X magnification prior to experimentation to ensure both neuronal network populations (up to 200 cells from each) are recorded throughout the assay. (C, D) Representative traces of neurons and astrocytes from ROIs highlighted in (B) from treated and naïve chambers direct vehicle (V) and 100  $\mu\text{M}$  glutamate (G) applications. Scale Bars: 450  $\mu\text{m}$  (A); 450  $\mu\text{m}$  (C).



### 3.4.4. Direct Stimulation of a Neuronal Network Indirectly Stimulates an Adjacent Naïve Neural Network

In order to correlate changes in the activity of the naïve neural network with the stimulated network, it is logical to use the same measurement of activity for both networks, rather than treating the directly stimulated network as a binary, off-on result. The rate of activity for both neural networks can therefore be assessed by determining the number of  $\text{Ca}^{2+}$  events, per neuron/astrocyte, per minute (ENM/EAM respectively), identified as increases in NFU > 0.5. The changes in network activity to the directly stimulated network was assessed, first by comparing the ENM/EAM in response to direct fluidic manipulations (Figure 3.5). In the treated chamber, the activity of neurons significantly rose from  $0.031 \pm 0.01$  to  $0.139 \pm 0.02$  ENM ( $n = 369$ ,  $P < 0.05$ ) in response to vehicle stimulation whilst astrocyte activity non-significantly increased from  $0.023 \pm 0.02$  to  $0.164 \pm 0.03$  EAM ( $n = 32$ ,  $P > 0.05$ ). The rate of activity for both neurons and astrocytes significantly increased in activity to  $0.355 \pm 0.01$  ENM and  $0.461 \pm 0.07$  EAM respectively following glutamate applications, when compared to baseline readings ( $P < 0.001$ ) and vehicle stimulation ( $P < 0.001$ ).

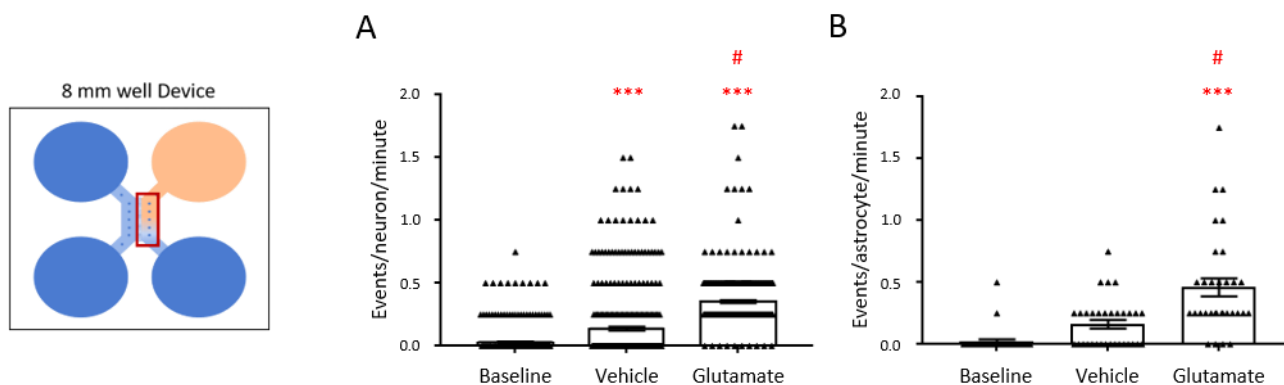


**Figure 3.5: Direct Activation of a Neural Network following Glutamate Applications.**

(A-B) Scatter graphs depict the average changes in neuronal and astrocytic activity within the treated chamber following direct vehicle and glutamate (100  $\mu\text{M}$  final concentration) applications respectively. Direct vehicle application significantly increased the activity of neurons ( $n = 369$ ) however this was not observed in astrocytes ( $n = 32$ ), with respect to baseline activity. Direct glutamate application significantly increased the activity of neurons and astrocytes with respect to baseline and vehicle activity. Data was pooled from 9 devices, from 4 separate cultures; One way ANOVA with Tukey's post-hoc analysis: \*denotes  $P < 0.05$  vs baseline, \*\*\*denotes  $P < 0.001$  vs baseline, #denotes  $P < 0.001$  vs vehicle.

Following vehicle and glutamate stimulation of the neural network in the treated chamber, the subsequent changes in the naïve neural network activity were then determined (Figure 3.6). In the naïve neural network, the activity of neurons was significantly increased following the application of vehicle, from  $0.011 \pm 0.004$  to  $0.051 \pm 0.01$  ENM ( $n = 250$ ,  $P < 0.05$ ), whilst astrocytes showed a non-significant increase in activity, from  $0.028 \pm 0.01$  to  $0.068 \pm 0.01$  EAM ( $n = 117$ ,  $P > 0.05$ ). This was followed by a significant increase in activity to  $0.22 \pm 0.01$  ENM and  $0.18 \pm 0.02$  EAM for neurons and astrocytes respectively, when compared to the rate of activity observed during the baseline readings ( $P < 0.001$ ) and vehicle stimulation ( $P < 0.001$ ).

To confirm this pharmacological research tool's ability to deliver consistent results, both directly stimulated and naïve networks were re-assessed by averaging responses from separate devices (instead of pooling neuronal and astrocyte responses from multiple devices). In the directly stimulated network, neurons presented with a basal activity of  $0.043 \pm 0.02$  ENM which increased to  $0.115 \pm 0.09$  ENM ( $P > 0.05$ ) following vehicle application (Supplementary Figure 2). Neuronal activity then significantly increased to  $0.367 \pm 0.05$  ENM ( $P < 0.05$  vs vehicle;  $P < 0.01$  vs baseline) in response to glutamate. Similarly, astrocyte basal activity increased in response to vehicle application, from  $0.009 \pm 0.01$  to  $0.147 \pm 0.08$  EAM ( $P > 0.05$ ), which increased further to  $0.512 \pm 0.17$  EAM ( $P > 0.05$  vs vehicle;  $P < 0.05$  vs baseline) following glutamate application. Within the naïve network (Supplementary Figure 3), vehicle application resulted in neuronal basal activity increasing from  $0.023 \pm 0.01$  to  $0.044 \pm 0.02$  ENM ( $P > 0.05$ ), and no observable change in astrocyte activity ( $0.028 \pm 0.01$  to  $0.028 \pm 0.01$ ;  $P > 0.05$ ). Neuronal activity then significantly increased to  $0.196 \pm 0.05$  ENM ( $P < 0.01$  vs baseline & vehicle) and astrocyte activity significantly increased to  $0.169 \pm 0.06$  EAM ( $P < 0.05$  vs baseline and vehicle) following glutamate application.

The results obtained demonstrate the presence of synaptically driven communication between the environmentally isolated neural networks following glutamate application to a single network. Despite the significant increase in astrocyte activity following direct glutamate stimulation, it is important to note that immunocytochemistry revealed only neuronal processes were able to traverse the microchannel array. As such, changes in the activity of the naïve neural network are predominantly induced by direct neuronal stimulation and subsequent synaptic communication.

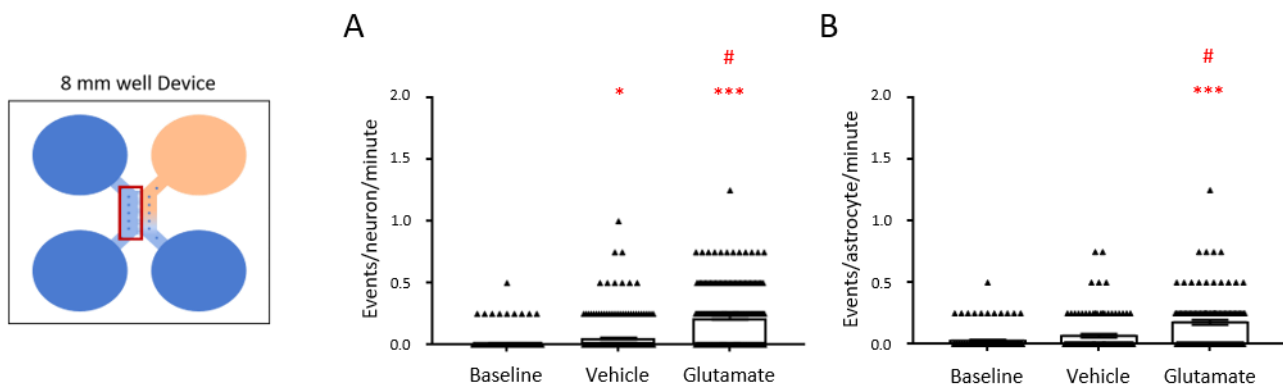


**Figure 3.6: Indirect Activation of a Naïve Neural Network.** (A-B) Scatter graphs depict the average changes in neuronal and astrocytic activity within the naive chamber following direct vehicle and glutamate (100  $\mu$ M final concentration) applications. Direct vehicle application significantly increased activity of neurons ( $n = 250$ ) however not astrocytes ( $n = 117$ ), with respect to baseline activity. Additionally, direct glutamate application significantly increased the activity of neurons and astrocytes with respect to baseline and vehicle activity. Data was pooled from 9 devices, from 4 separate cultures; One way ANOVA with Tukey's post-hoc analysis: \*denotes  $P < 0.05$  vs Baseline, \*\*\*denotes  $P < 0.001$  vs Baseline, #denotes  $P < 0.001$  vs Vehicle.

### 3.4.5. $\text{Ca}^{2+}$ Imaging is Unable to Resolve Action Potential Firing in the Microfluidic Setup

It is well documented that the  $\text{Ca}_i^{2+}$  dynamics of neurons is poorly correlated with the temporal profile of action potential firing which gives rise to synaptic activity. Additionally, the use of  $\text{Ca}^{2+}$  sensitive dyes to observe action potential firing is considered to be limited by the associated slow dissociative kinetics from  $\text{Ca}^{2+}$  ions. Thus, a single recording was performed in the microfluidic device with an increased rate of acquisition to experimentally validate the inability of Fluo-4-AM to detect sAPs and induced APs (Figure 3.7). To achieve a frame rate of 250 Hz (4 ms image acquisition) the FOV was reduced to a single strip of pixels (800:100; x:y) and 4x4 binning applied. The stimulant applied during recording was KCl (25 mM final concentration) to also permit the identification of neurons from astrocytes.

There were few spontaneous  $\text{Ca}^{2+}$  events observed prior to KCl application, with neurons displaying an activity rate of  $0.11 \pm 0.03$  ENM with an average duration of  $2.44 \pm 1.05$  s, from the initial increase in fluorescence back to baseline fluorescence. Following KCl application, the rate of activity then significantly increased to  $2 \pm 0.24$  ENM, with a non-significant decrease in event duration of  $2.23 \pm 0.24$  s, prior to achieving a fluorescent plateau. These data are unreliable representations of

neuronal synaptic activity, because well connected hippocampal neurons typically display synchronised burst activity with short AP recruitment times in the tens of milliseconds<sup>330</sup>. Thus, it is impossible to resolve action potential firing with the current setup using Ca<sup>2+</sup> imaging assays.

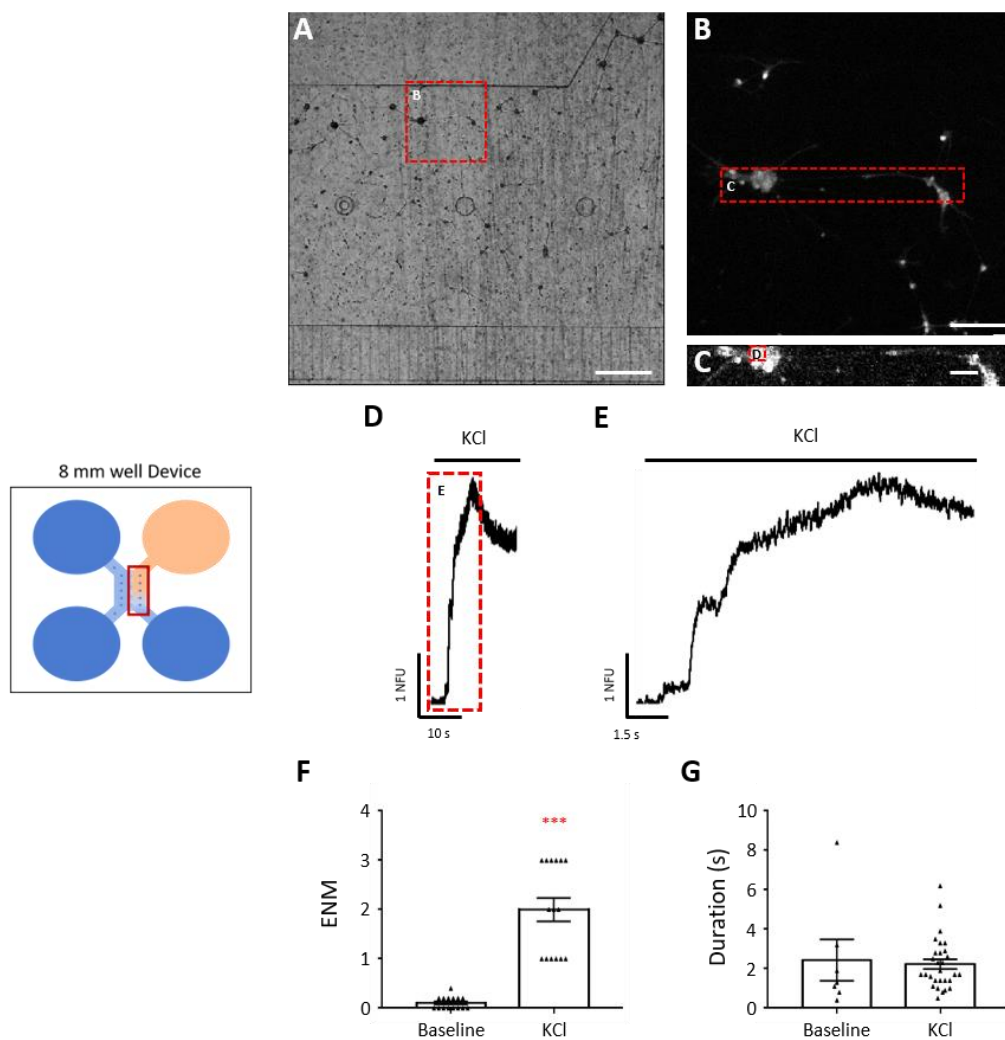


**Figure 3.7: Ca<sup>2+</sup> Imaging with Improved Temporal Resolution Fails to Resolve AP Firing.**

(A) A brightfield image (2.5X magnification) of the single culture chamber to be assessed, and the FOV centered over a group of cells at 10X magnification (B; inset). (C) To improve the temporal resolution of the recordings from 2 Hz to ~250 Hz, 4x4 pixel binning was applied and the FOV reduced to a strip of pixels. (D, E) A representative trace of a neuron stimulated by KCl (20 mM final concentration) displays step like increases in fluorescence, immediately prior to achieving a fluorescence plateau. (F, G) Neuronal basal activity is significantly increased in response to KCl application (25 mM final concentration), with non-significant reductions in Ca<sup>2+</sup> event duration (n = 15 neurons). Paired t-test: \*\*\* denotes P < 0.001; Scale Bars: 450  $\mu$ m (A); 100  $\mu$ m (B); 50  $\mu$ m (C).

### 3.5. Optimising Voltage Sensitive Dye Imaging using Di-3-ANEPPDHQ

The current use of  $\text{Ca}^{2+}$  imaging techniques for monitoring neural network activity in the microfluidic device has advantages in that the experimental setup is relatively simple and the  $\text{Ca}_i^{2+}$  response of cell activity can be monitored across hundreds of cells simultaneously in response to multiple drug applications. The drawback is the inability to provide the temporal resolutions offered by electrophysiological recording techniques, such as patch clamping, and observing synaptic activity in greater detail is unobtainable. Achieving these temporal resolutions using VSDs in the microfluidic setup would thus provide the same resolutions of synaptic activity provided by whole cell patch clamping, but with greater spatial resolutions for monitoring multiple neurons simultaneously. In doing so, we would have a better understanding of synaptic activity across multiple, synaptically connected neural networks. The chimeric, naphthylstyryl-pyridinium Di-3-ANEPPDHQ (D3AD), also known as JPW 3031<sup>331</sup>, was selected as the VSD of choice, having been originally synthesised from RH-795<sup>332</sup> & Di-8-ANEPPS<sup>333</sup> to reduce internalisation and phototoxicity previously observed in the respective, aforementioned dyes<sup>219</sup>. It is structurally similar to Di-4-ANEPPDHQ and so it is expected to present a comparably large Stoke shift of  $\sim 50$  nm towards the blue end of the spectrum<sup>334</sup> (blue-shift; Figure 3.8). This allows a large fluorescent change to be observed during membrane depolarisation when using an appropriate filter set.

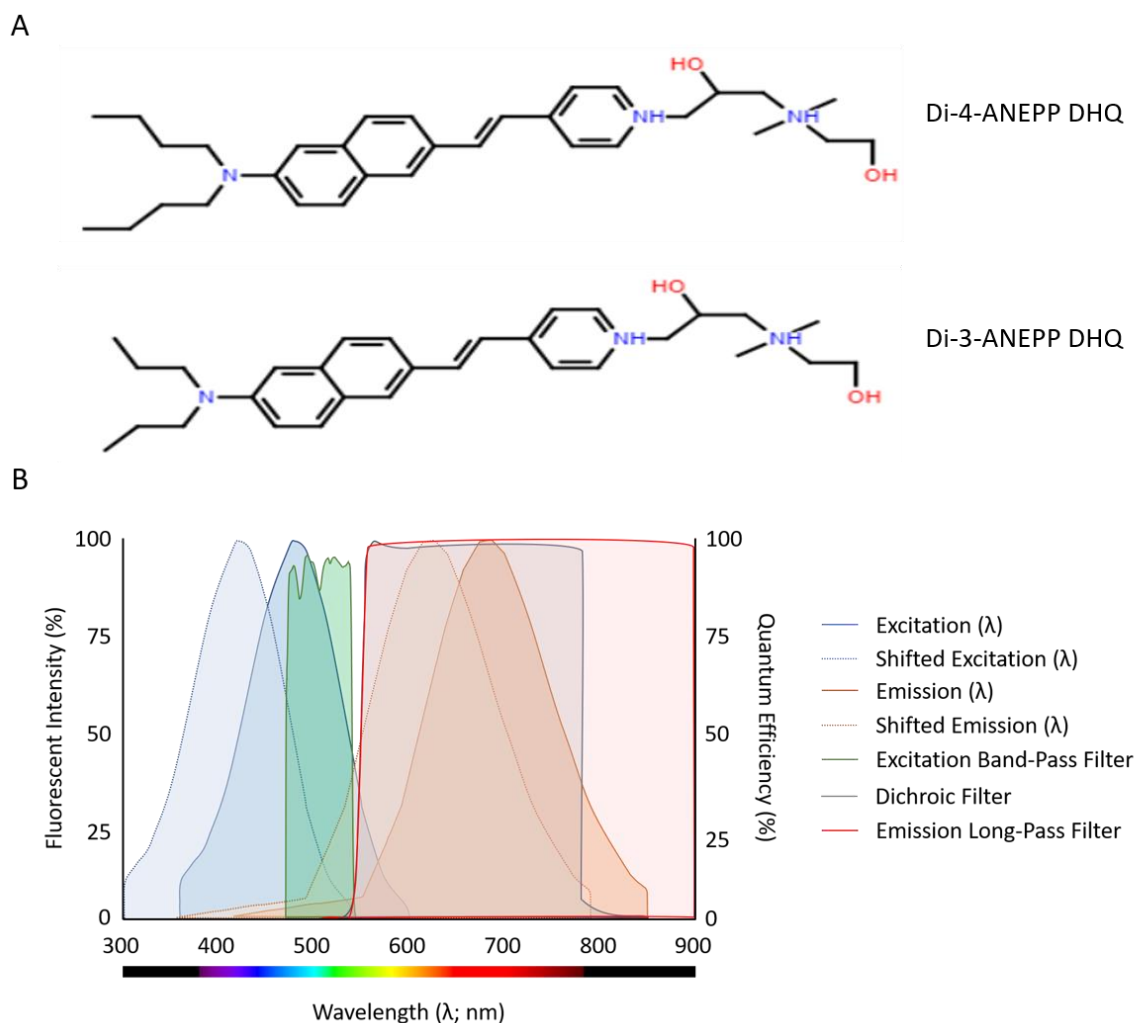


**Figure 3.8. Fluorescent Signals Obtained by Di-3-ANEPPDHQ during Blue-Shifts.**

(A) Structural similarities between Di-3-ANEPPDHQ and Di-4-ANEPPDHQ suggest their electromagnetic spectrum characteristics are highly comparable. (B) The electromagnetic spectrum graph displays the predicted physiological and blue-shifted excitation/emission spectra of D3AD. Following membrane depolarisation, the proportion of excitatory light available is reduced as the excitation spectra falls out-with the band-pass filter wavelength range. This in turn diminishes the signal emitted, which is observed experimentally as a reduction in fluorescence.

### 3.5.1. Preliminary VSDI Assessments with D3AD

Whilst the overall objective is to monitor synaptic activity in microfluidic hippocampal neuronal networks, the ability of D3AD to produce a fluorescent response to changes in membrane potential must first be demonstrated. To this end, assessment of VSDI was first performed on coverslip hippocampal neuronal networks transferred to a fabricated PDMS-based reservoir. Staining was performed in the absence/presence of surfactant Pluronic F127 (10 % w/v) and spatial resolutions adjusted for preliminary recording of neurons, with KCl application (40 mM final concentration) used to validate the functionality of D3AD (Figure 3.9).

The images obtained post-assessment reveal improved resolution of cell membrane and their projections when neural networks were stained with D3AD in the presence of Pluronic F127. D3AD responded to membrane depolarisation during recordings performed at 370 Hz (10X magnification, 4x4 binning), with modest reductions in fluorescence ( $\Delta F$ ) observed following KCl application ( $-23.54 \pm 0.02$  % (n = 41 neurons)). However, the signal to noise ratio (SNR), determined as the ratio between  $\Delta F$  & the square root of background noise, was noticeably poor and calculated as  $0.44 \pm 0.03$  arbitrary units (AU). This resulted in the inability to detect clean change in fluorescent signal corresponding to membrane depolarisation and action potential firing. Additionally, the magnification and binning used often impeded the ability to distinguish between cell soma and the surrounding projections, and so greater magnifications would be required for subsequent VSDI assessments.

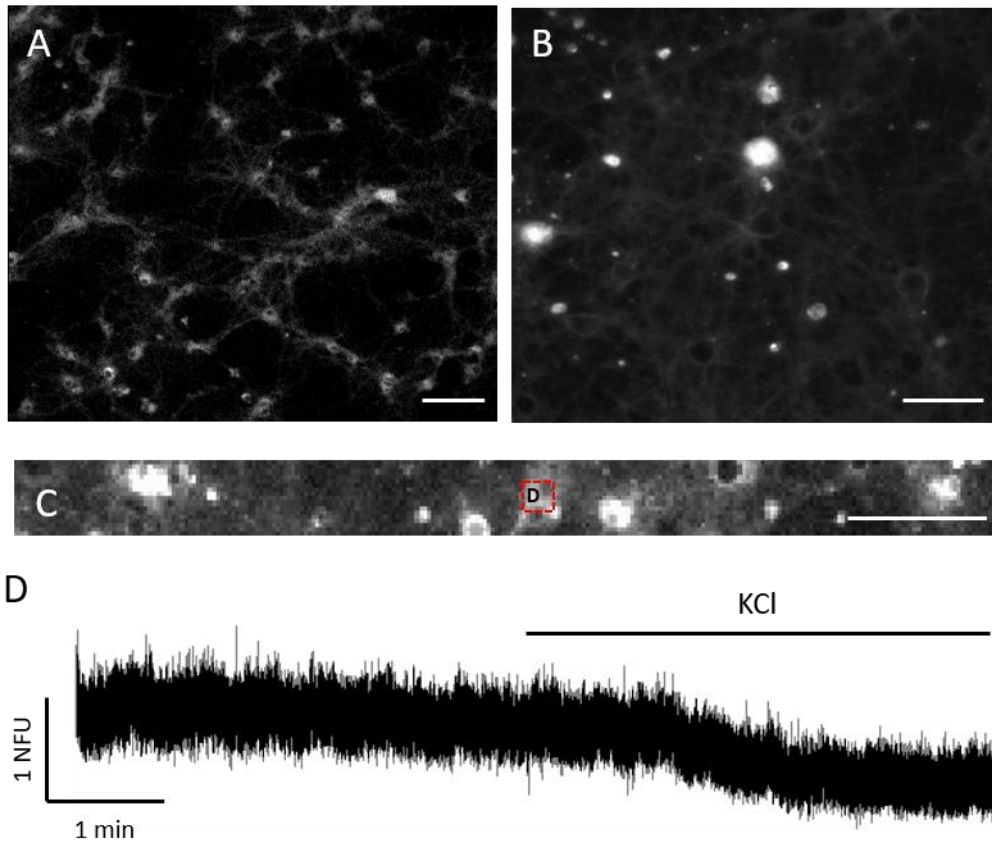


**Figure 3.9: Preliminary Assessments with the VSD Di-3-ANEPPDHQ.** (A, B) Representative images show neural networks stained with 1.57  $\mu\text{M}$  Di-3-ANEPPDHQ after 30 minutes in the absence/presence of the non-ionic surfactant Pluronic F-127 (10 % w/v) respectively. (C) A representative image of a neural network during VSD recordings at 370 Hz with 4x4 pixel binning, 10X magnification, illustrating up to 30 cells could be monitored simultaneously. (D) The normalised trace from a single neuron (inset, C) shows a reduction in fluorescence following stimulation with KCl (40 mM final concentration) demonstrating D3AD responds as predicted to membrane depolarisation. However, poor SNR prevents the observation of AP firing. Scale Bars: 100  $\mu\text{m}$  (A & C); 50  $\mu\text{m}$  (B).



### 3.5.2. Electrophysiological Recordings of Neuronal Activity

Following preliminary experiments with D3AD where KCl application *in situ* resulted in a reduction in fluorescence, whole cell patch clamp experiments were performed by Dr Louise Ritchie to quantify the membrane potential change responsible for change in fluorescence observed (Figure 3.10). Due to the limitations of the setup, it was not possible to perform simultaneous VSDI and patch clamp recordings, and so electrophysiological recordings were performed on unstained coverslips.

From the recordings obtained, neurons presented with a basal membrane potential of  $-64.3 \pm 1.2$  mV ( $n = 5$  neurons, 3 cultures) and generated sAPs at a rate of  $4.8 \pm 1.2$  sAP per second ( $\text{sAP s}^{-1}$ ). After two minutes of KCl perfusion (40 mM final concentration) however, the membrane potential significantly increased to  $-27.9 \pm 4.7$  mV ( $P < 0.01$ ) and the rate of action potential firing significantly decreased to  $0.4 \pm 1.2$  sAP ( $P < 0.05$ ). Neurons appear to fire sAP regularly therefore numerous negative fluorescent peaks should be observed during a minute of VSD optical recordings. Having now determined the membrane potential change during neuronal stimulation, it is possible to formulate a ratio between membrane potential change and fluorescence obtained during KCl treatment. Using the results from the preliminary D3AD recordings as an example, a  $36.4 \pm 5.8$  mV increase in membrane potential gave a  $-23.5 \pm 0.02$  %  $\Delta F$  post KCl application, giving a %  $\Delta F/\text{mV}$  ratio of  $\sim 0.65$ . Setting a membrane potential peak threshold at +20 mV for AP detection, a difference of  $\sim +84.3$  mV exists between resting membrane potential and the AP detection threshold. Theoretically, if an action potential were to be observed, it would display a  $\Delta F$  of -54.6 % under perfect conditions. As no such event took place during these recordings, the logical conclusion drawn is that temporal resolutions must be improved, at the sacrifice of spatial resolution, if attempts to optically record sAPs with D3AD are to succeed.

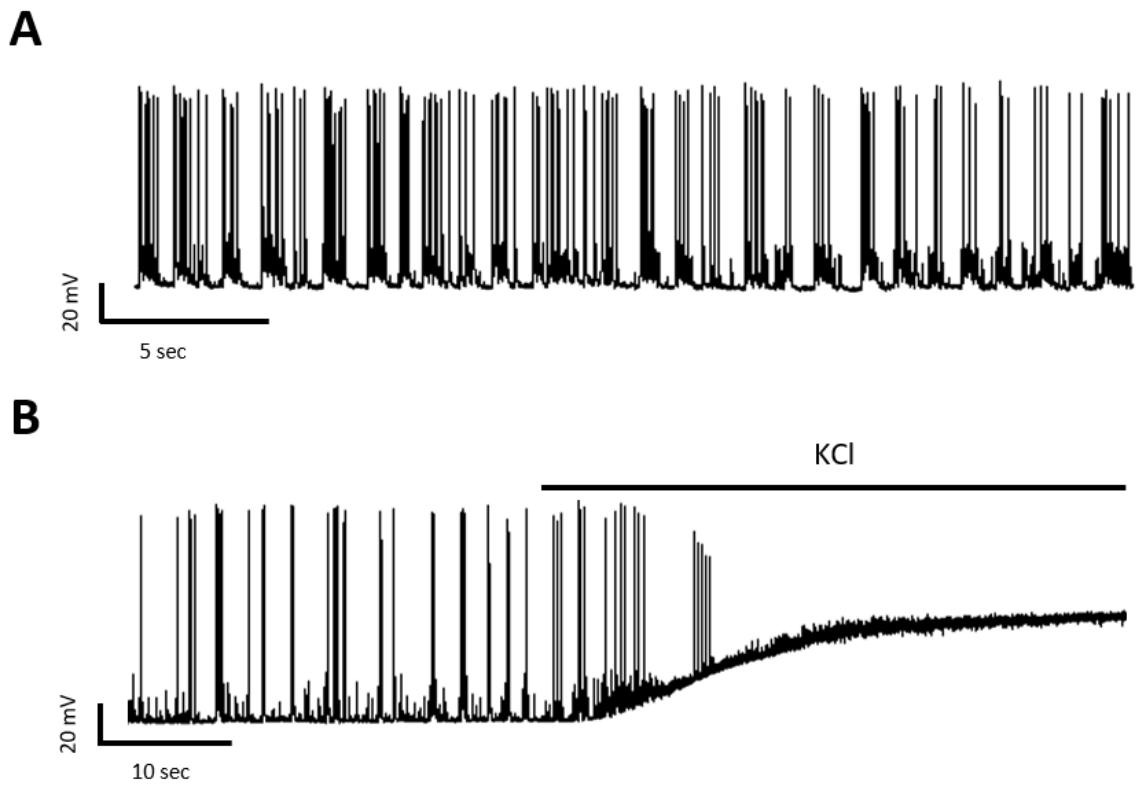


**Figure 3.10: The Application of KCl Depolarises Neuronal Membrane Potential.** (A, B) Representative traces depict the electrophysiological activity of a neuron during baseline recordings and the application of KCl (40 mM final concentration) respectively. Regular sAP firing is observed in neurons during baseline recordings, however shortly after KCl perfusion, the basal membrane potential increases, followed by a steady reduction in sAP firing. A potential plateau is then maintained for the rest of the recording, indicating complete membrane depolarisation.

### 3.5.3. Spatial Averaging Improves SNR in VSD Recordings

In the attempts to improve the SNR and identify spontaneous activity in neurons, the non-ionic surfactant Pluronic F-127 (10 % w/v) was used to improve the binding efficiency of D3AD in hippocampal cultures. Additionally, a 40X objective was used to improve the sensitivity of fluorescent readouts and noise reduced by using a pinhole to focus light on the cells of interest, thereby reducing background staining of neurites within the FOV. The immediate disadvantage of this approach is a significant reduction in spatial resolution, such that only 1-3 neurons could be assessed per recording. After experimentation, spatial averaging was performed on recorded neurons by selecting multiple ROIs across the neuronal membrane to reduce inherent background noise, with a minimal loss of signal (Figure 3.11).

The data suggests the modifications to the experimental and recording setup have led to noticeable improvements in background noise reduction and  $\Delta F$  during KCl application. When compared to the preliminary recordings, SNR significantly improved from  $0.44 \pm 0.03$  to  $1.03 \pm 0.12$  AU ( $P < 0.01$ ,  $n = 6$ ), and the observed  $\Delta F$  significantly decreased from  $-23.54 \pm 0.02$  % (previous observation; section 3.5.1.) to  $-46.09 \pm 4.33$  % ( $P < 0.01$ ). Referring to the membrane potential change observed during KCl application, the theoretical equivalent  $\Delta F$  for an action potential under perfect conditions would be  $-106.86$  % at a %  $\Delta F/mV$  ratio of 1.27. The temporal resolution of the current EM CCD Axio Observer (A1) has nearly reached its upper threshold and further experiments at this rate of acquisition are unlikely to resolve sAPs in the observed neuronal population. Final VSDI assays with D3AD would therefore require a camera with improved temporal resolution capabilities.

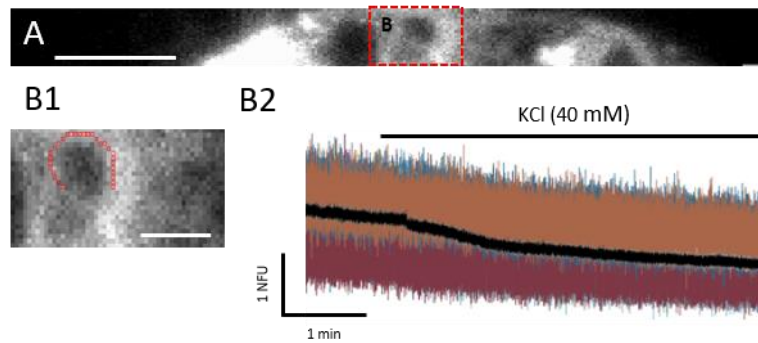


**Figure 3.11: Spatial Averaging Improves SNR During VSD Recordings.** (A) A representative image (40X magnification with pinhole; 4x4 binning) of neurons stained with D3AD and Pluronic F127 (10 % w/v). (B1) Image depicts a single neuron (inset A) with up to 30 ROIs (red boxes) selected around the membrane post-recording. (B2) Fluorescent traces obtained (faded) from the neuron (B1) were then averaged (black) before normalisation to the average signal of the initial 30 s of recording, resulting in a noticeable improvement in SNR. Nonetheless, sAPs were not observed at this temporal resolution. (A) Scale Bar: (A) 100  $\mu\text{M}$ ; (B1) 20  $\mu\text{M}$ .

#### 3.5.4. Improved Temporal Resolutions Fail to Identify Action Potential Firing

The EM-CCD Luca R was swapped for an Andor Zyla 4.2 (kindly loaned by Andor) which has an improved pixel density (2048 x 2048 pixels, 6.5 x 6.5  $\mu\text{m pixel}^{-1}$ ) and improved temporal readouts (100 Hz at full frame). VSD experiments were performed at acquisition rates between 0.9 - 1 kHz by applying an 8x8 binning and reducing the FOV to a strip of 2048 x 100 pixels, with the pinhole used to minimise unwanted background signal (Figure 3.12).

Following the application of KCl (40 mM final concentration) and reduction in fluorescence, the SNR had significantly reduced to  $0.51 \pm 0.07$  AU ( $P < 0.01$  vs previous recordings,  $n = 3$ ) and  $\Delta F$  non-significantly increased to  $-40.24 \pm 6.12$  % ( $P > 0.05$  vs previous recordings). However, large negative deflections in fluorescence indicative of sAPs were again absent during these recordings.

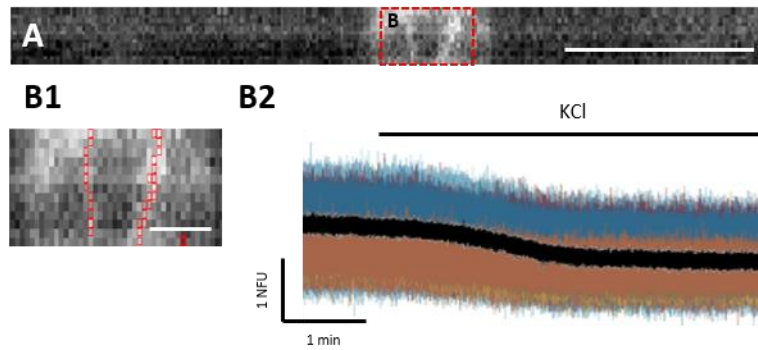


**Figure 3.12: Inability to Identify sAPs with Further Improvements to Temporal Resolutions.**

(A) Representative image of neuron (40X magnification with pinhole; 8x8 binning) recorded with improved temporal resolutions of 957 Hz. Due to the temporal resolutions used, spatial resolutions were sacrificed by recording single neurons in order to preserve SNR. (B1) Up to 30 ROIs (red boxes) were selected around the membrane of the single neuron (inset, A) for analysis after recordings. (B2) Fluorescent traces obtained (faded) were averaged (black) before normalisation to average signal during the initial 30 s of recording. Temporal resolutions near 1 kHz are not adequate for the detection of sAPs, highlighted by the lack of sharp negative fluorescent peaks. (A) Scale Bar: 100  $\mu$ M.

### 3.5.5. Signal Processing Unable to Resolve Action Potentials in Fluorescent Readouts

As a final attempt to determine if sAPs could be detected using D3AD with the current setup, the raw data collected from individual neurons recorded at 0.9 - 1kHz would be processed by the automated counting of +ve and -ve fluorescent peaks. Changes in membrane potential associated with depolarisation is reported as -ve  $\Delta F$ , therefore a greater number of -ve fluorescent peaks would be expected when observing sAPs, assuming the SNR and acquisition rate is great enough to resolve this information. It is worth considering that the duration of an sAP peak during the patch clamp experiments lasted for approximately 2-3 ms and as such, the majority of the fluorescent signal that might be observed is likely to be averaged and obscured by background noise, and the expected  $\Delta F$  from an sAP may be as low as a few percentile. By applying an appropriate +ve and -ve threshold across the recording however, the fluorescent peaks associated with background noise can be compared against those assumed to be derived of sAPs quantitatively.

Using an in-house MatLab program developed by Dr. Michele Zagnoni, the raw data of up to 30 ROIs per neuron obtained from 30 second recordings, were processed over separate 5 second segments to minimise the impact of photobleaching on peak detection. After averaging the fluorescent signal of the ROIs and determining the mean signal of the segment, a threshold arbitrarily set between

3 - 5 % of the mean was applied and the automated detection of fluorescent peaks exceeding this threshold was performed. The fluorescent peaks for a given neuron from each 5 second segment was totalled to give a single +/-ve fluorescent peak number per neuron, which could be then be converted into +/-ve fluorescent peaks per second (Figure 3.13).

Signal processing reveals the difference between the mean number of +/-ve fluorescent peaks as negligible, reporting as  $11.89 \pm 0.84$  and  $12.18 \pm 1.16$  peaks  $s^{-1}$  respectively. This demonstrates that the present SNR and acquisition rate near 1 kHz is insufficient for resolving sAPs in the current setup and is suggestive that further improvements to both are still required. At this point, I had exhausted the majority of steps that could be taken to improve the experimental setup, short of purchasing an expensive camera with significantly greater acquisition rates and combining VSDI with patch clamping to deliver a train of electrical stimuli. As such, experimentation of VSDI with D3AD was discontinued for the purpose of this thesis.

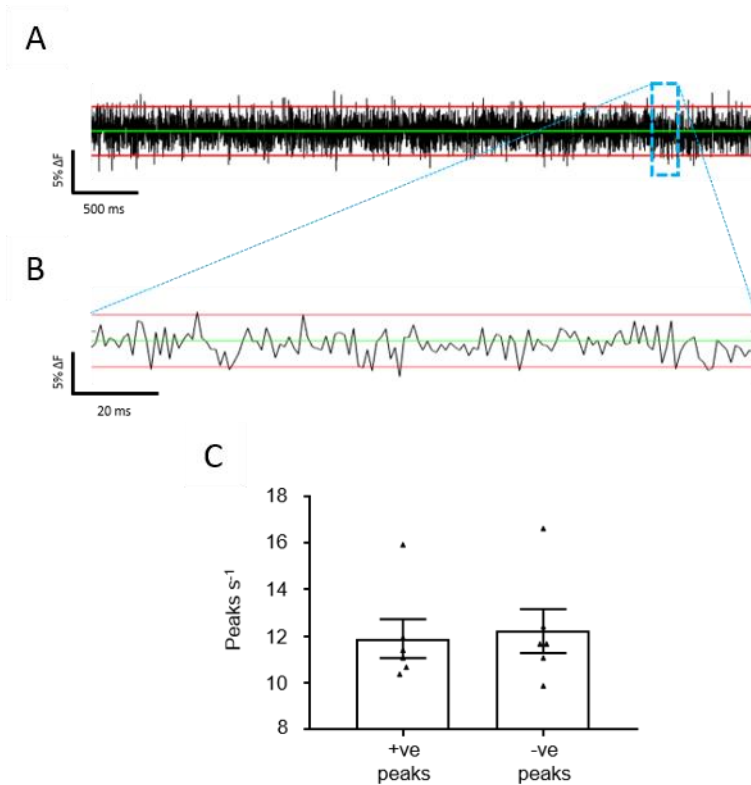


**Figure 3.13: Minimal Differences between +/-ve Peak Response Observed in Recordings.**

(A, B) A representative fluorescent trace during the analysis of a 5 second recording segment of a single neuron shows a 3 % threshold (red line) has been applied to the average signal (green line). (B) After determining the total number of +/-ve fluorescent peaks for each neuron per second out-with the threshold, and their means were compared to reveal a non-significant ( $P > 0.05$ ; Unpaired t-test) greater number of -ve fluorescent peaks observed. This indicates that the SNR and acquisition rate is not sufficient for monitoring sAPs in the neuronal population.  $N = 6$  neurons, pooled from 3 coverslips, 1 culture.

### 3.6. Discussion

At the start of this chapter, I demonstrated the chemical induction of functional, synaptic communication between two environmentally isolated neuronal networks, which confirmed previous observations from our group (Robertson et al., 2014)<sup>275</sup>, as a starting platform for further assay development. Following this, the temporal limitations of Ca<sup>2+</sup> imaging were identified and VSDI assays were chosen for development as an alternative with the potential to monitor the electrical activity of a neuronal network grown within a microfluidic device. Using Di-3-ANEPPDHQ as the VSD of choice, a variety of steps were then taken to optimise the experimental conditions in the attempt to monitor sAPs.

#### 3.6.1. Immunocytochemistry in Microfluidic Hippocampal Cultures

Neural networks formed within the microfluidic device developed comparably to those that were grown on coverslips. By 10 DIV, neuronal projections could be seen traversing the full width of the microchannel array to the adjacent neural network. The glial population and its projections were observed growing throughout the neuronal population and were seen occasionally entering through the microchannels. This indicated the likelihood that astrocytes were providing trophic support and maintenance to the neuronal network as observed *in vitro* and *in vivo*<sup>335–337</sup>. Importantly, glial projections did not appear to fully traverse the microchannel array at any stage, suggesting the unlikelihood of their involvement in directly influencing the activity of an adjacent neuronal network. The presence of pre-synaptic vesicles was also identified on neuronal projection bundles throughout the culture chambers and microchannel arrays, which has been observed previously in similar devices<sup>275,276</sup>. Collectively, the fluorescent images strongly suggested that synaptic connectivity between the adjacent environmentally neural networks existed.

#### 3.6.2. *In Situ* Microfluidic Assays for Functional Communication Studies

To use the dual chamber microfluidic device as a starting point for multiple assay development, it was imperative that functional synaptic communication between hippocampal networks was demonstrated. The optical recording technique of Ca<sup>2+</sup> imaging is a simple and recognised method of monitoring neural activity via Ca<sub>i</sub><sup>2+</sup> flux both *in vitro* and *in vivo*<sup>210,213,338–340</sup>. There are a couple of notable limitations to this setup, including poor temporal kinetics resulting in a binary on-off fluorescent signal, and photobleaching/phototoxicity which can confound results if the appropriate precautions have not been taken (shortened recording times, low excitation intensity etc). This



approach does however allow researchers to monitor the activity of hundreds of cells simultaneously and is therefore ideal for performing neuronal communication studies across environmentally isolated neural networks.

The method by which data is analysed can have a large impact on the interpretation of particular datasets and notably, their biological significance; it is therefore important to consider the appropriateness of such methods before determining if a particular treatment has had a meaningful, biologically significant effect. When analysing datasets for *in vitro* neuroscience research, pooling signals obtained from neurons and astrocytes (respectively) across multiple experiments is a common approach. The advantage of this is that a global trend in response to treatment can be determined, with individual experiments displaying unusual responses having less impact on the result due to the larger sample size used. There can be a slight risk in the context of measuring neural network activity in that stimulatory treatments can result in large calcium waves, resulting in a large response represented by a sample size composed of hundreds of cells, thereby potentially biasing the outcome of biological significance. An alternative approach to the analysis of data sets is averaging the mean response from each experiment, which can be particularly useful for identifying the consistency in responses between experiments. In this instance, the smaller sample size results in individual responses having a greater impact on the mean/standard error of the mean and could be considered a better reflection of a given treatments impact on biological significance. The difficulty with this approach is when interpreting the datasets correctly, one has to assume consistency in the sample size composing each individual experiment, experimental conditions, the maturation/interconnectivity and basal activity of the neural networks assessed which is not often the case<sup>341,342</sup>. Assessing both approaches following pharmacological assessments, glutamate treatment consistently and significantly increased activity of the directly treated, and indirectly stimulated neural networks relative to their baseline activity. The magnitude of the response and degree of significance obtained was greater when pooling results from multiple experiments, likely due to the greater sample size. Taking both approaches into account, this suggests that only results producing large changes in activity following treatment could be considered genuinely significant. However, given mixed hippocampal cultures produce variable networks when grown in culture and the number of cells per recording can vary significantly, it would be inappropriate to average the mean response to treatment across assays in subsequent *in vitro* assessments.

Fluorescent images obtained by immunocytochemical staining revealed the presence of synaptic protein on axonal projects, and pharmacological assessments using  $\text{Ca}^{2+}$  imaging demonstrated functional communication between the environmentally isolated neuronal networks. The experimental model was also validated experimentally prior to this, using calcein to demonstrate the lack of cross-contamination across the microfluidic array separating these two networks. Calcein's bright fluorescent properties permit the visualisation of fluid flow which can then be used to approximate the transport of glutamate in this system during calcium imaging assays. This experimental model is also supported by theoretical models of mass transport. Briefly, the relationship between diffusive forces and advective forces can be resolved using Péclet's number ( $Pe$ ), derived from Reynold's number and Schmidt's number (Equation 10). When the Peclet number is greater than 1 ( $Pe \gg 1$ ), one can reasonably assume that advective forces are the predominant method of transport. To determine Peclet's number, the hydraulic diameter ( $D_h$ ) of the system must first be solved, using Equation 11:

$$Pe = \frac{D_h V_{avg}}{D} \quad \text{Equation 10}$$

$$D_h = 4 \frac{A}{P} \quad \text{Equation 11}$$

Where solution flows with a defined velocity ( $V_{avg}$ ) and solute with a defined mass diffusion coefficient ( $D$ ) through the length of a microfluidic system, defined by its wetted perimeter ( $P$ ) and cross section ( $A$ ) perpendicular to the flow (where the chamber height  $\ll$  width). Calcein has a greater diffusion co-efficient of  $4.6 \times 10^{-10} \text{m}^2 \text{s}^{-1}$ , relative to glutamate (primary experimental stimulant) with a diffusion co-efficient of  $1.087 \times 10^{-10} \text{m}^2 \text{s}^{-1}$ . Using the mass diffusion co-efficient of calcein/glutamate, the dimensions of the culture chamber and the previously calculated flow rate following *in situ* application, it is possible to determine the Peclet number of both molecules in solution.

Culture Chamber Hydraulic Diameter:

$$D_h = 4 \frac{A}{P} = 4 \frac{wh}{w_1 + w_2 + h_1 + h_2} = 4 \frac{2 \times 10^{-3} \times 0.08 \times 10^{-3} \text{m}}{4 \times 10^{-3} \text{m} + 0.16 \times 10^{-3} \text{m}} = 1.538 \times 10^{-4} \text{m}$$

Culture Chamber Fluid Velocity:

$$V_{avg} = \frac{Q}{wh} = \frac{1.01 \times 10^{-10} \text{m}^3 \text{s}^{-1}}{2 \times 10^{-3} \text{m} \times 0.08 \times 10^{-3} \text{m}} = 6.313 \times 10^{-4} \text{m s}^{-1}$$

Calcein Peclet Number:

$$Pe = \frac{Dh V_{avg}}{D} = \frac{1.538 \times 10^{-4} m \times 6.313 \times 10^{-4} m s^{-1}}{4.6 \times 10^{-10} m^2 s^{-1}} = 211.07$$

Glutamate Peclet Number:

$$Pe = \frac{Dh V_{avg}}{D} = \frac{1.538 \times 10^{-4} m \times 6.313 \times 10^{-4} m s^{-1}}{1.087 \times 10^{-10} m^2 s^{-1}} = 893.23$$

Regardless of solution used during assays, the forces of advection are far greater than diffusive forces, therefore the risk of either calcein or glutamate diffusion can effectively be ignored. The application of KCl was appropriate for distinguishing neuronal from glial populations, because it effectively blocks the neuronal Na<sup>+</sup>/K<sup>+</sup> gate responsible for re-establishing electrochemical gradients observed at rest. The neuronal membrane remains depolarised whilst voltage gated Ca<sup>2+</sup> begin to open, resulting in rapid influx of Ca<sup>2+</sup> ions into the cytoplasm, and detected by Ca<sup>2+</sup> sensitive dyes. Astrocytes display a high density expression of potassium channels on their plasma membrane, and are responsible for the uptake and redistribution of excess K<sup>+</sup> ions from the surrounding cytoplasm, commonly regarded as potassium spatial buffering<sup>343,344</sup>. As such, signals obtained from astrocytes during KCl application are commonly a result of stimulation via local neurotransmitter release from synapses formed with neurons. Concerns regarding the influence of retrograde neuronal activation on the possible biasing of results will be addressed later in the thesis (see Chapter 4).

The use of VSDI techniques as an alternative to this has been previously demonstrated in standard neuronal cultures to offer the same level of detail but at a higher throughput<sup>219</sup>. By manipulating the optical recording and experimental conditions, integration of VSDI assays in the microfluidic format has the potential to permit recordings of pre-synaptic and post-synaptic activity from multiple networks when stimulated under experimentally controlled conditions. To justify the development of VSDI assays in the microfluidic format, it was reasonable to assess the temporal limitations of Fluo-4-AM experimentally in the microfluidic setup. Using KCl to both stimulate cells and identify neurons from glial cells, results showed very little spontaneous activity during recordings. Of those signals observed, the spontaneous fluorescent peaks did not return to baseline levels until seconds had passed, confirming the poor dissociation kinetics of Fluo-4-AM<sup>345</sup>. Interestingly, step-like bursts of fluorescent activity were observed immediately prior to fluorescent saturation following KCl application, which likely indicates neurons generate short bursts of APs before the membrane

becomes completely depolarised. These findings are in line with previously published studies that have attempted to resolve details in neuronal activity with  $\text{Ca}^{2+}$  sensitive dyes at temporal resolutions in the kHz frequency sampling range <sup>212,220,346</sup>, where the fluorescent signal shows step like increases in activity followed by signal plateau. Whilst designing a custom microscope and a series of algorithms to extract burst activity from  $\text{Ca}^{2+}$  imaging assays is beyond the scope of this thesis, employing VSDI techniques to accurately assess changes in neuronal membrane potential remains a viable approach.

### 3.6.3 Considerations for Voltage Sensitive Dye Imaging when Recording Neuronal Activity

The use of VSDs in neuroscientific research provides a non-invasive approach for monitoring neuronal activity and has been used extensively in a variety of applications <sup>224,332,347,348</sup>. As an optical imaging tool, the potential of monitoring numerous cells simultaneously exists, provided that the spatial resolution sacrificed to obtain the required temporal resolutions is reasonable. Due to the relatively in-expensive costs of VSDs, optimising the experimental and recording conditions for use with a low-spec camera would be particularly cost-effective and therefore advantageous to neuropathological/pharmacological avenues of research. Di-3-ANEPPDHQ has been used previously to monitor the changes in neuronal membrane activity, as well as global changes in activity across multiple network <sup>219,222,223,225,314,349,350</sup>. During the optimisation of experimental and recording conditions of VSDI, it was appropriate to test D3AD on coverslips instead of microfluidic devices to avoid additional degrees of assay complexity. The impact on synaptic communication and neuronal health was considered negligible as D3AD was specifically designed to demonstrate reduced neurotoxicity, the majority of the cells displayed the characteristic halo like appearance and neurons were still able to respond to KCl applications.

The non-ionic surfactant Pluronic F127 has been used to improve the binding of  $\text{Ca}^{2+}$  sensitive dyes in slice preparations <sup>351</sup> and insoluble VSDs such as Di-8-ANEPP and ANINE-6 in standard cultures <sup>352,353</sup>, however this typically isn't required for the amphiphilic D3AD. The studies assessing hippocampal networks with D3AD predominantly involve slice preparations, with global change in activity in response to stimulation recorded <sup>222,225,349,350</sup>. In this instance, Pluronic F127 (10 % w/v) was found to improve D3AD staining substantially in primary hippocampal cultures by resolving details of cell somas and neurite projections. The concentration used was not considered to have had an impact on neural network health <sup>354</sup>. Whilst the initial experiments demonstrated that D3AD does

indeed respond to membrane depolarisation with reductions in fluorescence, the magnification and frame acquisition rates were too low to detect sAPs. To increase the sensitivity of the recording setup, the magnification was increased to 40X and temporal resolutions increased to near 1 kHz with the use of a higher spec camera. This came with a substantial loss to spatial resolution, such that a single neuron could only be reliably monitored at any given time and therefore skewed the argument against using VSDs over conventional patch clamping techniques to record neuronal activity. Despite the attempts to optimise the recording setup, I was still unable to detect meaningful signals that would indicate the successful detection of sAPs. Whilst the intensity of excitatory light can be increased in the attempt to maximise the fluorescent signal, there is a risk of pixel saturation that may reduce fluorescent signal observed during membrane depolarisation. Unwanted effects of photobleaching/toxicity become increasingly likely with increased excitatory light and so recordings must be reduced to a duration of seconds, further limiting the applications of VSDs.

Separate patch clamp recordings on coverslips that were not exposed to D3AD, revealed regular network activity and the membrane potential change to KCl application at a final concentration of 40 mM was correlated to reductions in fluorescence observed during VSD recordings. Many studies in the literature have employed patch clamp techniques in combination to VSDI, often used to deliver electrical stimuli to the local field whilst simultaneously confirming increases in membrane potential are correlated with changes in fluorescence obtained from the VSD <sup>218,220,225,349,355,356</sup>. Carlson et al (2008) for example initially overlaid fluorescent signals with electrophysiological readouts from obtained from a dendrite branch perfectly before using a train of stimuli to assess the signal propagations from the stimulated dentate gyrus <sup>225</sup>. This was further demonstrated by Yu et al (2013) that assessed the postnatal dorsal ganglion development, correlating changes in electrophysiological readouts with fluorescent response in the granule cell layer, hilus and adjacent CA3 sub-region <sup>356</sup>.

Due to practical limitations present at the time, it was not possible to perform simultaneous patch clamp and VSDI recordings. In the absence of a controlled, electrical stimuli, multiple ROIs were selected on the neuronal membrane and the fluorescent signal spatially averaged to maximise any signal obtained from sAPs whilst negating background signal. Averaging fluorescent readouts obtained from VSDs is an accepted standard in the literature due to the relatively low signal observed during periods of neuronal activity, with  $\Delta F < 1\%$  relative to baseline fluorescence often reported<sup>223,225,348</sup>. Fluorescent readouts were further processed by applying a threshold across the average fluorescent signal to compare the number of +ve peaks associated with background noise, and -ve peaks associated with sAPs. Considering the duration of the sAPs observed in my cultures, signal typically obtained from VSDs and the averaging of signal near 1 kHz acquisition rates (signal averaged over  $\sim 1$  ms intervals), a 3-5%  $\Delta F$  threshold was appropriate for peak analysis during separate 5 second segments of recordings. Nonetheless, there were no significant differences observed between +/-ve peaks. Whilst many studies have successfully used VSDs, it is worth noting several have relied on high-spec cameras, most notably the NeuroCCD-SMQ (Red Shirt Imaging, JPN)<sup>219–221,225,350,356</sup>, to achieve acquisition rates beyond 2 kHz with incredibly low background noise. The spatial resolution of the NeuroCCD-SMQ is exceptionally limited to an 80x80 pixel range however, which reduces the number of cells that can be recorded accurately. Future attempts at optimising this technique could include the use of two-photon imaging, whereby the voltage sensitive dye is excited by two photons using light in the far infra-red range (700 - 900 nm), relative to single photons produced in the range of 390 - 700 nm. This approach has the advantage of exclusively stimulating the focal plane, therefore a pinhole is not required which otherwise reduces the number of cells that can be imaged simultaneously. Additionally, out of focus photobleaching is significantly reduced which improves SNR, and the longer wave lengths used would reduce the risk of phototoxicity<sup>357</sup>. Alternatively, further modifications to the customised filter cube such as replacing the long pass filter with a band pass filter between  $\sim 650 - 700$  nm could be used to maximise the captured band of emitted light following the red-shift during membrane depolarisation

### 3.6.4. Chapter 3 Summary

In this chapter, I have successfully grown primary hippocampal networks in dual chamber microfluidic devices, which is to be used as a platform for functional communication assay development. Indeed, neural networks communicate with each other via functional synapses under experimentally controlled conditions. This approach to neuronal communication studies shows promise for elucidating the underlying signalling mechanisms in neuropathologies and analysing the role of CNS acting compounds on communication across connected neural networks. Currently, drug application is applied *in situ* and requires a surprising amount of effort to avoid nudging the device and therefore impeding the accurate constant monitoring of neural network activity. The integration of a semi-automated perfusion system to minimise user interference mid experiment, manipulate network activity with multiple drug washes and improve data throughput will be demonstrated in Chapter 4: 'Development of a Microfluidic Perfusion Platform for CNS Drug Discovery in Functional Communication Assays'.

To improve the temporal resolutions of optical imaging assays performed on the microfluidic device, VSDI techniques were explored as a novel, cost-effective alternative to patch clamping with potentially greater spatial resolutions. Over the course of multiple optimisation steps, the experimental conditions used for VSDI assays with D3AD were lacking and sAPs could not be optically recorded. There were accepted limitations in the setup, which contrast to studies which have demonstrated the use of D3AD in neuronal communication studies<sup>219,222,225,314,349,350</sup>. These include the lack of a high spec camera specifically designed to achieve acquisition rates > 2 kHz, the inability to perform VSDI and patch clamping simultaneously, and the lack of an electrical stimuli to facilitate inducible APs in a controlled manner. VSDI assays have a few notable disadvantages namely the requirement of highly specialised equipment, and additional user skills and familiarity in electrophysiological recordings. Perhaps most importantly, the apparent lack of spatial resolution to achieve the necessary temporal resolutions is significant enough that only a few cells at most can be monitored simultaneously with reliable accuracy.

An alternative avenue of voltage imaging for the detection of network activity is through ongoing development of genetically encoded, fluorescent voltage indicators (GEVI) which involve fluorescent proteins coupled to voltage sensitive domains on voltage gated ion channels such as K<sup>+</sup> channels<sup>358</sup>, Na<sup>+</sup> channels<sup>359</sup>, or proton channels<sup>360</sup>. These GEVIs typically display large  $\Delta F$  and ideal temporal sensitivity to membrane potentials which can be found lacking in VSDs. One such indicator is the GEVI QuasAr2 which codes for the expression of a near infrared Archaelhodopsin-derived voltage indicator, and is employed in combination with the fluorescent anion dipicrylamine to induce Förster resonance energy transfer (FRET) interactions to observe membrane potential change<sup>361</sup>. Developed by Lou et al (2018), QuasAr2 was shown to detect subthreshold voltage events close to 5 mV with ideal SNR, and a temporal sensitivity that matches whole cell patch clamp recordings near perfectly, both *in vitro* and *in vivo*. Unless significant changes in the development of VSDs are made, the use of GEVIs are likely to become the predominant focus of high-resolution optical imaging in the future. Overall, the potential advantages that VSDI assays have over electrophysiological techniques for monitoring neuronal activity are not as clear cut as originally thought, and further development is needed before they become a practical tool for neuroscientific research.



## **4. Development of the Microfluidic Perfusion System for Early CNS Drug Discovery & Communication Studies**

### **4.1. Chapter Overview**

Work described in the previous chapter sought to develop VSDI assays within the microfluidic setup as an alternative to  $\text{Ca}^{2+}$  imaging assays, in the pursuit of revealing functional synaptic communication between two connected networks with greater temporal resolution. However, due to experimental limitations, this was not realised. An alternative approach to microfluidic assay development is to significantly increase data throughput and experimental conditions per device by the introduction of a perfusion system amenable to CNS drug discovery. Whilst neuropharmacological studies currently use bath perfusion systems for drug application, these are typically limited by poor temporal control over the delivery and removal of the perfusate and the responses obtained are limited to a single stimulated neural network.

During early stage drug discovery, the pre-clinical assessment of new compounds is usually performed across a range of concentrations in the presence or absence of antagonists within a single experiment. However, our current microfluidic  $\text{Ca}^{2+}$  imaging assay is limited to single drug applications without the ability to wash them out. The development of a microfluidic perfusion system would facilitate more rapid pharmacological characterisation of CNS acting compounds. This chapter describes the development of a semi-automated perfusion system, capable of multiple, temporally controlled drug applications to a single network. This permits the simultaneous assessment of CNS acting drug activity on the directly stimulated network and the subsequent impact this has on functional synaptic communication to an adjacent neural network.

## 4.2. Introduction and Chapter Objectives

Studies that pharmacologically profile CNS acting compounds *in vitro* typically rely on the presence of a laminar flow for drug delivery over cultured coverslips or brain slices within a recording chamber<sup>340,362,363</sup>. Experiments are designed as either short recordings with the perfusion of a single compound of interest in the presence/absence of an antagonist, or a continuous recording where cellular activity is assessed across multiple compound perfusates, depending on the assay objectives. In addition to relative potency & EC<sub>50</sub> determination, such systems can be used to investigate receptor function and intracellular signalling pathways<sup>362,364–366</sup>.

To achieve controllable perfusion, a constant flow rate is desirable to avoid introducing fluctuations in the flow. In addition to this, an ideal drug delivery system will be able to switch between vehicle and compound solutions rapidly, as extended delays introduce the risk of compound diluting into the surrounding vehicle solution and reaching the target cells at an unknown concentration or time. Indeed, sharp transition rates between vehicle and drug solutions provide a means of accurately delivering a compound with the required temporal and spatial resolution in laminar flow conditions. Care should also be taken when considering the flow rate for use with particularly vulnerable cells such as neurons, or those with mechanoreceptors that are sensitive to changes in flow rates, such as astrocytes and other glial cells. Research has shown that the introduction of flow rates can activate neuronal intracellular signalling pathways for axonal growth<sup>367</sup>, promote functional and morphological maturation<sup>368</sup>, but may also cause membrane dysfunction and cell death as observed in traumatic brain injury (TBI)<sup>369</sup>. In astrocytes, mechanical stimulation has also been shown to activate NMDA receptors<sup>370</sup>, as well as inducing propagating Ca<sup>2+</sup> waves via mechanically sensitive gap junctions<sup>371</sup> and similarly to neurons, is implicated in negative intracellular changes associated with TBI<sup>372</sup>. Whilst faster flow rates increase the speed at which compounds may be exchanged in solution, it also increases shear stress that can affect cell activity and therefore the experimental outcome. As such, the optimisation of any new system should be performed to balance the impact of flow rates on cell function and drug delivery kinetics.

Taking the above into consideration, it should be noted that although standard *in vitro* perfusion chambers used to record neuronal activity do provide constant laminar flow, the volumes required are large than those required using a microfluidic approach. This results in larger sample volumes required as well as an extended time taken to determine the pharmacological actions on neuronal activity. A typical setup for performing Ca<sup>2+</sup> imaging or electrophysiological studies on cell culture or organotypic slices involve the use of an external storage container & alternating drug reservoir connecting to and perfusing a bath recording chamber. A reasonable lag time of 30 seconds (dependent on tubing length and the hydraulic pressure exerted by the tubing) between drug application to arrival in the bath chamber can be assumed from gravity-fed tubing used<sup>202</sup>. At a flow rate between 1-2 mL/min and a chamber volume of 0.5-1 mL, it will take between 1-2 minutes from drug application to completely replace vehicle solution with compound solution and observe changes in neuronal activity<sup>340,362,373-375</sup>. Additionally, because of this duration, it is possible for connected cells exposed to drug application to influence the activity of those being recorded pre-emptively.

This chapter details the development of a semi-automated microfluidic drug discovery system, capable of delivering multiple drug perfusions with precise temporal control. This will require a microfluidic perfusion model to be validated and assumes that the induced shear stress has a negligible impact on neural network health. Then, the capabilities of the perfusion system must be tested using an appropriate stimulant to demonstrate proof of concept for pharmacological characterisation of CNS acting compounds.

To achieve this, microfluidic perfusions will be assessed experimentally within a single chamber for rapid alternation of perfusates, and an absence of cross contamination in the non-perfused (naïve) chamber, using calcein as the fluorescent marker. Then, viability assessments will be performed to confirm the integrity of microfluidic neural networks that are exposed to perfusion induced shear stress.

The physiologically relevant stimulant glutamate will be used as proof of concept to demonstrate the microfluidic perfusion systems pharmacological characterisation capabilities, with a concentration response curve generated to establish an EC<sub>50</sub> for both neurons and astrocytes. Competitive antagonism of glutamate induced network activation will be demonstrated using a combination of ionotropic and metabotropic antagonists in addition to the cessation of activity by the co-application of tetrodotoxin (TTX). The advantages of the microfluidic setup will be realised by the simultaneous recording of the naïve neural network and the changes it undergoes during pharmacological

assessments. Finally, synaptic driven communication between the two environmentally isolated networks will be validated by the perfusion of glutamate to axonal projections in single network cultured devices.

### **4.3. Optimising Microfluidic Perfusion for Neuropharmacological Assays**

Prior to the development of neuropharmacological assays, it is imperative that the system used for such is characterised and experimental conditions optimised to ensure minimal impact on neural network health and ideal fluid flow properties obtained. The theoretical model for microfluidic perfusion through the dual chamber device was previously described in Chapter 2, however the implications of microfluidic perfusion on assay design requires further attention. Live/dead imaging assays were performed using a range of flow rates to assess the impact of direct and indirect perfusion on the viability of hippocampal cultures. The theoretical model of compound delivery via microfluidic perfusion was then to be validated experimentally using calcein as a fluorescent marker.

#### **4.3.1. Considerations for Microfluidic Perfusion in Assay Design**

Whilst hydrodynamic pressure driven flow was previously established by selecting the required volume present within inlet/outlet wells *in situ*, this approach of drug delivery was limited by user interference, exponential pressure decay and restricted to the application of a limited number of stimuli. Fine control over the volumetric conditions of inlet/outlet wells was required because of the greater control of flow rate within the culture chamber. Maintaining a steady flow rate manually however, is incredibly impractical as this would require constant, precise applications of fluid to the inlet well, and withdrawal of fluid from the outlet well over the duration of the experiment. Thus, syringe pump driven systems can be employed to readily define and control perfusion and withdrawal flow rates in the inlet/outlet wells and culture chambers. Additionally, drug delivery via perfusion can be restricted to a single chamber by establishing a hydrodynamic pressure gradient from one culture chamber to another, as described previously (Chapter 3). The induced flow rates within the perfused chamber can therefore be considered devoid of interference by negligible flows across the microfluidic array because of the inherent large fluidic resistance present.

#### 4.3.1.1. Flow Induced Shear Stress

Shear stress in a microfluidic system can be defined as the force of fluid flow acting upon the wetted perimeter of a channel's cross-section, otherwise regarded as the solid boundary. When a Newtonian fluid under laminar flow passes through a channel, the shear stress induced is proportional to the viscosity and flow rate of fluid flow acting in parallel upon the solid boundary layer to create friction. A rough estimation of this shear stress within the microfluidic culture chamber can be determined using Equation 9<sup>376</sup>:

$$\tau = \frac{6\mu Q}{h^2 w} \quad \text{Equation 12}$$

Where shear stress ( $\tau$ ) is a function of the dynamic fluid viscosity ( $\mu$ ) and dynamic flow rate ( $Q$ ) travelling through a channel with a constant cross-section with defined height ( $h$ ) and width ( $w$ ). The above equation assumes a frictionless, no-slip boundary between the fluid flow and the solid boundary layer and is therefore not a true representation of shear stress conditions present in the chambers including hippocampal cultures. Indeed, the presence of a mono-layer culture will likely contribute to frictional forces, however defining this with precision would be difficult to achieve. Neural networks are sensitive cultures that are not typically exposed to high flow rates and changes to their microenvironment are reflected by changes in activity and signalling mechanisms. Prior to assay development, the optimal flow rate for this perfusion system must first be determined by assessing the impact that flow rates, which are practical for drug delivery, have on neural network health.

#### 4.3.2. Investigating Steady Flow Rate Perfusion on Neural Network Health

To minimise the impact of perfusion on microfluidic neural networks that could bias results during neuropharmacological assays, live/dead assays were performed on networks directly exposed to a range of flow rates, and those synaptically connected in the adjacent, naïve culture chamber. Cultured microfluidic devices were washed with HBS, connected to the semi-automated syringe-pump perfusion system and perfused with HBS at a constant flow rate. Specifically, a single culture chamber per device was perfused with a separate, single flow rate at either 0.4, 1, 4 or 10  $\mu\text{L min}^{-1}$  for an hour, resulting in the equivalent shear stress of 0.0278, 0.0695, 0.278 and 0.695  $\text{dyn cm}^{-2}$  respectively. To assess the downstream effects that perfusion may have on the naïve neural network, the cells of both perfused and non-perfused chambers were stained with Hoechst and PI (Figure 4.2) to examine cell viability (see Chapter 2). As a control, separate devices were stained immediately

after removal from the incubator, revealing a  $73.8 \pm 0.01\%$  ( $n = 3$ ; 1 device per culture) viable population within cultured microfluidic devices (Figure 4.2). A significant reduction in the culture viability was observed in devices that were left at room temperature in stasis for an hour, with  $54.1 \pm 0.9\%$  ( $n = 6$  devices; 2 per culture;  $P < 0.001$  static  $t_{0hr}$  vs static  $t_{1hr}$ ) of cells viable under these conditions. At a flow rate of  $0.4 \mu\text{L min}^{-1}$ , the viable population increased from  $54.1 \pm 0.9\%$  to  $59.6\%$  ( $n = 3$  devices; 1 per culture;  $P > 0.05$  vs static  $t_{1hr}$ ), which increased to  $65.6 \pm 0.4\%$  ( $n = 3$  devices; 1 per culture;  $P < 0.01$  vs static  $t_{1hr}$ ) with a flow rate of  $1 \mu\text{L min}^{-1}$ . The optimal perfusion flow rate was identified as  $4 \mu\text{L min}^{-1}$ , with  $72.6 \pm 1.6\%$  ( $n = 3$  devices; 1 per culture;  $P < 0.001$  vs static  $t_{1hr}$ ) viable cells observed. However, cell viability decreased to  $65.3 \pm 3.5\%$  ( $n = 3$  devices; 1 per culture;  $P < 0.05$  vs static  $t_{1hr}$ ) at a flow rate of  $10 \mu\text{L min}^{-1}$ . Importantly, there was no significant difference between the viable population at static  $t_{0hr}$  when compared to that of neural networks when perfused at  $4 \mu\text{L min}^{-1}$  ( $73.8 \pm 0.01\%$  vs  $72.6 \pm 1.6\%$  respectively;  $P > 0.05$ ). Having established that perfusion at  $4 \mu\text{L min}^{-1}$  maintains microfluidic neural network viability when removed from incubation, the temporal kinetics of syringe pump alternation was then assessed.

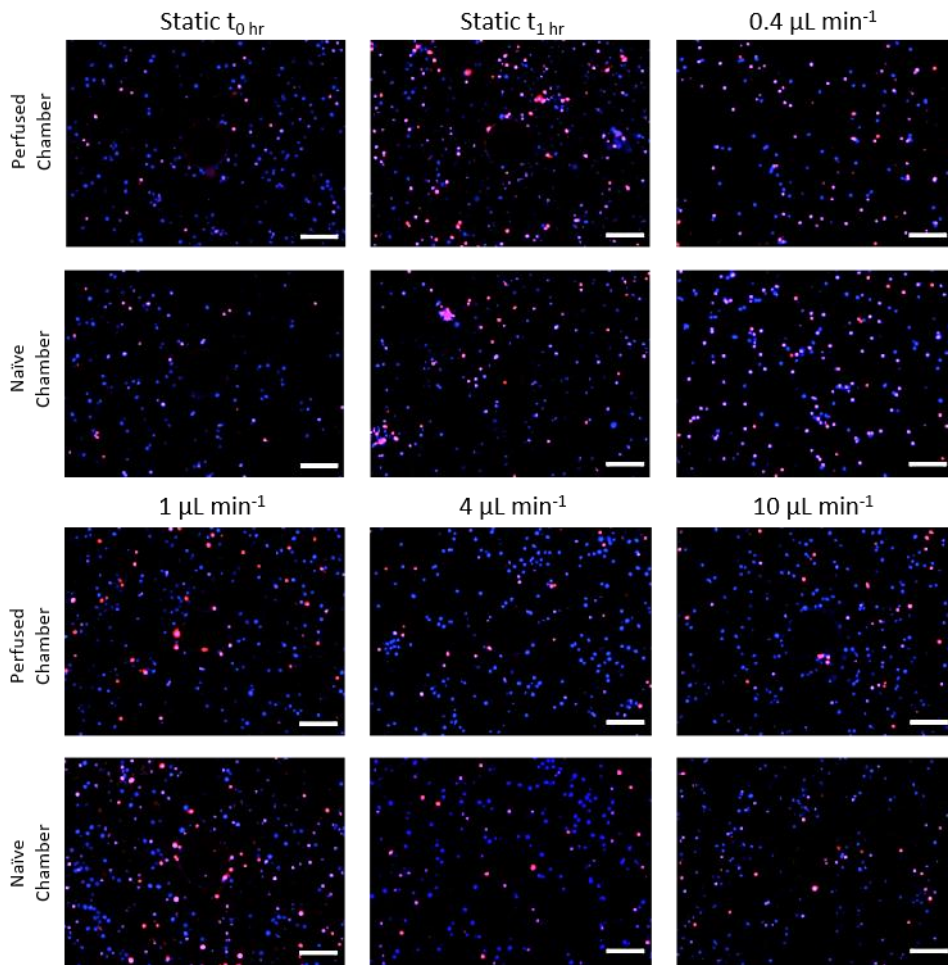


**Figure 4.1: Live/Dead Imaging Assay following Microfluidic Perfusion.** Representative images depicting the live/dead staining of neural networks that were either exposed or naïve to the direct perfusion of individual microfluidic flow rates across separate devices. Cells that were co-stained with PI & Hoechst were considered to be dead, or otherwise counted as viable.

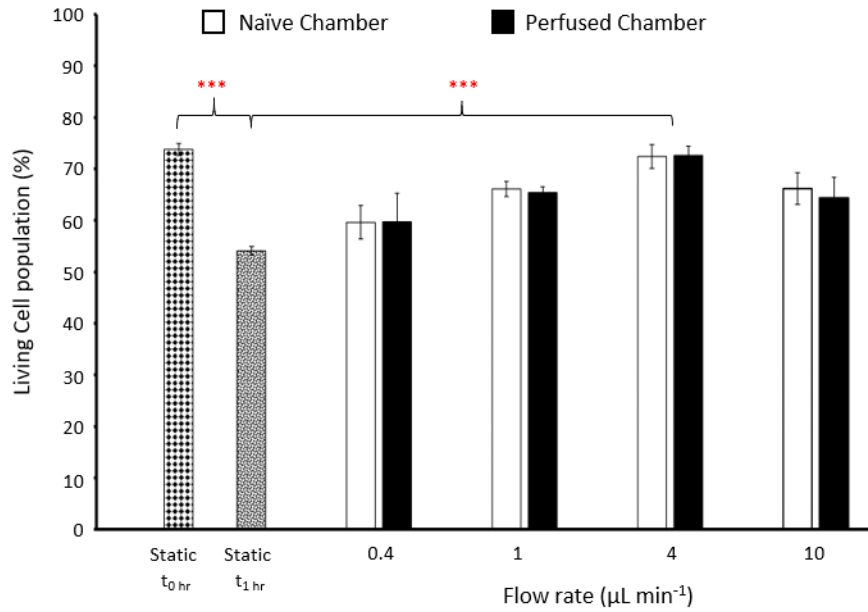


**Figure 4.2: Microfluidic Perfusion preserves Neural Network Viability.** Image analysis indicated a significant decrease in neural network viability when microfluidic neural networks were removed from the incubator and left in stasis at room temperature for an hour. Scale bars = 100 μm; Data was gathered from 21 devices, from 4 separate cultures; One way ANOVA with Tukey's post-hoc analysis: \*\*\* denotes  $P < 0.001$  vs Static t<sub>1hr</sub>.

### 4.3.3. Characterising the Temporal Kinetics of Microfluidic Drug Perfusion

Serial microfluidic perfusion of calcein (50 μM) was used to confirm that compound delivery in the chamber is in line with the theoretical model and that rapid exchange of solution is achieved. Non-cultured devices were used for these experiments. The optimal net flow rate for perfusion of the neural network was identified as 4 μL min<sup>-1</sup> and this was achieved by first, setting the perfusion flow rates for all syringes, containing DI water (vehicle) or calcein solution (50 μM), to 44 μL min<sup>-1</sup>, with a single perfusion pump active at any given time. Withdrawal flow rates for syringes connected to the inlet and outlet wells were set to 40 & 4 μL min<sup>-1</sup> and remained active throughout the experiment. Using the small well microfluidic device dimensions described previously (Chapter 2) and equation 3, the theoretical time taken for the full perfusate (100 % concentration) of drug solution to reach the mid-point of the culture chamber is approximately 35 seconds, assuming perfect conditions:

$$HRT \sim \frac{V_{I-well}}{Q_{I-P}} = \frac{10 \mu L}{44 \mu L \text{ min}^{-1}} = 13.62 \text{ s}$$

$$Tex \sim HRT + \frac{S_{Ch} * L}{Q_{Ch}} = 13.62 \text{ s} + \frac{0.32 \text{ mm}^2 * 4.5 \text{ mm}}{4 \mu L \text{ min}^{-1}} = 35.22 \text{ s}$$



From the fluorescent profiles obtained during separate 4 minute recordings (Figure 4.3), signal increase is observed in the perfused chamber after 10 seconds of syringe pump alternation. This sharp increase is followed by a fluorescent plateau  $43.3 \pm 2.2$ s after syringe pump alternation, with significant differences observed between 1 - 2 minutes of each calcein recording, relative to the signal obtained during the initial baseline recording. Importantly, fluorescent signal was not detected in the naïve culture chamber at any stage of the recordings, indicating a lack of cross contamination due to the hydraulic pressure acting through the microchannel array. Conclusively, these results experimentally validate the theoretical perfusion model and justify the use of the microfluidic perfusion system as an appropriate platform for performing neuropharmacological assays.

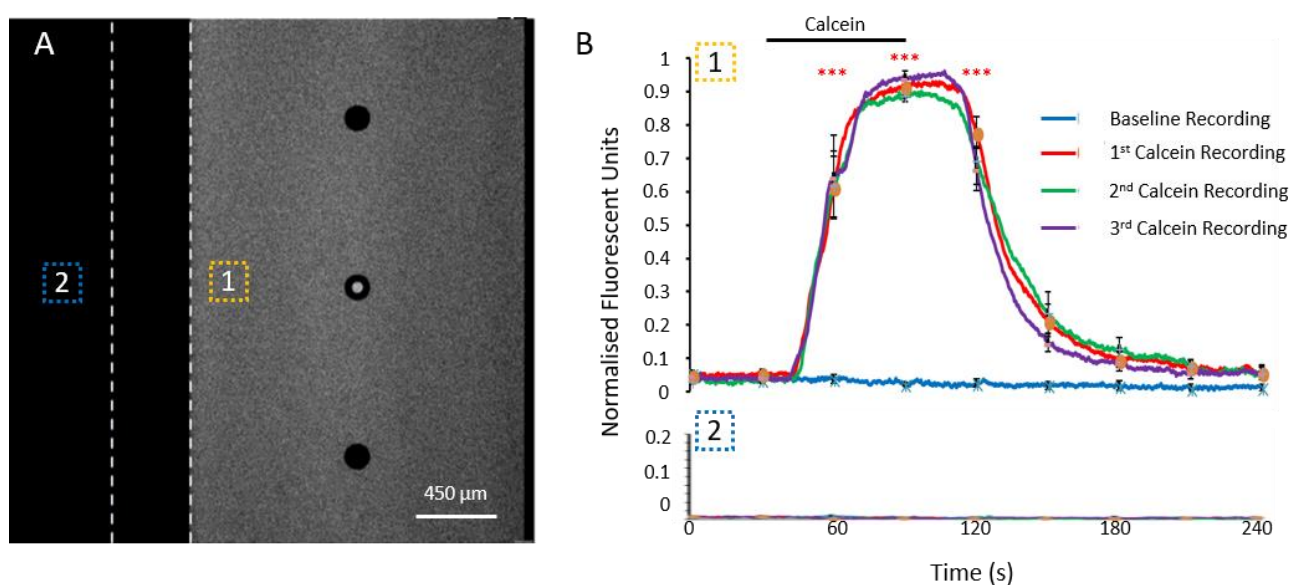


**Figure 4.3: Calcein Delivery Demonstrates Robustness of the Microfluidic Perfusion Model.**

(A) A representative image of a single culture chamber perfused with calcein solution ( $50 \mu\text{M}$ ), highlighting the microchannel array by white dashed lines, and a single ROI taken from both the perfused (orange) and naïve (blue) culture chambers adjacent to the microchannels. (B) Fluorescent profiles obtained from three separate syringe pumps during sequential recordings demonstrates a sharp transition between vehicle and calcein perfusions. Data was gathered from 9 devices; One way ANOVA with Tukey's post-hoc analysis: \*\*\* denotes  $P < 0.001$ , relative to readings obtained from baseline recordings.

#### 4.4. Neuropharmacological Assays using the Microfluidic Perfusion Platform

Having demonstrated the suitability of the microfluidic perfusion system for the reliable delivery of compound application without negatively impacting the assessed neural networks viability, standard neuropharmacological assays were to be designed and performed to test the system. Glutamate was chosen as the primary stimulatory agent because it is the primary CNS excitatory neurotransmitter and glutamatergic activity would be blocked by its ionotropic antagonists NBQX and DL-AP5, and metabotropic antagonist (R, S)-MCPG. This system allows the simultaneous assessment of CNS acting drugs impact on perfused neural networks and the subsequent effect on synaptically connected, naïve neural networks. As an appropriate control, the potent Na<sup>+</sup> channel antagonist TTX was used to block synaptic transmission induced by the stimulation of the perfused network. Finally, additional assays were performed to assess retrograde activation of axonal projections by glutamate perfusions, and the mechanistic impact that perfusion has on neural network activity.

##### 4.4.1. Concentration Response Curve generated using Glutamate Microfluidic Perfusion.

The development of pharmacological assays for a compound of interest is a standard approach to assessing its impact on biological activity and is typically performed during the early stages of pre-clinical pharmacological characterisation<sup>377</sup>. To demonstrate the capabilities of the microfluidic perfusion systems for pharmacological characterisation of compounds, we generated a glutamate concentration-response curve using Ca<sup>2+</sup> imaging. Specifically, single microfluidic neural networks were exposed to increasing glutamate concentrations (10 nM – 1 mM) and the peak response analysed on a cell by cell basis (Figure 4.4). The perfusion of glutamate led to reversible increases in Ca<sub>i</sub><sup>2+</sup> in both neurons and astrocytes to reveal concentration-response curves, with EC<sub>50</sub> values of 4.7 ± 0.6 μM for neurons (n = 154, ≥ 50 per concentration), and 3.61 ± 1.4 μM for astrocytes (n = 121, ≥ 42 per concentration) respectively (n = 14 devices, 6 cultures). The results obtained from cells within the perfused chamber illustrate the microfluidic perfusion system is capable of potency assays required for neuroactive compounds, with the capacity of highlighting differences in cell type dependent response to drug application.

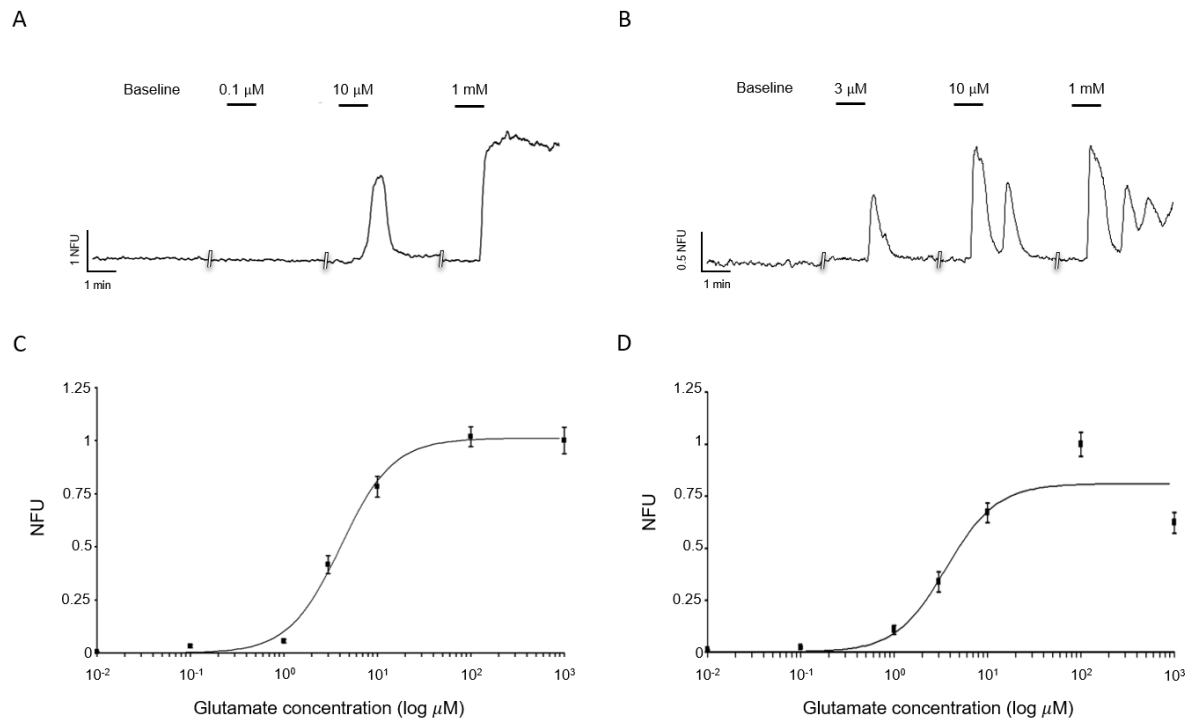


**Figure 4.4. Concentration Response Curves following Direct Glutamate Perfusions.**

(A & B) Representative Ca<sup>2+</sup> imaging traces depict fluorescent responses to repeated glutamate perfusions at increasing concentrations from a neuron and astrocyte (respectively). (C & D) Glutamate concentration response curves were plotted to reveal a neuronal EC<sub>50</sub> of 4.7 ± 0.6 μM and an astrocytic EC<sub>50</sub> of 3.6 ± 1.4 μM. N = ≥ 50 (neurons) & ≥ 42 (astrocytes) per concentration assessed; Data was pooled from 14 devices across 6 independent cultures.

#### 4.4.2. Assessment of Functional Changes in Neural Network Activity in Response to Repeated Glutamate Application

The change in peak fluorescent magnitude of neural networks perfused with glutamate was assessed to determine the repeatability of responses following sequential glutamate applications. The subsequent impact this repeated stimulation had on synaptic communication was also assessed. To avoid overstimulation of neural networks that may lead to desensitisation and unreliable responses in the naïve neural network, glutamate (3 μM) was chosen as the test concentration which was comparable to the determined EC<sub>50</sub> value. During repeated perfusions of glutamate (1 min duration), neurons directly stimulated revealed reproducible increases in Ca<sub>i</sub><sup>2+</sup> during the first two applications, at 1.00 ± 0.06 NFU and 0.99 ± 0.06 NFU respectively (n = 182, 4 devices, 3 cultures; Figure 4.5). The fluorescent response then reduced to 0.81 ± 0.05 NFU (P < 0.05 vs 1<sup>st</sup> application) during the final glutamate application. Astrocytes showed increases in fluorescent signal during the first glutamate

application ( $1 \pm 0.05$  NFU;  $n = 284$  astrocytes) however this significantly reduced  $0.86 \pm 0.04$  NFU ( $P < 0.05$ ) during the second application, and significantly reduced further during the final application to  $0.55 \pm 0.03$  NFU ( $P < 0.001$  vs 1<sup>st</sup> & 2<sup>nd</sup> application).

Adaptive changes in the activity of the synaptically connected naïve neural network were observed in response to repeated glutamate applications (Figure 4.6). During the first glutamate application, the activity of neurons increased to  $0.38 \pm 0.04$  ENM ( $n = 222$  neurons;  $P < 0.001$ ) and astrocyte activity increased to  $0.22 \pm 0.03$  EAM ( $n = 258$ ;  $P < 0.001$ ) with respect to baseline activity ( $0.16 \pm 0.04$  ENM &  $0.05 \pm 0.02$  EAM respectively). The second glutamate application showed consistent results, where neuronal activity increased from  $0.17 \pm 0.04$  to  $0.44 \pm 0.04$  ENM ( $P < 0.001$ ), whilst astrocyte activity increased from  $0.14 \pm 0.04$  to  $0.25 \pm 0.04$  EAM ( $P < 0.05$ ). During the recording for the final glutamate application, basal levels of activity appeared to be elevated for neurons ( $0.27 \pm 0.05$  ENM) and astrocytes ( $0.20 \pm 0.04$  EAM). The third glutamate application then resulted in a small but significant increase in neuronal activity ( $0.40 \pm 0.05$  ENM;  $P < 0.05$ ) and a non-significant increase in astrocyte activity ( $0.28 \pm 0.04$  EAM).

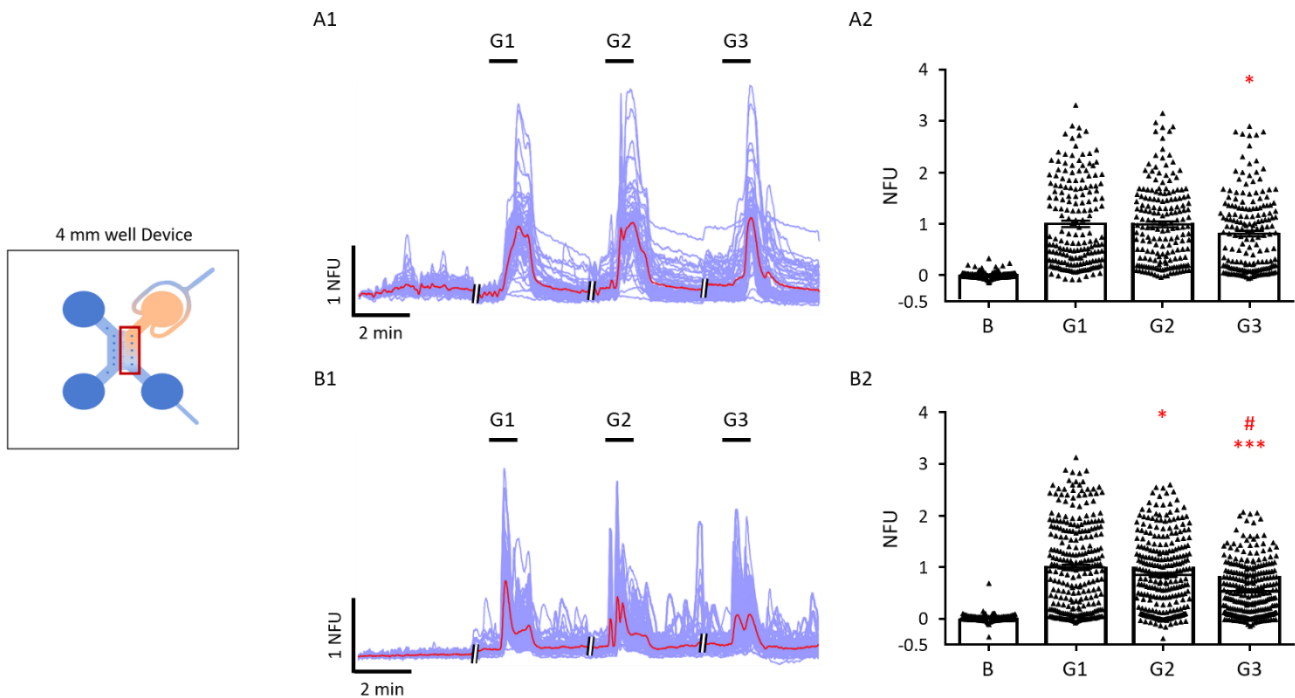


**Figure 4.5. Robust Increases in Intracellular Ca<sup>2+</sup> with Repeated Glutamate Applications.**

(A1, B1) Representative Ca<sup>2+</sup> imaging traces of neurons and astrocytes (respectively) show reversible increases in fluorescent signal in response to repeated perfusion of glutamate (G; 3 μM; purple trace: individual cell response; red trace: average response). (A2, B2) Results normalised to the first glutamate application reveal a small but significant reduction in neuronal response during the third application, and gradual reductions in astrocyte response during the second and third applications. N = 184 neurons & 284 astrocytes; Data was pooled from 4 devices across 3 separate cultures. One way ANOVA with Tukey's post-hoc analysis: \*denotes P < 0.05 (Neuronal G3 vs G1; Astrocytic G2 vs G1), \*\*\*denotes P < 0.001 (G3 vs G1) and #denotes P < 0.001 (G3 vs G2).

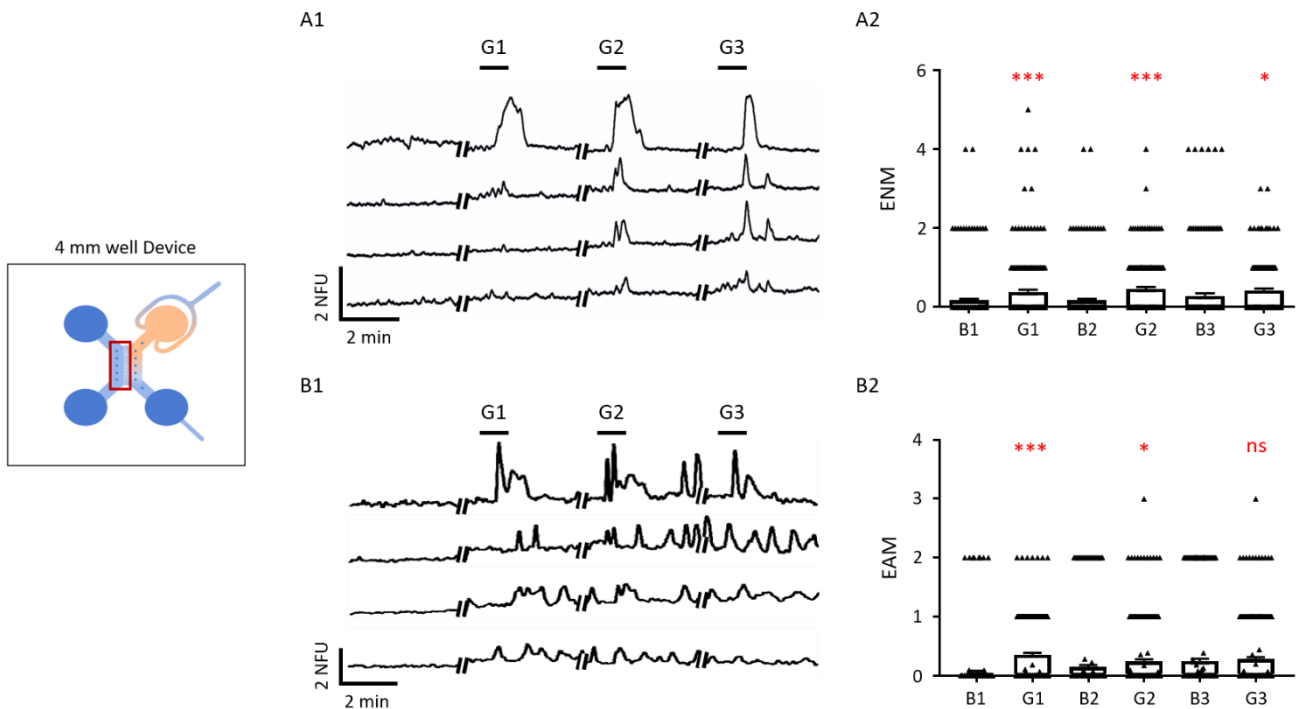


**Figure 4.6. Synaptic Activation of Naïve Neural Network during Glutamate Perfusions.**

(A1, B1) Examples of Ca<sup>2+</sup> imaging traces for neurons and astrocytes respectively (top trace: directly stimulated cell; subsequent traces: indirectly stimulated cells) during repeated glutamate applications (G; 3  $\mu$ M). (A2, B2) Changes in neural network activity reveal large increases in both neuronal and astrocytic activation during the first two glutamate applications. Basal levels of activity have increased during the final recording assessed for both neurons and astrocytes, and the final glutamate application produces a small, significant increase in neuronal activity, whilst no significant changes in astrocyte activity were observed. N = 222 neurons & 258 astrocytes; Data was pooled from 4 devices across 3 separate cultures. Paired t-test: \* denotes P < 0.05 (Neuronal G3 vs B3; Astrocytic G2 vs B2), \*\*\* denotes P < 0.001 (Neuronal G1 vs B1 & G2 vs B2; Astrocytic G1 vs B1) and <sup>ns</sup>denotes P > 0.05.

#### 4.4.3. Assessment of Functional Changes in Neural Network Activity during Glutamatergic Competitive Antagonism Assays

A standard approach to pharmacological characterisation is the blockade of a compound's mechanism of action by the obstruction of the receptor's ligand binding site. Having established changes in the activity of perfused and naïve neural networks in response to repeated glutamate applications, competitive antagonism assays were designed and performed with glutamatergic antagonists (Figure 4.7). Following the first glutamate (3  $\mu\text{M}$ ) application, alternation of the syringe pumps initiated the perfusion of antagonist solution containing NBQX (20  $\mu\text{M}$ ), DL-AP5 (100  $\mu\text{M}$ ) and (R, S)-MCPG (500  $\mu\text{M}$ ) during the 10 minute resting period in between recordings. Saturating concentrations of antagonists were perfused in the attempt of completely attenuating neural network excitation in the presence of glutamate. Subsequent to antagonist perfusion, glutamate induced  $\text{Ca}_i^{2+}$  in the presence of antagonists was reduced from  $1 \pm 0.06$  NFU to  $0.17 \pm 0.03$  NFU ( $n = 219$ , 4 devices, 4 cultures;  $P < 0.001$  compared to absence of antagonists).

$\text{Ca}^{2+}$  signals from astrocytes also reduced from  $1 \pm 0.05$  to  $0.76 \pm 0.05$  NFU (with respect to the first glutamate application;  $n = 243$ ;  $P < 0.001$ ). Following antagonist wash-out, recovery of the neuronal fluorescent readouts was observed during the final glutamate application ( $0.88 \pm 0.05$  NFU;  $P > 0.05$ ) with respect to the first glutamate application. Surprisingly, astrocytes did not appear to recover following antagonist wash-out with respect to the first glutamate application, with fluorescent readouts revealing a signal of  $0.77 \pm 0.04$  NFU ( $P < 0.001$ ).

Despite reductions in fluorescence following the co-perfusion of glutamate and its antagonists, increased naïve neural network activity was still observed (Figure 4.8). Consistent with previous assays, the first glutamate application elicited significant increases in neuronal and astrocytic activity, from  $0.16 \pm 0.03$  to  $0.33 \pm 0.04$  ENM, and  $0.02 \pm 0.01$  to  $0.15 \pm 0.03$  EAM respectively ( $n = 350$  neurons & 290 astrocytes;  $P < 0.001$ ). The competitive antagonism of glutamate revealed cell-type dependent responses to changes in activity. Contrary to expectations, neuronal activity significantly increased from  $0.19 \pm 0.03$  to  $0.42 \pm 0.04$  ENM ( $P < 0.001$ ). Basal levels of astrocytic activity appeared to be elevated at  $0.16 \pm 0.02$  EAM, and the co-perfusion of glutamate with its antagonists did not result in an observable change in activity ( $0.16 \pm 0.03$  EAM;  $P > 0.05$ ). Following antagonist wash-out, the final glutamate perfusion elicited significant increases in activity from both neurons and astrocytes, from  $0.27 \pm 0.04$  to  $0.68 \pm 0.03$  ENM and  $0.17 \pm 0.03$  to  $0.25 \pm 0.03$  EAM respectively.

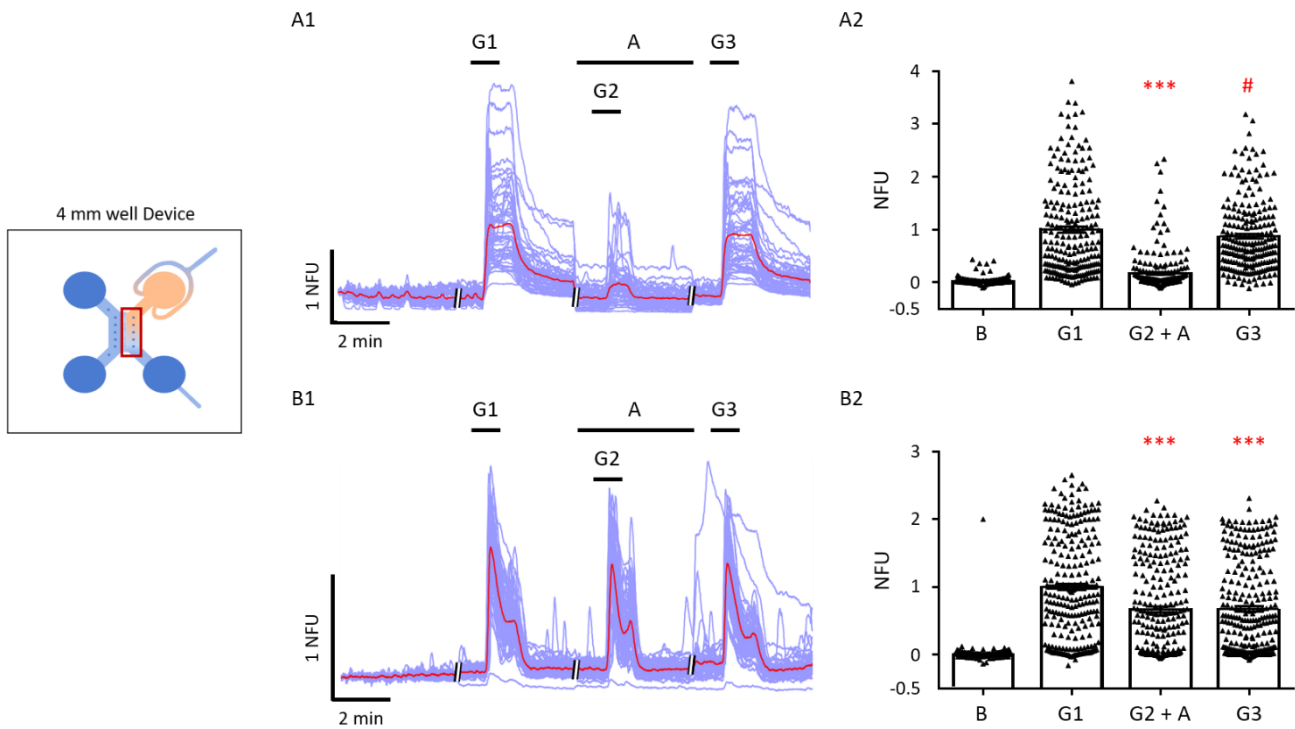


**Figure 4.7. Competitive Antagonism Reveals Cell Type-Dependent Responses to Perfusates.**

(A1, B1) Representative  $\text{Ca}^{2+}$  imaging traces of neurons and astrocytes (respectively) show reductions in fluorescent signal during the co-application of glutamate (G;  $3 \mu\text{M}$ ) and its antagonists (A; NBQX  $20 \mu\text{M}$ ; DL-AP5  $100 \mu\text{M}$ ; (R, S)-MCPG  $500 \mu\text{M}$ ; purple trace: individual cell response; red trace: average response). (A2 & B2) Results normalised to the first glutamate application reveal significant reductions in both neuronal and astrocytic response when glutamate is co-perfused with glutamatergic antagonists. The recovery of response is observed in neurons, but not astrocytes following antagonist washout and the re-perfusion of glutamate. N = 219 neurons & 243 astrocytes; Data was pooled from 4 devices across 4 separate cultures. One way ANOVA with Tukey's post-hoc analysis \*\*\* denotes  $P < 0.001$  (G2 + A vs G1; Neuronal: G3 vs G2 + A; Astrocytic G3 vs G1) and #denotes  $P < 0.001$  (Neuronal G3 vs G2 + A).



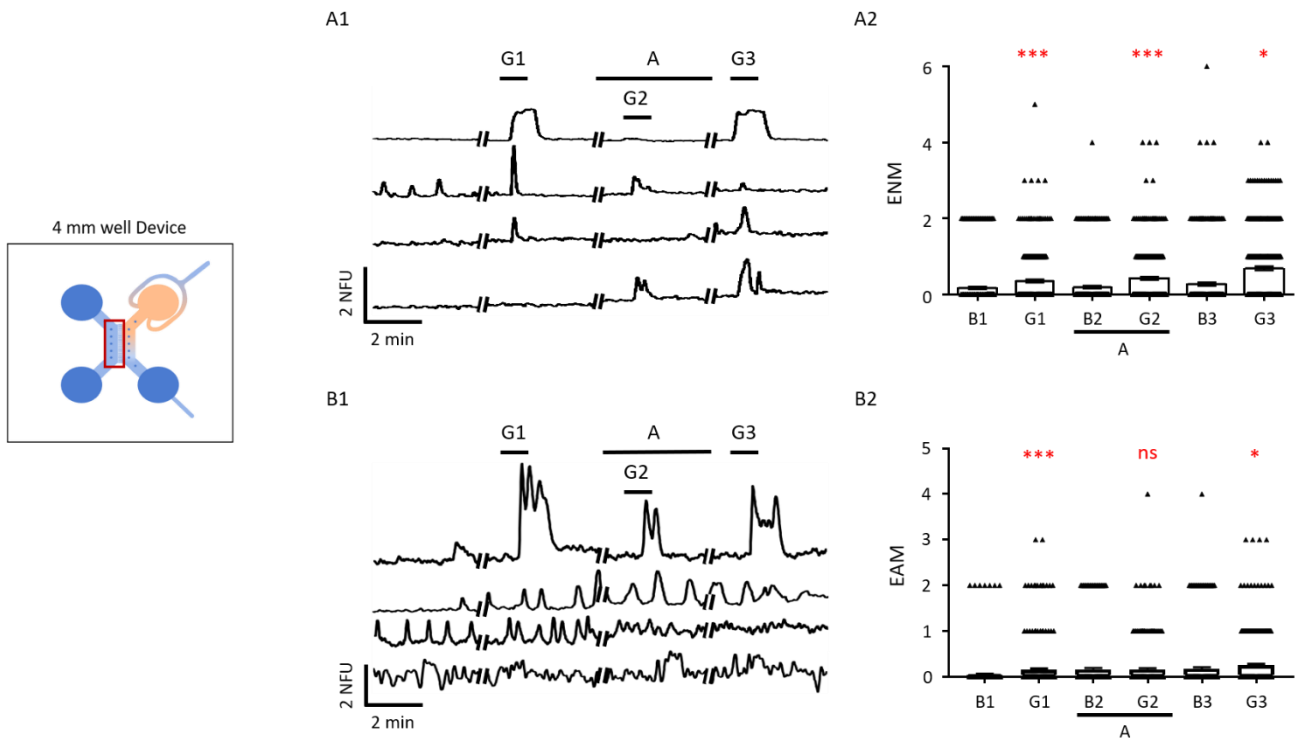


**Figure 4.8. Competitive Antagonism of Glutamate Synaptic Activation of Neurons.**

(A1 & B1) Examples of Ca<sup>2+</sup> imaging traces for neurons and astrocytes respectively (top trace: directly stimulated cell; subsequent traces: indirectly stimulated cells) during competitive antagonism of glutamate (G; 3  $\mu$ M) and its antagonists (A; NBQX 20  $\mu$ M; DL-AP5 100  $\mu$ M; (R, S)-MCPG 500  $\mu$ M). (A2 & B2) Changes in neural network activity reveal large increases in both neuronal and astrocytic activation during the first glutamate application. Significant increases in neuronal activity persist during competitive antagonism perfusions and the final glutamate application following antagonist washout. Washout of antagonists and re-perfusion with glutamate then results in a significant increase in astrocytic activity. N = 350 neurons & 290 astrocytes; Data was pooled from 4 devices across 4 separate cultures. Paired t-test: \*denotes P < 0.05 (G3 vs B3), \*\*\*denotes P < 0.001 (G1 vs B1; Neuronal G2 vs B2) and <sup>ns</sup>denotes P > 0.05 (G2 vs B2).

#### 4.4.4. Assessment of Synaptic Transmission via Neuronal Networks during the Co-Perfusion of Glutamate and TTX

Whilst results from the previous assays strongly suggest changes in naïve neural network activity directly correlate with perfused neural network function, synaptically driven communication has yet to be established with the performance of suitable controls. To this end, competitive antagonists were replaced with the Na<sup>+</sup> channel blocker tetrodotoxin (TTX, 1 μM, Figure 4.9). Fluorescent readouts obtained from the perfused chamber during these assays were similar to that observed for assays involving repeated stimulation by glutamate. Neurons were largely unaffected by the presence of TTX during the application of glutamate, with a non-significant decrease in fluorescent magnitude observed from  $1 \pm 0.06$  to  $0.83 \pm 0.05$  NFU ( $n = 551$ , 3 devices from 3 separate cultures;  $P > 0.05$ ) in the presence of TTX. Following TTX washout and re-perfusion with glutamate, the fluorescent magnitude of neurons non-significantly increased to  $0.85 \pm 0.06$  NFU ( $P > 0.05$ ). Similarly, astrocytes showed non-significant reductions in the fluorescent magnitude response observed between the first glutamate application ( $1 \pm 0.06$  NFU), and the application of glutamate in the presence of TTX ( $0.97 \pm 0.06$  NFU;  $n = 381$ ;  $P > 0.05$ ). Following TTX wash-out, the fluorescent magnitude induced by the final glutamate perfusion significantly decreased to  $0.66 \pm 0.04$  ( $P < 0.001$ ) with respect to the previous two applications.

Results obtained from the simultaneous readout of naïve neural network activity during the TTX assay were intriguing, as the co-perfusion of glutamate and TTX elicited cell type-dependent responses (Figure 4.10). The first glutamate application resulted in significant increases in neuronal and astrocytic activity, from  $0.10 \pm 0.02$  to  $0.19 \pm 0.02$  ENM ( $P < 0.01$ ), and  $0.13 \pm 0.02$  to  $0.20 \pm 0.02$  EAM ( $P < 0.05$ ) respectively ( $n = 381$  neurons & 554 astrocytes). The basal activity of neurons was elevated at  $0.22 \pm 0.03$  ENM and was found to be significantly greater than that previously observed ( $P < 0.01$ ). Glutamate application in the presence of TTX resulted in the non-significant increase in neuronal activity to  $0.27 \pm 0.02$  ENM ( $P > 0.05$ ). Contrarily, there was a significant increase in astrocytic activity during the application of glutamate and TTX, rising from  $0.17 \pm 0.03$  to  $0.26 \pm 0.02$  EAM ( $P < 0.001$ ). Following TTX wash-out, the final glutamate perfusion elicited significant increases in the activity of both neurons and astrocytes, from  $0.11 \pm 0.02$  to  $0.26 \pm 0.03$  ENM and  $0.19 \pm 0.03$  to  $0.30 \pm 0.03$  EAM respectively.

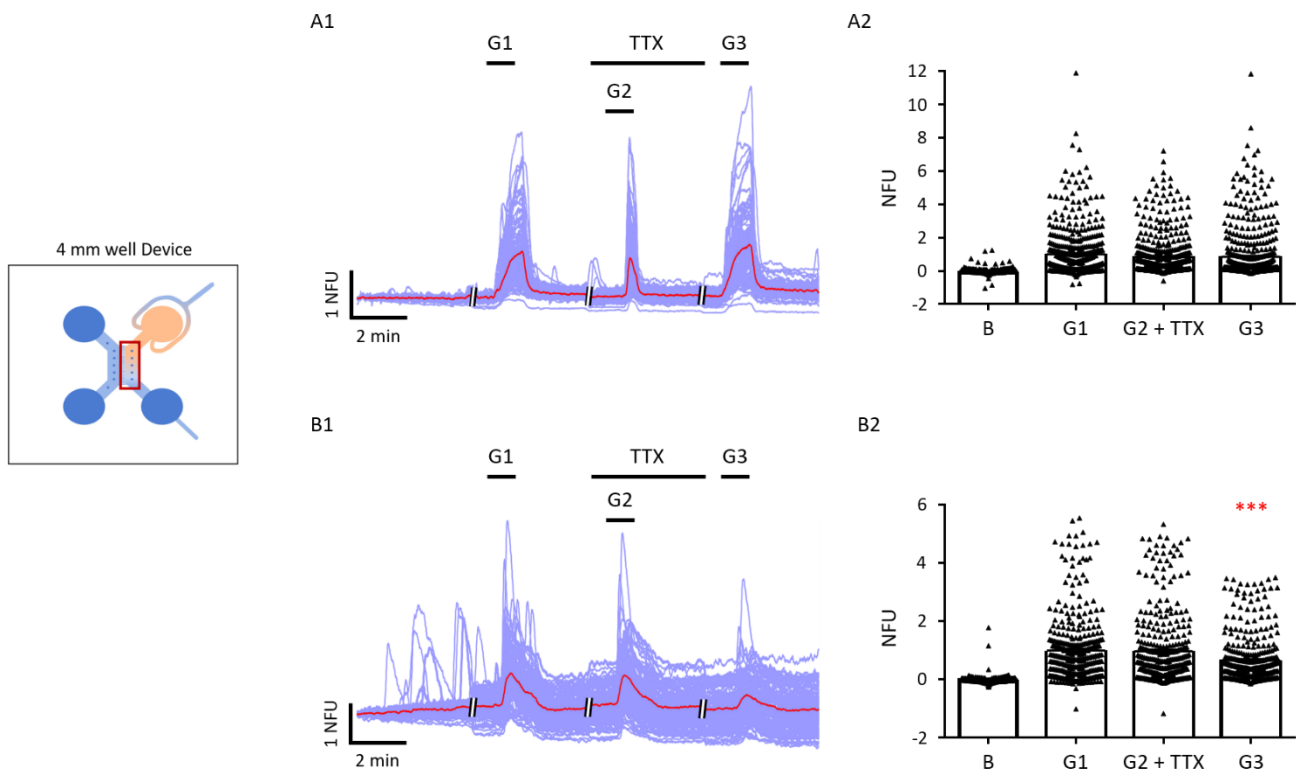


**Figure 4.9. Co-perfusion of Glutamate and TTX does not Significantly Reduce Neural Network Response to Glutamate.** (A1, B1) Representative Ca<sup>2+</sup> imaging traces of neurons and astrocytes (respectively) show non-significant reductions in fluorescent signal during the co-perfusion of glutamate (G; 3  $\mu$ M) and TTX (1  $\mu$ M; purple trace: individual cell response; red trace: average response). (A2, B2) Results normalised to the first glutamate application reveal non-significant changes in neuronal fluorescent signals throughout the assay. Significant reductions in signal were detected for astrocytes during the final application of glutamate. N = 551 neurons & 381 astrocytes; Data was pooled from 3 devices across 3 separate cultures. One way ANOVA with Tukey's post-hoc analysis: \*\*\* denotes P < 0.001 (G3 vs G1 & G2).

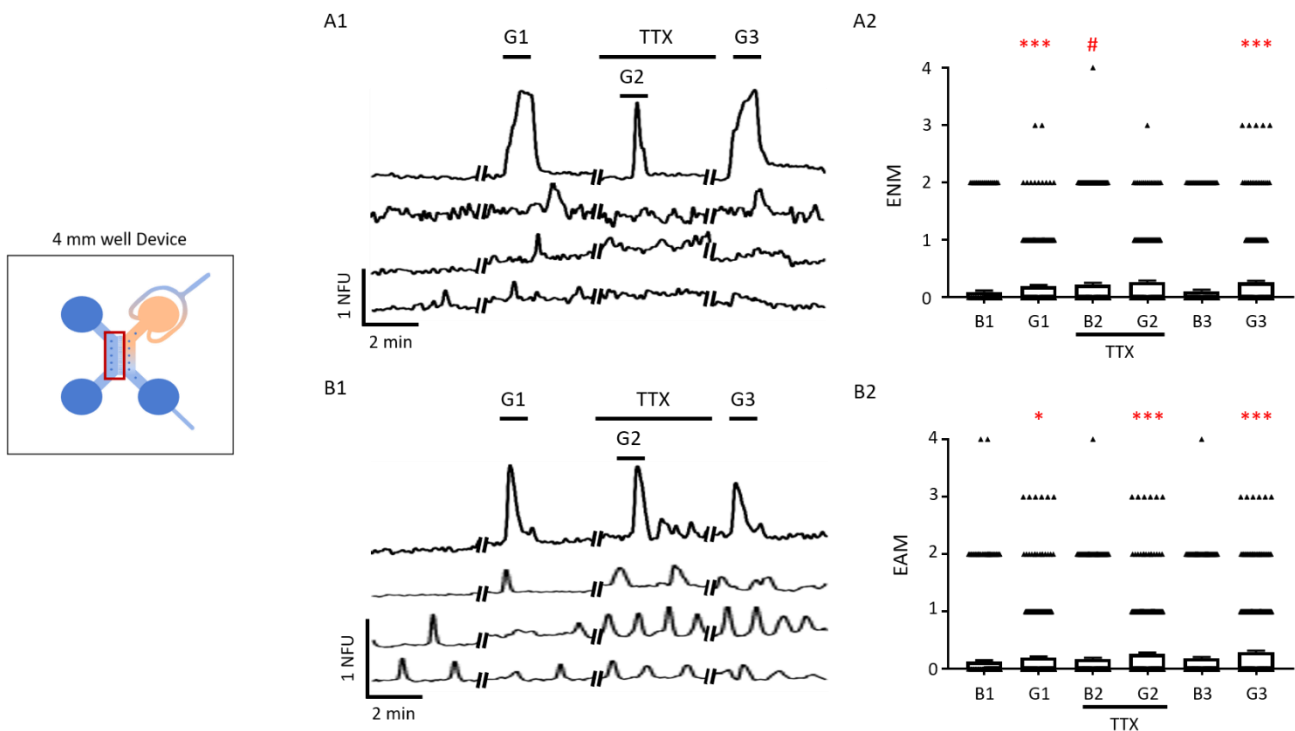


**Figure 4.10. Synaptic Activation of Astrocytes but not Neurons, occur during Co-Perfusion of TTX and Glutamate.** (A1, B1) Examples of Ca<sup>2+</sup> imaging traces for neurons and astrocytes respectively (top trace: directly stimulated cell; subsequent traces: indirectly stimulated cells) during microfluidic perfusion of glutamate (G; 3  $\mu$ M) in the presence of TTX (1  $\mu$ M). (A2, B2) Changes in neural network activity reveal large increases in both neuronal and astrocytic activation during the first glutamate application. Basal levels of neuronal activity were significantly raised during the perfusion of TTX alone, and the co-application of glutamate with TTX did not result in further significant changes. A significant increase in neuronal activity was observed following TTX wash-out and the re-perfusion of glutamate alone. Astrocytic activity significantly increased during each application of glutamate, persisting despite the presence of TTX during the second application. N = 381 neurons & 554 astrocytes; Data was pooled from 3 devices across 3 separate cultures. Paired t-test: \*denotes P < 0.05, \*\*denotes P < 0.01, \*\*\*denotes P < 0.001 (G3 vs B3; Astrocytic G2 vs B2) and #denotes P < 0.01 (Neuronal B2 + TTX vs B1).

#### 4.4.5. Assessment of Mechanical Stimulation on the Activation of Perfused and Naive Neural Networks

Whilst there are clear changes to the activity of the naïve neural network during the performance of these assays, it cannot be argued conclusively that these changes arise solely from the chemically induced activation of the perfused network. First, perfusion of vehicle solution at  $4 \mu\text{L min}^{-1}$  may itself induce changes in network activity over the duration of assay performance. Additionally, the possibility exists that the mechanical shift of fluid within the inlet well during syringe pump alternation is great enough to induce downstream propagation of signals to the cells present in the culture chamber and through to the adjacent network. Investigating these potential sources of stimulation responsible for the observed changes in neural network activation is imperative for demonstrating the capabilities of the microfluidic perfusion system without producing biased results. In the absence of compound perfusion and therefore lack of a pharmacological stimulus, it was logical to assess changes in the activity of the naïve neural network against the activity of the perfused neural network.

Microfluidic perfusion assays were performed without syringe pump alternation during recordings obtained at equivalent time points of those performed in previous assays, and the activity observed was averaged over the course of each respective recording. Interestingly, mutual fluctuations between the perfused and naïve neural networks were observed over time (Figure 4.11). Within the perfused chamber, neuronal activity was initially  $0.14 \pm 0.01$  ENM ( $n = 365$ , 4 devices from 2 separate cultures) during the first baseline recording, before increasing to  $0.19 \pm 0.01$  ENM ( $P < 0.05$ ) during the second recording, and reduced back to  $0.12 \pm 0.01$  ENM ( $P < 0.001$ ) during the final recording. Similarly, astrocytes within the perfused chamber, with an initial activity of  $0.18 \pm 0.01$  EAM ( $n = 423$ ), showed increases in activity during the second recording ( $0.23 \pm 0.01$  EAM;  $P < 0.001$ ) and fell back to  $0.16 \pm 0.01$  EAM ( $P < 0.001$ ) during the final recording. Within the naïve chamber, neuronal activity was initially  $0.12 \pm 0.01$  ENM ( $n = 440$ ) during the first baseline recording, and a small but significant increase in activity of  $0.16 \pm 0.01$  ENM ( $P < 0.05$ ) was observed during the second recording, before reducing to  $0.13 \pm 0.01$  ENM ( $P > 0.05$ ) during the final recording.

Astrocytes within the naïve chamber showed an initial activity of  $0.15 \pm 0.01$  EAM ( $n = 422$ ) which rose to  $0.22 \pm 0.02$  ( $P < 0.001$ ) during the second recording, before reducing to  $0.18 \pm 0.01$  EAM ( $P > 0.05$ ) during the final recording. At no point were there significant differences observed between the neuronal and astrocytic populations across their respective perfused and naïve networks, during their respective recordings.

Separate devices were then used to investigate changes in network activity induced by the alternation of active syringe pump using vehicle solution perfused at  $4 \mu\text{L min}^{-1}$  (Figure 4.12). Within the perfused chamber, non-significant changes in the neuronal activity were observed, from  $0.10 \pm 0.04$  to  $0.08 \pm 0.03$  ENM ( $n = 135$  neurons;  $P > 0.05$ ), and astrocyte activity significantly increasing from  $0.18 \pm 0.04$  to  $0.21 \pm 0.03$  EAM ( $n = 165$ ;  $P < 0.05$ ) during the first vehicle application, with respect to baseline activity ( $n = 2$  devices from 2 separate cultures). The second vehicle application showed similar results, where neuronal activity non-significantly increased from  $0.09 \pm 0.04$  to  $0.14 \pm 0.04$  ENM ( $P > 0.05$ ), whilst astrocyte activity non-significantly increased from  $0.33 \pm 0.06$  to  $0.35 \pm 0.04$  EAM ( $P > 0.05$ ). During the recording for the final vehicle application, neuronal activity displayed significant increases in activity, from  $0.12 \pm 0.04$  to  $0.24 \pm 0.05$  ENM ( $P < 0.001$ ), whilst astrocyte activity non-significantly increased from  $0.39 \pm 0.06$  to  $0.42 \pm 0.05$  EAM ( $P > 0.05$ ). These changes in activity of the perfused neural network were mirrored by that of the naïve neural network. Within the naïve network, the first vehicle application did not induce any observable change in neuronal activity ( $0.08 \pm 0.04$  to  $0.08 \pm 0.04$  ENM;  $n = 137$ ;  $P > 0.05$ ) whilst astrocytes displayed a non-significant reduction in activity, from  $0.12 \pm 0.03$  to  $0.11 \pm 0.02$  EAM ( $n = 199$ ;  $P > 0.05$ ) with respect to baseline activity. The second vehicle application similarly revealed little change in neuronal activity ( $0.11 \pm 0.03$  to  $0.12 \pm 0.02$  ENM;  $P > 0.05$ ), whilst astrocyte activity non-significantly increased from  $0.21 \pm 0.03$  to  $0.29 \pm 0.03$  EAM ( $P > 0.05$ ). The final vehicle application then resulted in a marked increase in neuronal activity, from  $0.14 \pm 0.03$  to  $0.38 \pm 0.04$  ENM ( $P < 0.001$ ) with respect to baseline activity, whereas non-significant increases in astrocyte activity ( $0.28 \pm 0.04$  to  $0.38 \pm 0.03$  EAM;  $P > 0.05$ ) were observed.

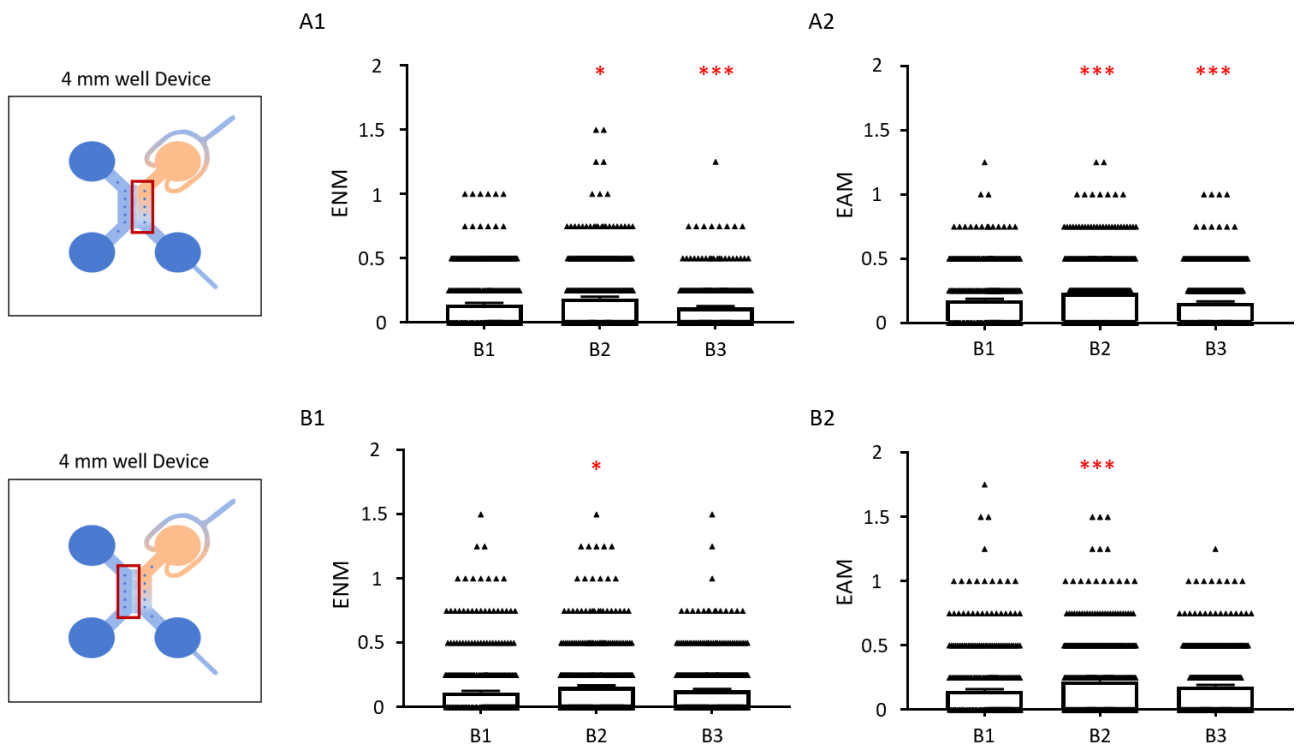


**Figure 4.11. Steady Vehicle Perfusion Induces Subtle Changes to Neural Network Activity.**

(A1, A2) Perfused neurons and astrocytes show significant increases in activity during the second baseline recording, relative to the initial level of activity observed. Significant reductions in the activity for both neurons and astrocytes were observed, relative to the activity during the second recording. (B1, B2) Responses from the naïve neurons and astrocytes similarly show significant increases in activity during the second recording, relative to the first baseline recording. Non-significant reductions in activity were observed for both neurons and astrocytes during the final recording, relative to the second baseline recording.  $N = \geq 365$  neurons,  $\geq 422$  astrocytes per network assessed; Data was pooled from 4 devices across 2 independent cultures. One way ANOVA with Tukey's post hoc analysis: \*denotes  $P < 0.05$  (B2 v B1) and \*\*\*denotes  $P < 0.001$  (Perfused astrocytic B2 vs B1; Perfused neuronal & astrocytic B3 vs B2; Naïve astrocytic B2 vs B1).

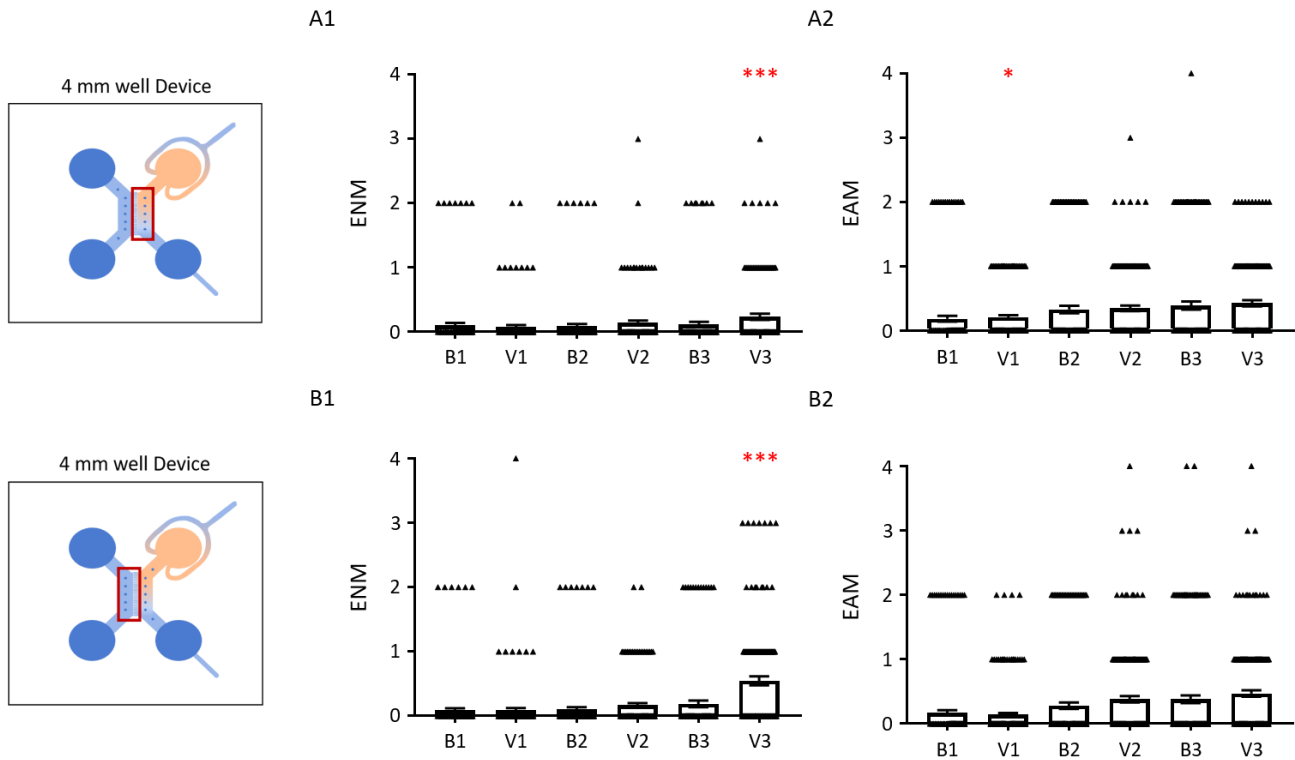


**Figure 4.12. Repeated Syringe Pump Alternation Induces Increased Neuronal Network Activity.**

(A1, A2) Perfused neurons and astrocytes (respectively) show gradual, non-significant increases in activity during the first two changes in perfused vehicle application. The activity of neurons, but not astrocytes, significantly increase during the final application of vehicle perfusion. (B1, B2) Responses from the naïve neurons and astrocytes (respectively) show similar, non-significant increases in activity during the first and second vehicle perfusions, relative to their baseline activity. There is a large, significant increase in neuronal activity during the final vehicle application, whilst no significant changes are observed in the astrocyte population. Notably however, the general level of astrocyte activity gradually increases over the course of the assay.  $N = \geq 135$  neurons,  $\geq 165$  astrocytes per network assessed; Data was pooled from devices across 2 independent cultures. Paired t-test: \*denotes  $P < 0.05$  (V1 vs B1) and \*\*\*denotes  $P < 0.001$  (V3 vs B3).



#### 4.4.6. Assessment of Retrograde Signalling on Axons Repeatedly Stimulated by Glutamate

Whilst mechanical stimulation of the perfused network appears to influence the activity of the naïve network, the level of activity and consistency in activation is not on par with that observed during chemical stimulation. However, experimental controls were still required to validate changes in naïve neural network activity are driven by chemically induced synaptic transmission from the perfused neural network, as opposed to retrograde activation of axonal projections. Whilst unlikely, neuronal dendrites may also grow through the microchannel array in parallel with axonal projections and become stimulated during glutamate application.

Single neural networks were therefore cultured within the naïve compartment of microfluidic devices and once connected to the microfluidic perfusion setup, the projections present in the perfused chamber were exposed to repeated glutamate applications (Figure 4.13). Functional neurons and astrocytes, demonstrated by the increased  $\text{Ca}^{2+}$  dependent fluorescent signal in response to direct KCl (25 mM final concentration) application, did not reveal significant changes in activity throughout the assay. During the first application of glutamate, neuronal activity non-significantly increased from  $0.12 \pm 0.03$  to  $0.16 \pm 0.02$  ENM ( $n = 469$ , data gathered from 3 devices across 3 separate cultures;  $P > 0.05$ ), whilst astrocyte activity non-significantly increased from  $0.29 \pm 0.07$  to  $0.32 \pm 0.06$  EAM ( $n = 455$ ;  $P > 0.05$ ). During the second perfusion of glutamate, neuronal activity non-significantly increased from  $0.09 \pm 0.02$  to  $0.11 \pm 0.02$  ENM ( $P > 0.05$ ) whilst astrocytic activity non-significantly increased from  $0.26 \pm 0.05$  to  $0.32 \pm 0.07$  EAM ( $P > 0.05$ ). Finally, the third application of glutamate resulted in non-significant ( $P > 0.05$ ) reductions in activity for both neurons ( $0.17 \pm 0.03$  to  $0.13 \pm 0.03$  ENM) and astrocytes ( $0.35 \pm 0.07$  to  $0.31 \pm 0.06$  EAM). Both compartments of the microfluidic devices were fixed and stained for  $\beta$ -III-Tubulin and MAP2 to highlight the presence of axonal and dendritic processes respectively, and images taken confirmed the absence of dendritic markers in the perfused chamber.

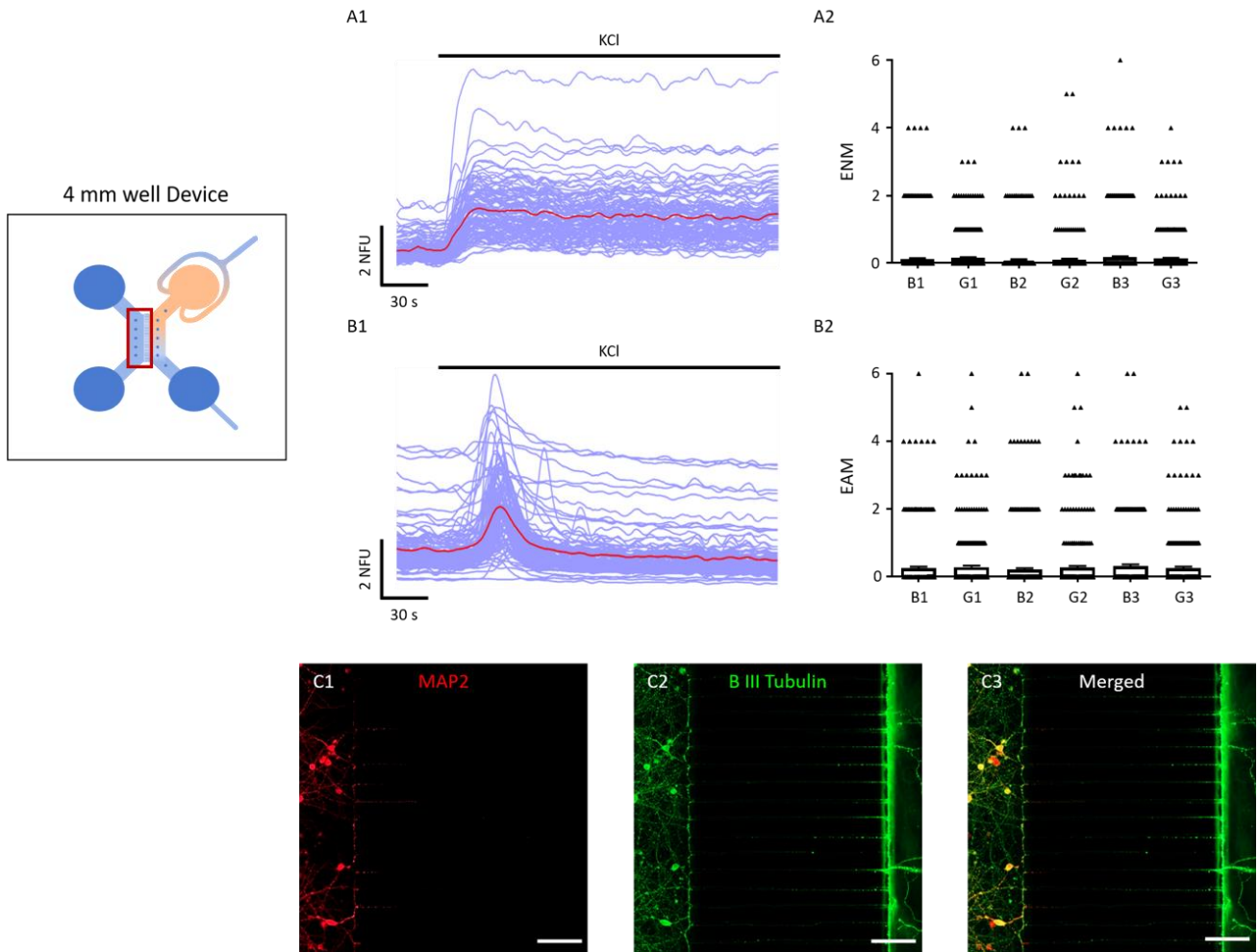


**Figure 4.13. Naïve Neural Network Activation is Dependent on Synaptic Communication from Perfused Neural Networks.** (A1, B1) Neurons and astrocytes (respectively) are functionally active following KCl application (25 mM final concentration) within the naïve culture chamber. (A2, B2) Repeated glutamate application (3  $\mu$ M) to exposed neuronal projections in the perfused chamber does not elicit significant changes in the activity of either neurons or astrocytes present in the naïve neural network. (C1-C3) Immunocytochemical images post-assay performance reveals that axonal, but not dendritic projections traverse through the microchannel array and into the adjacent, perfused culture chamber. N = 469 neurons & 455 astrocytes; Data was pooled from 3 devices across 3 separate cultures. Paired t-test: No significance observed. Scale bars = 100  $\mu$ m.

## 4.5. Chapter 4 Discussion

This chapter details the optimisation of a microfluidic perfusion system driven by syringe-pumps that allows the simultaneous assessment of neuropharmacological assays for direct neural network response and subsequent changes in synaptic communication to a naïve network. Multiple flow rates were assessed to determine an optimal flow rate that minimises the impact on neural network health in addition to determining the temporal kinetics of compound delivery by visualizing repeated calcein perfusions. A variety of neuropharmacological assays were performed to assess the system's ability to pharmacologically profile CNS acting compounds and thereby scrutinise its potential use as a CNS drug discovery platform. Changes in the activity of the naïve neural network were observed in response to multiple stimuli and chemically induced synaptic communication between networks was verified following the performance of control assays.

### 4.5.1. Optimisation of the Microfluidic Perfusion System

A variety of studies have demonstrated the impact of mechanical shear stress on functional neural network activity, as well as subsequent changes to gene expression, development and maladaptive responses in TBI models<sup>369–372,378–380</sup>. Additionally, neuropharmacological studies involving *in vitro* techniques typically use laminar flow perfusion for compound delivery, in which the flow rates used may range between 0.1 - 3 mL to completely replace solution present in the recording chamber<sup>375,381–383</sup>. Shear stress in these cases are minimised however by the large area perfused in comparison to microfluidic approaches. Other studies in microfluidic formats modelling TBI have demonstrated that acute insults of large shear stress directly applied to astrocytes (11.2 - 23 dyn cm<sup>-2</sup>)<sup>372</sup> and CNS cells (30 - 520 dyn cm<sup>-2</sup>)<sup>384</sup> can trigger large propagating calcium waves, demonstrating that shear stress (albeit in excessive force) can impact CNS cell signalling. It was therefore logical to first assess the impact that differing flow rates and relative shear stress had on neural networks directly exposed to perfusion. Previous microfluidic studies investigating neural networks have demonstrated clear synaptic communication between directly stimulated and naïve networks<sup>275,291,309</sup>, including the spread of toxicity following an pharmacological insult<sup>276</sup>. As such, it was hypothesised that changes in the naïve, non-perfused network may also be present when perfusing the adjacent, synaptically connected neural network.

The range of shear stress induced by microfluidic perfusion here (0.0278 – 0.695 dyn cm<sup>-2</sup>) was found to be considerably less than that observed in the microvasculature of the brain (10 - 20 dyn cm<sup>-2</sup>) and

arterial circulation ( $4 - 30 \text{ dyn/cm}^{-2}$ )<sup>385</sup>, suggesting the impact of shear stress on my microfluidic cultures should be minimal. The duration of these perfusion experiments was restricted to a relatively short time period (1 hour) with live/dead staining performed thereafter to reflect the duration of subsequent pharmacological assays to be performed. Results from live/dead assays demonstrated flow rate dependent changes in the viability of perfused networks, which was closely mirrored by the naïve network. Whilst this indicates that synaptic communication exists is still present between the perfused and neural networks, it is also suggestive that changes in the activity of a stimulated network will be reflected in the activity of the naïve network. These results are in line with previous studies in a microfluidic perfusion system, where constant perfusion of media at increasing flow rates significantly increased the viability of 3-D cultured neural networks<sup>386</sup> and *ex vivo* brain slices<sup>387</sup>. Specific mechanisms responsible for improved culture viability at increasing flow rates were not demonstrated in either study. However, both postulated that the ability to maintain homeostasis within the microenvironment may be compromised at higher flow rates, whilst constant replenishment of nutrition and wash-out of toxic chemicals/proteins produced by the cultures may play a role in the increased viability induced by perfusion. As cultures were perfused continuously in exogenously prepared, extracellular HBS solution, media replenishment can't be considered a contributing factor to the findings of this study. Evidence in the literature suggests several possible underlying mechanisms that could explain the neuroprotection conferred by flow rates. Briefly, neuroprotection by shear stress could arise from stretch induced NMDAR mediated synaptic activity and subsequent ERK phosphorylation<sup>388</sup>. Although this has previously been demonstrated *in vivo* to result in the up-regulated expression of anti-apoptotic protein Bcl-2 in response to monosodium glutamate injections<sup>389</sup>, significant increases in BCL-2 expression<sup>389</sup>, were only observed after 6 hours of treatment. Thus, it is unclear at present if this mechanism is responsible for the neuroprotection conferred by microfluidic perfusion. Alternatively, stretch induced propagation of calcium waves and ATP release by astrocytes can activate neighbouring inhibitory neurons which suppress excitotoxicity<sup>390-393</sup>. These signalling mechanisms may be present in the neuronal network that is not directly exposed to microfluidic perfusion as well, as axonal projections from the naïve chamber that have traversed the microchannel array can be stimulated by shear stress to illicit calcium signals<sup>394</sup> and would be influenced by stretch induced NMDAR mediated synaptic activity. Future experiments could include allowing the microfluidic cultures to recover before staining for changes in synaptic protein expression or anti-apoptotic markers to elucidate the underlying mechanisms involved. These assessments lie beyond the scope of this study however and so were not investigated further.

The impact of perfusion on specific neuronal or astrocytic cell types was not considered due to the impracticality of fixing and staining for marker proteins, whilst ensuring the integrity of bound hoechst & PI following fixation, light exposure and multiple washing steps. It should be acknowledged a particular limitation of using PI as an appropriate marker for live/dead analysis is that cells in the early stages of apoptosis still have a relatively stable membrane and so dying cells could be detected as living (false positive). Due to staining being performed shortly after perfusion cessation, the results reflect changes in necrotic death present in the microfluidic cultures and so devices assessed should be allowed to recover for several hours before performing the live/dead stain for more accurate results. This would be impractical however due to the extended assay duration, additional control requirement to account for the impact of HBS on cultures, and a loss of sterility. An alternative approach would be the inclusion of an Annexin V conjugate alongside PI and hoescht, as the former binds to phospholipid phosphatidylserine which is translocated to the extracellular surface of cell membranes during early apoptosis.

Microfluidic techniques allow for greater control over experimental parameters and a variety of studies have demonstrated the precise control of fluid to compartments<sup>286,367,395,396</sup> through the use of microfluidic perfusion. The microfluidic perfusion protocol employed here environmentally isolates the non-perfused chamber by establishing a hydrodynamic pressure gradient across the microchannel array, preventing cross-contamination of the perfused fluid. Then, reliable delivery of a compound to the perfused chamber with precise temporal control was realised by the repeated application of calcein solution. Consistent delivery of the perfusate was evident by producing stable fluorescent plateaus over multiple recordings and complete washout demonstrated by reductions in fluorescence following calcein-vehicle alternation. The time taken for 100% perfusate concentration to reach the mid-point of the culture, whilst in close proximity to the theoretical time calculated, did appear to be delayed. Likely factors contributing to this lag time include the presence of micropillars in the culture chamber, which would impact flow behaviour. Additionally, needle ports at the inlet well were created manually and so the height at which the needles infuse solution into the inlet well will differ, resulting in subtle changes in the perfused flow rate via gravitational force. The potential for compound diffusion was determined to be negligible because a steady flow rate of  $4 \mu\text{L min}^{-1}$  resulted in Peclet numbers significantly greater than 1 for the CNS acting drug used during neuropharmacological assays.

#### 4.5.2. Neuropharmacological Profiling of Glutamate in Neural Networks with Microfluidic Perfusion

To demonstrate the proposed microfluidic perfusion system is amenable to pre-clinical CNS drug discovery, a series of assays were performed for the pharmacological characterisation of glutamate in neural networks. A concentration response curve was generated using results obtained from  $\text{Ca}_i^{2+}$  dependent peak fluorescent magnitudes following the direct application of glutamate at increasing concentrations. The  $\text{EC}_{50}$  values obtained for neurons and astrocytes are in close proximity to that reported in the literature<sup>397–402</sup>, which validates the robustness of the results presented here. It should be noted that as an endogenous excitatory neurotransmitter, glutamate will have activated both ionotropic and metabotropic glutamate receptors and their subunits to varying degrees. The peak fluorescent magnitudes used to generate the concentration response curves provided averaged fluorescent responses from cell somas during stimulation, and therefore the reported  $\text{EC}_{50}$  values here are not representative of specific glutamatergic receptors. To avoid the risk of inducing excitotoxicity or de-sensitisation to the repeated perfused stimulus, glutamate applications were limited to 1 minute and the highest concentration to be used was perfused during the final recording. Whilst there was no indication of abnormal responses observed in neurons exposed to increasing glutamate perfusions, there was a noticeably reduced sensitivity to perfusions of glutamate at 1mM concentrations in astrocytes. This resulted in a hooked shape at the upper asymptote, and so the reported  $\text{EC}_{50}$  value will be less accurate than that found in neurons. The observed desensitisation may be the result of mGluR5, present on astrocytes, being over-stimulated and this is in line with observations in the literature where desensitisation occurs following repeated stimulus by exogenously applied agonists<sup>79,403</sup>.

Assay repeatability can be described as the ability to produce consistent signals over multiple recordings from a single concentration and is a standard criterion for demonstrating reliable assay performance<sup>404</sup>. Assays were therefore designed to demonstrate that the microfluidic perfusion system can be used for the performance of compound repeatability assessments across multiple devices. Here, fluorescent responses observed by the repeated application of glutamate (3  $\mu$ M) were obtained for neuronal and astrocytic populations in the perfused neural network. Astrocytes displayed a non-recoverable fluorescent reduction in response to glutamate applications during the second and third recordings, relative to the signal observed during the first glutamate application. Neuronal response to repeated glutamate applications showed consistent increases in  $Ca_i^{2+}$  dependent fluorescence, however a significant reduction in response was observed during the final application of glutamate. This observation is likely the result of desensitised glutamatergic receptors in the extended presence of glutamate, a response which has been widely reported in the literature<sup>405–407</sup>. Synaptic events involving the release of glutamate last over a range of micro to milliseconds, and so it is a reasonable assumption that 1 minute perfusions of glutamate, at concentrations required for event detection by  $Ca^{2+}$  imaging, would result in receptor desensitisation. Reducing the concentration of glutamate perfused or optimising the microfluidic device further to minimise the duration of perfusate delivery are potential avenues for future experiments.

Demonstrating that a compound of interest acts by a mechanism to elicit a cellular response, in this case glutamate binding to glutamate receptors and inducing  $Ca^{2+}$  dependent activity, typically demands that its mechanism of action be blocked by an established antagonist. To this end, a multi-step microfluidic perfusion protocol was designed for the application of glutamate in the absence and presence of the glutamate receptor antagonists NBQX, DL-AP5 & (R, S)-MCPG, targeting AMPA, NMDA & mGluRs respectively. Neurons co-perfused with glutamate and its antagonists produced approximately 17 % of the original response to glutamate alone, however astrocytes remained relatively sensitive to glutamate-induced stimulation with a relative signal of ~76 %. Following antagonist washout, neuronal sensitivity to glutamate application recovered to ~88 % of the original application, however astrocytes did not recover, reporting a ~77 % relative signal presumably due to glutamatergic receptor desensitisation. Raised levels of  $Ca_i^{2+}$  in astrocytes during stimulation with AMPA & NMDA receptor antagonists have been observed in previous studies using light-evoked stimulation to induce synaptic activation of neighbouring neurons<sup>408,409</sup>. Similarly, an increase in astrocyte current induced by glutamate was only partially blocked by the co-application of

30  $\mu$ M NBQX<sup>410</sup>. The data presented and evidence found in the literature suggests that there are other mechanisms other than glutamatergic/metabotropic pathways responsible for the sustained astrocyte activation observed, however this was beyond the scope of this chapter. Nonetheless, these results demonstrate that the microfluidic device is fit for the purpose of performing standard pharmacological characterisation assessments on CNS acting compounds.

### 4.5.3. Dynamic Activation of Naïve Neural Networks During Neuropharmacological Assays are Synaptically Driven

Standard approaches to *in vitro* neuropharmacological studies exclusively assess the response of a single neural network to an exogenously applied compound, which significantly limits the capacity to determine the influence that such a compound may have on communication between synaptically connected networks. Indeed, by taking advantage of microfluidic techniques, simultaneous assessment of changes in naïve neural network activity, in addition to the pharmacological profiling of glutamate can be undertaken for the first time.

#### 4.5.3.1. Repeated Glutamate Applications Induce Increased Basal Activity in the Naïve Neural Network

Significant increases in naïve neuronal and astrocytic activity were observed during the first two applications of glutamate to the perfused chamber, suggestive of synaptic communication, which is in line with previous results observed during the performance of the *in situ* microfluidic Ca<sup>2+</sup> imaging assays (Chapter 3). Prior to the final glutamate application however, the basal activity of the neural network was raised, such that the magnitude of increased neuronal activity was less apparent during glutamate perfusion, whilst increases in astrocyte activity were non-significant. These findings are in line with previous studies which have shown, following induced or transient stimulation, increased sensitivity to excitatory stimulus in neural networks by synaptically connected neurons<sup>411–414</sup>. In this case, repeated stimulation of the perfused network may be driving postsynaptic up-regulation of AMPA & NMDA receptors on the dendritic spines of synaptically connected naïve neurons, a mechanism well established to be involved synaptic plasticity<sup>94,415,416</sup>. Whilst changes in the naïve neural network activity are suggestive of LTP induction, additional experiments involving the assessment of immunocytochemical staining for the expression of synaptic markers and glutamatergic receptors, in addition to communication studies over extended periods of time, would have to be performed.



#### 4.5.3.2. Differences in Cell-Type Activity in the Naïve Neural Network Observed During Competitive Antagonism of Glutamate

The naïve neural network displayed significantly increased activity during the first glutamate application, however different responses were observed between neuronal and astrocytic populations during competitive antagonism. Despite significantly reduced levels of  $\text{Ca}_i^{2+}$  dependent fluorescence observed in neurons exposed to the co-perfusion of glutamate and its antagonists, a significant increase in naïve neuronal activity was observed. In contrast, this increase in activity was not observed in the population of naïve astrocytes. The changes in naïve neuronal activity could be explained by the presence of low level stimulation from the perfused chamber, as the fluorescent signal was not completely abolished, suggesting synaptic communication could still be induced. Studies have implicated the role of AMPA receptors in homeostatic control of synaptic activity, where concentrations of presynaptic glutamate below saturation lead to an increase in postsynaptic neuronal activation<sup>417,418</sup>. Regarding the lack of increased activity observed in the naïve astrocytic population, a previous study demonstrated that astrocytes show bias in the selectivity of activity inducing stimuli, and specifically, require high frequency synaptic transmission mediated by the neuronal pre-synaptic release of glutamate<sup>419,420</sup>. Additionally, application of metabotropic glutamate antagonists resulted in the cessation of inducible astrocyte activity, which is in line with my reported results. Following antagonist washout and re-application of glutamate, significant increases in activity were observed across the naïve neural network, indicating cell-type dependent activity can be selectively modulated with the microfluidic perfusion system simultaneous to neuropharmacological characterisation assays.

#### 4.5.3.3. Reliable Synaptic Activation of the Naïve Neural Network is Induced by the Controlled Application of Stimuli to the Perfused Neural Network.

Results suggesting naïve neural network activity is inducible by the application of CNS acting compounds to a perfused neural network operates under the assumption that synaptic communication drives naïve neural network response. To assess the role of inducible synaptic transmission from the perfused neural network to the naïve network, glutamate perfusion assays were performed in the presence of the potent  $\text{Na}^+$  channel blocker, TTX to abolish perfused culture excitability. During the co-application of glutamate and TTX, cell-type dependent changes in activity were again observed and inverse to the activity produced following co-application of glutamate and

glutamatergic receptors. As expected, increases in neuronal activity were completely abolished during glutamate/TTX perfusions, however it was noted that basal levels of neuronal activity in the presence of TTX perfusion were elevated immediately prior to drug application and were resistant to change. This may suggest that TTX application to the perfused chamber is dampening the inhibitory tone on basal neuronal activity by reducing GABA release, which confers strong inhibitory currents in the hippocampal culture preparations used here<sup>421</sup>. Wave-form epileptic activity has been demonstrated in hippocampal preparations previously by the application of GABAergic antagonists<sup>422,423</sup> and this gives credence to the suggested role of interneuron mediated control of naïve neural network basal activity. Contrary to the neuronal response, naïve astrocytes still displayed a significant increase in activity during glutamate/TTX perfusions. This is in line with previous work demonstrating slow  $\text{Ca}^{2+}$  oscillations, following induced astrocyte activity, are not abolished by TTX, but are instead controlled through mGluR5 mediated activity<sup>424</sup>. These results therefore strengthen the argument that inducible changes in naïve neural network activity are driven by synaptic transmission from the perfused neural network.

Next, assays were performed to determine the impact that perfusion has on basal neural network activity, and if repeated mechanical stimulation induced by syringe pump alternation cause a biased response in the previously observed results. Assay performance of perfusion across multiple recordings in the absence of syringe pump alternation show fluctuations in activity over time and the same trend can be observed across both perfused and naïve neural networks. Peak activity was observed during the second recording for both neuronal and astrocytic populations and was significantly greater than activity observed in the previous recording. A significant reduction in activity was observed in the perfused neural network during the third recording, whereas non-significant reductions in activity were observed in the naïve neural network. During syringe pump alternation, significant increases in neuronal, but not astrocytic activity, were observed in both the perfused and naïve neural networks during the final application of a mechanical stimulus. The fluctuations in basal activity could be explained by spontaneous brain activity, which has been previously observed in the hippocampus of free moving rats in the absence of changes to the experimental conditions<sup>425</sup>. Assessing the mechanisms underlying shear stress on spontaneous neural network activity would be required to verify this however, and so was not pursued further.

There is a risk that chemically-induced synaptic communication in the microfluidic perfusion system is influenced by glutamate induced, retrograde activation of pre-synaptic terminals present on the axonal projections from the naïve neural network<sup>426</sup>. Despite previously published studies on synaptic communication in microfluidic hippocampal preparations suggesting the contrary<sup>275,276</sup>, no study to date has experimentally proven otherwise. Microfluidic perfusion assays were therefore performed in single neural network cultured devices to assess repeated glutamate application on retrograde axonal activation in the non-cultured perfusion chamber. There were no significant changes in the activation of neurons or astrocytes throughout assay performance, and immunocytochemical staining for MAP2 confirmed the complete absence of dendritic projections in the perfused culture chamber. Whilst subtle changes in either glutamate induced excitatory currents, or the recruitment of glutamatergic receptors at the presynaptic terminal can't be ruled out, there was no detectable change in neural network activity in the present study. The hypothesis of chemically induced retrograde activation of a naïve neural network was therefore rejected.

#### **4.6. Chapter 4 Summary**

This chapter describes the development of a microfluidic perfusion system with associated protocols for neuropharmacological characterisation of CNS acting compounds and simultaneous assessment of inducible synaptic transmission. An optimal flow rate of 4  $\mu\text{L min}^{-1}$  and fine temporal control of perfusate delivery was first achieved, followed by the generation of sigmoidal glutamate concentration response curves for both populations of perfused neurons and astrocytes. Cell-type dependent changes were observed in both perfused and naïve neural networks in response to different stimuli across multiple assay stages. Using the microfluidic perfusion system, the simultaneous neuropharmacological profiling of a CNS acting compound from a directly stimulated neural network, and the subsequent impact this has on synaptic communication can be realised for the first time. Details concerning the development of chemogenetic assays in adjunct with the microfluidic perfusion system presented here will be described in Chapter 5. In conclusion, I have shown through the integration of microfluidic perfusion and  $\text{Ca}^{2+}$  imaging techniques that the presented system is a suitable microfluidic platform amenable to early CNS drug discovery.

## **5. Assessing Network Activity via DREADD Activation**

### **5.1. Chapter Overview**

The work detailed in the previous chapter demonstrated a working semi-automated microfluidic perfusion system for the development of neuropharmacological assays in early CNS drug discovery. A relatively new method of inducing neural network activity change is via the activation of chemogenetic receptors, otherwise known as DREADDs (Designed Receptors Exclusively Activated by Designed Drugs). DREADDs are increasingly being used as a tool to manipulate neuronal function in order to investigate how specific brain regions contribute to normal behaviour as well as how neuronal dysfunction contributes to CNS disorders<sup>427,428</sup>. This can be achieved by designing plasmids encoding for chemogenetic protein with cell-specific promoters such as WFS1 for targeting excitatory neurons in the CA1 sub-region of the hippocampus<sup>429</sup>. Alternatively, glial cells may be targeted with plasmids encoding the promoter GFAP, which Adamsky et al (2018) used to investigate astrocyte dependent neuronal long-term potentiation *in vivo*<sup>430</sup>. To complement the development of the microfluidic perfusion system, chemogenetic assays would be achieved by the transfection of microfluidic primary hippocampal networks with a modified human M3 (hM3) muscarinic receptor<sup>431</sup> co-expressed with mCherry (hM3Dq-mCherry) that is exclusively activated by the application of the otherwise inert clozapine N-oxide (CNO)<sup>432,433</sup>.

With the increasing prevalence of CNS related disorders, there is an increasing need to develop new research tools to facilitate the investigation of how neuronal function and dysfunction is associated with CNS diseases. Recent emphasis on neuroscientific tool development over the last decade has included gene-targeting, circuitry manipulation, and microfluidic systems<sup>324,432,434</sup>. The current microfluidic perfusion system permits multiple drug applications in a single experiment for manipulating neural network activity in both perfused and naïve networks. Global stimulation of the network occurs as a result of perfusion however, it is difficult to determine which perfused cells are directly responsible for exerting influence over naïve network activity. This chapter describes the early investigation of incorporating DREADD technology into standard Ca<sup>2+</sup> imaging and microfluidic perfusion assays to enable and visualise the exclusive stimulation of a subset of neurons within a network and the subsequent synaptic communication across the surrounding network.

## 5.2. Introduction and Chapter Objectives

The superfamily of G-proteins (GPCRs) are associated with critical signalling pathways in homeostatic function, neural network communication and indeed, a wide range of neuropathologies. In the context of Parkinson's disease for example, studies suggest that allosteric activation of mGluR4 receptors can significantly reduce inflammatory markers, improve motor function and halt the loss of dopaminergic neurons *in vivo*<sup>435,436</sup>. As such, GPCRs are an important therapeutic target for neuropharmacological research and considerable work has been undertaken to assess their function, including but not limited to standard transgenic and knockout models<sup>437,438</sup> or pharmacological trials<sup>439,440</sup>. There are disadvantages associated with these approaches however, the most common include the lack of successful targeted gene expression, and minimal translational relevance<sup>322,441</sup>. Pharmacological assay results obtained using neural networks, such as mixed hippocampal preparations composed of multiple neuronal and glia cell types, can be difficult to interpret. This is typically due to non-specific cellular activation by a particular ligand (such as glutamate), and the inherent cross signalling that may occur between pyramidal, interneuronal and glial cell populations. Tools such as optogenetics and chemogenetics however, provide excellent control over neural network activity by the precise activation or inhibition of specific cells within a population, and thus the observed changes in network activity are easier to elucidate.

The use of optogenetics and chemogenetics involves the introduction and manipulation of foreign receptor function by the stimulation of light at defined frequencies or by the application of otherwise inert ligands, respectively. Optogenetics has been used to reverse Parkinson like symptoms<sup>442</sup> and memory loss associated with Alzheimer's disease<sup>443</sup> and has been demonstrated to be compatible with Ca<sup>2+</sup> imaging and microfluidic platforms<sup>291</sup>. This technique requires specialised equipment however for stimulation and recording with temporal precision. An alternative approach to manipulating network activity is through the use of chemogenetics, which have been used to assess the spread of tau pathology<sup>444</sup>, the manipulation of LTP<sup>445</sup> and investigating signalling pathways in Parkinson's disease<sup>428</sup>. Whilst chemogenetic *in vivo* studies are often limited by poor temporal control of the otherwise inert ligands reaching the intended target following treatment, this becomes less of an issue during *in vitro* studies where the user has greater control over drug applications.

To my knowledge, only one study, by Weir et al (2017) has combined chemogenetic techniques with a microfluidic format <sup>446</sup>, using an engineered glutamate gated calcium channel GluCl v2.0 that activates in response to low concentrations of ivermectin to silence action potential generation in DRG neurons. Importantly, there does not appear to be published studies in the literature combining microfluidic and chemogenetic techniques with perfusion integration which is unusual given the immediate advantage one would have over experimental control of chemogenetic activation and network activity. This approach therefore represents a relatively unexplored avenue of research for exploring signalling pathways and functional communication between environmentally isolated but functionally connected neural networks.

Multiple DREADDs exist for manipulating neuronal activity, expressed in the form of G-coupled receptors (Gq, Gi & Gs) whereupon activation by ligand binding results in changes to downstream intracellular signalling. Gi-coupled DREADDs, such as hM4Di for example, hyperpolarise neurons by activating G protein coupled inwardly-rectifying potassium channels and have been shown to inhibit neurotransmitter release to effectively silence synaptic transmissions <sup>431,447,448</sup>. In contrast, the Gq-coupled DREADD, hM3D3q, results in IP<sub>3</sub> signalling via phospholipase-C (PLC) activation and the subsequent Ca<sub>i</sub><sup>2+</sup> mobilisation from the endoplasmic reticulum leads to neuronal excitability. Through this mechanism, hM3Dq has been used to demonstrate the relationship between gliotransmission and NMDA associated LTP <sup>430</sup>, induction of behavioural changes in hM3Dq transgenic mice via CA1 activation <sup>449</sup>, and mapping global serotonergic transmission <sup>450</sup>. As such, increases in fluorescence within transfected cells upon CNO application can be directly correlated with hM3Dq activation, and changes in neural network activity are consequently brought about by Ca<sub>i</sub><sup>2+</sup> induced presynaptic neurotransmitter release.

Several methods are employed to introduce DREADDs into neural networks, with adeno-associated virus (AAV) approaches the most common practice, especially when used in *in vivo* research. An alternative and simpler approach for *in vitro* research is transfection by liposomal delivery, which does not require specialist training, strict biosafety handling procedures, or the significant amount of time or costs associated with generating AAV plasmids.

This chapter details the early investigation of chemogenetics in primary hippocampal cultures using the hM3Dq DREADD to determine its applicability in functional communication assays and consequently, its potential as a novel neuroscience research tool following further development. This requires successful transfection of neural networks with the DREADD of interest and assumes that the expressed DREADD protein is functional. Then, changes in neural network activity are to be assessed to determine signal propagation in neural networks following activation of the transfected cells.

First, preliminary assessments using a standard transfection protocol will be used for hippocampal networks grown in 4-well culture plates. Neural networks are traditionally extremely difficult to transfect, as neurons are post-mitotic and neural membranes are tightly regulated, therefore one would expect low transfection efficiencies through liposomal gene delivery. Additionally, this method of transfection is associated with cytotoxicity which may impact the integrity of sensitive neural networks. As such, epifluorescent images will be assessed to determine the transfection efficiency, whilst live/dead assays will be performed to determine the impact of transfection on network health. Simultaneous to this, basic  $\text{Ca}^{2+}$  imaging assays will be performed to validate the functionality of the hM3Dq DREADD.

Following initial experimentation, the transfection protocol will be optimised for microfluidic hippocampal cultures. Finally, changes in the activity of local and adjacent neural networks will be determined following perfusion integration and stimulation of transfected cells via CNO perfusates.

### 5.3. Preliminary Assessment of DREADD Transfected Primary Hippocampal Networks

Transfection of primary hippocampal networks is traditionally difficult to achieve due to the toxicity associated with liposomal membrane disruption, and poor neuronal transfection efficiency, therefore there is no guarantee of successful expression with the gene of interest. Microfluidic assessments confer additional degrees of complexity to experimental design, therefore standard transfection protocols were performed using primary hippocampal networks cultured in 4-well assay plates as proof of principle. This setup permits two wells to serve as controls against two transfected wells, whereby transfected cells are identified prior to the performance of live/dead imaging and  $\text{Ca}^{2+}$  imaging assays.

#### 5.3.1. Assessing Impact of Transfection on Neural Network Viability in 4-well Assay Plates

To assess the impact of transfection on neural network health, live/dead assays were performed on transfected neural networks, with non-transfected networks and those transfected with plasmids in the absence of hM3Dq serving as controls (Figure 5.1). The impact of transfection on specific neuronal or astrocyte bodies was not considered due to the impracticality of fixing and staining for marker proteins, whilst ensuring the integrity of bound Hoechst & PI following fixation, light exposure and multiple washing steps. Additionally, images of transfected wells were taken in the absence of mCherry expressing cells due to the conflicting fluorescent channel of PI.

Non-transfected wells, serving as the primary negative control, revealed an  $89.9 \pm 3.4\%$  viable population within 4-well assay plates ( $n = 10$  wells, 4 cultures). The neural networks transfected with a plasmid for mCherry, serving as a secondary negative control, demonstrated a non-significant reduction in the viable population relative to non-transfected networks, with this being  $83.7 \pm 2.8\%$  ( $P > 0.05$ ) living cells of the total cell population ( $n = 4$  wells, 4 cultures). The viability of networks transfected with plasmid for mCherry-hM3Dq revealed a non-significant reduction relative to non-transfected networks with  $86.4 \pm 2.9\%$  ( $P > 0.05$ ) living cells of the total cell population ( $n = 6$  wells, 4 cultures). These data indicate that under these conditions, transfection of primary hippocampal cultures in 4-well assay plates is not detrimental to their viability. Following live/dead imaging,  $\text{Ca}^{2+}$  imaging was immediately performed in the adjacent wells of the 4-well assay plate.



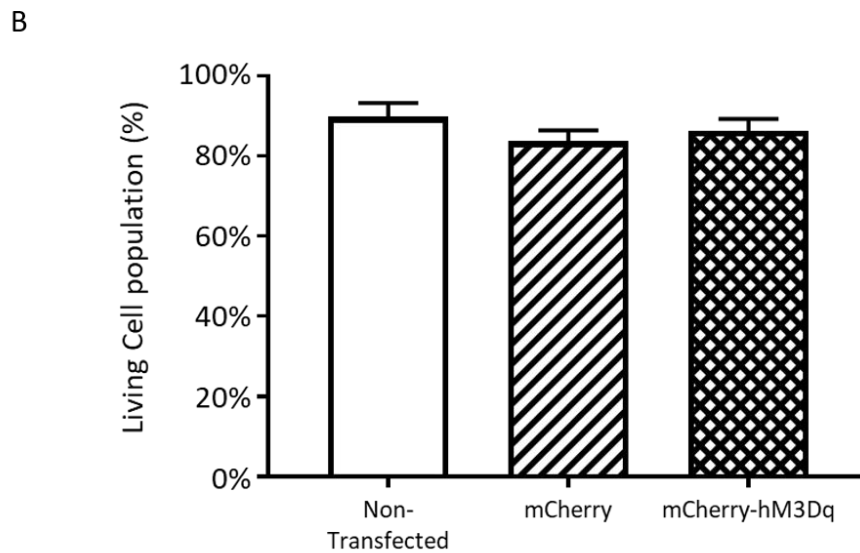
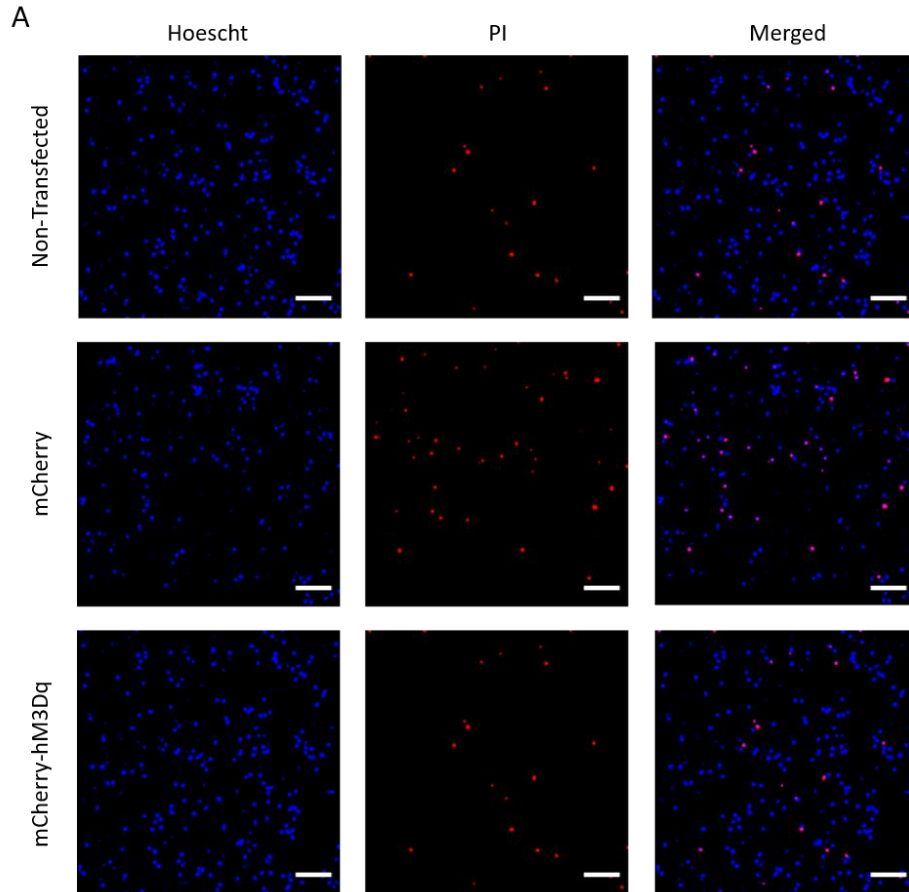


**Figure 5.1: hM3Dq Transfection does not Impact Neural Network Viability in 4-Well Assay Plates.**

(A) Representative images depict the live/dead staining of neural networks that were either exposed or naïve to the liposomal transfection of plasmids for mCherry, or mCherry-hM3Dq. (B) Analysis indicates no significant reductions in neural network viability following the transfection. Scale bars = 100  $\mu$ m.; Data was gathered from 10, 4-well assay plates, from 4 different cultures.

### 5.3.2. Direct Application of CNO Activates Chemogenetic Transfected Neural Networks

As there were no significant differences in network viability with respect to controls following transfection, the functional activity and communication of cells expressing mCherry-hM3Dq was first assessed to determine the functionality of the transfected hMD3q protein (Figure 5.2), before determining the impact that chemogenetic activation has on local neural network activity (Figures 5.3 & Figure 5.4). The transfection efficiency was typically poor for either mCherry (1 µg/mL), or mCherry-hM3Dq, displaying transfection efficiencies of  $0.15 \pm 0.02 \%$  and  $0.09 \pm 0.02 \%$  ( $P < 0.05$ , mCherry vs mCherry-hM3Dq) respectively (Supplementary Figure 4).

The activity of the hM3Dq receptor was determined by assessing the peak fluorescent magnitude of transfected cells in response to CNO (10 µM) application, with responses normalised to basal fluorescence (Figure 5.2). An observation made was that neurons transfected with mCherry-hMD3q did not recover from CNO applications and thus failed to respond to KCl applications. This contrasted with transfected astrocytes, which displayed stereotypical responses to KCl application after CNO stimulation. The peak fluorescent magnitude of transfected cells stimulated with CNO applications was then quantified, using mCherry transfected cells as controls. The response of mCherry transfected neurons during vehicle application was  $0.99 \pm 0.02$  NFU ( $n = 14$ ; 3 cultures), which non-significantly increased to  $1.00 \pm 0.02$  NFU ( $P > 0.05$ ) immediately following CNO application. In neurons transfected with mCherry-hMD3q, the peak magnitude response during vehicle application was  $1.02 \pm 0.02$  NFU ( $n = 18$ ; 3 cultures), which significantly increased to  $1.77 \pm 0.02$  NFU ( $P < 0.001$ ) in response to CNO. Meanwhile, mCherry transfected astrocytes displayed  $1.01 \pm 0.01$  NFU ( $n = 6$ ) after vehicle application, which did not change in response to CNO ( $1.01 \pm 0.02$  NFU;  $P > 0.05$ ). mCherry-hMD3q transfected astrocytes initially displayed  $0.99 \pm 0.02$  NFU ( $n = 6$ ) which significantly increased to  $1.48 \pm 0.17$  NFU ( $P < 0.01$ ). These data therefore validate the functional activation of the DREADD receptor hMD3q in transfected sub-populations of both neurons and astrocytes, thus presenting a possible alternative for stimulating neural networks.

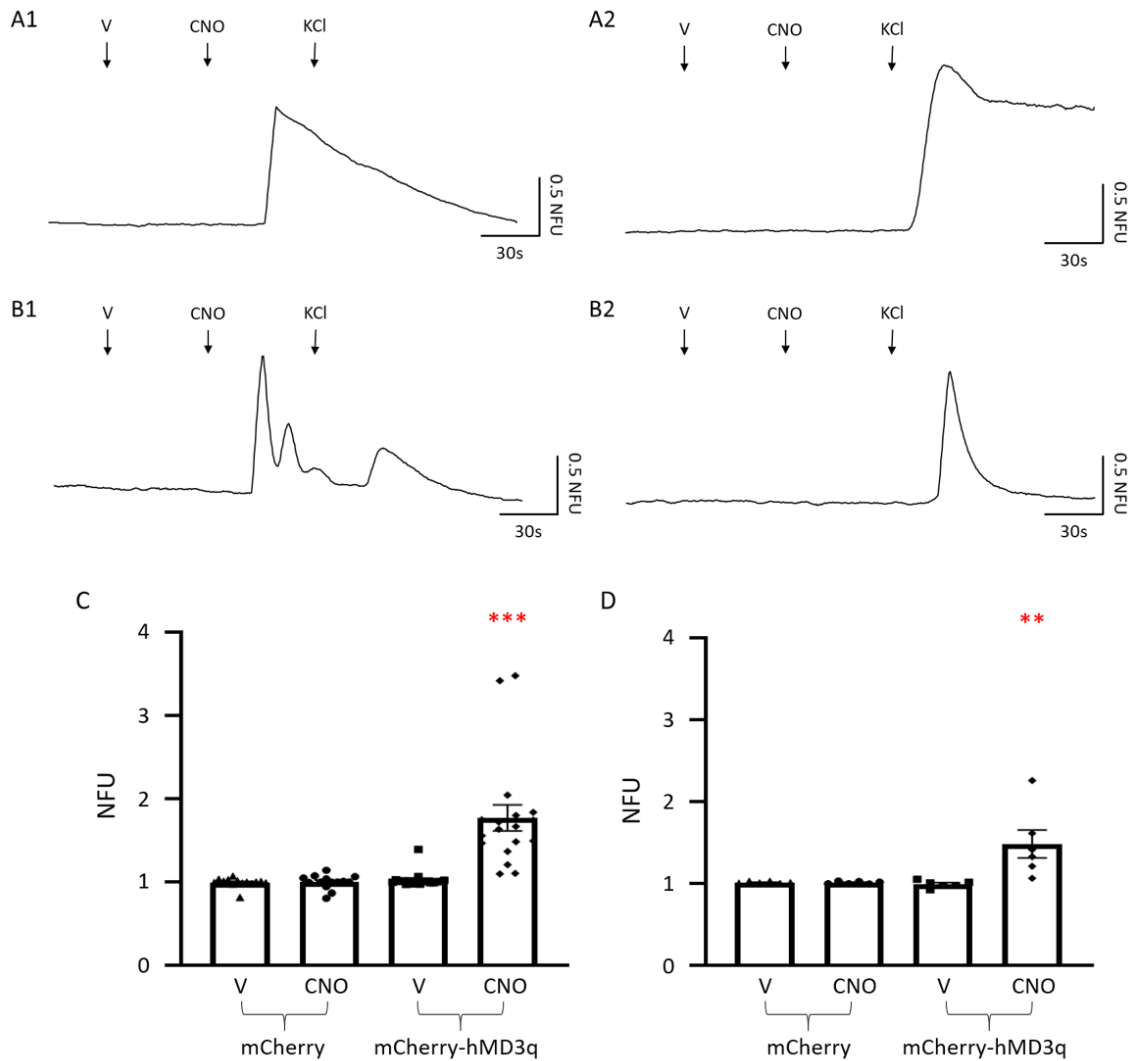


**Figure 5.2: CNO Application Exclusively Activates hM3Dq Transfected Cells.**

(A, B) Representative traces of neurons (A) and astrocytes (B) transfected with mCherry-hM3Dq (A1, B1) and mCherry (A2, B2) in response to vehicle (V), CNO (10 μM final concentration) and KCl (25 mM final concentration). (C, D) Peak fluorescent magnitudes of neurons (A) and astrocytes (B) reveal non-significant increases following CNO application, relative to vehicle response, when transfected with mCherry. However, neurons and astrocytes transfected with mCherry-hM3Dq respond to CNO application with significant increases in fluorescence, relative to vehicle response. Data from mCherry transfected networks were pooled from 4, 4-well assay plates (n = 14 neurons, 6 astrocytes; 4 cultures), meanwhile data generated from mCherry-hM3Dq transfected networks were pooled from 5, 4-well assay plates (n = 18 neurons, 6 astrocytes; 4 cultures). Paired t-test: \*\* denotes  $P < 0.01$  vs V; \*\*\* denotes  $P < 0.001$  vs V.

From the same experiments described above, it was possible to assess changes in the activity of the local neural network as a direct response to chemogenetic activation. In non-transfected wells, neurons displayed a basal activity of  $0.07 \pm 0.01$  ENM ( $n = 949$ , 8x 4-well assay plates, 4 cultures; Figure 5.3), which significantly increased to  $0.54 \pm 0.03$  ENM ( $P < 0.001$ ) during vehicle application, and remained elevated at  $0.53 \pm 0.03$  ENM following CNO application ( $10 \mu\text{M}$ ;  $P < 0.001$  vs baseline). Basal activity of astrocytes on the other-hand was notably absent ( $0$  EAM;  $n = 207$ , 8x 4-well assay plates, 4 cultures; Figure 5.4), non-significantly increasing to  $0.03 \pm 0.01$  EAM, with a slight significant increase in activity observed upon application with CNO ( $10 \mu\text{M}$ ;  $0.06 \pm 0.02$  EAM;  $P < 0.05$  vs baseline). Within mCherry transfected wells, neurons displayed a low basal activity  $0.04 \pm 0.02$  ENM ( $n = 307$ , 5x 4-well assay plates, 4 cultures) which significantly increased to  $0.19 \pm 0.03$  ENM ( $P < 0.001$ ) upon vehicle application. The local neuronal network activity displayed a non-significant decrease in activity at  $0.12 \pm 0.02$  ENM ( $P > 0.05$  vs vehicle) following CNO application ( $10 \mu\text{M}$ ) however, activity was still considered significantly greater than the basal activity ( $P < 0.05$ ). Astrocytes similarly displayed a low basal activity of  $0.03 \pm 0.03$  EAM ( $n = 73$ , 5x 4-well assay plates, 4 cultures) which non-significantly increased to  $0.07 \pm 0.03$  EAM ( $P < 0.05$  vs baseline) during vehicle application, and non-significantly increased again to  $0.11 \pm 0.04$  EAM ( $P < 0.05$  vs baseline) upon the application of CNO ( $10 \mu\text{M}$ ). Within mCherry-hM3Dq transfected wells, neurons reported a basal activity of  $0.32 \pm 0.05$  ENM ( $n = 305$ , 5x 4-well assay plates, 4 cultures) which non-significantly increased to  $0.35 \pm 0.04$  ENM during vehicle application. Neuronal activity then increased significantly to  $0.60 \pm 0.05$  ENM ( $P < 0.001$  vs baseline & vehicle) following application with CNO ( $10 \mu\text{M}$ ). The astrocyte population meanwhile displayed a basal activity of  $0.10 \pm 0.3$  EAM ( $n = 255$ , 5x 4-well assay plates, 4 cultures) which non-significantly increased to  $0.18 \pm 0.03$  EAM ( $P < 0.05$ ) during vehicle application. Upon stimulation with the application of CNO ( $10 \mu\text{M}$  final concentration), astrocyte activity significantly increased to  $0.37 \pm 0.05$  EAM ( $P < 0.001$  vs baseline & vehicle).

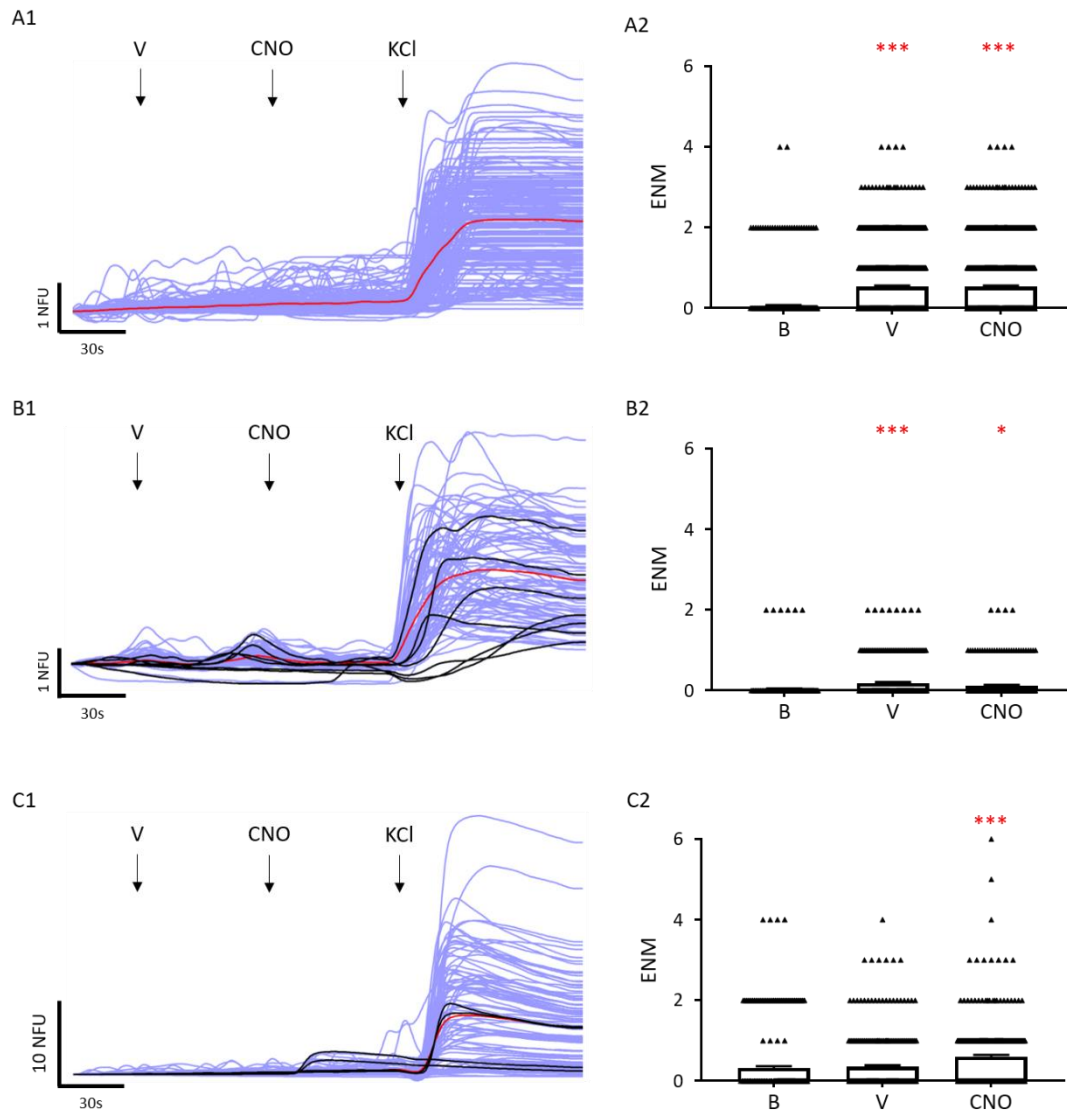


**Figure 5.3: CNO Application Activates Local Neurons in mCherry-hMD3q Transfected Neural Networks.** (A1, B1, C1) Representative traces of neuronal activity for non-transfected neurons (purple), their averaged response (red), and transfected cells (black) within non-transfected, mCherry, and mCherry-hM3Dq transfected cultures respectively. (A2) Vehicle (V) applications significantly increased non-transfected neuronal network activity which was sustained during CNO applications. (B2) Neuronal activity in mCherry transfected networks significantly increased following vehicle and CNO application. (C2) Neuronal activity in mCherry-hMD3q transfected networks significantly increased following CNO application. Non-transfected networks: n = 949 neurons, 4 cultures; mCherry & mCherry-hMD3q transfected networks: n = 307 & 305 neurons respectively; One way ANOVA with Tukey's post-hoc analysis: \*denotes  $P < 0.05$  and \*\*\*denotes  $P < 0.001$ , relative to baseline recordings.

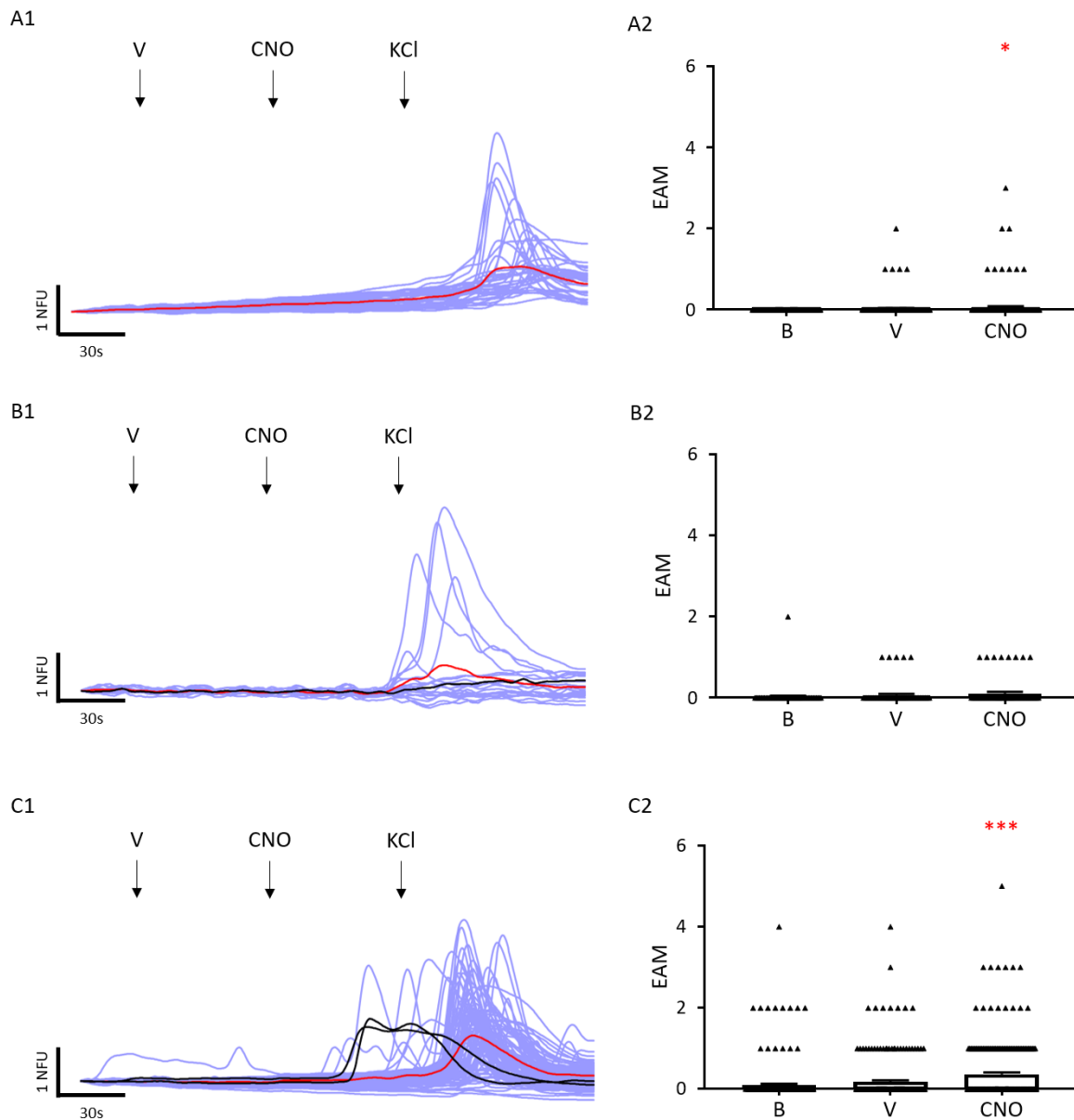


**Figure 5.4: CNO Application Activates Local Astrocytes in mCherry-hMD3q Transfected Neural Networks.** (A1, B1, C1) Representative traces of astrocytic activity for non-transfected astrocytes (purple), their averaged response (red), and transfected cells (black) within non-transfected, mCherry, and mCherry-hMD3q transfected cultures respectively. (A2) CNO application results in significant increases in non-transfected astrocyte activity. (B2) No significant increases in astrocytic activity were observed following vehicle and CNO applications. (C2) Significant increases in activity were observed upon application with CNO. Non-transfected networks: n = 207 astrocytes, 4 cultures; mCherry & mCherry-hMD3q transfected networks: n = 73 & 255 astrocytes respectively; One way ANOVA with Tukey's post-hoc analysis: \* denotes  $P < 0.05$  and \*\*\* denotes  $P < 0.001$ , relative to baseline recordings.

Cells that were transfected with mCherry-hM3Dq responded to the direct application of CNO, demonstrated by a large increase in fluorescent signal. The non-transfected neuronal populations within the control groups responded to vehicle application with increases in activity, thereby confounding findings that CNO applications activate the surrounding neural network. Subsequently, preliminary chemogenetic assessments were performed to investigate transfected neural networks in microfluidic devices.

### **5.3. Preliminary Development of Chemogenetic Microfluidic Perfusion Assays**

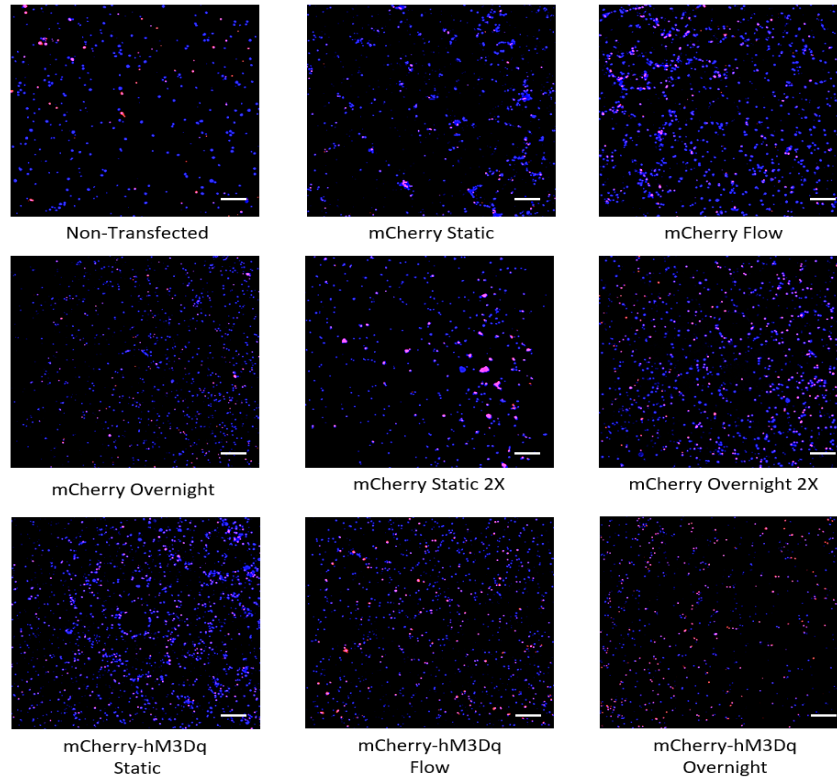
Transfection of microfluidic devices presented a unique challenge due to the significantly reduced volumes present for liposomal delivery and the low transfection efficiencies observed in 4-well culture plates. A range of transfection methods were employed to assess and improve upon previously observed transfection efficiencies and the subsequent impact on neural network viability. Despite attempts, transfection efficiency was lower than that observed in 4-well assay plates, with many devices displaying no transfected cells at all, typically presenting with no more than 4-6 transfected cells in a culture chamber at any given time, regardless of transfection preparation (~0.01 % maximum transfection efficiency). Specifically, devices transfected with mCherry at standard plasmid concentration (1  $\mu\text{g}/\text{mL}$ ) under static, flow induced, and overnight incubation conditions presented with transfection efficiencies of  $0.009 \pm 0.001 \%$ ,  $0.007 \pm 0.001 \%$  and  $0.006 \pm 0.001 \%$  (respectively; Supplementary Figure 4). Those incubated at double plasmid concentration (2  $\mu\text{g}/\text{mL}$ ) under static or overnight incubations had transfection efficiencies of  $0.005 \pm 0.002 \%$  and  $0.003 \pm 0 \%$  respectively. Meanwhile, devices that were transfected with mCherry-hM3Dq under static, flow induced, and overnight incubation conditions presented with transfection efficiencies of  $0.007 \pm 0.001 \%$ ,  $0.006 \pm 0.002 \%$  and  $0.003 \pm 0 \%$  (respectively). Assays were then performed by combining  $\text{Ca}^{2+}$  imaging, microfluidic perfusion and chemogenetic techniques to assess changes in transfected and naïve neural networks in response to CNO perfusates.

### 5.3.1. Assessing Impact of Transfection on Neural Network Viability in Microfluidic Devices

The sensitivity of microfluidic cultures to changes in their microenvironment was previously established in Chapter 4, where flow rates used for perfusion influenced network viability. The effect of transfection on sensitive microfluidic neural networks is yet to be established, and so an assay design for transfection was designed and performed, followed by live/dead imaging assays (Figure 5.5). Images of transfected devices were taken in the absence of mCherry expressing cells due to the conflicting fluorescent channel of PI. Non-transfected devices were used as negative controls and revealed an  $85.7 \pm 3.6\%$  mean viable population ( $n = 3$  devices, 2 cultures; Figure 5.5). Neural networks transfected with the mCherry for 3 hours under static conditions at standard ( $1 \mu\text{g}/\text{mL}$ ) plasmid concentration resulted in significant reductions in viability to  $74.6 \pm 1.5\%$  ( $n = 8$  devices, 4 cultures;  $P < 0.01$ ). Networks transfected with the mCherry plasmid overnight at standard ( $1 \mu\text{g}/\text{mL}$ ) plasmid concentration similarly reported significant reductions in viability relative to negative controls, at  $73.9 \pm 1.2\%$  ( $n = 4$  devices, 3 cultures;  $P < 0.01$ ). A preliminary assessment of transfection with the mCherry plasmid under static or overnight condition at  $2 \mu\text{g}/\text{mL}$  plasmid concentration revealed further reductions in viability relative to negative controls at  $56.6 \pm 2.3\%$  ( $n = 2$  devices, 2 cultures) and  $67.9 \pm 2.7\%$  ( $n = 2$  devices, 2 cultures) respectively. Transfections with the mCherry ( $1 \mu\text{g}/\text{mL}$ ) under an induced flow for 3 hours also reported significant reductions in viability relative to negative controls, with a mean viable population of  $66.5 \pm 1.3\%$  ( $n = 3$  devices, 2 cultures). Neural networks transfected with the mCherry-hM3Dq plasmid ( $1 \mu\text{g}/\text{mL}$ ) similarly reported significant reductions in viability, where those undergoing transfection for 3 hours under static conditions had a viable population of  $71 \pm 1\%$  ( $n = 5$  devices, 2 cultures;  $P < 0.001$ ). When transfected for 3 hours with an induced flow, the viable population was  $69.5 \pm 1.2\%$  ( $n = 3$  devices, 2 cultures;  $P < 0.001$ ) and when transfected overnight as a preliminary assessment, the viable population was  $67.2 \pm 2.2\%$  ( $n = 2$  devices, 1 culture). Despite significant reductions in viability,  $\text{Ca}^{2+}$  imaging with the microfluidic perfusion setup proceeded in the attempt to determine if chemogenetic activation has an impact on local neural networks, and indeed, if this is enough to induce functional communication between the perfused/naive neural networks. Subsequent mCherry-hM3Dq transfections were performed for 3 hours under static conditions as this displayed the least impact on network viability.



A



B

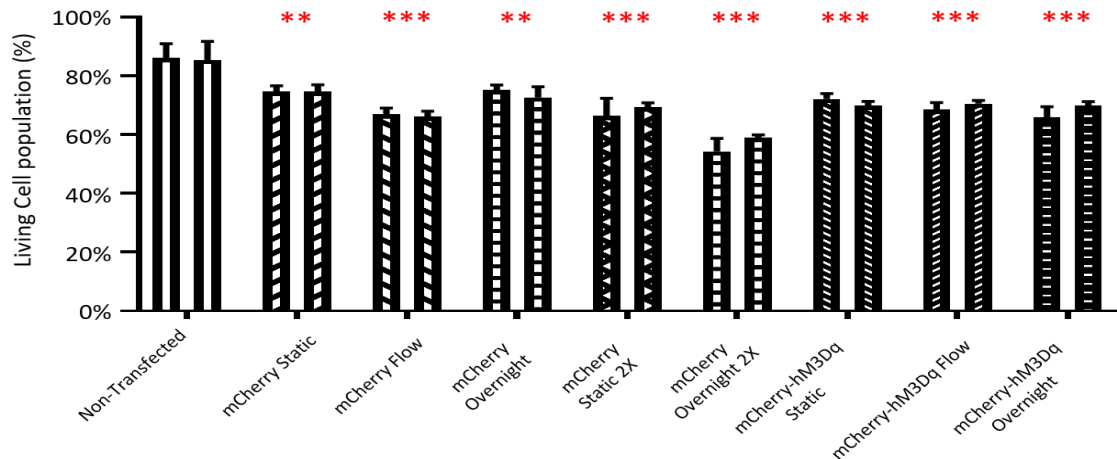


**Figure 5.5: Liposomal Transfection Reduces Viability of Microfluidic Neural Networks.**

(A) Representative images depict the live/dead staining of neural networks that were either exposed or naïve to the liposomal transfection of plasmids for mCherry, or mCherry-hM3Dq. (B) Bar charts for each conditions represent data gathered from left and right chambers (respectively) for each condition assessed. Analysis indicates significant reductions in neural network viability following all transfection conditions assessed with respect to non-transfected controls. There were no significant differences observed between neural networks within the left and right microfluidic culture chambers. Scale bars = 100  $\mu$ m; \* denotes  $P < 0.05$ , \*\* denotes  $P < 0.01$ , \*\*\* denotes  $P < 0.001$ , relative to non-transfected devices.

### 5.3.2. Changes in Local Network Activity following Direct CNO Perfusions

For chemogenetic assays to be developed as novel research tools for microfluidic neuroscientific research, it was imperative that induction of local network activity be demonstrated via chemogenetic activation of hMD3q transfected cells. Devices were connected to the perfusion setup, and transfected cells identified prior to microfluidic perfusion assays, whereupon the direct application of CNO (10  $\mu$ M) via perfusion resulted in an increase in fluorescent signal and changes in local network activity assessed (Figure 5.6). Due to the limited number of transfected cells, the field of view focussed on directly perfused chambers during the first set of assessments, followed by assessments observing activity with the adjacent chambers. Neurons within the directly perfused network had a basal activity of  $0.22 \pm 0.02$  ENM ( $n = 1208$ , 6 devices, 3 cultures; Figure 5.7), which then significantly increased to  $0.29 \pm 0.02$  ENM ( $P < 0.001$ ) following vehicle perfusions. Neuronal activity returned to basal levels at  $0.19 \pm 0.2$  ENM before significantly increasing to  $0.28 \pm 0.2$  ENM ( $P < 0.001$ ) during CNO (10  $\mu$ M) perfusions. Astrocytes displayed a basal activity of  $0.28 \pm 0.03$  EAM which significantly increased to  $0.4 \pm 0.03$  EAM ( $n = 635$ , 6 devices, 3 cultures) during vehicle perfusions. Basal activity did not return to previously observed levels, at  $0.32 \pm 0.03$  EAM, however did significantly increase to  $0.51 \pm 0.03$  EAM during CNO (10  $\mu$ M) perfusions. The impact that local neural network activity has on the naïve, non-perfused neural network during vehicle and CNO perfusion was then assessed to determine if functional communication is indeed dependent on chemogenetic activation.

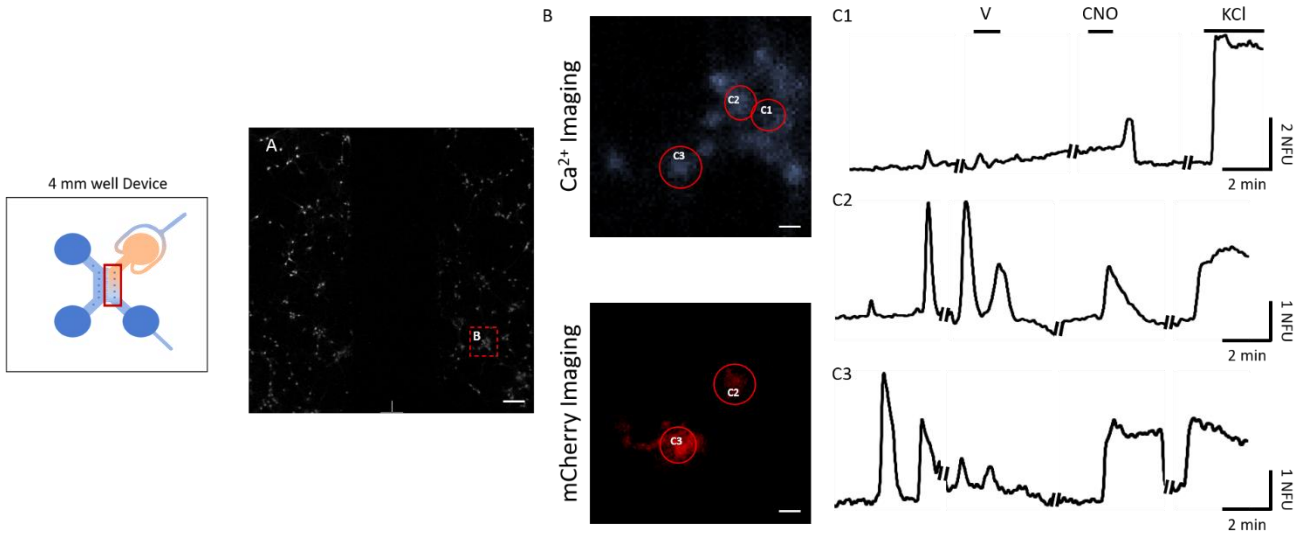


**Figure 5.6: hMD3q Transfected Cells Respond to Vehicle and CNO Perfusions.** (A-B) Representative images show, prior to microfluidic perfusion assays, cells transfected with the mCherry-hM3Dq identified within the neural network population stained with Fluo-4-AM. (C1-3) Representative fluorescent traces of the highlighted cells in (B) reveal an increase in fluorescent signal to CNO perfusions (10  $\mu$ M) in hM3Dq transfected cells (C2, C3), whilst the non-transfected cell (C1) displayed a delayed increase in fluorescence during CNO washout. Scale Bars: (A1) = 100  $\mu$ m, (A2) = 20  $\mu$ m.

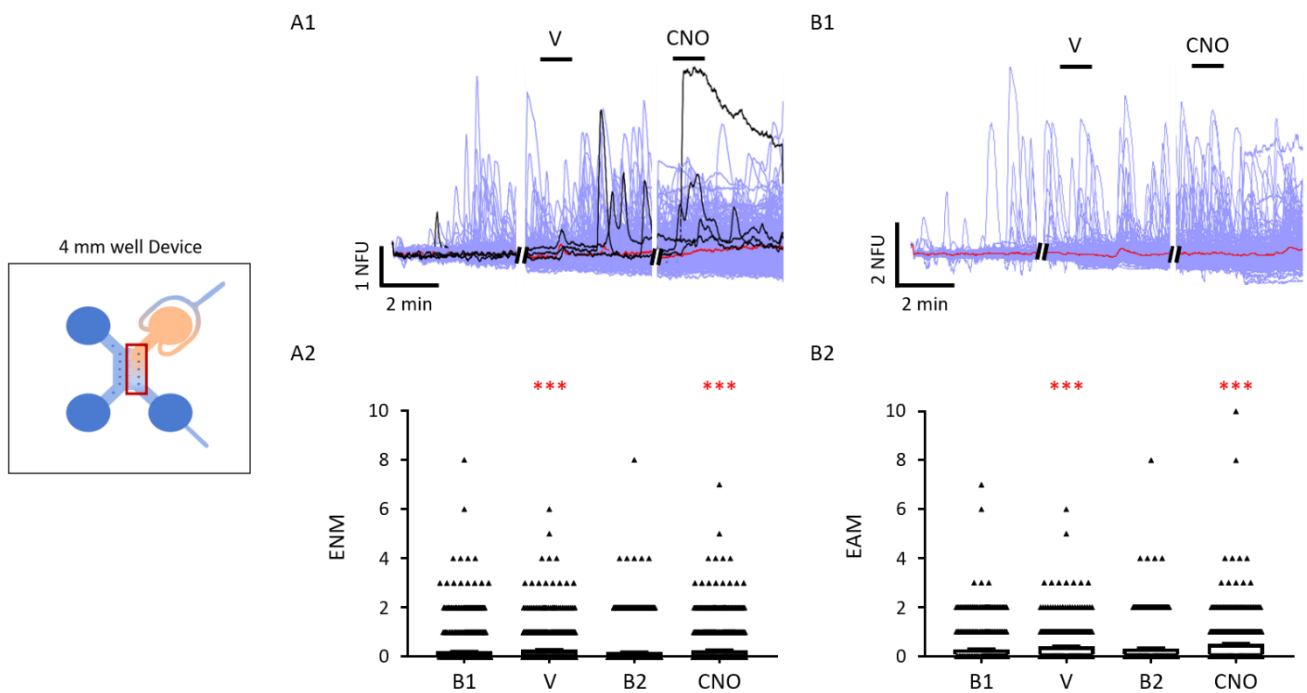


**Figure 5.7: Vehicle and CNO Perfusions Significantly Increase Activity of hMD3q Transfected Microfluidic Networks.** (A1 & B1) Representative traces of neurons and astrocytes (respectively) from a single device show fluorescent response to vehicle (V) and CNO perfusions (purple trace: individual cell response; black trace: transfected cell response; red trace: average response). (A2 & B2) Neuronal and astrocyte activity within the perfused chamber significantly increased in response to vehicle and CNO perfusions, with respect to the basal activity (B1 & B2). Data was pooled from 6 devices, 3 cultures (n = 1208 neurons, 635 astrocytes); Paired t-test:\*\*\* denotes P < 0.001 (V vs B1 & CNO vs B2).

### 5.3.3. Changes in Naïve Network Activity following Direct CNO Perfusions

Whilst activity within the perfused neural network significantly increased following both vehicle and CNO perfusions, it was unknown how this would translate as synaptic communication to the naïve neural network. Focussing on the naïve, non-perfused chamber, separate devices were setup for microfluidic perfusion and the same chemogenetic assay design performed. Neurons within the naïve network had a basal activity of  $0.23 \pm 0.03$  ENM ( $n = 645$ , 3 devices, 3 cultures; Figure 5.8), which then non-significantly decreased to  $0.22 \pm 0.02$  ENM ( $P > 0.05$ ) upon vehicle perfusion. Neuronal activity maintained basal levels of activity at  $0.23 \pm 0.3$  ENM before significantly increasing to  $0.29 \pm 0.3$  ENM ( $P < 0.05$ ) during CNO ( $10 \mu\text{M}$ ) perfusions. Astrocytes meanwhile displayed a basal activity of  $0.22 \pm 0.04$  EAM, which non-significantly increased to  $0.23 \pm 0.04$  EAM ( $n = 335$ , 3 devices, 3 cultures;  $P > 0.05$ ) during vehicle perfusions. Basal activity was then elevated above previously observed levels, at  $0.30 \pm 0.05$  EAM ( $P > 0.05$ ), and significantly increased to  $0.41 \pm 0.04$  EAM during CNO ( $10 \mu\text{M}$ ) perfusions. Immediately following recordings of the naïve network in response to CNO perfusions, the functionality of transfected cells in the perfused chamber were confirmed by fluorescent increase in response to KCl application ( $25 \text{ mM}$ ). Combining these data with that obtained from the perfused network, there is evidence to suggest that functional communication between perfused and naïve neural networks is dependent on the chemogenetic activation of transfected cells that induce local neural network activity.

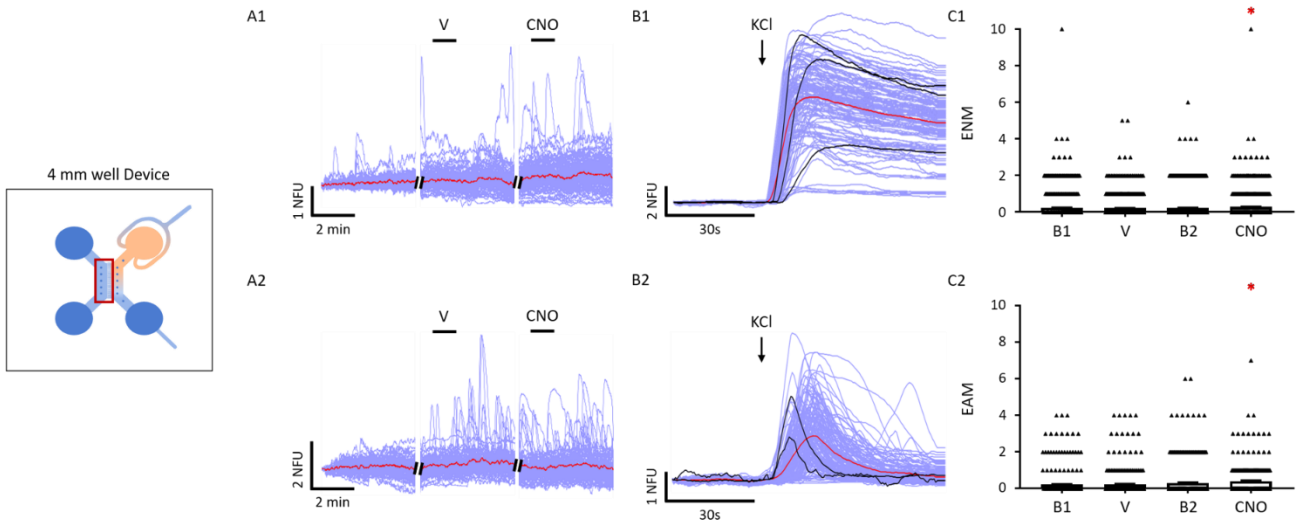


**Figure 5.8: CNO Perfusions Increase Naïve Neuronal Network Activity.**

(A1 & A2) Representative traces of naïve, non-perfused neurons and astrocytes respectively reveal increases in activity following vehicle and CNO perfusions (B1 & B2) Representative traces of directly perfused neurons and astrocytes (respectively) from a single device show individual fluorescent response to KCl application after the cessation of perfusion, illustrating functionally active non/transfected cells within the network (purple trace: individual cell response; black trace: transfected cell response; red trace: average response). (C1 & C2) Neuronal and astrocyte activity respectively within the naïve, non-perfused chamber significantly increased in response to CNO but not vehicle perfusions, with respect to the basal activity of the separate recordings (B1 & B2). Data was pooled from 3 devices, 3 cultures (n = 645 neurons, 335 astrocytes); Paired t-test: \* denotes  $P < 0.05$  (CNO vs B2).

## 5.4. Chapter 5 Discussion

In this chapter, I transfected primary hippocampal cultures with the chemogenetic DREADD hM3Dq in 4-well assay plates as a proof of principal and demonstrated negligible impact on network viability. Activation of hM3Dq transfected cells displayed fluorescent increases upon direct CNO application. Further work was performed as proof of principal via transfection of microfluidic hippocampal cultures to determine the future potential for chemogenetic assay development. In contrast to cultures grown on coverslips, transfection was determined to have a negative impact on microfluidic neural network viability but CNO induced increases in intracellular  $\text{Ca}^{2+}$  in hM3Dq transfected cells were still observed. The data obtained from assessing changes in network activity are relatively inconclusive and require further investigation.

### 5.4.1. Transfection Efficiencies Within 4-Well Assay Plates & Microfluidic Devices

Successful gene expression in cultured cells varies considerably when using lipofectamine as the method of gene delivery is typically influenced by reagents used, the plasmid size, the type of gene (DNA and RNA) and the cell type in question. Here, Lipofectamine® 3000 was used to transfect cells with either mCherry (pAAV-CMV-mCherry) or mCherry-hM3Dq (pAAV-CaMKIIa-hM3D) at plasmid concentrations of 1-2  $\mu\text{g}/\text{mL}$ . Transfection efficiency of 4-well assay plates at  $\sim 1\%$  is not entirely unheard of, as a few papers have detailed similar success when performing DNA transfection in neural networks or neuroblastoma cell lines<sup>451,452</sup>. This is opposed to RNA, which does not require penetration of a second membrane (nucleus) before protein translation<sup>453–455</sup>. Transfection efficiency in microfluidic devices was lower than that observed in 4-well assay plates by approximately 100-fold (2-3 transfected cells/chamber), and this lack of effective control over liposomal transfection is surprising given the level of experimental control microfluidics provides. The surface area to volume ratio in the microfluidic chamber is significantly greater than that of a well in an assay plate, with microfluidic inlet/outlet wells containing only a fraction of the total neural network. The mCherry-hM3Dq plasmid DNA-liposome complex (lipoplex) is a heavy ( $>2 \times 10^6$  Da) and large molecule in a viscous solution, therefore advective forces have a greater impact than diffusive forces on complex movement through the microfluidic device. As such, replacing conditioned media in the inlet/outlet wells with transfection solution is unlikely to expose the entire network and instead, the lipoplex will settle in the wells or adhere to the PDMS prior to degradation.

Flow rates generated by inducing a small pressure gradient across the culture chamber during the transfection process was not sufficient to increase the apparent transfection efficiency, and large flow rates of  $> 10 \mu\text{L}/\text{min}$  will significantly increase shear stress and negatively impact network viability, as demonstrated in Chapter 4 (Figure 4.2).

The means of entry by which the lipoplex enters the cell is primarily mediated by endocytosis<sup>456</sup>, which is responsible for mechanisms such as recycling of synaptic protein<sup>457,458</sup> and growth factor uptake from the local microenvironment<sup>459</sup>. Endocytosis is tightly regulated in post-mitotic neurons however, which could account for the low transfection efficiencies observed. To improve upon the transfection efficiency of the lipoplex, the addition of  $\text{Ca}^{2+}$  to the lipid reaction has been used previously to significantly increase the efficiency of liposomal gene delivery up to 20% in cell lines by enhancing the formation of lipoplexes and increasing endocytosis<sup>460,461</sup>. However, this approach could prove detrimental in sensitive neuronal cultures as subtle increases in exogenous  $\text{Ca}^{2+}$  would likely encourage network hyperexcitability<sup>462,463</sup>, and further disruption to the membrane by increased endocytosis could increase the cytotoxic effect of lipofectamine. Alternative approaches to improving transfection efficiency include carrying out transfections at an earlier time point between 1-3 DIV which can improve transfection efficiency up to 30%<sup>464,465</sup>. Additionally, magnetofection can be used to deliver plasmids in the presence of PEG conjugated nanoparticles under an external magnetic field with modest transfection efficiency (~7%) with minimal neurotoxicity<sup>466</sup>. Given the distinctly poor transfection efficiency within the microfluidic device, future development should strongly consider the use of viral transfection with the use of either adeno associated, or lentiviral vector which consistently display superior transduction efficiencies in neural networks<sup>446,467</sup>.

#### 5.4.2. Impact of Transfection on Neural Network Viability

The use of liposomal gene delivery comes with the risk of cytotoxicity, and is mediated by the lipoplex disrupting the cell membrane and activation of apoptotic signalling pathways<sup>468</sup>. Indeed, significant reductions in neural network viability have been previously reported during liposomal transfection by up to 27% with respect to controls<sup>469,470</sup>. The contrast in neural network viability following transfection between 4-well assay plate and microfluidic devices was striking, where the former showed negligible reductions in viability with respect to controls, whilst significant reductions of up to 22 % were observed in the former. Whilst the concentration of plasmid DNA used during transfections was  $1 \mu\text{g}/\text{mL}$  (unless otherwise stated), there is a significantly greater volume of media



immediately accessible to neural networks within 4-well assay plates which may have provided a buffer to the cytotoxic effects of liposomal gene delivery. The microfluidics cultures however are at a disadvantage in this respect due to reduced surface areas within the culture chamber and are only immediately exposed to a few  $\mu\text{L}$  of media at any given time. The ability to recover from acute toxic insults for example is likely exacerbated in this instance by the density of cells confined to the chambers and a delayed diffusive transport of toxic proteins and chemical neurotransmitters leaving the culture chamber and into the bulk volume within the inlet/outlet wells <sup>471</sup>. The further reductions observed in transfected microfluidic networks using 2  $\mu\text{g}/\text{mL}$  plasmid DNA is consistent with previous research demonstrating the dose-dependent relationship between plasmid DNA concentration and increasing cytotoxicity<sup>468</sup>.

Whilst modifications could be made to the design of the microfluidic culture to negate the negative impact on network viability, the impact on microflows to drug application and perfusate delivery are likely to be great and render this approach inadvisable for a modest gain. Instead, future approaches should instead consider assessing a range of variables in the transfection protocol, including but not limited to, the maturity of the network at time of transfection, alternating  $\text{Ca}^{2+}$  concentration (in the  $\mu\text{M}$  range) during transfections, and assessing a range of plasmid DNA concentrations.

### 5.4.3 Assessing CNO Induced Changes in Neural Network Activity

Given the poor transfection efficiency, it was incredibly rare to observe a transfected neuron's axonal projections traverse the microfluidic array into the naïve neural network, and so the simultaneous recording of both neural networks was not feasible. Instead, changes in local neural network activity following CNO perfusions onto transfected neural networks would be observed, with the subsequent activation of the naïve neural network to be recorded separately. A combined approach of using 4-well assay plates and microfluidic devices to assess these local network changes was performed, with the results and limitations discussed in brief.

#### 5.4.3.1 Inconclusive Evidence of CNO induced Activation of Local Neural Networks in 4-well Assay Plates

The functionality of mCherry-hM3Dq transfected neurons and astrocytes within neural networks was demonstrated successfully by clear increases in fluorescence upon exposure to CNO, in line with observations from previous studies<sup>430,472,473</sup>. Meanwhile, this was not observed in non-transfected or mCherry transfected cells. However, there is conflicting evidence as to whether hM3Dq receptor activation is responsible for local network change.

Significant increases in network activity were observed in both non-transfected and transfected networks, in response to vehicle application. In contrast, mCherry-hM3Dq transfected networks were not stimulated by vehicle application however the activity of both neurons and astrocytes were significantly elevated upon activation via CNO applications. It is possible that in the 4-well assay format that *in situ* applications pose a risk of mechanically stimulating neural networks due to the large volumes used.

It is difficult to compare the local network activity of the different conditions assessed due to the apparent mechanical stimulation, and the primary limitation is likely because of the 4-well assay plate format used. Whilst an ideal assay design would have multiple recordings to demonstrate local network change to vehicle and CNO applications over an extended period, there is an immediate time-constraint for assay performance of all four networks once the plate is removed from the incubator. In those wells stained with Fluo-4-AM, at least one of the networks will have been left under static conditions for at least 70 minutes before recordings begin, and so vehicle and CNO applications must be performed within the same brief recording window.

#### 5.4.3.2 CNO Induced Neural Networks Activation in Microfluidic Devices

Assessment of chemogenetic Ca<sup>2+</sup> imaging assays in the microfluidic format were incomplete due to the absence of appropriate transfection controls such as non-transfected or mCherry transfected device and so observations made cannot be resolved with definitive conclusions. Nonetheless, my preliminary findings show that cells transfected with the mCherry hM3Dq within the perfused chamber did respond to CNO with sustained increases in fluorescence, which was not observed in non-transfected cells. In contrast to Ca<sup>2+</sup> imaging of hM3Dq transfected networks in 4-well assay plates, and indeed repeated vehicle perfusion assays on non-transfected microfluidic cultures previously performed (Chapter 4), transfected microfluidic cultures were sensitive to mechanical

stimulation by vehicle application. In the subsequent recording, both populations showed significant increases in activity, relative to baseline readings, following CNO perfusion. There is little published work in the literature for a fair comparison against this data set, as chemogenetic assays involving hM3Dq (and other DREADDs) are almost exclusively used for *in vivo* research to assess behavioural changes<sup>433,450,474,475</sup>. However, given the lack of additional experimental control here (multiple vehicle perfusions) and the gradual sensitisation of neural networks to mechanical stimulation (potentially more so when transfected), it is possible that the significant increase in network activity surrounding transfected cells is independent of chemogenetic activation.

When considering the assay design used for either *in vivo* or *in vitro* assessments, CNO induced changes to activity are commonly compared against either the vehicle control instead of a baseline<sup>428,474,476</sup>, or the vehicle control is absent altogether<sup>431,445,474,476,477</sup>. I would propose that the significant reduction in network viability following transfection results in an increased sensitivity to mechanical stimulation, with previously published work demonstrating the sensitivity of hippocampal networks to mechanically induced stress<sup>284,380,478–480</sup>.

Previous datasets strongly indicate that changes in the naïve network are correlated with changes in the activity of the directly stimulated network<sup>275,276,284</sup>, as demonstrated in Chapter 3 and Chapter 4. Given the significant increases in neuronal and astrocytic activity in the directly perfused chamber during vehicle perfusate delivery, it is surprising to note there were no such increases in the naïve neural network activity. Instead, it was only upon the perfusion of CNO where significant increases in activity were observed. Additionally, the second perfusion of vehicle during control experiments in Chapter 4 did not elicit significant increases in naïve neural network activity either. There are two reasons considered that may explain the response of the naïve network to the activated local network during CNO perfusions but not vehicle perfusions. The first and ideal scenario would suggest naïve network activation arose via CNO-hM3Dq induced activation, as indicated by large increases in transfected somal fluorescence during CNO but not vehicle perfusions. This scenario requires a multi-stage process of activation of the connected microfluidic networks, where the transfected cell is first stimulated, followed by local synaptically connected neurons that in turn stimulate the naïve network in the adjacent chamber. In turn, the frequency of synaptic activity transmitted from the activated, perfused network may have achieved levels of detection greater than that arising from mechanical stimulation during vehicle perfusion. The increases in naïve network activity following CNO perfusions are unlikely to be a direct effect of transfected neuron activation as transfection

efficiencies were so low that it was rare to observe transfected axonal projections traversing from the perfused chamber through the microchannel array and into the naïve chamber. Alternatively, whilst it is difficult to effectively compare the datasets of non/transfected networks without the appropriate assessments, previous experiments demonstrated that naïve networks become stimulated following multiple vehicle perfusions (Chapter 4). Given the viability of the microfluidic networks is compromised following transfection and neural networks become sensitised to vehicle perfusions, the significant increase in naïve network activity could indeed be a product of increasing sensitisation to a mechanical stimulus, resulting in the increased synaptic activity.

## **5.5. Chapter 5 Summary**

The objective of this chapter was to investigate the use of chemogenetics in primary hippocampal cultures and assess the feasibility of performing functional communication assays in a microfluidic format using the hM3Dq DREADD. To this end, I have successfully transfected primary hippocampal cultures with the chemogenetic hM3Dq receptor in both 4-well assay plates and microfluidic devices and demonstrated CNO induced activation of transfected cells, relative to non-transfected and non-chemogenetic mCherry controls. The limitations of liposomal gene delivery in primary hippocampal cultures have been highlighted to illustrate the poor transfection efficiency (< 1 %) and considerable reductions in microfluidic neural network viability. Ca<sup>2+</sup> imaging assays were performed to assess the changes in transfected local network activity which suggests transfected microfluidic are hypersensitive to mechanical stimulation induced by vehicle application. As such, increased network activity via CNO induced activation of transfected cells remains unclear. However, it was only following CNO perfusion that the naïve neural network demonstrated significant increases in activity, demonstrating the potential of chemogenetics to modulate not only local network activity, but functionally connected neural networks as well.

These preliminary assays lay the groundwork for future chemogenetic assays in microfluidic formats to develop a novel neuroscientific research tool to assess functional neural network communication. To improve upon the expression of hm3Dq or other DREADDs in primary hippocampal cultures, continued efforts using liposomal gene delivery should be abandoned. Instead, chemogenetic assay development should focus on taking advantage of viral gene delivery systems such as adeno-associated virus 2 (AAV2) vector, which is widely used for CNS applications because of the favourable transduction efficiency, long term transgene expression and minimal impact on viability <sup>481–483</sup>. With improved expression of DREADD protein, there is an increased likelihood that the changes in network activity become more apparent following CNO induced activation. Overall, there is promise that chemogenetic assays can be developed in microfluidic functional communication assays for use as a novel tool for neuroscientific research.

## **6. Thesis Discussion**

### **6.1. Chapter Overview**

The work presented in this thesis has explored the development of microfluidic assays as novel research tools for the purpose of performing *in vitro* neuroscientific research. A variety of microfluidic and neuroscientific approaches were utilised to assess communication between two environmentally isolated, but synaptically connected neural networks. Limitations were identified within the literature on current microfluidic assays used to observe synaptic activity, such as the temporal constraints of  $\text{Ca}^{2+}$  imaging, the lack of efficient drug application and the inability to stimulate sub-populations within neural networks. Significant challenges were encountered during VSDI experiments which led to this route of assay development being disbanded for the time being. Then, microfluidic perfusion was integrated into the assay setup to permit pharmacological characterisation of CNS acting compounds with simultaneous readouts of the synaptically connected neural network. Finally, preliminary work was performed using chemogenetic techniques which has provided results to suggest such an approach may be feasible for further manipulation of synaptically connected neural networks.

In this final chapter, I will summarise the major findings from each chapter whilst discussing their relevance in the field of neuroscience. Then, future studies will be considered, based on the work that has been demonstrated within this thesis.

## 6.2. Chapter 3 Outcomes

This chapter sought to explore the potential of VSDI assays as an alternative to  $\text{Ca}^{2+}$  imaging assays that could resolve synaptic activity between two functional neural networks, but with improved spatial resolutions in comparison to the gold standard whole cell patch clamp technique. Initially, standard  $\text{Ca}^{2+}$  imaging assays and immunocytochemical staining was performed to reveal synaptic communication between the environmentally isolated neural networks. Then a simple assay design was performed to demonstrate the inability of  $\text{Ca}^{2+}$  imaging to detect AP firing prior to, and during stimulation. A series of experiments were then performed to optimise the VSDI assay in standard *in vitro* neural network cultures.

The VSD D3AD was selected for its minimal cytotoxicity (owing to its amphiphilic structure), a greater SNR when compared to alternative VSDs which doesn't diminish overtime and demonstrates resistance to cell internalisation<sup>219,484</sup>. It was noted early during assay development however that significant reductions in spatial resolution were required to improve temporal resolutions, and later observed that maximal acquisition rates of  $\sim 1$  kHz could not detect AP firing. Considering the results obtained collectively, there were two noticeable limitations to using VSDs for monitoring neuronal activity with the same precision as the whole cell patch clamp technique. Firstly, there is a great emphasis on high temporal resolutions necessary for successfully observing AP firing using VSDs. Indeed, a vast number of studies that have performed VSDI assays both *in vitro* and *in vivo* have used a Neuro CCD-SMQ camera (Red Shirt Imaging)<sup>219,220,225,350,484</sup> which permits temporal resolutions up to 5 kHz at the cost of spatial resolution (80 x 80 pixel field) relative to standard  $\text{Ca}^{2+}$  imaging (1000 x 1000 pixels). Whilst these studies often recorded action potentials during VSDI assays with 1 kHz temporal resolutions, the use of an electrode to stimulate neurons grants a great deal of experimental control over the amplitude and train of stimuli. This makes it considerably easier to correlate fluorescent change in response to action potential generation, particularly so when temporal averaging is applied to reduce background noise and elevate the SNR. Even then, recordings would be limited to several cells, otherwise the techniques were used to monitor global changes in slice preparations. Considering the change in neuronal membrane potential during AP firing occurs within 5 ms<sup>485</sup>, a minimum of 2 kHz is likely required to successfully perform VSDI assays with modest background noise present in the absence of an electrical stimulus with fine temporal control. Secondly, substantial reductions in spatial resolution were required when using standard recording equipment, resulting in a significantly reduced number of cells that could be monitored

simultaneously. As the primary advantage of VSDIs is non-invasive recording of synaptic activity across multiple cells simultaneously, the sacrifice to spatial resolutions observed here diminished any advantage of using this approach over conventional electrophysiology techniques as only a single cell could be imaged at any given time. Thus, researchers will struggle to perform VSDI assays using standard imaging equipment and should consider non-conventional approaches to resolve synaptic activity in neural networks, such as custom made camera's, signal processing algorithms and averaged single spike trials to improve SNR <sup>486-488</sup>. Nonetheless, fully developed VSDI or GEVI assays, could provide excellent information on synaptic communication and importantly, the maladaptive changes that occur in pathological conditions, such as excitotoxicity as observed in Alzheimer's and how this impacts synaptic degradation. Incorporating this assay into microfluidic devices would provide the benefit of understanding these changes between functionally connected neural networks, which is currently impossible using standard *in vitro* techniques.

### 6.3. Chapter 4 Outcomes

The work presented in Chapter 4 builds upon the early development of microfluidic perfusion by Dr Graham Robertson, Dr Michele Zagnoni and Dr Trevor Bushell, and sought to expand on this by developing a series of pharmacological assays as proof of principal for early CNS drug discovery. This is considered to be a relatively unexplored avenue of neuroscientific research in the microfluidic setup, and therefore a unique opportunity to perform semi-automated functional communication assessments. Live/dead imaging assays were performed to assess perfusion induced shear stress on neural networks, and the microfluidic perfusion protocol validated experimentally. Then, pharmacological assessment of glutamate was performed using multiple experimental protocols.

The platform presented combines Ca<sup>2+</sup> imaging techniques with microfluidic perfusion by interfacing multiple syringe pumps with the inlet/outlet wells of a single chamber (of a dual chamber device). This allowed multiple drug applications confined to a single chamber to record neural network activity in response to direct stimulation, whilst simultaneously recording changes in the naïve, synaptically connected neural network. Whilst multi-phase pharmacological assays have been performed previously, these have often been limited manual applications *in situ* and poor wash on/wash off kinetics <sup>286,489</sup>, which is resolved here by the semi-automated control of the syringe pumps. There are two standard approaches for employing microfluidic perfusion, namely by pressure driven systems, or syringe pump systems. Pressure driven systems have a defined working pressure, and typically achieve a constant flow rate more rapidly (with greater stability) than syringe pump



driven systems because of the negligible compliance associated with tubing and syringe deformation. These systems are often more expensive however, can be difficult to employ and backflows may occur due to the change in pressure when switching between perfusates. Alternatively, syringe pump systems are easy to use, and the setup may be adapted by changing the diameter and size of syringes as required for assay performance. As the volumes required for routine microfluidic perfusion assays were minimal, small syringes could be used to achieve steady perfusions at small flow rates.

Neuropharmacological research is currently facing great challenges, with limited success of new CNS acting compounds in pre/clinical trials over the last two decades, resulting in pharmaceutical companies abandoning drug development altogether. The use of standard *in vitro* techniques for pharmacological characterisation is time consuming and limited to single network applications, therefore it is impossible to determine the subsequent effects on connected neural networks until *in vivo* studies are performed. Developing microfluidic systems that can screen hundreds of compounds rapidly and reveal changes in otherwise naïve neural networks would therefore be particularly advantageous to the field of neuropharmacology. Specifically, this could be used to address the complete lack of recent success in stroke therapy by identifying CNS acting agents that confer neuroprotection by blocking NMDA dependent excitotoxicity and subsequent neural network death. Whilst the current setup is designed for the perfusion of up to three compounds, the assays developed here using the microfluidic perfusion platform demonstrate the potential of this system for *in vitro* CNS drug discovery studies, with potential for further development.

#### **6.4. Chapter 5 Outcomes**

Chapter 5 explores the integration of chemogenetics into microfluidic assays, whilst combining  $\text{Ca}^{2+}$  imaging and microfluidic perfusion techniques established in Chapter 3 and Chapter 4 (respectively). The purpose of this chapter would be to create a novel method for stimulating a sub-population of transfected neural networks via Gq receptor signalling in response to the inert compound CNO. Preliminary assessments were performed in the 4-well assay plates to determine transfection efficiency, the impact of transfection on neural networks, the functionality of the hMD3q DREADD receptor and induced changes to the local neural network activity. These assessments were then repeated in the microfluidic setup and the findings disseminated.

A recurring theme during chemogenetic assay development was the incredibly low transfection efficiency obtained through liposomal gene delivery, and one alternative proposed to improve expression of hMD3q was through viral transduction. Viral gene delivery is regularly used for the expression of foreign proteins however the researcher has minimal control over viral spread into the surrounding brain tissue once introduced due to retrograde and anterograde viral trafficking between synaptically connected neurons<sup>490</sup>. Whilst this is less of an issue with optogenetic assays where a limited number of cells are stimulated, transfection of CNO may influence the activity of multiple networks, thus confounding results obtained. Additionally, transduction occasionally results in abnormal basal activity and sensitivity to mechanical stimulation<sup>491–493</sup>, which was observed in the chemogenetic assay development using transfection. Despite this sensitivity to mechanical stimulation, it was the activation of functional hMD3q receptors in transfected networks that resulted in significant increases in naïve network activity, suggestive of DREADD dependent synaptic communication. Meanwhile, the sensitivity of non-transfected neural networks to mechanical stimuli in 4-well assay plates is likely the result of large mechanical stress during fluid manipulation *in situ*, arising from operational error.

The chemogenetic research tool is commonly used to investigate neural circuitry with applications including elucidating memory retention<sup>494,495</sup>, synaptic plasticity<sup>445,496</sup> and behavioural change<sup>475,497</sup>. Its use is increasingly being used for investigating CNS disorders such as epilepsy and is beginning to demonstrate translational promise for clinical trials<sup>498,499</sup>. Research assessing neural circuitry would therefore benefit from the development of chemogenetic assays in a microfluidic format where multiple neural networks may be assessed simultaneously. Indeed, such work has demonstrated the possibility of CNO induced hM4Di activation to effectively eliminate epileptic activity in three models of neocortical seizures *in vivo*: focal picrotoxin, focal pilocarpine and tetanus toxin<sup>500</sup>. The work presented here paves the way for additional assay optimisation in the development of chemogenetic microfluidic assays with integrated perfusion as a novel research tool.

## 6.5. Future Studies

Whilst the research performed in this thesis has explored the development of three novel research tools for neuroscientific research, a considerable number of methods to optimise these assays remain.

Concerning the development of VSDI assays, the potential for D3AD to dampen spontaneous synaptic activity was never demonstrated and could explain the inability to detect AP firing in stained neurons. Whilst not possible at the time of assessments, simultaneous VSDI and whole cell patch clamp recordings would determine the impact of VSD staining. Additionally, a train of stimuli could be delivered to the cell to induce AP firing, and change in fluorescence assessed to visualise synaptic activity. Moving forward with microfluidic assay development, waveform activity in microfluidic neural networks could be induced by placing an electrode within an inlet well to provide a train of stimuli, with changes in direct and indirectly activated networks optically assessed.

Whilst the microfluidic perfusion platform successfully demonstrated its potential use for early CNS drug discovery, the effects of only a few perfusates can be assessed per device. Optimising the geometry of the device to permit additional perfusion inlets would permit additional compounds to be assessed. Additionally, reducing the height of the inlet/outlet wells could be used to reduce hydraulic retention times however would be limited to reduced flow rates to prevent overflow from the inlet well. Using an increasing number of syringe pumps in such a setting would be cumbersome and impractical, however this could be replaced with a multi-valve pressure driven system which would improve the stability of constant flows in the microfluidic device. Whilst glutamate was used as the stimulatory agent as proof of principal, additional assays could be performed to characterise receptor specific ligands such as NMDA and DL-AP5.

Alternatively, physiological mechanisms such as receptor desensitisation and synaptic plasticity could be investigated by taking advantage of manipulating network activity with multiple perfusates. Disease models such as epilepsy could also be mimicked, whereby bicuculine perfusions could induce hyperexcitability in the neural network, and physiological states of activity restored by perfusion with carbamezapine or progabide.

The impact of introducing DREADDs to neural networks requires further investigation and could benefit again from whole cell patch clamp recordings to assess changes in basal activity and sensitivity to mechanical stimulation. Viral transduction is the likely alternative over liposomal transfection if transfection efficiency is to be improved, and this may be improved further by transducing immature neural networks in the presence of hyaluronic acid, as demonstrated by Wanish et al (2013)<sup>501</sup>. Improved expression of the hMD3q protein would substantially increase the chances observing transfected neuronal projections crossing the microfluidic array and into the naïve neural network. This would then negate the need to assess individual culture chambers during independent assessments as performed here. The spread of viral gene delivery by anterograde signalling, from neuron axonal projections to the synaptically connected naïve network, should be assessed by environmental isolation of the transduced neural network. Only then should due consideration be made for the excitability of transfected neural networks when designing chemogenetic microfluidic assays.

## **6.6. Thesis Conclusions**

The research performed during this thesis sought to develop novel assays that could be used as research tools for assessing communication between synaptically connected neural networks. Replacing  $\text{Ca}^{2+}$ sensitive dyes with VSDs to improve the temporal resolutions of functional communication studies was investigated, and the limitations involved with the development of VSDI assays highlighted. Assays were developed using the microfluidic perfusion system to perform the pharmacological characterisation of glutamate with rapid alternation of perfusate delivery, without affecting neural network activity. This system can also be used to assess changes in synaptically connected, naïve neural networks in response to drug application, as demonstrated by the increasingly activated network observed during repeated glutamate stimulations. Preliminary work for the development of chemogenetic assays meanwhile demonstrated the functional of the transfected protein hMD3q, and there is some evidence to suggest that hMD3q activation via CNO perfusions can activate adjacent, synaptically connected neural networks. The assays presented here could be used to assess CNS acting drugs and with further development, investigate physiological mechanisms underlying synaptic communication.

## References

1. Wilkins RH. Neurosurgical Classics. 2nd ed. Illinois: American Association of Neurological Surgeons; 1992.
2. Willis T, Feindel W. The Anatomy of the Brain and Nerves. The Classics of Medicine Library; 1978.
3. Renshaw B, Forbes A, Morison B. Activity of Isocortex and Hippocampus: Electrical Studies With Micro-Electrodes. *J Neurophysiol.* 1940;
4. JH M, JA C. Epilepsy and the temporal lobes. A clinical, electroencephalographic and neuropathological study of the brain in epilepsy, with particular reference to the temporal lobes. *Brain.* 1966;89(3):499–530.
5. Benabid AL, Pollak P, Louveau A, Henry S, Rougemont J de. Combined (thalamotomy and stimulation) stereotactic surgery of the VIM thalamic nucleus for bilateral Parkinson disease. In: *Proceedings of the Meeting of the American Society for Stereotactic and Functional Neurosurgery.* Montreal; 1987.
6. Caton R. The Electric Currents of the Brain. *Br Medical J.* 1875;
7. Beck A. On the excitability of various parts of the same nerve. *Akad Umiejtności.* 1888;15:165–95.
8. R J, W B. Fiftieth anniversary of Hans Berger’s publication of the electroencephalogram. *Arch Psychiatr Nervenkr.* 1979;227(4):279–300.
9. Thomas CA, Springer PA, Loeb GE, Berwald-Netter Y, Okun LM. A Miniature Microelectrode Array to Monitor the Bioelectric Activity of Cultured Cells. *Exp Cell Res.* 1972;74:61–6.
10. Ergorul C, Eichenbaum H. Essential Role of the Hippocampal Formation in Rapid Learning of Higher-Order Sequential Associations. *J Neurosci.* 2006;26(15):4111–7.
11. Richter-Levin G. The Amygdala, the Hippocampus, and Emotional Modulation of Memory. *Neuroscientist.* 2004;10(1):31–9.
12. Eichenbaum H, Dudchenko P, Wood E, Shapiro M, Tanila H. The Hippocampus, Memory, Review and Place Cells: Is It Spatial Memory or a Memory Space? might occur at different locations. Olton and colleagues *Neuron* 210 Figure 1. Schematic Overhead Views of Four

- Different Types of Apparatus and Examples of Location-S. *Neuron*. 1999;23:209–26.
13. Bartsch T, Dohring J, Rohr A, Jansen O, Deuschl G. CA1 neurons in the human hippocampus are critical for autobiographical memory, mental time travel, and auto-noetic consciousness. *Proc Natl Acad Sci*. 2011;108(42):17562–7.
  14. Dudek SM, Alexander GM, Farris S. Rediscovering area CA2: Unique properties and functions. *Nat Rev Neurosci*. 2016;17(2):89–102.
  15. Cherubini E, Miles R. The CA3 region of the hippocampus: how is it? What is it for? How does it do it? *Front Cell Neurosci*. 2015;9(February):9–11.
  16. Witter MP. The perforant path: projections from the entorhinal cortex to the dentate gyrus. *Prog Brain Res*. 2007;163:43–61.
  17. Jaffe DB, Gutiérrez R. Mossy fiber synaptic transmission: communication from the dentate gyrus to area CA3. *Prog Brain Res*. 2007;163.
  18. Kumar A. Long-term potentiation at CA3-CA1 hippocampal synapses with special emphasis on aging, disease, and stress. *Front Aging Neurosci*. 2011;3(MAY):1–20.
  19. Yeckel MF, Berger TW. Feedforward excitation of the hippocampus by afferents from the entorhinal cortex: Redefinition of the role of the trisynaptic pathway. *Proc Natl Acad Sci U S A*. 1990;87(15):5832–6.
  20. Aksoy-Aksel A, Manahan-Vaughan D. Synaptic strength at the temporoammonic input to the hippocampal CA1 region in vivo is regulated by NMDA receptors, metabotropic glutamate receptors and voltage-gated calcium channels. *Neuroscience* [Internet]. 2015;309:191–9. Available from: <http://dx.doi.org/10.1016/j.neuroscience.2015.03.014>
  21. Mara SO. The subiculum : what it does , what it might do , and what neuroanatomy has yet to tell us. *J Anat*. 2005;271–82.
  22. O’Mara SM, Sanchez-Vives M V., Brotons-Mas JR, O’Hare E. Roles for the subiculum in spatial information processing, memory, motivation and the temporal control of behaviour. *Prog Neuro-Psychopharmacology Biol Psychiatry*. 2009;33(5):782–90.
  23. Yamamoto J, Tonegawa S. Direct Medial Entorhinal Cortex Input to Hippocampal CA1 Is Crucial Synchronous MUA during SWR. 2017;96(1):217–27.

24. Masurkar A V., Srinivas K V., Brann DH, Warren R, Lowes DC, Siegelbaum SA. Medial and Lateral Entorhinal Cortex Differentially Excite Deep versus Superficial CA1 Pyramidal Neurons. *Cell Rep.* 2017;18(1):148–60.
25. Melzer S, Michael M, Caputi A, Eliava M, Fuchs EC, Whittington MA, et al. Long-range-projecting gabaergic neurons modulate inhibition in hippocampus and entorhinal cortex. *Science* (80- ). 2012;335(6075):1506–10.
26. Ortega-Martínez S. Adult Hippocampal Neurogenesis and Memory. *Int J Adv Biol Biomed Res.* 2017;06(01):360–79.
27. Shelanski ML, Taylor EW. Biochemistry of Neurofilaments and Neurotubules. In: Ciba Foundation Symposium - Alzheimer's Disease and Related Conditions. Novartis Foundation Symposia; 1970.
28. Nimchinsky EA, Sabatini BL, Svoboda K. Structure and function of dendritic spines. *Annu Rev Physiol.* 2002;64:313–53.
29. Villa KL, Berry KP, Subramanian J, Cha JW, Oh WC, Kwon HB, et al. Inhibitory Synapses Are Repeatedly Assembled and Removed at Persistent Sites In Vivo. *Neuron.* 2016;89(4):756–69.
30. Bannister NJ, Larkman AU. Dendritic morphology of CA1 pyramidal neurones from the rat hippocampus: I. Branching patterns. *J Comp Neurol.* 1995;360(1):150–60.
31. Trommald M, Jensen V, Andersen P. Analysis of dendritic spines in rat CA1 pyramidal cells intracellularly filled with a fluorescent dye. *J Comp Neurol.* 1995;353(2):260–74.
32. Darnell JE, Lodish H, Berk A, Zipursky L, Matsudaira P, Baltimore D. Neurotransmitters, Synapses, and Impulse Transmission. In: *Molecular Cell Biology.* 4th ed. 2000.
33. Wefelmeyer W, Cattaert D, Burrone J. Activity-dependent mismatch between axo-axonic synapses and the axon initial segment controls neuronal output. *Proc Natl Acad Sci U S A.* 2015;112(31):9757–62.
34. Gonzales RB, Galvan CJD, Rangel YM, Claiborne BJ. Distribution of thorny excrescences on CA3 pyramidal neurons in the rat hippocampus. *J Comp Neurol.* 2001;430(3):357–68.
35. Pelkey KA, Chittajallu R, Craig MT, Tricoire L, Wester JC, McBain CJ. Hippocampal GABAergic Inhibitory Interneurons. *Physiol Rev* [Internet]. 2017;97(4):1619–747. Available from: <http://physrev.physiology.org/lookup/doi/10.1152/physrev.00007.2017>

36. Tricoire L, Pelkey KA, Erkkila BE, Jeffries BW, Yuan X, McBain CJ. A Blueprint for the Spatiotemporal Origins of Mouse Hippocampal Interneuron Diversity. *J Neurosci*. 2011;31(30):10948–70.
37. R LDN. Studies on the structure of the cerebral cortex – II. Continuation of the study of the ammonic system. *J fur Psychol und Neurol*. 1934;46:113–77.
38. S RC. Estructura del asta de Ammon y fascia dentate. *Ann Soc Esp His Nat*. 1893;22.
39. Kosaka T, Katsumaru H, Hama K, Wu JY, Heizmann CW. GABAergic neurons containing the Ca<sup>2+</sup>-binding protein parvalbumin in the rat hippocampus and dentate gyrus. *Brain Res*. 1987;419(1–2):119–30.
40. Klausberger T, Magill PJ, Cobden PM, Somogyi P. Brain-state and cell-type specific firing of hippocampal interneurons in vivo. *Nature*. 2003;421(February).
41. Maccaferri G, Roberts JDB, Szucs P, Cottingham CA, Somogyi P. Cell surface domain specific postsynaptic currents evoked by identified GABAergic neurones in rat hippocampus in vitro. *J Physiol*. 2000;524(1):91–116.
42. Losonczy A, Zhang L, Shigemoto R, Somogyi P, Nusser Z. Cell type dependence and variability in the short-term plasticity of EPSCs in identified mouse hippocampal interneurons. *J Physiol*. 2002;542(1):193–210.
43. Vreugdenhil M, Jefferys JGR, Celio MR, Schwaller B, Hoftman GD, Lewis DA, et al. Parvalbumin-Deficiency Facilitates Repetitive IPSCs and Gamma Oscillations in the Hippocampus Parvalbumin-Deficiency Facilitates Repetitive IPSCs and Gamma Oscillations in the Hippocampus. *J Neurophysiol*. 2003;89:1414–22.
44. Migliore R, Lupascu CA, Bologna LL, Romani A, Courcol JD, Antonel S, et al. The physiological variability of channel density in hippocampal CA1 pyramidal cells and interneurons explored using a unified data-driven modeling workflow. *PLoS Comput Biol*. 2018;14(9):1–25.
45. Alvarez JI, Katayama T, Prat A. Glial Influence on the Blood Brain Barrier. 2013;1939–58.
46. Herculano-Houzel S. The glia/neuron ratio: How it varies uniformly across brain structures and species and what that means for brain physiology and evolution. *Glia*. 2014;62(9):1377–91.
47. Rose CR, Felix L, Zeug A, Dietrich D, Reiner A, Henneberger C. Astroglial Glutamate Signaling



and Uptake in the Hippocampus. *Front Mol Neurosci* [Internet]. 2018;10(January):1–20. Available from: <http://journal.frontiersin.org/article/10.3389/fnmol.2017.00451/full>

48. Lee M, Schwab C, Mcgeer PL. Astrocytes are GABAergic cells that modulate microglial activity. *Glia*. 2011;59(1):152–65.
49. Hoft S, Griemsmann S, Seifert G, Steinhauser C. Heterogeneity in expression of functional ionotropic glutamate and GABA receptors in astrocytes across brain regions: insights from the thalamus. *Philos Trans R Soc B Biol Sci* [Internet]. 2014;369(1654):20130602–20130602. Available from: <http://rstb.royalsocietypublishing.org/cgi/doi/10.1098/rstb.2013.0602>
50. Robitaille R, Volterra A, Araque A, Carmignoto G, Haydon P, Oliet S. Gliotransmitters travel in time and space. *Neuron*. 2014;81(4):728–39.
51. Dallérac G, Rouach N. Astrocytes as new targets to improve cognitive functions. *Prog Neurobiol*. 2016;144:48–67.
52. Chung W, Allen NJ, Eroglu C. Astrocytes Control Synapse Formation, Function, and Elimination. *Cold Spring Harb Perspect Biol*. 2015;7(9).
53. Olsen ML, Khakh BS, Skatchkov SN, Zhou M, Lee CJ, Rouach N. New Insights on Astrocyte Ion Channels: Critical for Homeostasis and Neuron-Glia Signaling. *J Neurosci*. 2015;35(41):13827–35.
54. Sepp KJ. RhoA and Rac1 GTPases mediate the dynamic rearrangement of actin in peripheral glia. *Development*. 2003;130(9):1825–35.
55. Potokar M, Kreft M, Li L, Andersson JD, Pangršič T, Chowdhury HH, et al. Cytoskeleton and vesicle mobility in astrocytes. *Traffic*. 2007;8(1):12–20.
56. McKenzie AT, Wang M, Hauberg ME, Fullard JF, Kozlenkov A, Keenan A, et al. Synaptic Pruning by Microglia Is Necessary for Normal Brain Development. *Sci Rep*. 2018;8(1):8868.
57. Hong S, Dissing-Olesen L, Stevens B. New insights on the role of microglia in synaptic pruning in health and disease. *Curr Opin Neurobiol*. 2016;36:128–34.
58. Wu Y, Dissing-Olesen L, MacVicar BA, Stevens B. Microglia: Dynamic Mediators of Synapse Development and Plasticity. *Trends Immunol*. 2015;36(10):605–13.
59. Gibson EM, Purger D, Mount CW, Goldstein AK, Lin L, Wood LS, et al. Neuronal activity

- promotes oligodendrogenesis and adaptive myelination in the mammalian brain. *Science* (80- ). 2014;344(6183):1–27.
60. Li Q, Brus-Ramer M, Martin JH, McDonald JW. Electrical stimulation of the medullary pyramid promotes proliferation and differentiation of oligodendrocyte progenitor cells in the corticospinal tract of the adult rat. *Neurosci Lett*. 2010;479(2):128–33.
  61. Stevens B, Porta S, Haak LL, Gallo V, Fields RD. Adenosine: A neuron-glia transmitter promoting myelination in the CNS in response to action potentials. *Neuron*. 2002;36(5):855–68.
  62. Souza PVS de, Pinto WBV de R, Rezende Filho FM, Oliveira ASB. Far beyond the motor neuron: the role of glial cells in amyotrophic lateral sclerosis. *Arq Neuropsiquiatr*. 2016;74(10):849–54.
  63. H L, A B, SL Z. Intracellular Ion Environment and Membrane Electric Potential. In: *Molecular Cell Biology*. New York: W. H. Freeman; 2000.
  64. Forrest MD. The sodium-potassium pump is an information processing element in brain computation. *Front Physiol*. 2014;5(Nov):1–4.
  65. Ellerkmann RK, Riazanski V, Elger CE, Urban BW, Beck H. Slow recovery from inactivation regulates the availability of voltage-dependent Na<sup>+</sup> channels in hippocampal granule cells, hilar neurons and basket cells. *J Physiol*. 2001;532(2):385–97.
  66. Moosmang S. Role of Hippocampal Cav1.2 Ca<sup>2+</sup> Channels in NMDA Receptor-Independent Synaptic Plasticity and Spatial Memory. *J Neurosci*. 2005;25(43):9883–92.
  67. Brivio V, Faivre-Sarrailh C, Peles E, Sherman DL, Brophy PJ. Assembly of CNS Nodes of Ranvier in Myelinated Nerves Is Promoted by the Axon Cytoskeleton. *Curr Biol*. 2017;27(7):1068–73.
  68. Dale P, Augustine GJ, Fitzpatrick D, Katz LC, Lamantia A-S, Mcnamara JO, et al. Increased Conduction Velocity as a Result of Myelination. In: *Neuroscience*. 2nd Editio. Sinauer Associates; 2001.
  69. Augustine GJ, Santamaria F, Tanaka K. Local calcium signaling in neurons. *Neuron*. 2003;40(2):331–46.
  70. Emptage NJ, Reid CA, Fine A. Calcium stores in hippocampal synaptic boutons mediate short-term plasticity, store-operated Ca<sup>2+</sup> entry, and spontaneous transmitter release. *Neuron*.

2001;29(1):197–208.

71. Simms BA, Zamponi GW. Neuronal voltage-gated calcium channels: Structure, function, and dysfunction. *Neuron*. 2014;82(1):24–45.
72. Südhof TC. The Synaptic Vesicle Cycle in the Nerve Terminal. In: *Basic Neurochemistry: Molecular, Cellular and Medical Aspects*. 6th Editio. Lippincott Williams and Wilkins; 1998.
73. Südhof TC, Rizo J. Synaptic Vesicle Exocytosis. *Cold Spring Harb Perspect Biol*. 2011;3.
74. Lewerenz J, Maher P. Chronic glutamate toxicity in neurodegenerative diseases-What is the evidence? *Front Neurosci*. 2015;9(DEC):1–20.
75. Schousboe A, Scafidi S, Bak LK, Waagepetersen HS, Mary C, Sciences M. Glutamate Metabolism in the Brain Focusing on Astrocytes. *Adv Neurobiol*. 2014;11:13–30.
76. Nett WJ, Oloff SH, McCarthy KD. Hippocampal Astrocytes In Situ Exhibit Calcium Oscillations That Occur Independent of Neuronal Activity. *J Neurophysiol*. 2002;87(1):528–37.
77. Perea G, Araque A. Properties of Synaptically Evoked Astrocyte Calcium Signal Reveal Synaptic Information Processing by Astrocytes. *J Neurosci*. 2005;25(9):2192–203.
78. Verkhratsky A, Kirchhoff F. NMDA receptors in glia. *Neuroscientist*. 2007;13(1):28–37.
79. Balázs R, Miller S, Romano C, De Vries A, Chun Y, Cotman CW. Metabotropic Glutamate Receptor mGluR5 in Astrocytes: Pharmacological Properties and Agonist Regulation. *J Neurochem [Internet]*. 2002;69(1):151–63. Available from: <http://doi.wiley.com/10.1046/j.1471-4159.1997.69010151.x>
80. Boddum K, Jensen TP, Magloire V, Kristiansen U, Rusakov DA, Pavlov I, et al. Astrocytic GABA transporter activity modulates excitatory neurotransmission. *Nat Commun*. 2016;7:1–10.
81. Aguado F, Espinosa-Parrilla JF, Carmona MA, Soriano E. Neuronal activity regulates correlated network properties of spontaneous calcium transients in astrocytes in situ. *J Neurosci*. 2002;22(21):9430–44.
82. Duan S, Anderson CM, Keung EC, Chen Y, Chen Y, Swanson R a. P2X7 receptor-mediated release of excitatory amino acids from astrocytes. *J Neurosci*. 2003;23(4):1320–8.
83. Bezzi P, Vesce S, Rossi D, Rizzini BL, Volterra A, Carmignoto G, et al. Prostaglandins stimulate calcium-dependent glutamate release in astrocytes. *Nature*. 1998;391(6664):281–5.

84. Sherwood MW, Arizono M, Hisatsune C, Bannai H, Ebisui E, Sherwood JL, et al. Astrocytic IP3Rs: Contribution to Ca<sup>2+</sup> signalling and hippocampal LTP. *Glia*. 2017;65(3):502–13.
85. Araque A, Parpura V, Sanzgiri RP, Haydon PG. Glutamate-dependent astrocyte modulation of synaptic transmission between cultured hippocampal neurons. *Eur J Neurosci*. 1998;10(6):2129–42.
86. Harrison JF, Rinne ML, Kelley MR, Druzhyina NM, Wilson GL, Ledoux SP. Vesicular transmitter release from astrocytes. *Glia*. 2006;54:700–15.
87. Petravicz J, Fiacco TA, McCarthy KD. Loss of IP3 receptor-dependent Ca<sup>2+</sup> increases in hippocampal astrocytes does not affect baseline CA1 pyramidal neuron synaptic activity. *J Neurosci*. 2008;28(19):4967–73.
88. Petravicz J, Boyt KM, McCarthy KD. Astrocyte IP3R2-dependent Ca<sup>2+</sup> signaling is not a major modulator of neuronal pathways governing behavior. *Front Behav Neurosci*. 2014;8(November):1–13.
89. Fiacco TA, McCarthy KD. Multiple lines of evidence indicate that gliotransmission does not occur under physiological conditions. *J Neurosci*. 2018;38(1):3–13.
90. Cohen-Cory S. The developing synapse: Construction and modulation of synaptic structures and circuits. *Science (80- )*. 2002;298(5594):770–6.
91. Popoli M, Yan Z, McEwen BS, Sanacora G. The stressed synapse: The impact of stress and glucocorticoids on glutamate transmission. *Nat Rev Neurosci*. 2012;13(1):22–37.
92. Mayer ML. Glutamate receptors at atomic resolution. *Nature*. 2006;440:456–62.
93. Watson JF, Ho H, Greger IH. Synaptic transmission and plasticity require AMPA receptor anchoring via its N-terminal domain. *Elife*. 2017;6:1–20.
94. Chater TE, Goda Y. The role of AMPA receptors in postsynaptic mechanisms of synaptic plasticity. *Front Cell Neurosci*. 2014;8(November):1–14.
95. Ascher P, Nowak L. The role of divalent cations in the N-methyl-D-aspartate responses of mouse central neurones in culture. *J Physiol*. 1988;399:247–66.
96. Tong G, Takahashi H, Tu S, Shin Y, Talantova M, Zago W, et al. Modulation of NMDA receptor properties and synaptic transmission by the NR3A subunit in mouse hippocampal and

- cerebrocortical neurons. 2008;99(1):122–32.
97. Tekieh E, Kazemi M, Tavakoli H, Saberi M, Ghanaati H, Hajinasrollah M, et al. The Effect of Extremely Low Frequency Electromagnetic Fields on Visual Learning, Memory and Anatomical Structures of the Brain in Male Rhesus Monkeys. *Basic Clin Neurosci*. 2018;9(3).
  98. Henley JM, Wilkinson KA. AMPA receptor trafficking and the mechanisms underlying synaptic plasticity and cognitive aging. *Dialogues Clin Neurosci*. 2013;15(1):11–27.
  99. Chittajallu R, Braithwaite SP, Clarke VRJ, Henley JM. Kainate receptors: Subunits, synaptic localization and function. *Trends Pharmacol Sci*. 1999;20(1):26–35.
  100. Balázs R, Bridges RJ, Cotman CW. Kainate Receptors. *Excit Amin Acid Transm Heal Dis*. 2010;1–25.
  101. Sommer B, Burnashev N, Verdoorn TA, Keinänen K, Sakmann B, Seeburg PH. A glutamate receptor channel with high affinity for domoate and kainate. *EMBO J*. 1992;11(4):1651–6.
  102. Heckmann M, Bufler J, Franke C, Dudel J. Kinetics of homomeric GluR6 glutamate receptor channels. *Biophys J*. 1996;71(October):1743–50.
  103. Paternain A V., Rodríguez-Moreno A, Villarroel A, Lerma J. Activation and desensitization properties of native and recombinant kainate receptors. *Neuropharmacology*. 1998;37(10–11):1249–59.
  104. Barberis A, Sachidhanandam S, Mulle C. GluR6/KA2 kainate receptors mediate slow-deactivating currents. *J Neurosci*. 2008;28(25):6402–6.
  105. Fisher JL, Mott DD. Distinct functional roles of subunits within the heteromeric kainate receptor. *J Neurosci*. 2011;31(47):17113–22.
  106. Cossart R, Tyzio R, Dinocourt C, Esclapez M, Hirsch JC, Ben-Ari Y, et al. Presynaptic kainate receptors that enhance the release of GABA on CA1 hippocampal interneurons. *Neuron*. 2001;29(2):497–508.
  107. Shigemoto R, Kinoshia A, Wada E, Nomura S, Ohishi H, Takada Masahiko, et al. Differential Presynaptic Localization of Metabotropic Glutamate Receptor Subtypes in the Rat Hippocampus. *J Neuoriscience*. 1997;17(19):7503–22.
  108. Skeberdis VA, Lan JY, Opitz T, Zheng X, Bennett MVL, Suzanne Zukin R. mGluR1-mediated

potentiation of NMDA receptors involves a rise in intracellular calcium and activation of protein kinase C. *Neuropharmacology*. 2001;40(7):856–65.

109. Bikbaev A, Manahan-Vaughan D. Metabotropic glutamate receptor, mGlu5, regulates hippocampal synaptic plasticity and is required for tetanisation-triggered changes in theta and gamma oscillations. *Neuropharmacology*. 2017;115:20–9.
110. Scanziani M, Salin PA, Vogt KE, Malenka RC, Nicoll RA. Use-dependent increases in glutamate concentration activate presynaptic metabotropic glutamate receptors. *Nature*. 1997;385.
111. Bruno V, Battaglia G, Ksiazek I, van der PH, Catania M V, Giuffrida R, et al. Selective activation of mGlu4 metabotropic glutamate receptors is protective against excitotoxic neuronal death. *J Neurosci*. 2000;20(17):6413–20.
112. Olsen RW, DeLorey TM. GABA Receptor Physiology and Pharmacology. In: *Basic Neurochemistry: Molecular, Cellular and Medical Aspects*. 6th ed. 1999.
113. Zhang D, Pan ZH, Awobuluyi M, Lipton SA. Structure and function of GABAC receptors: A comparison of native versus recombinant receptors. *Trends Pharmacol Sci*. 2001;22(3):121–32.
114. Emson PC. GABAB receptors: structure and function. In: *Progress in Brain Research* [Internet]. 2007. p. 43–57. Available from: <https://linkinghub.elsevier.com/retrieve/pii/S0079612306600046>
115. Harrison NL. On the presynaptic action of baclofen at inhibitory synapses between cultured rat hippocampal neurones. *J Physiol*. 1990;422(1):433–46.
116. Scholz KP, Miller RJ. GABAB receptor-mediated inhibition of Ca<sup>2+</sup> currents and synaptic transmission in cultured rat hippocampal neurones. *J Physiol*. 1991;444(1):669–86.
117. Billups B, Graham BP, Wong AYC, Forsythe ID. Unmasking group III metabotropic glutamate autoreceptor function at excitatory synapses in the rat CNS. *J Physiol*. 2005;565(3):885–96.
118. Lee V, Maguire J. The impact of tonic GABA<sub>A</sub> receptor-mediated inhibition on neuronal excitability varies across brain region and cell type. *Front Neural Circuits*. 2014;8(February):1–27.
119. Bonin RP, Martin LJ, Macdonald JF, Orser BA.  $\alpha$ 5GABA<sub>A</sub> Receptors Regulate the Intrinsic Excitability of Mouse Hippocampal Pyramidal Neurons.pdf. *J Neurophysiol*. 2007;98:2244–54.

120. Feigenspan A, Bormann J. Differential pharmacology of GABAA and GABAC receptors on rat retinal bipolar cells. *Eur J Pharmacol.* 1994;288(1):97–104.
121. Chebib M. GABA<sub>C</sub> receptor ion channels. *Clin Exp Pharmacol Physiol.* 2004;31(11):800–4.
122. Zhang D, Pan ZH, Zhang X, Brideau AD, Lipton SA. Cloning of a gamma-aminobutyric acid type C receptor subunit in rat retina with a methionine residue critical for picrotoxinin channel block. *Proc Natl Acad Sci U S A.* 1995;92(25):11756–60.
123. Zhu Y, Ripps H, Qian H. A single amino acid in the second transmembrane domain of GABA<sub>A</sub> receptors regulates channel conductance. *Neurosci Lett.* 2007;418(2):205–9.
124. Alakuijala A, Alakuijala J, Pasternack M. Evidence for a functional role of GABAC receptors in the rat mature hippocampus. *Eur J Neurosci.* 2006;23(2):514–20.
125. Wang X, Lambert NA, Wang X, Lambert NA. GABA<sub>B</sub> Receptors Couple to Potassium and Calcium Channels on Identified Lateral Perforant Pathway Projection Neurons GABA<sub>B</sub> Receptors Couple to Potassium and Calcium Channels on Identified Lateral Perforant Pathway Projection Neurons. *Am J Physiol.* 2006;1073–8.
126. Axmacher N, Hartmann K, Draguhn A. Presynaptic Ionotropic GABA Receptors. In: Stanton PK, Bramham C, Scharfman HE, editors. *Synaptic Plasticity and Transsynaptic Signaling.* Springer US; 1970. p. 79–89.
127. Davies CH, Collingridge GL. Regulation of EPSPs by the synaptic activation of GABA<sub>B</sub> autoreceptors in rat hippocampus. *J Physiol.* 1996;496(2):451–70.
128. Scanziani M. GABA spillover activates postsynaptic GABA<sub>B</sub> receptors to control rhythmic hippocampal activity. *Neuron.* 2000;25(3):673–81.
129. Craig MT, Mayne EW, Bettler B, Paulsen O, McBain CJ. Distinct roles of GABA<sub>B</sub>1a- and GABA<sub>B</sub>1b-containing GABA<sub>B</sub> receptors in spontaneous and evoked termination of persistent cortical activity. *J Physiol.* 2013;591(4):835–43.
130. Li XL, Hu N, Tan MS, Yu JT, Tan L. Behavioral and Psychological Symptoms in Alzheimer's Disease. *Biomed Res Int.* 2014;2014.
131. Karantzoulis S, Galvin JE. Distinguishing Alzheimer's disease from other major forms of dementia. *Expert Rev Neurother.* 2011;11(11):1579–91.

132. Hardy JA, Higgins GA, Hardy JA, Higgins GA. Alzheimer ' s Disease : The Amyloid Cascade Hypothesis Published by : American Association for the Advancement of Science Alzheimer ' s Disease : The Amyloid Cascade Hypothesis. *Science* (80- ). 1992;256(5054):184–5.
133. Carter J, Lippa C. Beta-amyloid, neuronal death and Alzheimer's disease. *Curr Mol Med*. 2001;1(6):733–7.
134. Durst F, Tropea C. The amyloid hypothesis of Alzheimer's disease at 25 years. *EMBO Mol Med* [Internet]. 2016;8(6):595–608. Available from: [http://www.springerlink.com/index/10.1007/978-3-642-81991-9\\_5](http://www.springerlink.com/index/10.1007/978-3-642-81991-9_5)
135. Christian Holscher. Possible Causes of Alzheimer's Disease: Amyloid Fragments, Free Radicals, and Calcium Homeostasis. *Neurobiol Dis* [Internet]. 1998;141(5):129–41. Available from: [http://ac.els-cdn.com/S0969996198901930/1-s2.0-S0969996198901930-main.pdf?\\_tid=d3a6ab44-888f-11e5-b923-00000aab0f26&acdnat=1447258881\\_659c5a70efc03392aa9fe2528771d2ea](http://ac.els-cdn.com/S0969996198901930/1-s2.0-S0969996198901930-main.pdf?_tid=d3a6ab44-888f-11e5-b923-00000aab0f26&acdnat=1447258881_659c5a70efc03392aa9fe2528771d2ea)
136. Di Scala C, Yahi N, Boutemour S, Flores A, Rodriguez L, Chahinian H, et al. Common molecular mechanism of amyloid pore formation by Alzheimer's  $\beta$ -amyloid peptide and  $\alpha$ -synuclein. *Sci Rep* [Internet]. 2016;6(28781):1–11. Available from: [http://ac.els-cdn.com/S0969996198901930/1-s2.0-S0969996198901930-main.pdf?\\_tid=d3a6ab44-888f-11e5-b923-00000aab0f26&acdnat=1447258881\\_659c5a70efc03392aa9fe2528771d2ea](http://ac.els-cdn.com/S0969996198901930/1-s2.0-S0969996198901930-main.pdf?_tid=d3a6ab44-888f-11e5-b923-00000aab0f26&acdnat=1447258881_659c5a70efc03392aa9fe2528771d2ea)
137. Cowburn R, Messamore E, Li ML, Winbald B, Sundstrom E.  $\beta$ -amyloid related peptides exert differential effects on [3H]MK-801 binding to rat cortical membranes. *Neuroreport*. 1994;5(4):405–8.
138. Cowburn RF, Wiehager B, E. T, Li Li M., Sundstrom E. Effects of beta-amyloid-(25-35) peptides on radioligand binding to excitatory amino acid receptors and voltage-dependent calcium channels: evidence for a selective affinity for the glutamate and glycine recognition sites of the NMDA receptor. *Neurochem Res*. 1997;22(12):1437–42.
139. Kirvell SL, Esiri M, Francis PT. Down-regulation of vesicular glutamate transporters precedes cell loss and pathology in Alzheimer's disease. *J Neurochem*. 2006;98(3):939–50.
140. Scott HA, Gebhardt FM, Mitrovic AD, Vandenberg RJ, Dodd PR. Glutamate transporter variants reduce glutamate uptake in Alzheimer's disease. *Neurobiol Aging* [Internet].



2011;32(3):553.e1-553.e11. Available from:  
<http://dx.doi.org/10.1016/j.neurobiolaging.2010.03.008>

141. Nelson AR, Sagare AP, Zlokovic B V. Blood – Brain Barrier Transport of. In: Developing Therapeutics for Alzheimer’s Disease [Internet]. Elsevier Inc.; 2016. p. 251–70. Available from: <http://dx.doi.org/10.1016/B978-0-12-802173-6/00009-5>
142. Driscoll I, Resnick SM, Troncoso JC, An Y, O’Brien R, Zonderman AB. Impact of Alzheimer’s pathology on cognitive trajectories in nondemented elderly. *Ann Neurol*. 2006;60(6):688–95.
143. Cummings J, Lee G, Ritter A, Zhong K. Alzheimer’s disease drug development pipeline: 2018. *Alzheimer’s Dement Transl Res Clin Interv* [Internet]. 2018;4(2018):195–214. Available from: <https://doi.org/10.1016/j.trci.2018.03.009>
144. Gong C-X, Iqbal K. Hyperphosphorylation of Microtubule-Associated Protein Tau: A Promising Therapeutic Target for Alzheimer Disease. *Curr Med Chem* [Internet]. 2008;15(23):2321–8. Available from:  
<http://www.eurekaselect.com/openurl/content.php?genre=article&issn=0929-8673&volume=15&issue=23&spage=2321>
145. Reese LC, Taghialatela G, Ghirardi V, Bjorklund NL, Sadagoparamanujam V-M, Woltjer RL. Absence of amyloid  $\beta$  oligomers at the postsynapse and regulated synaptic Zn<sup>2+</sup> in cognitively intact aged individuals with Alzheimer’s disease neuropathology. *Mol Neurodegener*. 2012;7(1):23.
146. Clos AL, Sengupta U, Kaye R, Jackson GR, Castillo-Carranza DL, Lasagna-Reeves CA. Tau oligomers impair memory and induce synaptic and mitochondrial dysfunction in wild-type mice. *Mol Neurodegener*. 2011;6(1):39.
147. Voss K, Koren J, Dickey CA. The earliest tau dysfunction in Alzheimer’s disease?: Tau phosphorylated at S422 as a toxic seed. *Am J Pathol* [Internet]. 2011;179(5):2148–51. Available from: <http://dx.doi.org/10.1016/j.ajpath.2011.08.020>
148. Sousa A, Gomar JJ, Goldberg TE. Neural and behavioral substrates of disorientation in mild cognitive impairment and Alzheimer’s disease. *Alzheimer’s Dement Transl Res Clin Interv*. 2015;1(1):37–45.
149. Roberson ED, Scarce-Lewie K, Palop JJ, Yan F, Cheng IH, Wu T, et al. Reducing endogenous

- tau ameliorates amyloid  $\beta$ -induced deficits in an Alzheimer's disease mouse model. *Science* (80- ). 2007;316(5825):750–4.
150. Shipton OA, Leitz JR, Dworzak J, Acton CEJ, Tunbridge EM, Denk F, et al. Tau protein is required for amyloid  $\beta$ -induced impairment of hippocampal long-term potentiation. *J Neurosci*. 2011;31(5):1688–92.
  151. Sander MCT, Chia K. The Role of Our Immune System in Alzheimer's [Internet]. 2017. Available from: <https://columbiasciencereview.com/2017/04/07/the-role-of-our-immune-system-in-alzheimers/>
  152. Muro VM, Connolly MB. Classifying Epileptic Seizures and the Epilepsies. In: *Epilepsy*. John Wiley & Sons; 2014. p. 10–4.
  153. Bromfield EB, Cavazos JE, Sirven J. Clinical Epilepsy. In: *An Introduction to Epilepsy*. American Epilepsy Society; 2006.
  154. Kotov AS, Rudakova IG, Belova I, Kotov SV. Occipital lobe epilepsy in adults. *Zh Nevrol Psikhiatr Im S S Korsakova*. 2009;109(7):4–8.
  155. Scheffer IE, Berkovic S, Capovilla G, Connolly MB, French J, Guilhoto L, et al. ILAE classification of the epilepsies: position paper of the ILAE Commission for Classification and Terminology. *Int Leag Against Epilepsy*. 2017;58(4):512–21.
  156. Wallace RH, Marini C, Petrou S, Harkin LA, Bowser DN, Panchal RG, et al. Mutant GABA A receptor  $\gamma$ 2-subunit in childhood absence epilepsy and febrile seizures. *Nat Genet*. 2001;28(1):49–52.
  157. Baulac S, Huberfeld G, Gourfinkel-An I, Mitropoulou G, Beranger A, Prud'homme JF, et al. First genetic evidence of GABAA receptor dysfunction in epilepsy: A mutation in the  $\gamma$ 2-subunit gene. *Nat Genet*. 2001;28(1):46–8.
  158. Rivera C, Voipio J, Payne JA, Ruusuvuori E, Lahtinen H, Lamsa K, et al. The K<sup>+</sup>/Cl<sup>-</sup> co-transporter KCC2 renders GABA hyperpolarizing during neuronal maturation. *Nature*. 1999;397(6716):251–5.
  159. Moore YE, Deeb TZ, Chadchankar H, Brandon NJ, Moss SJ. Potentiating KCC2 activity is sufficient to limit the onset and severity of seizures. *Proc Natl Acad Sci*. 2018;115(40):10166–71.

160. Naylor DE, Hantao L, Niquet J, Wasterlain CG. Rapid surface accumulation of NMDA receptors increases glutamatergic excitation during status epilepticus. *Neurobiol Dis.* 2013;54:225–38.
161. Joshi S, Rajasekaran K, Sun H, Williamson J, Kapur J. Enhanced AMPA receptor-mediated neurotransmission on CA1 pyramidal neurons during status epilepticus. *Neurobiol Dis.* 2017;103:45–53.
162. Rajasekaran K, Todorovic M, Kapur J. Calcium-permeable AMPA receptors are expressed in a rodent model of status epilepticus. *Ann Neurol.* 2012;72(1):91–102.
163. Prasad A, Williamson JM, Bertram EH. Phenobarbital and MK-801, but not phenytoin, improve the long-term outcome of status epilepticus. *Ann Neurol.* 2002;51(2):175–81.
164. Rice AC, Delorenzo RJ. NMDA receptor activation during status epilepticus is required for the development of epilepsy. *Brain Res.* 1998;782(1–2):240–7.
165. Fang Y, Wang X. Ketamine for the treatment of refractory status epilepticus. *Seizure* [Internet]. 2015;30:14–20. Available from: <http://dx.doi.org/10.1016/j.seizure.2015.05.010>
166. Zeiler FA. Early use of the NMDA receptor antagonist ketamine in refractory and superrefractory status epilepticus. *Crit Care Res Pract.* 2015;2015.
167. Joshi S, Rajasekaran K, Williamson J, Kapur J. Neurosteroid-sensitive  $\delta$ -GABAA receptors: A role in epileptogenesis? *Epilepsia.* 2017;58(3):494–504.
168. Joshi S, Kapur J. N-Methyl-D-Aspartic acid receptor activation downregulates expression of  $\delta$  subunit-containing GABAA receptors in cultured hippocampal neurons. *Mol Pharmacol.* 2013;84(1):1–11.
169. Kwan P, Brodie MJ. Early identification of refractory epilepsy. *N Engl J Med.* 2000;342(5):314–9.
170. Brodie MJ. Outcomes in newly diagnosed epilepsy in adolescents and adults: Insights across a generation in Scotland. *Seizure* [Internet]. 2017;44(2017):206–10. Available from: <http://dx.doi.org/10.1016/j.seizure.2016.08.010>
171. Hanada T, Hashizume Y, Tokuhara N, Takenaka O, Kohmura N, Ogasawara A, et al. Perampanel: A novel, orally active, noncompetitive AMPA-receptor antagonist that reduces seizure activity in rodent models of epilepsy. *Epilepsia.* 2011;52(7):1331–40.

172. French JA, Krauss GL, Biton V, Squillacote D, Yang H, Laurenza A, et al. Adjunctive perampanel for refractory partial-onset seizures. *Neurology* [Internet]. 2012;79(6):589 LP-596. Available from: <http://n.neurology.org/content/79/6/589.abstract>
173. French JA, Krauss GL, Steinhoff BJ, Squillacote D, Yang H, Kumar D, et al. Evaluation of adjunctive perampanel in patients with refractory partial-onset seizures: Results of randomized global phase III study 305. *Epilepsia*. 2013;54(1):117–25.
174. Steinhoff BJ, Bacher M, Bast T, Kornmeier R, Kurth C, Scholly J, et al. First clinical experiences with perampanel-The Kork experience in 74 patients. *Epilepsia*. 2014;55(SUPPL.1):16–8.
175. Hendrich J, Van Minh AT, Hebllich F, Nieto-Rostro M, Watschinger K, Striessnig J, et al. Pharmacological disruption of calcium channel trafficking by the  $\alpha 2\delta$  ligand gabapentin. *Proc Natl Acad Sci U S A*. 2008;105(9):3628–33.
176. Silverman RB, Andruszkiewicz R, Nanavati SM, Silverman RB, Silverman RB, Taylor CP, et al. 3-Alkyl-4-aminobutyric Acids: The First Class of Anticonvulsant Agents That Activates L-Glutamic Acid Decarboxylase. *J Med Chem*. 1991;34(7):2295–8.
177. Taylor CP, Vartanian MG, Andruszkiewicz R, Silverman RB. 3-Alkyl GABA and 3-alkylglutamic acid analogues: two new classes of anticonvulsant agents. *Epilepsy Res*. 1992;11(2):103–10.
178. Panebianco M, Al-Bachari S, Weston J, Hutton JL, Marson AG. Gabapentin add-on treatment for drug-resistant focal epilepsy. *Cochrane Database Syst Rev*. 2018;2018(10).
179. Griffin A, Krasniak C, Baraban SC. Advancing epilepsy treatment through personalized genetic zebrafish models. In: *Progress in Brain Research* [Internet]. 1st ed. Elsevier; 2016. p. 195–207. Available from: <http://dx.doi.org/10.1016/bs.pbr.2016.03.012>
180. Bialer M, Johannessen SI, Levy RH, Perucca E, Tomson T, White HS. Progress report on new antiepileptic drugs: A summary of the Thirteenth Eilat Conference on New Antiepileptic Drugs and Devices (EILAT XIII). *Epilepsia*. 2017;58(2):181–221.
181. Roth GA, Feigin VL, Nguyen G, Cercy K, Johnson CO, Alam T, et al. Global, regional, and country-specific lifetime risks of stroke, 1990 and 2016. *N Engl J Med*. 2018;379(25):2429–37.
182. Bang OY, Ovbiagele B, Kim JS. Nontraditional risk factors for ischemic stroke: An update. *Stroke*. 2015;46(12):3571–8.
183. Huang H, Chen YM, Zhu F, Tang ST, Xiao JD, Li LL, et al. Down-regulated Na<sup>+</sup>/K<sup>+</sup>-ATPase

- activity in ischemic penumbra after focal cerebral ischemia/reperfusion in rats. *Int J Clin Exp Pathol.* 2015;8(10):12708–17.
184. Li LH, Tian XR, Hu ZP. The key target of neuroprotection after the onset of ischemic stroke: Secretory pathway Ca<sup>2+</sup>-ATPase 1. *Neural Regen Res.* 2015;10(8):1271–8.
185. O'Donnell ME. Blood-brain barrier Na transporters in ischemic stroke. In: *Advances in Pharmacology.* 2014. p. 113–46.
186. Wilkins HM, Swerdlow RH. TNF $\alpha$  in cerebral ischemia: Another stroke against you? *J Neurochem.* 2015;132(4):369–72.
187. Thornton P, Pinteaux E, Gibson RM, Allan SM, Rothwell NJ. Interleukin-1-induced neurotoxicity is mediated by glia and requires caspase activation and free radical release. *J Neurochem.* 2006;98(1):258–66.
188. Szabo K, Förster A, Jäger T, Kern R, Griebe M, Hennerici MG, et al. Hippocampal lesion patterns in acute posterior cerebral artery stroke: Clinical and MRI findings. *Stroke.* 2009;40(6):2042–5.
189. Li J, Hu WL. Bilateral hippocampal abnormalities in magnetic resonance imaging in transient global amnesia. *Am J Emerg Med.* 2013;31(4):1–3.
190. Takahashi S, Higano S, Kurihara N, Mugikura S, Sakamoto K, Nomura H, et al. Correlation of lesions in the hippocampal region noted on MR images with clinical features. *Eur Radiol.* 1997;7(2):281–6.
191. Al-Qazzaz NK, Ali SH, Ahmad SA, Islam S, Mohamad K. Cognitive impairment and memory dysfunction after a stroke diagnosis: A post-stroke memory assessment. *Neuropsychiatr Dis Treat.* 2014;10:1677–91.
192. Baumgartner P, El Amki M, Bracko O, Luft AR, Wegener S. Sensorimotor stroke alters hippocampo-thalamic network activity. *Sci Rep [Internet].* 2018;8(1):1–11. Available from: <http://dx.doi.org/10.1038/s41598-018-34002-9>
193. Ouhaz Z, Ba-M'hamed S, Mitchell AS, Elidrissi A, Bennis M. Behavioral and cognitive changes after early postnatal lesions of the rat mediodorsal thalamus. *Behav Brain Res [Internet].* 2015;292:219–32. Available from: <http://dx.doi.org/10.1016/j.bbr.2015.06.017>
194. Dalrymple-Alford JC, Harland B, Loukavenko EA, Perry B, Mercer S, Collings DA, et al. Anterior

- thalamic nuclei lesions and recovery of function: Relevance to cognitive thalamus. *Neurosci Biobehav Rev* [Internet]. 2015;54:145–60. Available from: <http://dx.doi.org/10.1016/j.neubiorev.2014.12.007>
195. Feigin VL, Nichols E, Alam T, Bannick MS, Beghi E, Blake N, et al. Global, regional, and national burden of neurological disorders, 1990–2016: a systematic analysis for the Global Burden of Disease Study 2016. *Lancet Neurol*. 2019;18(5):459–80.
  196. Macrae IM, Allan SM. Stroke: The past, present and future. *Brain Neurosci Adv*. 2018;2:239821281881068.
  197. da Silva-Candal A, Pérez-Díaz A, Santamaría M, Correa-Paz C, Rodríguez-Yáñez M, Ardá A, et al. Clinical validation of blood/brain glutamate grabbing in acute ischemic stroke. *Ann Neurol*. 2018;84(2):260–73.
  198. Ballarin B, Tymianski M. Discovery and development of NA-1 for the treatment of acute ischemic stroke. *Acta Pharmacol Sin* [Internet]. 2018;39(5):661–8. Available from: <http://dx.doi.org/10.1038/aps.2018.5>
  199. Hill MD, Goyal M, Menon BK, Nogueira RG, McTaggart RA, Demchuk AM, et al. Efficacy and safety of nerinetide for the treatment of acute ischaemic stroke (ESCAPE-NA1): a multicentre, double-blind, randomised controlled trial. *Lancet*. 2020;395(10227):878–87.
  200. Opitz A, Falchier A, Linn GS, Milham MP, Schroeder CE. Limitations of ex vivo measurements for in vivo neuroscience. *Proc Natl Acad Sci U S A*. 2017;114(20):5243–6.
  201. Carter M, Shieh JC. Guide to Research Techniques in Neuroscience. 2010. 91-118 p.
  202. Kornreich BG. The patch clamp technique: Principles and technical considerations. *J Vet Cardiol*. 2007;9(1):25–37.
  203. Nick B. Standen, Peter T. A. Gray Michael JW. Using Microelectrodes. In: *Microelectrode Techniques: The Plymouth Workshop Handbook*. 1997.
  204. Gunhanlar N, Shpak G, Kroeg M Van Der, Gouty-colomer LA, Munshi ST, Lendemeijer B, et al. A simplified protocol for differentiation of electrophysiologically mature neuronal networks from human induced pluripotent stem cells. *Mol Psychiatry*. 2018;23:1336–44.
  205. Geddes LA. *Electrodes and the Measurement of Bioelectric Events*. 1972.

206. Feber J, Stegenga J, Rutten WLC. The Effect of Slow Electrical Stimuli to Achieve Learning in Cultured Networks The Effect of Slow Electrical Stimuli to Achieve Learning in Cultured Networks of Rat Cortical Neurons. *PLoS One*. 2010;5(1).
207. Potter SM, Wagenaar DA, DeMarse TB. Closing the Loop: Stimulation Feedback Systems for Embodied MEA Cultures. In: *Advances in Network Electrophysiology*. New York: Springer; 2006. p. 215–42.
208. van Hooijdonk LWA, Ichwan M, Dijkmans TF, Schouten TG, de Backer MWA, Adan RAH, et al. Lentivirus-mediated transgene delivery to the hippocampus reveals sub-field specific differences in expression. *BMC Neurosci*. 2009;10(2):1–19.
209. Tinning PW, Franssen AJP., Hridi SU, Bushell TJ, Mcconnell G. A 340/380 nm light-emitting diode illuminator for Fura-2 AM ratiometric Ca<sup>2+</sup> imaging of live cells with better than 5 nM precision.pdf.
210. Grienberger C, Konnerth A. Imaging Calcium in Neurons. *Neuron* [Internet]. 2012;73(5):862–85. Available from: <http://dx.doi.org/10.1016/j.neuron.2012.02.011>
211. Teichert RW, Smith NJ, Raghuraman S, Yoshikami D, Light AR, Olivera BM. Functional profiling of neurons through cellular neuropharmacology. *Proc Natl Acad Sci U S A* [Internet]. 2012;109(5):1388–95. Available from: <http://www.pubmedcentral.nih.gov/articlerender.fcgi?artid=3277115&tool=pmcentrez&rendertype=abstract>
212. Grewe BF, Langer D, Kasper H, Kampa BM, Helmchen F. High-speed in vivo calcium imaging reveals neuronal network activity with near-millisecond precision. *Nat Methods*. 2010;7(5):399–405.
213. Stosiek C, Garaschuk O, Holthoff K, Konnerth A. In vivo two-photon calcium imaging of neuronal networks. *Proc Natl Acad Sci U S A* [Internet]. 2003;100(12):7319–24. Available from: [http://www.ncbi.nlm.nih.gov/sites/entrez?Db=pubmed&DbFrom=pubmed&Cmd=Link&LinkName=pubmed\\_pubmed&LinkReadableName=RelatedArticles&IdsFromResult=12777621&ordinalpos=3&itool=EntrezSystem2.PEntrez.Pubmed.Pubmed\\_ResultsPanel.Pubmed\\_RVDocSum%5Cnhttp://www.ncbi](http://www.ncbi.nlm.nih.gov/sites/entrez?Db=pubmed&DbFrom=pubmed&Cmd=Link&LinkName=pubmed_pubmed&LinkReadableName=RelatedArticles&IdsFromResult=12777621&ordinalpos=3&itool=EntrezSystem2.PEntrez.Pubmed.Pubmed_ResultsPanel.Pubmed_RVDocSum%5Cnhttp://www.ncbi)

214. Dorn A, Hermann F, Ebneith A, Bothmann H, Trube G, Christensen K, et al. Evaluation of a High-Throughput Fluorescence Assay Method for hERG Potassium Channel Inhibition. *2005*;339–47.
215. Baxter DF, Kirk M, Garcia AF, Raimondi A, Holmqvist MH, Flint KF, et al. A novel membrane potential-sensitive fluorescent dye improves cell-based assays for ion channels.pdf. *J Biomol Screen*. 2002;7(1).
216. Herron TJ, Lee T, Jalife J. Optical Imaging of Voltage and Calcium in Cardiac Cells & Tissues. *Circ Res*. 2012;110(4):609–23.
217. Girouard SD, Kenneth MS, Laurita R, Rosenbaum DS. Unique Properties of Cardiac Action Potentials Recorded with Voltage-Sensitive Dyes. *J Cardiovasc Electrophysiol*. 1996;7(11).
218. Fairless R, Beck A, Kravchenko M, Williams SK, Wissenbach U, Diem R, et al. Membrane Potential Measurements of Isolated Neurons Using a Voltage-Sensitive Dye. *PLoS One*. 2013;8(3).
219. Obaid AL, Loew LM, Wuskell JP, Salzberg BM. Novel naphthylstyryl-pyridinium potentiometric dyes offer advantages for neural network analysis. *2004*;134:179–90.
220. Michel K, Michaelis M, Mazzuoli G, Mueller K, Berghe P Vanden, Schemann M. Fast calcium and voltage-sensitive dye imaging in enteric neurones reveal calcium peaks associated with single action potential discharge. *2011*;24:5941–7.
221. Zhou W-L, Short SM, Rich MT, Oikonomou KD, Singh MB, Sterjanaj E V., et al. Branch specific and spike-order specific action potential invasion in basal, oblique, and apical dendrites of cortical pyramidal neurons. *Neurophotonics* [Internet]. 2014;2(2):021006. Available from: <http://neurophotonics.spiedigitallibrary.org/article.aspx?doi=10.1117/1.NPh.2.2.021006>
222. Yang S, Yang S, Moreira T, Hoffman G, Carlson GC, Bender KJ, et al. Interlamellar CA1 network in the hippocampus. *Proc Natl Acad Sci* [Internet]. 2014;111(35):12919–24. Available from: <http://www.pnas.org/cgi/doi/10.1073/pnas.1405468111>
223. Wester JC, Contreras D. Columnar Interactions Determine Horizontal Propagation of Recurrent Network Activity in Neocortex. *J Neurosci* [Internet]. 2012;32(16):5454–71. Available from: <http://www.jneurosci.org/cgi/doi/10.1523/JNEUROSCI.5006-11.2012>
224. Fehérvári TD, Okazaki Y, Sawai H, Yagi T. In vivo voltage-sensitive dye study of lateral



spreading of cortical activity in mouse primary visual cortex induced by a current impulse. PLoS One. 2015;10(7).

225. Carlson GC, Coulter DA. In vitro functional imaging in brain slices using fast voltage-sensitive dye imaging combined with whole-cell patch recording. *Nat Protoc.* 2008;3(2):249–55.
226. Waggoner AS, Wang CH, Tolles RL. Mechanism of Potential-Dependent Light Absorption Changes of Lipid Bilayer Membranes in the Presence of Cyanine and Oxonol Dyes. *J Membr Biol.* 1977;33(1):109–40.
227. Loew LM. Design and Use of Organic Voltage Sensitive Dyes. In: *Membrane Potential Imaging in the Nervous System; Methods and Applications.* Springer; 2011. p. 13–23.
228. Clarke RJ, Zouni A, Holzwarth JF. Voltage Sensitivity of the Fluorescent Probe RH421 in a Model Membrane System. *Biophys J.* 1995;68:1406–15.
229. Miiller W, Windisch H, Tritthart HA. Fluorescent styryl dyes applied as fast optical probes of cardiac action potential. *Eur Biophys J.* 1986;14:103–11.
230. Fluhler E, Burnham VG, Loew LM. Spectra , Membrane Binding , and Potentiometric Responses of New Charge Shift Probest. *Biochemistry.* 1985;24:5749–55.
231. Loew LM, Scully S, Simpson L, Waggoner AS. Evidence for a charge-shift electrochromic mechanism in a probe of membrane potential.pdf. *Nature.* 1979;281.
232. Carter M, Shieh J. Manipulating Neural Activity. In: *Guide to Research Techniques in Neuroscience (Second Edition).* Academic Press; 2015. p. 185–201.
233. Samulski RJ, Muzyczka N. AAV-Mediated Gene Therapy for Research and Therapeutic Purposes. *Annu Rev Virol.* 2014;1:427–51.
234. Dekelver RC, Choi VM, Moehle EA, Paschon DE, Hockemeyer D, Meijnsing SH, et al. Functional genomics , proteomics , and regulatory DNA analysis in isogenic settings using zinc finger nuclease-driven transgenesis into a safe harbor locus in the human genome. *Cold Spring Harb Lab Press.* 2010;20:1133–42.
235. Daya S, Berns KI. Gene Therapy Using Adeno-Associated Virus Vectors. *Clin Microbiol Rev.* 2008;21(4):583–93.
236. Sarkis C, Serguera C, Petres S, Buchet D, Ridet J, Edelman L, et al. Efficient transduction of

- neural cells in vitro and in vivo by a baculovirus-derived vector. *Proc Natl Acad Sci USA*. 2000;97(26):14638–43.
237. Ellis BL, Hirsch ML, Barker JC, Connelly JP, Iii RJS, Porteus MH. A survey of ex vivo / in vitro transduction efficiency of mammalian primary cells and cell lines with Nine natural adeno-associated virus ( AAV1-9 ) and one engineered adeno-associated virus serotype. *Virology*. 2013;10(74):1–10.
238. Klein RL, Meyer EM, Peel AL, Zolotukhin S, Meyers C, Muzyczka N, et al. Neuron-Specific Transduction in the Rat Septohippocampal or Nigrostriatal Pathway by Recombinant Adeno-associated Virus Vectors. *Experimental Neurol*. 1998;194(150):183–94.
239. Nayak S, Herzog RW. Progress and Prospects: Immune Responses to Viral Vectors. *Gene Ther*. 2010;17(3):295–304.
240. Sahoo SK, Labhasetwar V. Nanotech approaches to drug delivery and imaging. *Drug Discov Today*. 2003;8(24):1112–20.
241. Bedu-Addo FK, Uang LH. Effect of Matrix Lipid Chain Length on Liposomes Containing Cholesterol and Ganglioside G M1 : Implications in Drug Delivery AND. *J Pharm Sci*. 1996;85(7):714–9.
242. Felgner JH, Kumar R, Sridhar CN, Wheeler CJ, Tsai YJ, Border R, et al. Enhanced Gene Delivery and Mechanism Studies with a Novel Series of Cationic Lipid Formulations \*. *J Biol Chem*. 1994;269(4):2550–61.
243. Felgner PL, Gadek TR, Holm M, Roman R, Chan HW, Wenz M, et al. Lipofection : A highly efficient , lipid-mediated DNA-transfection procedure. *Proc Natl Acad Sci USA*. 1987;84(November):7413–7.
244. Papahadjopoulos D, Poste G, Schaeffer B. Fusion of mammalian cells by unilamellar lipid vesicles: Influence of lipid surface charge, fluidity and cholesterol. *Biochim Biophys Acta - Mol Cell Res*. 1973;323:23–42.
245. Bareford LM, Swaan PW. ENDOCYTIC MECHANISMS FOR TARGETED DRUG DELIVERY. *Adv Drug Deliv Rev*. 2007;59(8):748–58.
246. Souza VMD, Bareford LM, Ray A, Swaan PW. Cytoskeletal scaffolds regulate riboflavin endocytosis and recycling in placental trophoblasts B. *J Nutr Biochem*. 2006;17:821–9.

247. Tarahovsky YS, Koynova R, Macdonald RC. DNA Release from Lipoplexes by Anionic Lipids : Correlation with Lipid Mesomorphism , Interfacial Curvature , and Membrane Fusion. *Biophys J*. 2004;87:1054–64.
248. Pellegrino C, Gubkina O, Schaefer M, Becq H, Ludwig A, Mukhtarov M, et al. Knocking down of the KCC2 in rat hippocampal neurons increases intracellular chloride concentration and compromises neuronal survival. *J Physiol*. 2011;589(10):2475–96.
249. Balducci C, Mancini S, Minniti S, La Vitola P, Zotti M, Sancini G, et al. Multifunctional Liposomes Reduce Brain  $\beta$ -Amyloid Burden and Ameliorate Memory Impairment in Alzheimer's Disease Mouse Models. *J Neurosci*. 2014;34(42):14022–31.
250. Matsuoka Y, Saito M, LaFrancois J, Gaynor K, Olm V, Wang L, et al. Novel therapeutic approach for the treatment of Alzheimer's disease by peripheral administration of agents with an affinity to  $\beta$ -amyloid. *J Neurosci* [Internet]. 2003;23(1):29–33. Available from: [http://www.ncbi.nlm.nih.gov/entrez/query.fcgi?cmd=Retrieve&db=PubMed&dopt=Citation&list\\_uids=12514198](http://www.ncbi.nlm.nih.gov/entrez/query.fcgi?cmd=Retrieve&db=PubMed&dopt=Citation&list_uids=12514198)<http://www.jneurosci.org/cgi/reprint/23/1/29.pdf>
251. Spuch C, Navarro C. Liposomes for Targeted Delivery of Active Agents against Neurodegenerative Diseases (Alzheimer's Disease and Parkinson's Disease). *J Drug Deliv* [Internet]. 2011;1–12. Available from: [http://www.ncbi.nlm.nih.gov/entrez/query.fcgi?cmd=Retrieve&db=PubMed&dopt=Citation&list\\_uids=12514198](http://www.ncbi.nlm.nih.gov/entrez/query.fcgi?cmd=Retrieve&db=PubMed&dopt=Citation&list_uids=12514198)<http://www.jneurosci.org/cgi/reprint/23/1/29.pdf>
252. Qu M, Lin Q, He S, Wang L, Fu Y, Zhang Z, et al. A brain targeting functionalized liposomes of the dopamine derivative N-3,4-bis(pivaloyloxy)-dopamine for treatment of Parkinson's disease. *J Control Release* [Internet]. 2018;277:173–82. Available from: <https://doi.org/10.1016/j.jconrel.2018.03.019>
253. Yuan Y, Seong E, Yuan L, Singh D, Arikath J. Differential regulation of apical–basolateral dendrite outgrowth by activity in hippocampal neurons. *Front Cell Neurosci*. 2015;9(August):1–8.
254. dos Santos Rodrigues B, Oue H, Banerjee A, Kanekiyo T, Singh J. Dual functionalized liposome-mediated gene delivery across triple co-culture blood brain barrier model and specific in vivo neuronal transfection. *J Control Release* [Internet]. 2018;286:264–78. Available from: <https://doi.org/10.1016/j.jconrel.2018.07.043>

255. Akbarzadeh A, Rezaei-Sadabady R, Davaran S, Joo SW, Zarghami N, Hanifehpour Y, et al. Liposome: Classification, preparation, and applications. *Nanoscale Res Lett* [Internet]. 2013;8(1):1–8. Available from: *Nanoscale Research Letters*
256. Sercombe L, Veerati T, Moheimani F, Wu SY, Sood AK, Hua S. Advances and challenges of liposome assisted drug delivery. *Front Pharmacol*. 2015;6:1–13.
257. Kube S, Hersch N, Naumovska E, Gensch T, Hendriks J, Franzen A, et al. Fusogenic Liposomes as Nano Carriers for Delivery of Intracellular Proteins. *Langmuir*. 2017;33(4):1051–9.
258. Feigin VL, Krishnamurthi R V., Theadom AM, Abajobir AA, Mishra SR, Ahmed MB, et al. Global, regional, and national burden of neurological disorders during 1990–2015: a systematic analysis for the Global Burden of Disease Study 2015. *Lancet Neurol*. 2017;16(11):877–97.
259. Prince M, Knapp M, Guerchet M, McCrone P, Prina M, Comas-Herrera A, et al. *Dementia UK Update*. 2014.
260. Wanna AGB, Noble JH, Carlson ML, Gifford H, Dietrich MS, Haynes DS, et al. The burden of neurological disease in the United States: A summary report and call to action. *Ann Neurol*. 2017;81(4):479–84.
261. Choi DW, Armitage R, Brady LS, Coetzee T, Fisher W, Hyman S, et al. Medicines for the mind: Policy-based “Pull” incentives for creating breakthrough CNS drugs. *Neuron* [Internet]. 2014;84(3):554–63. Available from: <http://dx.doi.org/10.1016/j.neuron.2014.10.027>
262. Marshall JF. *Fabrication of Semiconductor Devices Utilizing Ion Implantation* [Internet]. US3122817, 1977. Available from: <https://patents.google.com/patent/US3122817A/en>
263. Bassous E, Taub HH, Kuhn L. Ink jet printing nozzle arrays etched in silicon. *Appl Phys Lett*. 1977;31(2):135–7.
264. Gadegaard N, Mosler S, Larsen NB. Biomimetic polymer nanostructures by injection molding. *Macromol Mater Eng*. 2003;288(1):76–83.
265. Kane RS, Stroock AD, Li Jeon N, Ingber DE, Whitesides GM. Soft Lithography and Microfluidics. In: *Optical Biosensors*. Elsevier; 2002. p. 571–95.
266. Kim, Enoch Younan, Xia & George W. Polymer microstructures formed by moulding in capillaries. *Nature*. 1995;376:581–4.

267. Xia Y, Kim E, Zhao X, Rogers JA, Prentiss M, Whitesides GM. Complex Optical Surfaces Formed by Replica Molding Against Elastomeric Masters. *Science* (80- ). 1996;273(5273):347–9.
268. Kumar A, Whitesides GM. Features of gold having micrometer to centimeter dimensions can be formed through a combination of stamping with an elastomeric stamp and an alkanethiol “ink” followed by chemical etching. *Appl Phys Lett*. 1993;63(14):2002–4.
269. Terry SC, Herman JH, Angell JB. A Gas Chromatographic Air Analyzer Fabricated on a Silicon Wafer. *IEEE Trans Electron Devices*. 1979;26(12):1880–6.
270. Jerman H. Electrically-activated, micromachined diaphragm valves. *Micromechanics and MEMS: Classic and Seminal Papers to 1990*. 1997. p. 363–7.
271. Smits JG. Piezoelectric micropump with three valves working peristaltically. *Sensors Actuators A Phys*. 1990;21(1–3):203–6.
272. Berg JM, Anderson R, Anaya M, Lahlouh B, Holtz M, Dallas T. A two-stage discrete peristaltic micropump. *Sensors Actuators, A Phys*. 2003;104(1):6–10.
273. Halldorsson S, Lucumi E, Gómez-Sjöberg R, Fleming RMT. Advantages and challenges of microfluidic cell culture in polydimethylsiloxane devices. *Biosens Bioelectron* [Internet]. 2015;63:218–31. Available from: <http://dx.doi.org/10.1016/j.bios.2014.07.029>
274. Taylor AM, Rhee SW, Tu CH, Cribbs DH, Cotman CW, Jeon NL. Microfluidic Multicompartment Device for Neuroscience Research. *Langmuir*. 2003;19(5):1551–6.
275. Robertson G, Bushell TJ, Zagnoni M. Chemically induced synaptic activity between mixed primary hippocampal co-cultures in a microfluidic system. *Integr Biol* [Internet]. 2014;6(6):636–44. Available from: <http://www.ncbi.nlm.nih.gov/pubmed/24796407>
276. Samson AJ, Robertson G, Zagnoni M, Connolly CN. Neuronal networks provide rapid neuroprotection against spreading toxicity. *Sci Rep* [Internet]. 2016;6:33746. Available from: <http://www.nature.com/articles/srep33746>
277. Honegger T, Thielen MI, Feizi S, Sanjana NE, Voldman J. Microfluidic neurite guidance to study structure-function relationships in topologically-complex population-based neural networks. *Sci Rep* [Internet]. 2016;6:28384. Available from: <http://www.nature.com/articles/srep28384>
278. Gao Y, Broussard J, Haque A, Revzin A, Lin T. Functional imaging of neuron–astrocyte

- interactions in a compartmentalized microfluidic device. *Microsystems Nanoeng* [Internet]. 2016;2(August 2015):15045. Available from: <http://www.nature.com/articles/micronano201545>
279. Shi M, Majumdar D, Gao Y, Brewer BM, Goodwin CR, McLean JA, et al. Glia Co-Culture with Neurons in Microfluidic Platforms Promotes the Formation and Stabilization of Synaptic Contacts. *Lab Chip* [Internet]. 2013;13(207890):3008–21. Available from: <http://pubs.rsc.org/en/Content/ArticleLanding/2013/LC/c3lc50249j%5Cnhttp://www.ncbi.nlm.nih.gov/pubmed/23736663>
280. Berdichevsky Y, Staley KJ, Yarmush ML. Building and manipulating neural pathways with microfluidics. *Lab Chip*. 2010;10(8):999–1004.
281. Bang S, Na S, Jang JM, Kim J, Jeon NL. Engineering-Aligned 3D Neural Circuit in Microfluidic Device. *Adv Healthc Mater*. 2016;5(1):159–66.
282. Campenot RB. Local control of neurite development by nerve growth factor. *Proc Natl Acad Sci U S A*. 1977;74(10):4516–9.
283. Taylor AM, Blurton-Jones M, Rhee SW, Cribbs DH, Cotman CW, Jeon NL. A microfluidic culture platform for CNS axonal injury, regeneration and transport. *Nat Methods*. 2005;2(8):599–605.
284. MacKerron C, Robertson G, Zagnoni M, Bushell TJ. A Microfluidic Platform for the Characterisation of CNS Active Compounds. *Sci Rep* [Internet]. 2017;7(1):1–11. Available from: <http://dx.doi.org/10.1038/s41598-017-15950-0>
285. Tarze A, Deniaud A, Le Bras M, Maillier E, Molle D, Larochette N, et al. GAPDH, a novel regulator of the pro-apoptotic mitochondrial membrane permeabilization. *Oncogene*. 2007;26(18):2606–20.
286. Taylor AM, Dieterich DC, Ito HT, Kim S a, Erin M. Schuman. Microfluidic local perfusion chambers for the visualization and manipulation of synapses. *Neuron*. 2010;66(7491):57–68.
287. Benito E, Barco A. CREB's control of intrinsic and synaptic plasticity: implications for CREB-dependent memory models. *Trends Neurosci* [Internet]. 2010;33(5):230–40. Available from: <http://dx.doi.org/10.1016/j.tins.2010.02.001>
288. Pugazhenth S, Wang M, Pham S, Sze CI, Eckman CB. Downregulation of CREB expression in

- Alzheimer's brain and in A $\beta$ -treated rat hippocampal neurons. *Mol Neurodegener.* 2011;6(1):1–16.
289. N P, Mm P. Orientation of Neurite Electric Growth. *J Neurosci.* 1982;2(4):483–96.
290. Kamudzandu M, Köse-Dunn M, Evans MG, Fricker RA, Roach P. A micro-fabricated in vitro complex neuronal circuit platform . *Biomed Phys Eng Express.* 2019;5(4):045016.
291. Renault R, Sukenik N, Descroix S, Malaquin L, Viovy JL, Peyrin JM, et al. Combining microfluidics, optogenetics and calcium imaging to study neuronal communication in vitro. *PLoS One.* 2015;10(4):1–15.
292. Liu J, Sternberg AR, Ghiasvand S, Berdichevsky Y. Epilepsy-on-a-chip system for antiepileptic drug discovery. *IEEE Trans Biomed Eng.* 2019;66(5):1231–41.
293. Fernandes JTS, Chutna O, Chu V, Conde JP, Outeiro TF. A novel microfluidic cell co-culture platform for the study of the molecular mechanisms of Parkinson's disease and other synucleinopathies. *Front Neurosci.* 2016;10(NOV):1–11.
294. Bolognin S, Fossépré M, Qing X, Jarazo J, Ščančar J, Moreno EL, et al. 3D Cultures of Parkinson's Disease-Specific Dopaminergic Neurons for High Content Phenotyping and Drug Testing. *Adv Sci.* 2019;6(1):1–14.
295. Schwarz J, Bierbaum V, Merrin J, Frank T, Hauschild R, Bollenbach T, et al. A microfluidic device for measuring cell migration towards substrate-bound and soluble chemokine gradients. *Sci Rep.* 2016;6(November):1–12.
296. Cho H, Hashimoto T, Wong E, Hori Y, Wood LB, Zhao L, et al. Microfluidic chemotaxis platform for differentiating the roles of soluble and bound amyloid- $\beta$  on microglial accumulation. *Sci Rep [Internet].* 2013;3:1823. Available from: <http://www.pubmedcentral.nih.gov/articlerender.fcgi?artid=3650586&tool=pmcentrez&rendertype=abstract>
297. Dujardin S, Lecolle K, Caillierez R, Begard S, Zommer N, Lachaud C, et al. Neuron-to-neuron wild-type Tau protein transfer through a trans-synaptic mechanism: relevance to sporadic tauopathies. *Acta Neuropathol Commun [Internet].* 2014;2:14. Available from: <http://www.ncbi.nlm.nih.gov/pubmed/24479894>
298. Park J, Lee BK, Jeong GS, Hyun JK, Lee CJ, Lee S-H. Three-dimensional brain-on-a-chip with an

interstitial level of flow and its application as an in vitro model of Alzheimer's disease. *Lab Chip* [Internet]. 2014;15(1):141–50. Available from: <http://pubs.rsc.org/en/content/articlehtml/2015/lc/c4lc00962b%5Cnhttp://www.ncbi.nlm.nih.gov/pubmed/25317977>

299. Choi YJ, Chae S, Kim JH, Barald KF, Park JY, Lee SH. Neurotoxic amyloid beta oligomeric assemblies recreated in microfluidic platform with interstitial level of slow flow. *Sci Rep*. 2013;3:1–7.
300. Wu JW, Hussaini SA, Bastille IM, Rodriguez GA, Mrejeru A, Rilett K, et al. Neuronal activity enhances tau propagation and tau pathology in vivo. *Nat Neurosci* [Internet]. 2016;19(8):1085–92. Available from: <http://dx.doi.org/10.1038/nn.4328%5Cnhttp://10.1038/nn.4328%5Cnhttp://www.nature.com/neuro/journal/v19/n8/abs/nn.4328.html#supplementary-information>
301. Lee JS, Ryu J, Park CB. High-throughput analysis of alzheimer's  $\beta$ -amyloid aggregation using a microfluidic self-assembly of monomersf. *Anal Chem*. 2009;81(7):2751–9.
302. Harris J, Lee H, Vahidi B, Tu C, Cribbs D, Cotman C, et al. Non-plasma Bonding of PDMS for Inexpensive Fabrication of Microfluidic Devices. 2007;4–6.
303. Chan EKL, Yang C, Yuen MMF. UV-activated surface modification of photo-cleavage polymer for contact printing applications. *Proc - Electron Components Technol Conf*. 2008;1346–50.
304. Adly NY, Hassani H, Tran AQ, Balski M, Yakushenko A, Offenhäusser A, et al. Observation of chemically protected polydimethylsiloxane: Towards crack-free PDMS. *Soft Matter*. 2017;13(37):6297–303.
305. Phaniendra A, Jestadi DB, Periyasamy L. Free Radicals: Properties, Sources, Targets, and Their Implication in Various Diseases. *Indian J Clin Biochem*. 2015;30(1):11–26.
306. Ariano P, Zamburlin P, Gilardino A, Mortera R, Onida B, Tomatis M, et al. Interaction of spherical silica nanoparticles with neuronal cells: Size-dependent toxicity and perturbation of calcium homeostasis. *Small*. 2011;7(6):766–74.
307. Ritchie L, Tate R, Chamberlain LH, Robertson G, Zagnoni M, Sposito T, et al. Toll-like receptor 3 activation impairs excitability and synaptic activity via TRIF signalling in immature rat and human neurons . Short title : TLR3 activation impairs neuronal function . Strathclyde Institute



- of Pharmacy and Biomedical Sciences , Univer. Neuropharmacology. 2018;135:1–10.
308. Dauth S, Maoz BM, Sheehy SP, Hemphill MA, Murty T, Kate M, et al. Neurons derived from different brain regions are inherently different in vitro: A novel multi-regional Brain-On-A-Chip. *J Neurophysiol*. 2016;(Rm 321).
  309. Kanagasabapathi TT, Ciliberti D, Martinoia S, Wadman WJ, Decré MMJ. Dual-compartment neurofluidic system for electrophysiological measurements in physically segregated and functionally connected neuronal cell culture. *Front Neuroeng [Internet]*. 2011;4(October):13. Available from:  
<http://www.pubmedcentral.nih.gov/articlerender.fcgi?artid=3198030&tool=pmcentrez&rendertype=abstract>
  310. Killian NJ, Vernekar VN, Potter SM, Vukasinovic J. A device for long-term perfusion, imaging, and electrical interfacing of brain tissue in vitro. *Front Neurosci*. 2016;10(MAR):135.
  311. Badhiwala KN, Gonzales DL, Vercosa DG, Avants BW, Robinson JT. Microfluidics for Electrophysiology, Imaging, and Behavioral Analysis of Hydra. *bioRxiv [Internet]*. 2018;257691. Available from: <https://www.biorxiv.org/content/early/2018/02/08/257691>
  312. Scott A, Weir K, Easton C, Huynh W, Moody WJ, Folch A. Microfluidics for Electrophysiology, Imaging, and Behavioral Analysis of Hydra. 2014;13(4):527–35. Available from:  
<https://www.biorxiv.org/content/early/2018/02/08/257691>
  313. Tsytsarev V, Liao L-D, Kong KV, Liu Y-H, Erzurumlu RS, Olivo M, et al. Recent Progress in Voltage-Sensitive Dye Imaging for Neuroscience. *J Nanosci Nanotechnol [Internet]*. 2014;14(7):4733–44. Available from:  
<http://openurl.ingenta.com/content/xref?genre=article&issn=1533-4880&volume=14&issue=7&spage=4733>
  314. Fisher JAN, Barchi JR, Welle CG, Kim G-H, Kosterin P, Obaid AL, et al. Two-Photon Excitation of Potentiometric Probes Enables Optical Recording of Action Potentials From Mammalian Nerve Terminals In Situ. *J Neurophysiol [Internet]*. 2008;99(3):1545–53. Available from:  
<http://jn.physiology.org/cgi/doi/10.1152/jn.00929.2007>
  315. Adesnik H, Li G, During MJ, Pleasure SJ, Nicoll RA. NMDA receptors inhibit synapse unsilencing during brain development. *Proc Natl Acad Sci*. 2008;105(14):5597–602.

316. Fernandez-Ruiz A, Makarov VA, Herreras O. Sustained increase of spontaneous input and spike transfer in the CA3-CA1 pathway following long-term potentiation in vivo. *Front Neural Circuits* [Internet]. 2012;6(October):71. Available from: <http://www.ncbi.nlm.nih.gov/pubmed/23060752>
317. Madison D. Mechanisms Underlying Long-Term Potentiation Of Synaptic Transmission. *Annu Rev Neurosci*. 1991;14(1):379–97.
318. Stayte S, Vissel B. Advances in non-dopaminergic treatments for Parkinson’s disease. *Front Neurosci*. 2014;8(May):1–29.
319. Laferla FM, Green KN. Animal Models of Alzheimer Disease. 2012;1–13.
320. Blesa J, Phani S, Jackson-lewis V, Przedborski S. Classic and New Animal Models of Parkinson ’ s Disease. 2012;2012.
321. Laurijssens B, Aujard F, Rahman A. Animal models of Alzheimer’s disease and drug development. *Drug Discov Today Technol* [Internet]. 2013;10(3):e319–27. Available from: <http://dx.doi.org/10.1016/j.ddtec.2012.04.001>
322. Potashkin JA, Blume SR, Runkle NK. Limitations of Animal Models of Parkinson ’ s Disease. *Parkinsons Dis*. 2011;1–7.
323. Hyman SE. Animal Models of Neuropsychiatric Disorders. 2013;13(10):1161–9.
324. Neto XE, Leita XL, Sousa XDM, Alves X CJ, Ine X, Alencastre S. Compartmentalized Microfluidic Platforms : The Unrivaled Breakthrough of In Vitro Tools for Neurobiological Research. 2016;36(46):11573–84.
325. Gonzalez-Sulser A, Wang J, Queenan BN, Avoli M, Vicini S, Dzakpasu R. Hippocampal neuron firing and local field potentials in the in vitro 4-aminopyridine epilepsy model. *J Neurophysiol*. 2012;108(9):2568–80.
326. Spira ME, Hai A. Multi-electrode array technologies for neuroscience and cardiology. *Nat Nanotechnol* [Internet]. 2013;8(2):83–94. Available from: <http://dx.doi.org/10.1038/nnano.2012.265>
327. Fletcher TL, Camilli P De, Banker G. The Distribution of Synapsin I and Synaptophysin in Hippocampal Neurons Developing in Culture. *J Neurosci*. 1991;11(6):1617–26.

328. Tarsa L, Goda Y. Synaptophysin regulates activity-dependent synapse formation in cultured hippocampal neurons. *Proc Natl Acad Sci U S A*. 2002;99(2):1012–6.
329. Koizumi S, Fujishita K, Tsuda M, Shigemoto-Mogami Y, Inoue K. Dynamic inhibition of excitatory synaptic transmission by astrocyte-derived ATP in hippocampal cultures. *Proc Natl Acad Sci U S A* [Internet]. 2003;100(19):11023–8. Available from: <http://www.ncbi.nlm.nih.gov/pubmed/12958212>  
<http://www.ncbi.nlm.nih.gov/pmc/articles/PMC196920/pdf/10011023.pdf>
330. Penn Y, Segal M, Moses E. Network synchronization in hippocampal neurons. *Proc Natl Acad Sci* [Internet]. 2016;113(12):3341–6. Available from: <http://www.pnas.org/lookup/doi/10.1073/pnas.1515105113>
331. Salzberg BM. *Functional Imaging of Nervous Systems Using Voltage-Sensitive Dyes*. John Wiley Sons. 2009;
332. Grinvald A, Lieke EE, Frostig RD, Hildesheim R. Cortical Point-Spread Function and Long-Range Lateral Interactions Revealed by Real-Time Optical Imaging of Macaque Monkey Primary Visual Cortex. *J Neurosci*. 1994;14(May):2545–68.
333. Loew LM. Potentiometric dyes : Imaging electrical activity of cell membranes. *Pure Appl Chem*. 1996;68(7):1405–9.
334. Dinic J, Biverståhl H, Måler L, Parmryd I. Laurdan and di-4-ANEPPDHQ do not respond to membrane-inserted peptides and are good probes for lipid packing. *Biochim Biophys Acta - Biomembr* [Internet]. 2011;1808(1):298–306. Available from: <http://dx.doi.org/10.1016/j.bbamem.2010.10.002>
335. Kucukdereli H, Allen NJ, Lee AT, Feng A, Ozlu MI, Conatser LM, et al. Control of excitatory CNS synaptogenesis by astrocyte-secreted proteins Hevin and SPARC. 2011;
336. Fellin T, Carmignoto G. Neurone-to-astrocyte signalling in the brain represents a distinct multifunctional unit. *J Physiol*. 2004;559(Pt 1):3–15.
337. Bazargani N, Attwell D. Astrocyte calcium signaling: the third wave. *Nat Neurosci*. 2016;19(2):182–9.
338. Takahashi N, Takahara Y, Ishikawa D, Matsuki N, Ikegaya Y. Functional multineuron calcium imaging for systems pharmacology. *Anal Bioanal Chem*. 2010;398(1):211–8.

339. Haak LL. Metabotropic glutamate receptor modulation of glutamate responses in the suprachiasmatic nucleus. *J Neurophysiol.* 1999;81(3):1308–17.
340. Bushell TJ, Plevin R, Cobb S, Irving AJ. Characterization of proteinase-activated receptor 2 signalling and expression in rat hippocampal neurons and astrocytes. *Neuropharmacology.* 2006;50(6):714–25.
341. Kononov A V., Ball N V., Zinchenko VP. Variability of calcium responses to agonists of glutamate receptors in hippocampal neurons. *Biochem Suppl Ser A Membr Cell Biol.* 2011;5(2):153–61.
342. Shadlen MN, Newsome WT. The Variable Discharge of Cortical Neurons: Implications for Connectivity, Computation, and Information Coding. *J Neurosci.* 1998;18(10):3870–96.
343. Walz W, Hertz L. Comparison between fluxes of potassium and of chloride in astrocytes in primary cultures. *Brain Res.* 1983;277(2):321–8.
344. Bellot-Saez A, Kékesi O, Morley JW, Buskila Y. Astrocytic modulation of neuronal excitability through K<sup>+</sup> spatial buffering. *Neurosci Biobehav Rev* [Internet]. 2017;77:87–97. Available from: <http://dx.doi.org/10.1016/j.neubiorev.2017.03.002>
345. Lock JT, Parker I, Smith IF. A comparison of fluorescent Ca<sup>2+</sup> indicators for imaging local Ca<sup>2+</sup> signals in cultured cells. *Cell Calcium.* 2015;58(6):638–48.
346. Martens MA, Boesmans W, Vanden Berghe P. Calcium imaging at kHz frame rates resolves millisecond timing in neuronal circuits and varicosities. *Biomed Opt Express* [Internet]. 2014;5(8):2648–61. Available from: <http://www.ncbi.nlm.nih.gov/pubmed/25136492>  
<http://www.pubmedcentral.nih.gov/articlerender.fcgi?artid=PMC4132995>
347. Jin L, Millard AC, Wuskell JP, Dong X, Wu D, Clark HA, et al. Characterization and application of a new optical probe for membrane lipid domains. *Biophys J.* 2006;90(7):2563–75.
348. Fisher JAN, Barchi JR, Welle CG, Kim G, Kosterin P, Li A, et al. Two-Photon Excitation of Potentiometric Probes Enables Optical Recording of Action Potentials From Mammalian Nerve Terminals In Situ. 2018;1545–53.
349. Müller C, Beck H, Coulter D, Remy S. Inhibitory Control of Linear and Supralinear Dendritic Excitation in CA1 Pyramidal Neurons. *Neuron.* 2012;75(5):851–64.

350. Ang CW, Carlson GC, Coulter DA. Massive and Specific Dysregulation of Direct Cortical Input to the Hippocampus in Temporal Lobe Epilepsy Chyze. *J Neurosci*. 2006;26(46):11850–6.
351. Hamad MIK, Krause M, Wahle P. Improving AM ester calcium dye loading efficiency. *J Neurosci Methods* [Internet]. 2015;240:48–60. Available from: <http://dx.doi.org/10.1016/j.jneumeth.2014.11.010>
352. Shynkar V V., Klymchenko AS, Duportail G, Demchenko AP, Mély Y. Two-color fluorescent probes for imaging the dipole potential of cell plasma membranes. *Biochim Biophys Acta - Biomembr*. 2005;1712(2):128–36.
353. Fromherz P, Hübener G, Kuhn B, Hinner MJ. ANNINE-6plus, a voltage-sensitive dye with good solubility, strong membrane binding and high sensitivity. *Eur Biophys J*. 2008;37(4):509–14.
354. Thonhoff JR, Lou DI, Jordan PM, Zhao X, Wu P. Compatibility of human fetal neural stem cells with hydrogel biomaterials in vitro. *Brain Res*. 2008;1187(Jan):42–51.
355. Leão RN, Reis A, Emirandetti A, Lewicka M, Hermanson O, Fisahn A. A voltage-sensitive dye-based assay for the identification of differentiated neurons derived from embryonic neural stem cell cultures. *PLoS One*. 2010;5(11).
356. Yu EP, Dengler CG, Frausto SF, Putt ME, Yue C, Takano H, et al. Protracted postnatal development of sparse, specific dentate granule cell activation in the mouse hippocampus. *J Neurosci* [Internet]. 2013;33(7):2947–60. Available from: <http://www.pubmedcentral.nih.gov/articlerender.fcgi?artid=3711669&tool=pmcentrez&rendertype=abstract>
357. Denk W, Strickler JH, Webb WW. Two-photon laser scanning fluorescence microscopy. *Science* (80- ). 1990;248(4951):73–6.
358. Siegel MS, Isacoff EY. A genetically encoded optical probe of membrane voltage. *Neuron*. 1997;19(4):735–41.
359. Ataka K, Pieribone VA. A genetically targetable fluorescent probe of channel gating with rapid kinetics. *Biophys J*. 2002;82(January):509–16.
360. Kang BE, Baker BJ. Pado, a fluorescent protein with proton channel activity can optically monitor membrane potential, intracellular pH, and map gap junctions. *Sci Rep* [Internet]. 2016;6(October 2015):10–4. Available from: <http://dx.doi.org/10.1038/srep23865>

361. Lou S, Adam Y, Weinstein EN, Williams E, Williams K, Parot V, et al. Genetically targeted all-optical electrophysiology with a transgenic cre-dependent optopatch mouse. *J Neurosci*. 2016;36(43):11059–73.
362. Ledgerwood CJ, Greenwood SM, Brett RR, Pratt JA, Bushell TJ. Cannabidiol inhibits synaptic transmission in rat hippocampal cultures and slices via multiple receptor pathways. *Br J Pharmacol*. 2011;162(1):286–94.
363. Kullmann PHM, Ene FA, Kandler K. Glycinergic and GABAergic calcium responses in the developing lateral superior olive. *Eur J Neurosci*. 2002;15(7):1093–104.
364. Pook P, Brugger F, Hawkins NS, Clark KC, Watkins JC, Evans RH. A Comparison of the Actions of Agonists and Antagonists at Non-Nmda Receptors of C-Fibers and Motoneurons of the Immature Rat Spinal-Cord Invitro. *Br J Pharmacol*. 1993;108(1):179–84.
365. Miller LJ, Gillette MU. New perspectives on neuronal development via microfluidic environments. *Trends Neurosci*. 2012;35(12):752–61.
366. Fucile S, Miledi R, Eusebi F. Effects of cyclothiazide on GluR1/AMPA receptors. *Proc Natl Acad Sci U S A*. 2006;103(8):2943–7.
367. Bhattacharjee N, Li N, Keenan TM, Folch A. A neuron-benign microfluidic gradient generator for studying the response of mammalian neurons towards axon guidance factors. *Integr Biol*. 2010;2(0):669–79.
368. Jeon KJ, Park SH, Shin JW, Kang YG, Hyun JS, Oh MJ, et al. Combined effects of flow-induced shear stress and micropatterned surface morphology on neuronal differentiation of human mesenchymal stemcells. *J Biosci Bioeng [Internet]*. 2014;117(2):242–7. Available from: <http://dx.doi.org/10.1016/j.jbiosc.2013.08.002>
369. LaPlaca MC, Prado GR, Cullen DK, Irons HR. High rate shear insult delivered to cortical neurons produces heterogeneous membrane permeability alterations. *Annu Int Conf IEEE Eng Med Biol - Proc*. 2006;2384–7.
370. Maneshi MM, Maki B, Gnanasambandam R, Belin S, Popescu GK, Sachs F, et al. Mechanical stress activates NMDA receptors in the absence of agonists. *Sci Rep [Internet]*. 2017;7(November 2016):1–10. Available from: <http://dx.doi.org/10.1038/srep39610>
371. Fujii Y, Maekawa S, Morita M. Astrocyte calcium waves propagate proximally by gap junction

and distally by extracellular diffusion of ATP released from volume-regulated anion channels. *Sci Rep* [Internet]. 2017;7(1):1–15. Available from: <http://dx.doi.org/10.1038/s41598-017-13243-0>

372. Maneshi MM, Sachs F, Hua SZ. A Threshold Shear Force for Calcium Influx in an Astrocyte Model of Traumatic Brain Injury. *J Neurotrauma* [Internet]. 2015;32(13):1020–9. Available from: <http://online.liebertpub.com/doi/10.1089/neu.2014.3677>
373. Gan J, Greenwood SM, Cobb SR, Bushell TJ. Indirect modulation of neuronal excitability and synaptic transmission in the hippocampus by activation of proteinase-activated receptor-2. *Br J Pharmacol*. 2011;163:984–94.
374. Molleman A. *Patch Clamping: An Introductory Guide To Patch Clamp Electrophysiology*. John Wiley & Sons; 2003.
375. Haas HL, Schaerer B, Vosmansky M. A simple perfusion chamber for the study of nervous tissue slices in vitro. *J Neurosci Methods*. 1979;1(4):323–5.
376. Toh YC, Voldman J. Multiplex Microfluidic Perfusion Identifies Shear Stress. *Differentiation*. 2010;(October):10–2.
377. Hughes JP, Rees SS, Kalindjian SB, Philpott KL. Principles of early drug discovery. *Br J Pharmacol*. 2011;162(6):1239–49.
378. Singh P, Doshi S, Spaethling JM, Hockenberry AJ, Patel TP, Geddes-Klein DM, et al. N-methyl-D-aspartate receptor mechanosensitivity is governed by C terminus of NR2B subunit. *J Biol Chem*. 2012;287(6):4348–59.
379. Koser DE, Thompson AJ, Foster SK, Dwivedy A, Pillai EK, Sheridan GK, et al. Mechanosensing is critical for axon growth in the developing brain. *Nat Neurosci*. 2016;19(12):1592–8.
380. Wang Y, Wang W, Li Z, Hao S, Wang B. A novel perspective on neuron study: damaging and promoting effects in different neurons induced by mechanical stress. *Biomech Model Mechanobiol*. 2016;15(5):1019–27.
381. Forsythe ID, Coates RT. A chamber for electrophysiological recording from cultured neurones allowing perfusion and temperature control. *J Neurosci Methods*. 1988;25(1):19–27.
382. Nicoll RA, Alger BE. A simple chamber for recording from submerged brain slices. *J Neurosci Methods*. 1981;4(2):153–6.

383. Frost White W, Victor Nadler J, Cotman CW. A perfusion chamber for the study of CNS physiology and pharmacology in vitro. *Brain Res.* 1978;152(3):591–6.
384. Ravin R, Morgan NY, Blank PS, Ravin N, Guerrero-Cazares H, Quinones-Hinojosa A, et al. Response to Blast-like Shear Stresses Associated with Mild Blast-Induced Brain Injury. *Biophys J* [Internet]. 2019;117(7):1167–78. Available from: <https://doi.org/10.1016/j.bpj.2019.07.052>
385. Wong AD, Ye M, Levy AF, Rothstein JD, Bergles DE, Searson PC. The blood-brain barrier: An engineering perspective. *Front Neuroeng.* 2013;6(JUL):1–22.
386. Cullen DK, Vukasinovic J, Glezer A, LaPlaca MC. High cell density three-dimensional neural co-cultures require continuous medium perfusion for survival. *Annu Int Conf IEEE Eng Med Biol - Proc.* 2006;636–9.
387. Rambani K, Vukasinovic J, Glezer A, Potter SM. Culturing thick brain slices - An interstitial 3D microperfusion system for enhanced viability. *J Neurosci Methods.* 2009;180(2):243–54.
388. Leveille F, El gaamouch F, Gouix E, Lecocq M, Lobner D, Nicole O, et al. Neuronal viability is controlled by a functional relation between synaptic and extrasynaptic NMDA receptors. *FASEB J* [Internet]. 2008;22(12):4258–71. Available from: <http://www.fasebj.org/cgi/doi/10.1096/fj.08-107268>
389. Ortuño-Sahagún D, González RM, Verdaguer E, Huerta VC, Torres-Mendoza BM, Lemus L, et al. Glutamate excitotoxicity activates the MAPK/ERK signaling pathway and induces the survival of rat hippocampal neurons in vivo. *J Mol Neurosci.* 2014;52(3):366–77.
390. Guthrie PB, Knappenberger J, Segal M, Bennett MVL, Charles AC, Kater SB. ATP Released from Astrocytes Mediates Glial Calcium Waves. *J Neurosci.* 1999;19(2):520–8.
391. van der Helm MW, van der Meer AD, Eijkel JCT, van den Berg A, Segerink LI. Micro fluidic organ-on-chip technology for blood- brain barrier research. *Tissue Barriers.* 2016;4(August):e1142493.
392. Zhang JM, Wang HK, Ye CQ, Ge W, Chen Y, Jiang ZL, et al. ATP Released by Astrocytes Mediates Glutamatergic Activity-Dependent Heterosynaptic Suppression. *Neuron.* 2003;40(5):971–82.
393. Pascual O, Casper KB, Kubera C, Zhang J, Revilla-Sanchez R, Sul J-Y, et al. Astrocytic Purinergic



- Signaling Coordinates Synaptic Networks. *Science* (80- ) [Internet]. 2005;310(5745):113–6. Available from: <http://www.sciencemag.org/cgi/doi/10.1126/science.1116916>
394. Gaub BM, Kasuba KC, Mace E, Strittmatter T, Laskowski PR, Geissler SA, et al. Neurons differentiate magnitude and location of mechanical stimuli. *Proc Natl Acad Sci U S A*. 2020;117(2):848–56.
395. Park DH, Jeon HJ, Kim MJ, Nguyen XD, Morten K, Go JS. Development of a microfluidic perfusion 3D cell culture system. *J Micromechanics Microengineering*. 2018;28(4).
396. Zhang X, Roper MG. Microfluidic perfusion system for automated delivery of temporal gradients to islets of Langerhans. *Anal Chem*. 2009;81(3):1162–8.
397. Anson LC, Chen PE, Wyllie DJ, Colquhoun D, Schoepfer R. Identification of amino acid residues of the NR2A subunit that control glutamate potency in recombinant NR1/NR2A NMDA receptors. *J Neurosci*. 1998;18(2):581–9.
398. Yuan H, Hansen KB, Vance KM, Ogden KK, Traynelis SF. Control of NMDA receptor function by the NR2 subunit amino-terminal domain. *J Neurosci* [Internet]. 2009;29(39):12045–58. Available from: <http://www.ncbi.nlm.nih.gov/pubmed/19793963>  
<http://www.pubmedcentral.nih.gov/articlerender.fcgi?artid=PMC2776059>
399. Patneau DK, Mayer ML. Structure-activity relationships for amino acid transmitter candidates acting at N-methyl-D-aspartate and quisqualate receptors. *J Neurosci* [Internet]. 1990;10(7):2385–99. Available from: <http://www.ncbi.nlm.nih.gov/pubmed/2165523>
400. Dai WM, Egebjerg J, Lambert JD. Characteristics of AMPA receptor-mediated responses of cultured cortical and spinal cord neurons and their correlation to the expression of glutamate receptor subunits, GluR1-4. *Br J Pharmacol*. 2001;Apr 8, 132:1859–75.
401. Niswender CM, Conn PJ. Metabotropic Glutamate Receptors: Physiology, Pharmacology, and Disease. *Annu Rev Pharmacol Toxicol* [Internet]. 2010;50(1):295–322. Available from: <http://www.annualreviews.org/doi/10.1146/annurev.pharmtox.011008.145533>
402. Dingledine R, Borges K, Bowie D, Traynelis SF. The glutamate receptor ion channels. *Pharmacol Rev* [Internet]. 1999;51(1):7–61. Available from: <http://www.ncbi.nlm.nih.gov/pubmed/15218076>

403. Peavy RD, Sorensen SD, Conn PJ. Differential regulation of metabotropic glutamate receptor 5-mediated phosphoinositide hydrolysis and extracellular signal-regulated kinase responses by protein kinase C in cultured astrocytes. *J Neurochem*. 2002;83(1):110–8.
404. Chesher D. Evaluating assay precision. *Clin Biochem Rev* [Internet]. 2008;29 Suppl 1(i):S23–6. Available from:  
<http://www.ncbi.nlm.nih.gov/pubmed/18852851>  
<http://www.pubmedcentral.nih.gov/articlerender.fcgi?artid=PMC2556577>
405. Hansen KB, Yuan H, Traynelis SF. Structural aspects of AMPA receptor activation, desensitization and deactivation. *Curr Opin Neurobiol*. 2007;17(3):281–8.
406. Nahum-Levy R, Lipinski D, Shavit S, Benveniste M. Desensitization of NMDA receptor channels is modulated by glutamate agonists. *Biophys J*. 2001;80(5):2152–66.
407. Dale LB, Babwah A V., Ferguson SSG. Mechanisms of metabotropic glutamate receptor desensitization: Role in the patterning of effector enzyme activation. *Neurochem Int*. 2002;41(5):319–26.
408. Parpura V, Haydon PG. Physiological astrocytic calcium levels stimulate glutamate release to modulate adjacent neurons. *Proc Natl Acad Sci* [Internet]. 2000;97(15):8629–34. Available from: <http://www.pnas.org/cgi/doi/10.1073/pnas.97.15.8629>
409. Shen W, Nikolic L, Meunier C, Pfrieger F, Audinat E. An autocrine purinergic signaling controls astrocyte-induced neuronal excitation. *Sci Rep* [Internet]. 2017;7(1):1–13. Available from: <http://dx.doi.org/10.1038/s41598-017-11793-x>
410. Lalo U. NMDA Receptors Mediate Neuron-to-Glia Signaling in Mouse Cortical Astrocytes. *J Neurosci* [Internet]. 2006;26(10):2673–83. Available from: <http://www.jneurosci.org/cgi/doi/10.1523/JNEUROSCI.4689-05.2006>
411. Frick A, Magee J, Johnston D. LTP is accompanied by an enhanced local excitability of pyramidal neuron dendrites. *Nat Neurosci* [Internet]. 2004;7(2):126–35. Available from: <http://dx.doi.org/10.1038/nn1178>
412. Ivenshitz M, Segal M. Simultaneous NMDA-Dependent Long-Term Potentiation of EPSCs and Long-Term Depression of IPSCs in Cultured Rat Hippocampal Neurons. *J Neurosci* [Internet]. 2006;26(4):1199–210. Available from:

<http://www.jneurosci.org/cgi/doi/10.1523/JNEUROSCI.2964-05.2006>

413. Molnár E. Long-term potentiation in cultured hippocampal neurons. *Semin Cell Dev Biol* [Internet]. 2011;22(5):506–13. Available from: <http://linkinghub.elsevier.com/retrieve/pii/S1084952111001030%5Cnpapers3://publication/doi/10.1016/j.semcdb.2011.07.017>
414. Bliss T V, Collingridge GL. A synaptic model of memory: long-term potentiation in the hippocampus. *Nature*. 1993;361(6407):31–9.
415. Luscher C, Malenka RC. NMDA Receptor-Dependent Long-Term Potentiation and Long-Term Depression (LTP/LTD). *Cold Spring Harb Perspect Biol* [Internet]. 2012;4(6):5710. Available from: <http://cshperspectives.cshlp.org/lookup/doi/10.1101/cshperspect.a005710>
416. Ota Y, Zanetti AT, Hallock RM. The role of astrocytes in the regulation of synaptic plasticity and memory formation. *Neural Plast*. 2013;2013.
417. Liu G, Choi S, Tsien RW. Variability of neurotransmitter concentration and nonsaturation of postsynaptic AMPA receptors at synapses in hippocampal cultures and slices. *Neuron*. 1999;22(2):395–409.
418. Mitchell MJ, King MR. Homeostatic control of synaptic transmission by distinct glutamate receptors. *Neuron*. 2013;78(4):687–99.
419. Wallach G, Lallouette J, Herzog N, De Pittà M, Jacob E Ben, Berry H, et al. Glutamate Mediated Astrocytic Filtering of Neuronal Activity. *PLoS Comput Biol*. 2014;10(12).
420. Schipke CG, Haas B, Kettenmann H. Astrocytes discriminate and selectively respond to the activity of a subpopulation of neurons within the barrel cortex. *Cereb Cortex*. 2008;18(10):2450–9.
421. Benson DL, Watkins FH, Steward O, Banker G. Characterization of GABAergic neurons in hippocampal cell cultures. *J Neurocytol*. 1994;23(5):279–95.
422. Colombi I, Mahajani S, Frega M, Gasparini L, Chiappalone M. Effects of antiepileptic drugs on hippocampal neurons coupled to micro-electrode arrays. *Front Neuroeng* [Internet]. 2013;6(November):1–11. Available from: <http://journal.frontiersin.org/article/10.3389/fneng.2013.00010/abstract>
423. Li Y, Popko J, Krogh KA, Thayer SA. Epileptiform stimulus increases Homer 1a expression to

modulate synapse number and activity in hippocampal cultures. *J Neurophysiol* [Internet]. 2013;109(6):1494–504. Available from:  
<http://jn.physiology.org/cgi/doi/10.1152/jn.00580.2012>

424. Tamura A, Yamada N, Yaguchi Y, Machida Y, Mori I, Osanai M. Both neurons and astrocytes exhibited tetrodotoxin-resistant metabotropic glutamate receptor-dependent spontaneous slow Ca<sup>2+</sup> oscillations in striatum. *PLoS One*. 2014;9(1).
425. Dash MB, Ajayi S, Folsom L, Gold PE, Korol DL. Spontaneous Infralow Fluctuations Modulate Hippocampal EPSP-PS Coupling. *Eneuro* [Internet]. 2018;5(February):ENEURO.0403-17.2017. Available from: <http://eneuro.sfn.org/lookup/doi/10.1523/ENEURO.0403-17.2017>
426. Hsu WL, Chung HW, Wu CY, Wu HI, Lee YT, Chen EC, et al. Glutamate stimulates local protein synthesis in the axons of rat cortical neurons by activating  $\alpha$ -amino-3-hydroxy-5-methyl-4-isoxazolepropionic acid (AMPA) receptors and metabotropic glutamate receptors. *J Biol Chem*. 2015;290(34):20748–60.
427. Assaf F, Schiller Y. A chemogenetic approach for treating experimental Parkinson's disease. *Mov Disord*. 2018;10(1002):27554.
428. Alcacer C, Andreoli L, Sebastianutto I, Jakobsson J, Fieblinger T, Cenci MA. Chemogenetic stimulation of striatal projection neurons modulates responses to Parkinson's disease therapy. *J Clin Invest*. 2017;127(2):720–34.
429. Takeda K. WFS1 (Wolfram syndrome 1) gene product: predominant subcellular localization to endoplasmic reticulum in cultured cells and neuronal expression in rat brain. *Hum Mol Genet*. 2001;10(5):477–84.
430. Adamsky A, Kol A, Kreisel T, Doron A, Ozeri-Engelhard N, Melcer T, et al. Astrocytic Activation Generates De Novo Neuronal Potentiation and Memory Enhancement. *Cell*. 2018;174(1):59–71.
431. Armbruster BN, Li X, Pausch MH, Herlitze S, Roth BL. Evolving the lock to fit the key to create a family of G protein-coupled receptors potently activated by an inert ligand. *Proc Natl Acad Sci U S A*. 2007;104(12):5163–8.
432. Bickle J. Revolutions in neuroscience: Tool development. *Front Syst Neurosci*. 2016;10(MAR):1–13.

433. Roth BL. DREADDs for Neuroscientists. *Neuron*. 2016;89(4):683–94.
434. Jorgenson LA, Newsome W, Anderson DJ, Bargmann CI, Brown EN, Deisseroth K, et al. The BRAIN initiative: Developing technology to catalyse neuroscience discovery. *Philos Trans R Soc B Biol Sci*. 2015;370(1668).
435. Betts MJ, O’Neill MJ, Duty S. Allosteric modulation of the group III mGlu4 receptor provides functional neuroprotection in the 6-hydroxydopamine rat model of Parkinson’s disease. *Br J Pharmacol*. 2012;166(8):2317–30.
436. Charvin D, Di Paolo T, Bezard E, Gregoire L, Takano A, Duvey G, et al. An mGlu4-Positive Allosteric Modulator Alleviates Parkinsonism in Primates. *Mov Disord*. 2018;33(10):1619–31.
437. Myczek K, Yeung ST, Castello N, Baglietto-Vargas D, LaFerla FM. Hippocampal adaptive response following extensive neuronal loss in an inducible transgenic mouse model. *PLoS One*. 2014;9(9).
438. Jiang M, Bajpayee NS. Molecular mechanisms of Go signaling. *NeuroSignals*. 2009;17(1):23–41.
439. Muir KW. Glutamate-based therapeutic approaches: Clinical trials with NMDA antagonists. *Curr Opin Pharmacol*. 2006;6:53–60.
440. Traynelis SF, Wollmuth LP, McBain CJ, Menniti FS, Vance KM, Ogden KK, et al. Glutamate receptor ion channels: structure, regulation, and function. *Pharmacol Rev*. 2010;62:405–96.
441. Lau S, Jardine K, McBurney MW. DNA methylation pattern of a tandemly repeated lacZ transgene indicates that most copies are silent. *Dev Dyn*. 1999;215(2):126–38.
442. Yu Z, Asaad W, Nurmikko A, Ozden I. Optogenetics-based Neuromodulation for the Treatment of Parkinson ’ s Disease. 2017;6664.
443. Perusini JN, Cajigas SA, Cohensedgh O, Lim SC, Ina P, Donaldson ZR, et al. Optogenetic stimulation of dentate gyrus engrams restores memory in Alzheimer’s disease mice. 2018;27(10):1110–22.
444. Herman M, Nahmani E, Emrani S, Figueroa YH, Marc I. Neuronal activity enhances tau propagation and tau pathology in vivo. 2016;19(8):1085–92.
445. Lopez AJ, Kramar E, Matheos DP, White AO, Kwapis J, Vogel-Ciernia A, et al. Promoter-

Specific Effects of DREADD Modulation on Hippocampal Synaptic Plasticity and Memory Formation. *J Neurosci*. 2016;36(12):3588–99.

446. Weir GA, Middleton SJ, Clark AJ, Daniel T, Khovanov N, McMahon SB, et al. Using an engineered glutamate-gated chloride channel to silence sensory neurons and treat neuropathic pain at the source. *Brain*. 2017;140(10):2570–85.
447. Stachniak TJ, Ghosh A, Sternson SM. Chemogenetic synaptic silencing of neural circuits localizes a hypothalamus→midbrain pathway for feeding behavior. *Neuron*. 2014;82(4):797–808.
448. Doležal V, Tuček S. The effects of brucine and alcuronium on the inhibition of [3H]acetylcholine release from rat striatum by muscarinic receptor agonists. *Br J Pharmacol*. 1998;124(6):1213–8.
449. Alexander GM, Rogan SC, Abbas AI, Armbruster BN, Pei Y, Allen JA, et al. Remote control of neuronal activity in transgenic mice expressing evolved G protein-coupled receptors. *Neuron*. 2016;29(4):246–7.
450. Giorgi A, Migliarini S, Galbusera A, Maddaloni G, Mereu M, Margiani G, et al. Brain-wide Mapping of Endogenous Serotonergic Transmission via Chemogenetic fMRI. *Cell Rep*. 2017;21(4):910–8.
451. Karra D, Dahm R. Transfection techniques for neuronal cells. *J Neurosci*. 2010;30(18):6171–7.
452. Alabdullah AA, Al-Abdulaziz B, Alsalem H, Magrashi A, Pulicat SM, Almzroua AA, et al. Estimating transfection efficiency in differentiated and undifferentiated neural cells. *BMC Res Notes* [Internet]. 2019;12(1):1–7. Available from: <https://doi.org/10.1186/s13104-019-4249-5>
453. Zou S, Scarfo K, Nantz MH, Hecker JG. Lipid-mediated delivery of RNA is more efficient than delivery of DNA in non-dividing cells. *Int J Pharm*. 2010;389(1–2):232–43.
454. Williams DJ, Puhl HL, Ikeda SR. A simple, highly efficient method for heterologous expression in mammalian primary neurons using cationic lipid-mediated mRNA transfection. *Front Neurosci*. 2010;4:1–20.
455. Uchida E, Mizuguchi H, Ishii-Watabe A, Hayakawa T. Comparison of the efficiency and safety of non-viral vector-mediated gene transfer into a wide range of human cells. *Biol Pharm Bull*.

2002;25(7):891–7.

456. Zabner J, Fasbender AJ, Moninger T, Poellinger KA, Welsh MJ. Cellular and Molecular Barriers to Gene Transfer by a Cationic Lipid. 1995.
457. Morgan JR, Skye Comstra H, Cohen M, Faundez V. Presynaptic membrane retrieval and endosome biology: Defining molecularly heterogeneous synaptic vesicles. *Cold Spring Harb Perspect Biol.* 2013;5(10):1–16.
458. Cousin MA. Integration of synaptic vesicle cargo retrieval with endocytosis at central nerve terminals. *Front Cell Neurosci.* 2017;11(August):1–10.
459. Hupalowska A, Miaczynska M. The new faces of endocytosis in signaling. *Traffic.* 2012;13:9–18.
460. Lam AMI, Cullis PR. Calcium enhances the transfection potency of plasmid DNA-cationic liposome complexes. *Biochim Biophys Acta - Mol Cell Res.* 1999;279–90.
461. Eliasson L, Proks P, Ammala C, Ashcroft FM, Bokvist K, Renstrom E, et al. Endocytosis of secretory granules in mouse pancreatic beta-cells evoked by transient elevation of cytosolic calcium.pdf. *J Physiol.* 1996;
462. Xiong Z-G, Lu W-Y, MacDonald JF. Extracellular calcium sensed by a novel cation channel in hippocampal neurons. Vol. 94, *Proceedings of the National Academy of Sciences.* 1997. p. 7012–7.
463. Jones BL, Smith SM. Calcium-sensing receptor: A key target for extracellular calcium signaling in neurons. *Front Physiol.* 2016;7(MAR):1–7.
464. Hallinan GI, Vargas-Caballero M, West J, Deinhardt K. Tau Misfolding Efficiently Propagates between Individual Intact Hippocampal Neurons. *J Neurosci.* 2019;39(48):9623–32.
465. Dalby B, Cates S, Harris A, Ohki EC, Tilkins ML, Price PJ, et al. Advanced transfection with Lipofectamine 2000 reagent: Primary neurons, siRNA, and high-throughput applications. *Methods.* 2004;33(2):95–103.
466. Cui Y, Li X, Zeljic K, Shan S, Qiu Z, Wang Z. Effect of PEGylated Magnetic PLGA-PEI Nanoparticles on Primary Hippocampal Neurons: Reduced Nanoneurotoxicity and Enhanced Transfection Efficiency with Magnetofection. *ACS Appl Mater Interfaces.* 2019;11(41):38190–204.

467. Berglund K, Tung JK, Higashikubo B, Gross RE, Moore CI, Hochgeschwender U. Combined Optogenetic and Chemogenetic Control of Neurons. *Methods Mol Biol.* 2016;
468. Nguyen LT, Atobe K, Barichello JM, Ishida T, Kiwada H. Complex formation with plasmid DNA increases the cytotoxicity of cationic liposomes. *Biol Pharm Bull.* 2007;30(4):751–757.
469. Bauer M, Kristensen BW, Meyer M, Gasser T, Widmer HR, Zimmer J, et al. Toxic effects of lipid-mediated gene transfer in ventral mesencephalic explant cultures. *Basic Clin Pharmacol Toxicol.* 2006;98(4):395–400.
470. Zhang X-S, Huang J, Zhan C-Q, Chen J, Li T, Kaye AD, et al. Different Influences of Lipofection and Electrotransfection on In Vitro Gene Delivery to Primary Cultured Cortex Neurons. *Pain Physician.* 2016;19(3):189–96.
471. Ha JS, Lee CS, Maeng JS, Kwon KS, Park SS. Chronic glutamate toxicity in mouse cortical neuron culture. *Brain Res.* 2009;1273:138–43.
472. Hurni N, Kolodziejczak M, Tomasello U, Badia J, Jacobshagen M, Prados J, et al. Transient Cell-intrinsic Activity Regulates the Migration and Laminar Positioning of Cortical Projection Neurons. *Cereb Cortex.* 2017;27(5):3052–63.
473. Jendryka M, Palchoudhuri M, Ursu D, van der Veen B, Liss B, Kätzel D, et al. Pharmacokinetic and pharmacodynamic actions of clozapine-N-oxide, clozapine, and compound 21 in DREADD-based chemogenetics in mice. *Sci Rep.* 2019;9(1):1–14.
474. Alexander GM, Alexander GM, Rogan SC, Rogan SC, Abbas AI, Abbas AI, et al. Remote control of neuronal activity in transgenic mice expressing evolved G protein-coupled receptors. *Neuron.* 2009;63(1):27–39.
475. Campbell EJ, Marchant NJ. The use of chemogenetics in behavioural neuroscience: receptor variants, targeting approaches and caveats. *Br J Pharmacol.* 2018;175(7):994–1003.
476. Gomez JL, Bonaventura J, Lesniak W, Mathews WB, Sysa-Shah P, Rodriguez LA, et al. Chemogenetics revealed: DREADD occupancy and activation via converted clozapine. *Science (80- ).* 2017;357(6350):503–7.
477. Ji B, Kaneko H, Minamimoto T, Inoue H, Takeuchi H, Kumata K, et al. Multimodal Imaging for DREADD-Expressing Neurons in Living Brain and Their Application to Implantation of iPSC-Derived Neural Progenitors. *J Neurosci.* 2016;36(45):11544–58.



478. Chen LJ, Wang YJ, Chen JR, Tseng GF. NMDA receptor triggered molecular cascade underlies compression-induced rapid dendritic spine plasticity in cortical neurons. *Exp Neurol*. 2015;266:86–98.
479. Geddes DM, Cargill RS, LaPlaca MC. Mechanical Stretch to Neurons Results in a Strain Rate and Magnitude-Dependent Increase in Plasma Membrane Permeability. *J Neurotrauma*. 2003;20(10):1039–49.
480. Lusardi TA, Smith DH, Wolf JA, Meaney DF. The separate roles of calcium and mechanical forces in mediating cell death in mechanically injured neurons. *Biorheology*. 2003;40:401–9.
481. McCown T. Adeno-Associated Virus (AAV) Vectors in the CNS. *Curr Gene Ther*. 2011;11(3):181–8.
482. Gray SJ, Woodard KT, Samulski RJ. Viral vectors and delivery strategies for CNS gene therapy. *Ther Deliv*. 2010;1(4):517–34.
483. Howard DB, Powers K, Wang Y, Harvey BK. Tropism and toxicity of adeno-associated viral vector serotypes 1,2,5,6,7,8,9 in rat neurons and glia in vitro. *West Soc Malacol Annu Rep*. 1987;19(1):16.
484. Mullah S, R K, P Y, S H, M I, Yoko M-S, et al. Evaluation of voltage-sensitive fluorescence dyes for monitoring neuronal activity in the embryonic central nervous system. *J Membr Biol*. 2013;246(9):679–88.
485. Bean BP. The action potential in mammalian central neurons. *Nat Rev Neurosci*. 2007;8(6):451–65.
486. Leao RN, Burne JA. Continuous wavelet transform in the evaluation of stretch reflex responses from surface EMG. *J Neurosci Methods*. 2004;133(1–2):115–25.
487. Raguet H. A Signal Processing Approach to Voltage-Sensitive Dye Optical Imaging. Dauphine Universite Pris; 2014.
488. Chemla S, Muller L, Reynaud A, Takerkart S, Destexhe A, Chavane F. Improving voltage-sensitive dye imaging: with a little help from computational approaches. *Neurophotonics*. 2017;4(3):031215.
489. Kanagasabapathi TT, Franco M, Barone RA, Martinoia S, Wadman WJ, Decré MMJ. Selective pharmacological manipulation of cortical-thalamic co-cultures in a dual-compartment device.

- J Neurosci Methods [Internet]. 2013;214(1):1–8. Available from:  
<http://dx.doi.org/10.1016/j.jneumeth.2012.12.019>
490. Enquist LW. Five questions about viral trafficking in neurons. *PLoS Pathog.* 2012;8(2):8–10.
491. Brask J, Chauhan A, Hill RH, Ljunggren HG, Kristensson K. Effects on synaptic activity in cultured hippocampal neurons by influenza A viral proteins. *J Neurovirol.* 2005;11(4):395–402.
492. Kaplitt MG, Feigin A, Tang C, Fitzsimons HL, Mattis P, Lawlor PA, et al. Safety and tolerability of gene therapy with an adeno-associated virus (AAV) borne GAD gene for Parkinson’s disease: an open label, phase I trial. *Lancet.* 2007;369:2097–105.
493. Soloperto A, Boccaccio A, Contestabile A, Moroni M, Hallinan GI, Palazzolo G, et al. Mechano-sensitization of mammalian neuronal networks through expression of the bacterial large-conductance mechanosensitive ion channel. *J Cell Sci.* 2018;131(5).
494. Garner AR, Rowland DC, Hwang SY, Baumgaertel K, Roth BL, Kentros C, et al. Generation of a synthetic memory trace. *Science (80- ).* 2012;335(6075):1513–6.
495. Yoshii T, Hosokawa H, Matsuo N. Pharmacogenetic reactivation of the original engram evokes an extinguished fear memory. *Neuropharmacology [Internet].* 2017;113:1–9. Available from: <http://dx.doi.org/10.1016/j.neuropharm.2016.09.012>
496. Shrestha P, Ayata P, Vidal PMH, Longo F, Gastone A, LeDoux J, et al. Chemogenetic evidence that rapid neuronal de novo protein synthesis is required for consolidation of long-term memory. *bioRxiv [Internet].* 2019;704965. Available from: <https://www.biorxiv.org/content/10.1101/704965v1>
497. Burnett CJ, Krashes MJ. Resolving behavioral output via chemogenetic designer receptors exclusively activated by designer drugs. *J Neurosci.* 2016;36(36):9268–82.
498. Weston M, Kaserer T, Wu A, Mouravlev A, Carpenter JC, Snowball A, et al. Olanzapine: A potent agonist at the hM4D(Gi) DREADD amenable to clinical translation of chemogenetics. *Sci Adv.* 2019;5(4):4–9.
499. Magnus CJ, Lee PH, Bonaventura J, Zemla R, Gomez JL, Ramirez MH, et al. Ultrapotent chemogenetics for research and potential clinical applications. *Science (80- ).* 2019;364(6436):1–15.

500. Kätzel D, Nicholson E, Schorge S, Walker MC, Kullmann DM. Chemical-genetic attenuation of focal neocortical seizures. *Nat Commun.* 2014;5(May).
501. Wanisch K, Kovac S, Schorge S. Tackling Obstacles for Gene Therapy Targeting Neurons: Disrupting Perineural Nets with Hyaluronidase Improves Transduction. *PLoS One.* 2013;8(1).

## **Appendix**

### **Microfluidic Protocol for Calcium Imaging Assays**

This protocol details the step by step process of setting up and performing pharmacological assessments on cultured, small well (4 mm diameter) microfluidic devices, using calcium imaging as the readout for neural network activity.

### **Reagents, Equipment & Software**

#### **Reagent Setup**

HEPES-buffered saline (HBS) solution:

Dissolve the following materials in DI water to the stated final concentrations: containing:

- NaCl 140 mM
- KCl 5 mM
- MgCl<sub>2</sub> 2 mM
- HEPES 10 mM
- D-glucose 10 mM
- CaCl<sub>2</sub> 2 mM
- pH adjusted to  $7.4 \pm 0.1$  with NaOH
- Osmolarity adjusted to  $310 \text{ mOsm} \pm 0.1$  with sucrose

Glutamate solution

Dissolve glutamate in HBS to a final concentration of 3  $\mu\text{M}$

KCl solution

Dissolve KCl in HBS to a final concentration of 50 mM

Fluo-4 AM solution

First dissolve 50  $\mu\text{g}$  Fluo-4-AM in 50  $\mu\text{L}$  DMSO and prepare 1  $\mu\text{L}$  master stock aliquots, stored at  $-15$  to  $-25$  °C for future use. Dissolve 1  $\mu\text{L}$  of master stock in 300  $\mu\text{L}$  of HBS (5  $\mu\text{M}$  final concentration; 0.003 % v/v)

## Equipment

Axio Observer (A1); Carl Zeiss, AG

Filter Cube Set 46 HE; Carl Zeiss, AG

AxioCam mRM; Carl Zeiss, AG

6x Syringe pumps; AL-1000; WPI, UK

Glass syringes (5 mL, 10.3 mm diameter); SGE, UK

PTFE tubing (0.255 mm diameter, ~70 cm); Cole-Parmer, UK

Blunted needle tips (0.4 mm diameter, ~20 mm length)

Tygon tubing (~20 mm)

## Software

Andor SOLIS (DL-01339)

MATLAB (2015a)

## Experimental Setup

1. Following 10-14 DIV, remove the microfluidic device containing the mixed hippocampal culture from the incubator and gently remove the conditioned media from each inlet/outlet well, discarding to waste.
2. Gently dispense 50  $\mu\text{L}$  of HBS solution to each well before discarding this to waste also, repeating twice to wash the microfluidic culture.
3. Gently dispense 25  $\mu\text{L}$  of Fluo-4-AM (5  $\mu\text{M}$ ) to the inlet wells connected to their respective culture chambers, followed by 25  $\mu\text{L}$  to the outlet wells, and incubate for 50 - 60 minutes in the dark, at room temperature.
4. Turn on the mercury arc lamp and allow to pre-heat for at least 30 minutes prior to assay performance to ensure the appropriate intensity of excitatory light is achieved.
5. Ensure the Filter Cube Set 46 HE is in place; the neutral density filter should be set to position 6 (minimal light intensity) to minimise photobleaching/phototoxicity.
6. Open the Andor SOLIS program and apply a frame acquisition of 2 Hz with 0.4 ms exposure, with a frame limit of 480 (4-minute recording) and an EM Gain of 100, under 'Setup Acquisition'. The spool should be saved to an appropriate location as a .Sif file under 'Spooling' settings.
7. Load three glass syringes with HBS solution, one with 5 mL, used for continuous perfusion of vehicle (HBS) during and in between recordings, and two with 2 mL, to be used for the continuous withdrawal of fluid.
8. Load three glass syringes with 5 mL of glutamate (3  $\mu\text{M}$ ) solution, used for acute perfusion during recordings.

9. Connect each syringe to PTFE tubing with blunted needle tips on either end (linked via Tygon tubing) and dispense 1 mL of each solution to waste to ensure the tubing is pre-wetted.
10. Setup the syringe pumps such that they are connected in series to the desktop, before locking the glass syringes to the syringe pumps.
11. Ensure all subsequent steps are performed in a darkened working environment to reduce background noise during recordings.
12. Following incubation with Fluo-4 AM, gently remove the solution from the inlet/outlet wells before discarding to waste.
13. Gently dispense 50  $\mu$ L of HBS solution to each well before discarding this to waste also, repeating twice to wash the microfluidic culture.
14. Gently dispense 50  $\mu$ L of HBS solution to each inlet/outlet well of the microfluidic device
15. Coat the blunted needle tips at the end of each PTFE tubing with silicon grease before connecting to the vertical/horizontal needle ports in the PDMS wall of the microfluidic device (Figure 1).
16. Carefully lift the microfluidic device and fix it to the inverted microscope, using red tape to secure the edges of the glass coverslip and prevent the tubing from lifting the microfluidic device out of place.
17. Open MATLAB and run an in-house program designed to control the flow rate and directionality of each syringe pump. Of the two syringe pumps set for withdrawal of fluid, set the pump connecting to the inlet well to 40  $\mu$ L/min, and the pump connected to the outlet well to 4  $\mu$ L/min. The remaining four syringes containing either HBS or glutamate solution, directly connected to the inlet well, should be set to perfused fluid at a flow rate of 44  $\mu$ L/min.
18. Using Andor Solis with a combination of brightfield and epifluorescence, adjust the focus to bring the neural networks into view, with the microchannel array centred in the field of view. This should be performed quickly to minimise the risk of photobleaching/phototoxicity.

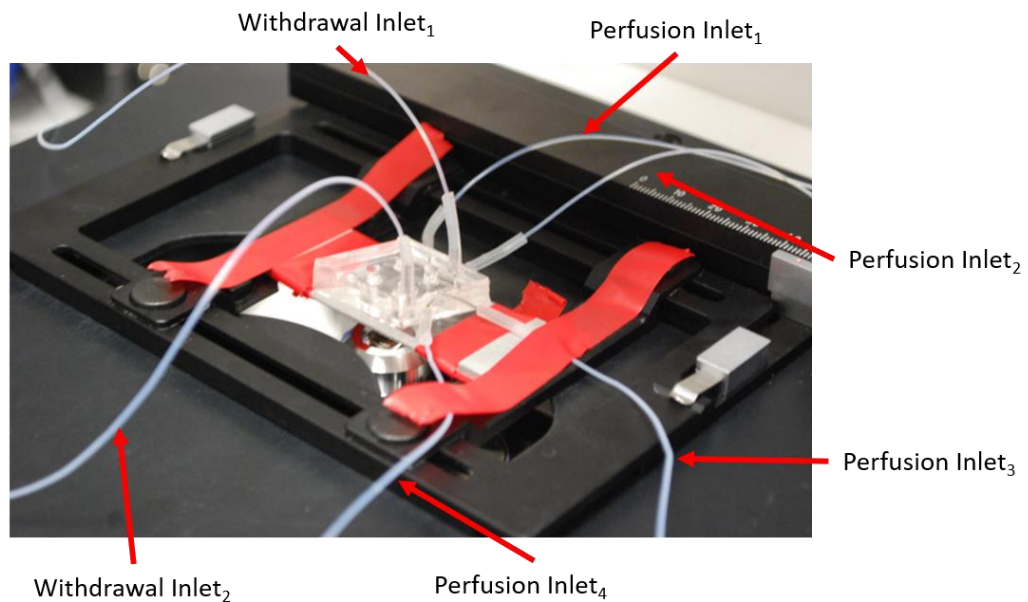
A



Syringe driven pumps  
(Withdrawal)

Syringe driven pumps  
(Perfusion)

B



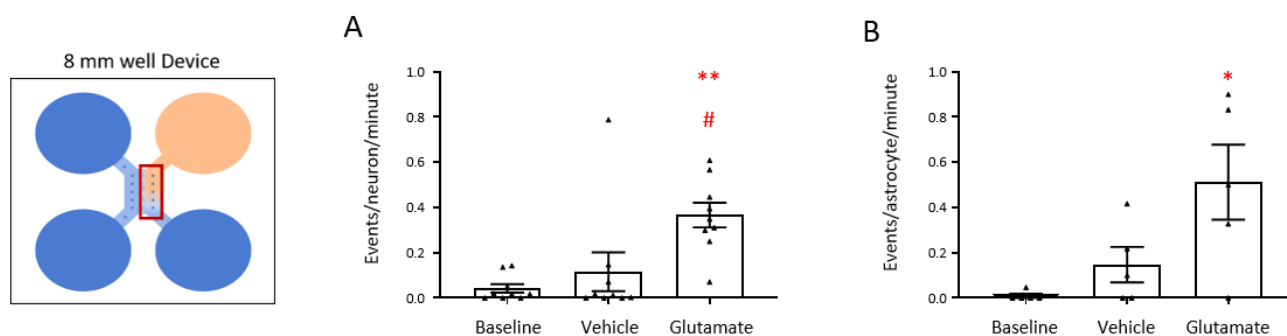
**Supplementary Figure 1: Syringe Driven Pump Setup for Microfluidic Perfusion.** (A) Semi-automated syringe driven pumps are positioned around the inverted microscope; two are used for the withdrawal of fluid from the microfluidic device, whilst 4 are used for the perfusion of fluid. (B) The microfluidic device and tubing are secured to the inverted microscope using red tape. Needle ports are used to connect tubing between the syringe pumps and the device via horizontal (perfusion) and vertical (withdrawal) inlets.

## Calcium Imaging Assay Procedure

1. Once the experimental setup is complete, remove 40  $\mu\text{L}$  of HBS solution from the inlet/outlet well to be perfused and discard to waste.
2. Initiate the two syringe pumps responsible for the withdrawal of fluid, and the syringe pump responsible for perfusing HBS solution, allowing the continuous net flow of 4  $\mu\text{L}/\text{min}$  through the culture chamber to stabilise. The microfluidic device should be maintained under constant perfusion throughout this procedure to avoid unwanted significant changes in pressure that will compromise the assay.
3. Briefly adjust the EM Gain and the neutral density filter position such that a clear enough signal can be determined from individual cells without saturating the pixel count or risking photobleaching/phototoxicity.
4. Once 10 minutes have passed, initiate the first 4 minute recording; this is to be used as a baseline recording to determine the level of spontaneous activity, with careful attention paid to any disturbances to the field of view, unusual neural network activity, and the volume present in the inlet/outlet well undergoing perfusion.
5. Allow the neural network to recover after the recording by removing the excitatory light and leave to rest for 8-10 minutes.
6. Initiate the second 4 minute recording. Once 30 seconds (60 frames) have passed, alternate the syringe pump responsible for HBS perfusion with that for glutamate (3  $\mu\text{M}$ ), allowing glutamate perfusion for 1 minute (120 frames). At 180 frames of recording, alternate back to the perfusion of HBS solution to wash out glutamate from the perfused culture chamber throughout the remainder of the recording.
  - a. After approximately 35 seconds of glutamate perfusion, cells within the perfused chamber should reveal an increase in fluorescence in response to glutamatergic receptor activation, with cells in the adjacent, naïve chamber occasionally responding with brief increases in fluorescence as a result of synaptic communication.
7. Repeat steps 5 & 6 an additional two times, using different syringe pumps for glutamate perfusion each time. After the final recording of glutamate perfusion, allow the neural network to rest for 8-10 minutes before ceasing syringe pump function and gently removing HBS solution from each inlet/outlet well such that approximately 10  $\mu\text{L}/\text{well}$  remains.
8. Initiate a fifth and final recording. Once 30 seconds have passed, dispense 10  $\mu\text{L}$  of KCl (25 mM final concentration) directly to both inlet wells, and allow the recording to finish.
  - a. KCl solution permits the researcher to differentiate cellular fluorescent signal between neurons and astrocytes during analysis.



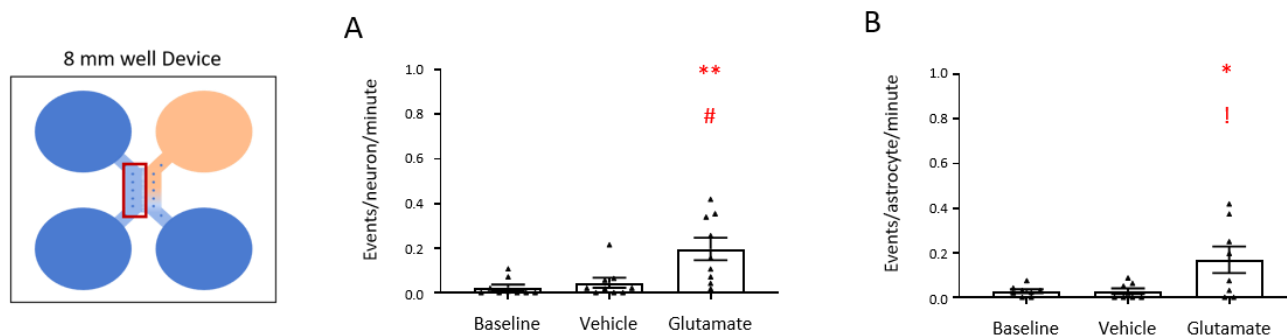
## Supplementary Figure 2



### Supplementary Figure 2: Direct Activation of a Neural Network following Glutamate Applications.

(A-B) Scatter graphs depict the average changes in neuronal and astrocytic activity within the treated chamber following direct vehicle and glutamate (100  $\mu$ M final concentration) applications respectively. Direct vehicle application did not significantly increase the activity of either neurons or astrocytes ( $n = 9$  devices, 4 separate cultures), with respect to baseline activity. Direct glutamate application significantly increased the activity of neurons with respect to baseline and vehicle; astrocyte activity significantly increased but only relative to baseline activity. One way ANOVA with Tukey's post-hoc analysis; \*denotes  $P < 0.05$  vs Baseline, #denotes  $P < 0.05$  vs Vehicle, \*\*denotes  $P < 0.01$  vs Baseline.

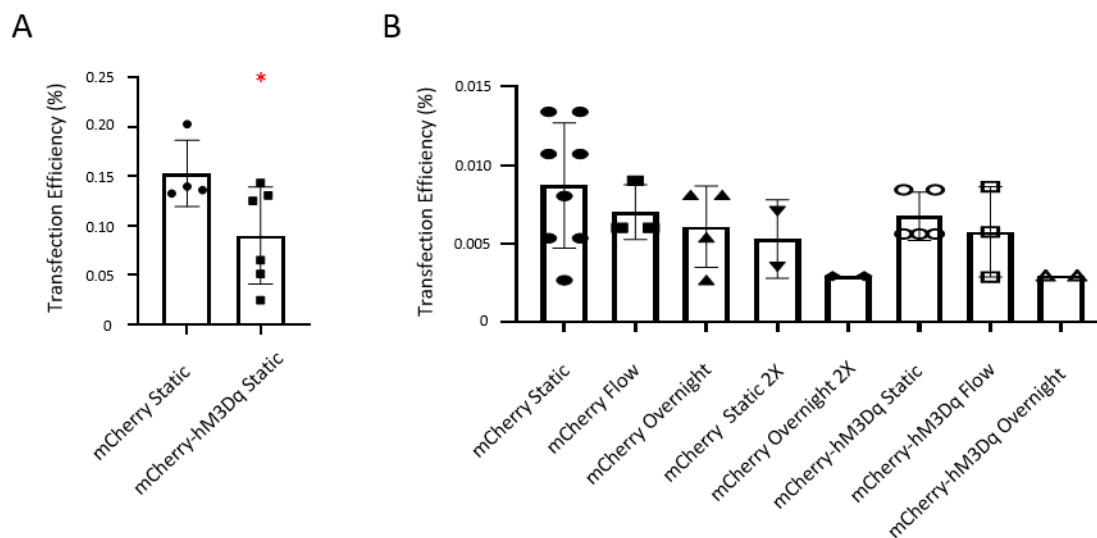
## Supplementary Figure 3



### Supplementary Figure 3: Indirect Activation of a Naïve Neural Network.

(A-B) Scatter graphs depict the average changes in neuronal and astrocytic activity within the naive chamber following direct vehicle and glutamate (100  $\mu$ M final concentration) applications. Direct vehicle application did not significantly increase the activity of either neurons or astrocytes ( $n = 9$  devices, 4 separate cultures), with respect to baseline activity. Additionally, direct glutamate application significantly increased the activity of neurons and astrocytes with respect to baseline and vehicle activity. One way ANOVA with Tukey's post-hoc analysis; \*denotes  $P < 0.05$  vs Baseline, †denotes  $P < 0.05$  vs vehicle, \*\*denotes  $P < 0.01$  vs Baseline, #denotes  $P < 0.01$  vs Vehicle.

## Supplementary Figure 4



### Supplementary Figure 4: Transfection Efficiency in 4-Well Assay Plates and Microfluidic Devices.

(A) Transfection efficiency present in 4-well assay plates was low ( $> 1\%$ ), with a significant reduction ( $P < 0.05$ ) observed when transfecting with the mCherry-hM3Dq plasmid ( $n = 6$  assay plates, 4 cultures) relative to mCherry plasmid ( $n = 4$  assay plates, 4 cultures). (B) Within microfluidic devices, transfection efficiency was even lower than that observed in 4-well assay plates, with no significant difference observed between any condition assessed (mCherry Static,  $n = 8$  devices, 4 cultures; mCherry Flow,  $n = 3$  devices, 2 cultures; mCherry Overnight,  $n = 4$  devices, 3 cultures; mCherry Static 2X & mCherry Overnight 2X,  $n = 2$  devices, 2 cultures; mCherry-hM3Dq Static,  $n = 5$  devices, 2 cultures, mCherry-hM3Dq Flow,  $n = 3$  devices, 2 cultures; mCherry-hM3Dq Overnight,  $n = 2$  devices, 1 culture). Unpaired t-test (A) & One way ANOVA with Tukey's post-hoc analysis (B); \* denotes  $P < 0.05$ .

# SCIENTIFIC REPORTS

## OPEN A Microfluidic Platform for the Characterisation of CNS Active Compounds

Received: 21 July 2017  
Accepted: 3 November 2017  
Published online: 16 November 2017

Christopher MacKerron<sup>1</sup>, Graham Robertson<sup>1</sup>, Michele Zagnoni<sup>1,2</sup> & Trevor J. Bushell<sup>1,2</sup>

New *in vitro* technologies that assess neuronal excitability and the derived synaptic activity within a controlled microenvironment would be beneficial for the characterisation of compounds proposed to affect central nervous system (CNS) function. Here, a microfluidic system with computer controlled compound perfusion is presented that offers a novel methodology for the pharmacological profiling of CNS acting compounds based on calcium imaging readouts. Using this system, multiple applications of the excitatory amino acid glutamate (10 nM–1 mM) elicited reproducible and reversible transient increases in intracellular calcium, allowing the generation of a concentration response curve. In addition, the system allows pharmacological investigations to be performed as evidenced by application of glutamatergic receptor antagonists, reversibly inhibiting glutamate-induced increases in intracellular calcium. Importantly, repeated glutamate applications elicited significant increases in the synaptically driven activation of the adjacent, environmentally isolated neuronal network. Therefore, the proposed new methodology will enable neuropharmacological analysis of CNS active compounds whilst simultaneously determining their effect on synaptic connectivity.

The burden of CNS disorders, combined with an increasingly aged population, is one of the key global health challenges of our time. Indeed, the World Health Organization has highlighted that up to 1 billion people suffer from neurological disorders and those suffering from dementia, currently exceeding 20 million, are expected to double every 20 years unless action is taken<sup>1</sup>. Despite global R&D pharmaceutical spending in brain disorders exceeding \$140 billion per annum, and its growth set to continue<sup>2</sup>, early stage drug discovery has serious cost implications and high attrition rates, as investigational CNS-leads fall due to the well-known bottleneck in late stage clinical trials<sup>3</sup>. A recent meta-analysis on the clinical success rates of drugs in the development pipeline revealed that approximately, only 1 in 10 CNS active compounds eventually meets FDA approval<sup>4</sup>. The most common reasons for this level of attrition ranged from inadequate *in vitro* and *in vivo* models, to poor drug physicochemical properties and efficacy, in addition to *in vivo* toxicity<sup>4,5</sup>. Therefore, new technologies and methodologies for characterising CNS active compounds are a priority if healthcare and well-being are to be improved.

Early stage drug development heavily relies upon *in vitro* cultures, with neurons grown on coverslips prior to drug screening. However, when combined with plate-based high-throughput instrumentation, there is often failure in monitoring synaptic activity typical of the *in vivo* microenvironment<sup>6,7</sup>, as only single neuronal networks can be investigated with this approach. Standard laboratory *in vitro* techniques used to screen for CNS active compounds include electrophysiological assays, such as patch clamping and multi-electrode arrays (MEAs), as well as optical calcium (Ca<sup>2+</sup>) imaging techniques. Whilst the use of patch clamping provides exceptional temporal resolutions of neuronal activity in response to drug application<sup>8–10</sup>, it is time consuming, requires specialist training and is low throughput. Alternatively, cells can be grown across MEA substrates to obtain electrophysiological readouts across an entire neuronal network<sup>11</sup>, however the likelihood of a cell interfacing with a single electrode is low, and recordings may not detect subthreshold readings which would indicate if either excitatory or inhibitory signals were received<sup>12</sup>. The use of Ca<sup>2+</sup> imaging instead allows repeated acute recordings of cellular activity without inducing toxicity, but the technique is typically constrained to low temporal resolutions. However, it provides single-cell spatial resolution over a wide cultured area and can be used to carry out cost-effective investigations of synaptic activity<sup>13</sup>.

<sup>1</sup>Centre for Microsystems and Photonics, Electronic and Electrical Engineering, University of Strathclyde, Glasgow, G1 1XW, UK. <sup>2</sup>Strathclyde Institute of Pharmacy and Biomedical Sciences, University of Strathclyde, Glasgow, G4 0RE, UK. Correspondence and requests for materials should be addressed to M.Z. (email: michele.zagnoni@strath.ac.uk)

The use of microfluidic procedures to model *in vitro* pathological conditions has gradually increased over the past decade, due to the level of control and manipulation available over the cellular microenvironment and experimental conditions<sup>14,15</sup>. These systems also show potential for use as drug discovery platforms, taking advantage of engineering techniques to facilitate high-throughput pharmacological assays, either by device design or the incorporation of perfusion systems to wash on/off multiple compounds<sup>16–19</sup>. Further advantages of microfluidic systems include low production costs, reduction in drug sample volumes, and the ability to analyse multiple, environmentally isolated but functionally connected cultures<sup>20–23</sup>, a degree of experimental capability that is lacking in conventional culturing techniques. Additionally, the transparent nature of poly-dimethylsiloxane (PDMS) based microfluidic devices make them ideal for carrying out both quantitative and qualitative pharmacological assays via  $\text{Ca}^{2+}$  imaging techniques<sup>20,21,24</sup>. As such, microfluidic systems are versatile tools that are well suited to perform pharmacological research<sup>15,20,21,25–27</sup>.

In this study, we present a microfluidic system that integrates computer-controlled perfusion of multiple compounds with  $\text{Ca}^{2+}$  imaging techniques to provide a platform for the characterisation of CNS active compounds. The novelty of this approach is its ability to simultaneously detect direct responses within a primary hippocampal culture to repeated drug applications whilst monitoring the consequent synaptic activity in an adjacent, functionally connected but environmentally isolated hippocampal culture. Hence, the proposed platform provides a novel, miniaturised solution amenable to CNS drug discovery, offering the ability to simultaneously screen both the direct effects of compounds on cells, as well as how such drugs influence communication between synaptically connected cultures.

## Materials and Methods

**Device fabrication and preparation.** Microfluidic devices were fabricated using photo/soft-lithography techniques as described previously<sup>20</sup>, comprising of an array of microchannels between two culture chambers that are fluidically addressable via inlet/outlet wells. In brief, a two-layer microfluidic master was fabricated by spinning SU8 photoresist (3000 series, Microchem, US) onto a silicon wafer. The first layer (SU8 3010) created the microchannels (7  $\mu\text{m}$  thick, 10  $\mu\text{m}$  wide and 450  $\mu\text{m}$  long), and the second layer (SU8 3035), the culture chambers (80  $\mu\text{m}$  thick, 2 mm wide and 9.5 mm long). The silicon master was then slanted by vapour deposition of 1 H, 1 H, 2 H, 2 H-perfluorooctyl-trichlorosilane (Sigma Aldrich, UK) for 1 hour. PDMS was poured onto the master at a 10:1 ratio of base to curing agent and degassed in a vacuum desiccator prior to curing at 80 °C for 3 hours. The PDMS layer was then peeled off the master and devices were cut to the desired size, with the inlet/outlet wells (4 mm diameter) of each chamber created using a biopsy punch. Microfluidic devices were finally cleaned and irreversibly bonded to coverslips using oxygen plasma. Bonded devices were UV sterilised for 15 minutes, treated with poly-L-lysine solution (PLL, 10  $\mu\text{g ml}^{-1}$ ) for 1.5 hours, and washed with sterile Neurobasal-A medium.

**Microfluidic perfusion protocol.** Using dual culture chamber microfluidic devices, a steady flow rate in a single culture chamber (perfused chamber; with a constant flow rate  $Q_{cb}$ ) was achieved by creating a constant hydrostatic pressure difference between its inlet and outlet wells. The adjacent culture chamber (naïve chamber) was kept in almost static fluid conditions. Polytetrafluoroethylene (PTFE) tubing (0.255 mm inner diameter, ~700 mm length, Cole-Parmer, UK) connected glass syringes to needle ports created through the PDMS wall of the inlet-outlet wells of the perfused chamber, and the fluid was actuated using syringe pumps (AL-1000, World Precision Instruments). Up to four syringe pumps were connected to one inlet well of the device for fluid injection, with only one of these syringe pumps active at any given time and set to a constant flow rate ( $Q_{i-p}$ ). Two further syringe pumps were used for fluid withdrawal at constant flow rates, one connected to the inlet ( $Q_{i-w}$ ) and one to the outlet ( $Q_{o-w}$ ) well, respectively (Fig. 1a). Syringe pumps were computer-controlled via an in-house developed MATLAB (R2015a) program and ensured reliable activation/deactivation of each flow rate at the desired times. At the beginning of the assay, the following conditions were set to achieve a steady flow rate in the perfused chamber ( $Q_{cb}$ ):

$$Q_{i-p} > Q_{i-w} >> Q_{o-w} \quad (1)$$

$$Q_{i-p} - Q_{i-w} = Q_{cb} = Q_{o-w} \quad (2)$$

These set of equations give rise to a self-adjusting hydrostatic pressure between the inlet and outlet wells of the perfusion chamber that reaches quickly a dynamic equilibrium. On/off alternation of the injection syringe pumps was only used to perfuse different solutions in the chamber. Due to the module of the flow rates in Eq. 1, a rapid exchange of the fluid solution in the inlet well was obtained without affecting its hydrostatic pressure and leading to a prompt injection of the new fluid solution into the chamber. The time to completely exchange a perfusate in the well was directly proportional to the inlet well's hydraulic retention time (HRT), where the fluid volume of the well ( $V_{i-well}$ ) was replaced under a steady flow rate, resulting in  $HRT \approx V_{i-well} / Q_{i-p}$  (estimated at ~25 seconds for the current setup). Therefore, for a given steady flow rate ( $Q_{cb}$ ) in the perfusion chamber with a defined cross-section ( $S_{cb}$ ), the time ( $T_{ex}$ ) taken for the full perfusate (i.e. 100% concentration) to travel a distance  $L$  within the chamber from the inlet well can be estimated as:

$$T_{ex} \approx HRT + \frac{S_{cb} \times L}{Q_{cb}} \quad (3)$$

Under these conditions,  $T_{ex}$  is the time required for the complete exchange of solution in the inlet well and the subsequent arrival of the new solution at an arbitrary point that is a distance  $L$  away from the inlet well within the perfused chamber. When  $L$  is half the length of the culture chamber,  $T_{ex}$  is estimated at ~35 seconds for the



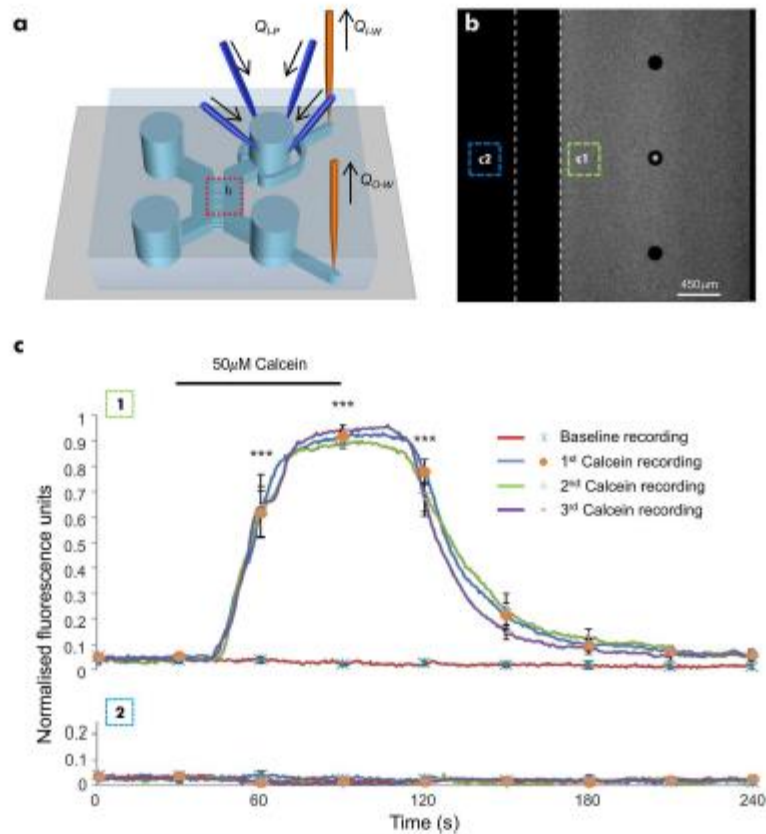


**Figure 1.** Development and characterisation of the microfluidic perfusion system. (a) Schematic representation of a dual chamber microfluidic device with inlet/outlet needle ports for the direct perfusion/withdrawal of fluid in/from the wells. Computer-controlled syringe pumps were used for fluid injection and withdrawal. (b) A representative image showing absence of cross contamination in the naïve chamber and microchannels during perfusion of calcein (50 µM) in the perfused chamber (dashed lines indicate the microchannel array separating the perfused chamber from the naïve chamber). (c) Fluorescent profiles in the perfused (c1) and naïve (c2) chambers, respectively upon repeated delivery of calcein solution from 3 different pumps. This demonstrated a lack of cross-contamination between the chambers and the robustness of the perfusion protocol (n = 9 devices). Data is expressed as mean ± S.E.M. (one-way ANOVA with post-hoc Tukey's test. \*\*\* Denotes  $P < 0.001$ , relative to baseline readings).

current device geometry. To avoid cross contamination between the perfused and naïve chambers, the initial volume of fluid in the wells connecting the naïve and perfused chambers were adjusted to 50 µl/well and 10 µl/well, respectively. This established a hydrostatic pressure gradient across the array of microchannels that was maintained throughout the assay. Considering the ratio between the hydraulic resistance of the microchannel array and culture chambers<sup>20</sup>, the hydrostatic pressure gradient resulted in the formation of a negligible flow of vehicle from the naïve to the perfused chamber that did not influence the perfusion protocol.

The robustness of this perfusion model was validated experimentally using calcein as a fluorescent marker (Fig. 1b,c). Non-cultured microfluidic devices were connected to the perfusion setup, delivering deionised (DI) water through the culture chamber at a steady flow rate ( $4 \mu\text{l min}^{-1}$ ), with three other syringes primed with calcein (50 µM in DI water). Devices were then transferred to an inverted microscope (Axio Observer A1, Zeiss) using a 2.5× objective and the field of view was set to span an area that monitored both the microchannel array and the culture chambers. Recordings were carried out using an EMCCD camera (LucaR, Andor Technologies) at a frame rate of 2.0 Hz and an exposure time of 0.4 seconds. Time-lapsed images were obtained using Andor SOLIS.

A single region of interest (ROI) was selected for the naïve and perfused culture chamber to obtain mean fluorescent readouts on either side of the microchannel array in response to calcein perfusions. The raw data (as mean value of the ROI) obtained from individual devices was then scaled using the following equation:

$$f(x) = \frac{(x - \min)}{(\max - \min)} \quad (4)$$

Where  $x$  is the mean raw fluorescent data of each time trace/ROI (sampled at 2 Hz) and  $\min$  and  $\max$  are the absolute minimal and maximal mean fluorescent intensity values. Processed data from separate recordings across multiple devices were then averaged.

**Primary hippocampal culture.** Primary hippocampal cultures were prepared as described previously<sup>8,20,28</sup>. Briefly, Sprague Dawley rat pups (1–2 days old) were killed via cervical dislocation, in accordance with the UK Home Office guidelines. The brain was then removed, hippocampi dissected out and placed in dissection solution containing (in mM) NaCl 6.78, KCl 0.40, NaHCO<sub>3</sub> 2.18, NaH<sub>2</sub>PO<sub>4</sub> 0.16, MgSO<sub>4</sub> 0.15, glucose 4.5, CaCl<sub>2</sub> 0.22. The hippocampi were then incubated for 20 minutes in papain solution (1.5 mg ml<sup>-1</sup>; Sigma Aldrich, UK) diluted in dissection solution. The tissue was then dissociated via trituration in bovine serum albumin solution (BSA; 10 mg ml<sup>-1</sup> in dissecting solution; Sigma Aldrich, UK), the cell solution was then spun down at 2000 rpm for 2 minutes and re-suspended in 1 ml of supplemented Neurobasal-A medium (L-glutamine 2 mM, B27 2% v/v; Life Technologies, UK) at a concentration of  $5 \times 10^4$  cells ml<sup>-1</sup>. Cells were introduced into either one or both chambers of the device ( $\sim 2.5 \times 10^4$  cells per inlet well) as required and incubated for 15 minutes before inlet/outlet wells were filled with 50  $\mu$ l of supplemented media. Devices remained in a humidified incubator for up to 14 days *in vitro* (DIV) prior to experimentation, with media replenished every 2–3 days.

**Assessment of perfusion effects on cell viability.** Hippocampal cultures (12–14 DIV) in microfluidic devices were washed with a HEPES based external solution (HBS, containing, in mM: NaCl 140, KCl 5, MgCl<sub>2</sub> 2, HEPES 10, D-glucose 10, CaCl<sub>2</sub> 2; pH = 7.4; 310 mOsm). Cultured devices were connected to the perfusion setup and volumes adjusted to 50  $\mu$ l and 10  $\mu$ l in the wells connected to the naive and perfused chamber, respectively. Subsequently, multiple values of steady-state flow rates (in a range of 0.4–10  $\mu$ l min<sup>-1</sup>) were sustained in the perfused chambers for an hour and the cells were then stained for live/dead assessment. As control experiments, devices were also either left in stasis for an hour (Static  $t_{st}$ , with all wells containing 50  $\mu$ l) or were stained for cell death immediately after removal from the incubator (Static  $t_{st}$ ). Cultures were treated with propidium iodide (PI, 20  $\mu$ M) & Hoechst (4.5  $\mu$ M) made up in HBS for 30 minutes, then washed and allowed to recover for 15 minutes. Devices were then transferred to an inverted microscope (Axio Observer Z1, Zeiss), with bright-field and fluorescent images for each culture chamber captured using a 10 $\times$  objective and a cooled CCD camera (AxioCam MRm, Zeiss), analysed with ZEN 2012 (Blue edition, Zeiss). Dead cells were identified by the co-staining of Hoechst and PI, whilst living cells were identified by the sole staining of Hoechst.

**Immunocytochemistry.** Microfluidic hippocampal cultures (12 DIV) were fixed and stained to identify neuronal and glial populations. Briefly, using a previously established protocol<sup>20</sup>, cultures were washed with phosphate buffered saline solution (PBS) and fixed with ice cold paraformaldehyde (4% w/v, 10 min), followed by ice cold methanol treatment (100%, 10 min). Cultures were then washed with PBS and permeabilised with Triton-X100 (0.01%, 10 min), prior to treatment with blocking solution (1% w/v; foetal bovine serum 5, BSA 1) for 1 hour to prevent non-selective binding. Cultures were incubated at 4°C overnight with primary antibodies  $\beta$ -III-Tubulin (Life Technologies, UK; neuronal specific cytoskeleton marker; 1:500 dilution), glial fibrillary acidic protein (GFAP; Sigma Aldrich, UK; astrocytic marker; 1:500 dilution), synaptophysin (Millipore, UK; synaptic vesicle marker; 1:500 dilution) and MAP2 (Sigma Aldrich, UK; somatodendritic marker; 1:500 dilution). The cells were then washed with PBS, and incubated with the relevant fluorescently labelled secondary antibodies (Alexa 488 or Alexa 555; Life Technologies, UK; 1:200 dilution) for 1 hour at room temperature. Devices were then transferred to the inverted microscope (Axio Observer Z1, Zeiss), and imaged using 10 $\times$ , 20 $\times$  and 63 $\times$  objectives with a cooled CCD camera (AxioCam MRm, Zeiss). Image analysis was performed using ZEN 2012 (Blue edition, Zeiss).

**Calcium imaging.** *Data acquisition.* Ca<sup>2+</sup> imaging was performed on cultures using techniques described previously<sup>8,20,29</sup>. Briefly, microfluidic cultures (10–14 DIV) were loaded with the fluorescent calcium sensitive dye Fluo-4-AM (5  $\mu$ M in HBS for 1 hour at room temperature) and washed with HBS (vehicle) before being transferred to an inverted microscope (Axio Observer A1, Zeiss). Devices were then connected to the perfusion setup, delivering HBS at a steady flow rate (4  $\mu$ l min<sup>-1</sup>). Three other syringe pumps, primed with either glutamate (0.01–1 mM), glutamate antagonists (NBQX 20  $\mu$ M, DL-AP5 100  $\mu$ M, (R,S)-MCPG 500  $\mu$ M) or glutamate (3  $\mu$ M) in the presence of glutamate antagonists, were used to perfuse drugs of interest at a steady flow rate of 4  $\mu$ l min<sup>-1</sup>. Syringe pumps were primed with glutamate (3  $\mu$ M), the Na<sup>+</sup> channel blocker tetrodotoxin (TTX, 1  $\mu$ M) or glutamate in the presence of TTX and the solutions were perfused at a steady flow rate of 4  $\mu$ l min<sup>-1</sup>. Devices used to generate a glutamate concentration response curve were randomly assigned three separate glutamate concentrations that were perfused in order of increasing concentration. Simultaneous recordings of Ca<sup>2+</sup> transients in the two environmentally isolated, independent cultures were obtained with a cooled EMCCD camera (LucaR, Andor Technologies) using either a 5 $\times$  or 10 $\times$  objective, at a frame rate of 2.0 Hz and exposure time of 0.4 s. L-glutamic acid (Tocris Bioscience, UK), the glutamate receptor antagonists (NBQX, DL-AP5 & (R,S)-MCPG; Abcam, UK) and tetrodotoxin (TTX citrate; Abcam, UK) were made up as 1000 $\times$  stock solutions and diluted to final concentrations in vehicle solution on the day of experimentation. Time-lapse images were processed and analysed using Andor SOLIS, MATLAB (R2015a), and BioGraph (V2.5.6; J. Dempster, University of Strathclyde). As is standard, glutamate receptor antagonists or TTX were perfused during the resting period following the first glutamate perfusion and during the subsequent glutamate application to determine their effects on glutamate-induced Ca<sup>2+</sup> transients. At the end of each experiment, the perfusion was stopped and KCl (25 mM final concentration)



was applied to each chamber. Cells that did not elicit an immediate and sustained increase in fluorescence were excluded from analysis (see Supplementary Fig. S1).

**Analysis.** Regions of interest (ROI) were obtained from individual cell somas and the mean fluorescent intensity per ROI per frame was used to create a graphic readout of neuronal  $\text{Ca}^{2+}$  activity, with each cell's response trace normalised to the basal value for each recording. To produce a concentration response curve, the mean peak magnitudes obtained from increasing glutamate concentrations were normalised to the mean peak magnitude obtained from the highest glutamate application (1 mM) and the concentration response curve generated using the Hill equation:

$$y = \frac{R_{Max}}{1 + \left(\frac{x}{EC_{50}}\right)^n} \quad (5)$$

where  $R_{Max}$  = maximum response observed,  $EC_{50}$  = effective concentration at which 50% maximum response is obtained, and  $n$  = Hill coefficient. Otherwise, changes in neuronal activity in response to indirect stimulation from the directly perfused neural network were identified by the automated counting of  $\text{Ca}^{2+}$  events. The signals of each neuron obtained over the course of the assay were stitched together, filtered (moving average filter, window size 11) and normalised to the first 24 frames of the baseline recording. Events were counted on the basis of significant increases in fluorescence exceeding 7 standard deviations of the median baseline fluorescence, occurring within a moving window of 10 seconds. This provided the number of events taking place per neuron during both the basal period and glutamate perfusion of each recording, with results normalised to time and the indirect activity expressed as events/neuron/minute (ENM).

**Statistics.** All data is presented as mean  $\pm$  S.E.M. using bar/scatter graphs and results compared using paired student's *t*-tests, unpaired *t*-tests or one-way ANOVA with Tukey's post-hoc comparison as appropriate, with differences considered significant when  $P < 0.05$ , or treated otherwise as non-significant (ns).

## Results

**A robust model for pharmacological perfusion assays.** To assess the reproducibility of consecutive drug applications using the proposed system, initial experiments were performed using calcein to visualise perfusion performance and results confirmed a close match with the predicted flow behaviour (equations 1–3). The protocol developed produced a stable fluorescent plateau for the intended duration of perfusion (~30 seconds), with increasing (~35 seconds) and decreasing (~45 seconds) transients for all experiments (Fig. 1). Importantly, the absence of cross contamination between the two culture chambers was experimentally confirmed, demonstrating their fluidic isolation.

Having validated the robustness of the perfusion protocol, the effect of shear stress on the health of perfused hippocampal cultures (12–14 DIV) was examined (Fig. 2) to determine an optimal flow rate for the pharmacological study. As a benchmark, live/dead imaging was carried out on microfluidic cultures immediately after being removed from the incubator, with live cells accounting for  $73.8 \pm 0.01\%$  ( $n = 3$  devices, each device from a separate culture) of the total cell population (Fig. 2b). However, this decreased to  $54.1 \pm 0.9\%$  ( $n = 6$  devices from 3 cultures;  $P < 0.001$ , static  $t_{6h}$  vs static  $t_{0h}$ ) of the total cell population when the devices were left at room temperature under static conditions for an hour. In contrast, constant perfusion at room temperature, with flow rates ranging from  $0.4$ – $10 \mu\text{l min}^{-1}$  ( $n = 3$  devices, each device from a separate culture), revealed varying effects on cell viability after an hour, with live cells accounting for  $72.6 \pm 1.6\%$  ( $P < 0.001$  vs static  $t_{6h}$ ) of the total cell population at the optimal flow rate of  $4 \mu\text{l min}^{-1}$  (Fig. 2b). Furthermore, the health of the directly perfused cultures was closely matched by that of the non-perfused naive culture across all experimental conditions (non-significant,  $P > 0.05$ ). Given these results, a flow rate of  $4 \mu\text{l min}^{-1}$  was used for the remainder of this study. Finally, microfluidic cultures were stained for  $\beta$ -III-Tubulin, GFAP and synaptophysin revealing that only neuronal, but not astrocytic processes, were able to traverse across the microchannel array to the adjacent chamber and that synapses were formed both within and outside the microchannels (see Supplementary Fig. S2). Collectively, continuous perfusion experiments and immunocytochemistry imaging indicate that synaptically driven functional communication exists between the two hippocampal cultures, as previously reported<sup>20</sup>.

**Perfusion permits the characterisation of CNS active compounds.** As proof-of-concept work, to demonstrate the system's ability to carry out pharmacological characterisation of neuroactive compounds, a concentration response curve was generated using the excitatory amino acid, glutamate. Perfusion of glutamate (10 nM – 1 mM) elicited reversible concentration-dependent increases in intracellular  $\text{Ca}^{2+}$  (Fig. 3a), resulting in a concentration response curve with an  $EC_{50}$  of  $4.7 \pm 0.6 \mu\text{M}$  (Fig. 3b).

Having established that our integrated perfusion system allows the generation of concentration response curves, we tested the platform's capability for the pharmacological screening of compounds. To this end, we investigated the actions of ionotropic and metabotropic glutamate receptor antagonists NBQX (20  $\mu\text{M}$ ), DL-AP5 (100  $\mu\text{M}$ ) and (R,S)-MCPG (500  $\mu\text{M}$ ) on glutamate (3  $\mu\text{M}$ )-induced changes in intracellular  $\text{Ca}^{2+}$ . Repeated glutamate perfusions elicited robust and reproducible increases in intracellular  $\text{Ca}^{2+}$  ( $n = 182$  neurons, 4 devices, each device from a separate culture; Fig. 4a & b), which were inhibited in the presence of the glutamate antagonists to  $17 \pm 2.5\%$  of the response elicited by glutamate alone ( $n = 219$  neurons, 4 devices, each device from a separate culture;  $P < 0.001$ ; Fig. 4c & d). In contrast, no significant difference in glutamate-induced increases of intracellular  $\text{Ca}^{2+}$  ( $n = 551$  neurons, 3 devices, each device from a separate culture; Fig. 4e & f) were observed in the presence of TTX (1  $\mu\text{M}$ ).

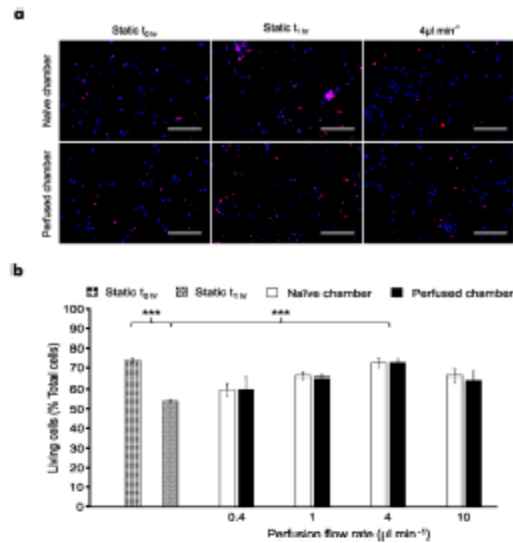


**Figure 2.** Continuous perfusion maintains cell viability between environmentally isolated neural networks. (a) Representative images obtained from perfused and naive cultures which were stained with Hoechst (blue) and PI (red) following continuous perfusion experiments for 1 hour. Scale bar = 200  $\mu\text{m}$ . (b) Microfluidic neural network viability increases in the presence of perfusion with respect to static condition after 1 hour, with an optimal flow rate of 4  $\mu\text{L min}^{-1}$ . Data are presented as mean  $\pm$  S.E.M. with one-way ANOVA with post-hoc Tukey's test performed;  $n = 21$  devices from 4 cultures; \*\*\*denotes  $P < 0.001$ .

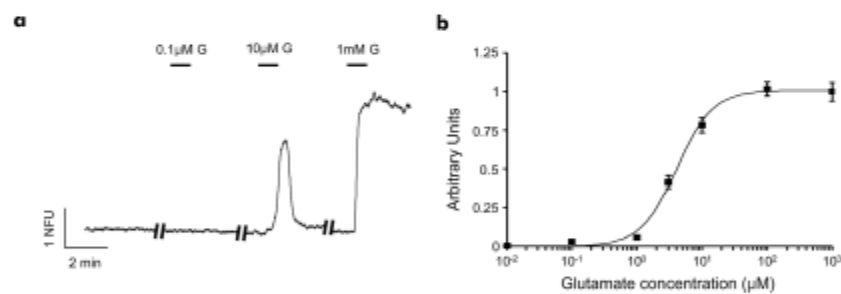


**Figure 3.** Microfluidic hippocampal cultures respond to direct glutamate (G) application in a concentration-dependent manner. (a) Ca<sup>2+</sup> imaging trace representative of a single neuron's response to perfusion of consecutive, increasing concentrations of glutamate (10–14 DIV). NFU = Normalised fluorescent unit. (b) Concentration response curve for glutamate (10 nm–1 mM) reveals an  $EC_{50} = 4.7 \pm 0.6 \mu\text{M}$ . Data is presented as mean  $\pm$  S.E.M. ( $n \geq 50$  neurons per concentration point, curve obtained from 14 devices from 6 cultures).

**Modulation of neuronal activity in synaptically connected hippocampal cultures.** Having previously demonstrated functional synaptic connectivity across two environmentally isolated hippocampal cultures following a single drug application<sup>20</sup>, here changes in postsynaptic responses in the naive chamber were examined as a consequence of repeated glutamate (3  $\mu\text{M}$ ) applications in the directly perfused chamber (Fig. 5, see Supplementary Video S1).

During the first glutamate application, neuronal activity within the naive chamber significantly increased from a baseline of  $0.16 \pm 0.04$  ENM to  $0.38 \pm 0.04$  ENM ( $P < 0.001$ ;  $n = 222$  neurons; Fig. 5b). Consistent with this, the second glutamate application also induced a significant increase in neuronal activity from  $0.17 \pm 0.04$  ENM to  $0.44 \pm 0.04$  ENM during glutamate application ( $P < 0.001$ ). Similarly, the final glutamate application elicited a significant increase in activity, from  $0.27 \pm 0.05$  ENM to  $0.4 \pm 0.05$  ENM ( $P > 0.05$ ). In the presence of glutamate antagonists in the perfused chamber, neuronal activity was unaltered in the naive chamber (Fig. 5c). A significant elevation in neuronal activity in the naive chamber was observed following glutamate application in the presence



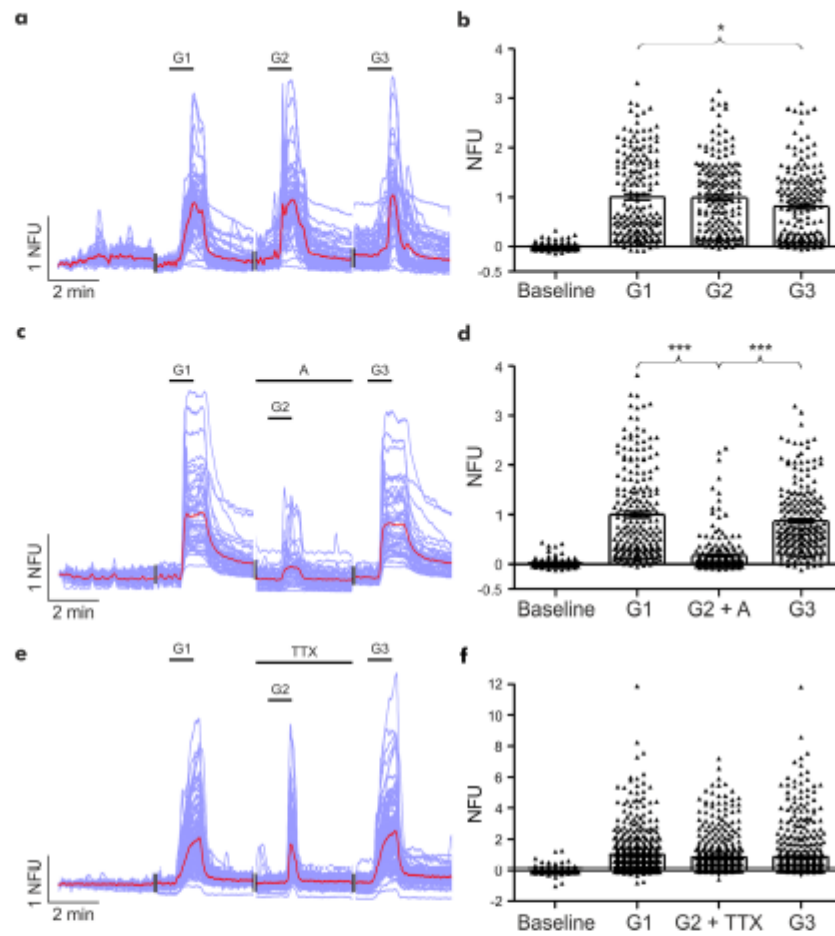


**Figure 4.** Reproducible glutamate responses are inhibited by glutamate antagonists. (a, c + e) Representative  $\text{Ca}^{2+}$  imaging traces of neuronal responses to repeated glutamate applications in the absence or presence of antagonists or TTX (purple trace: individual neuronal responses; red trace: average response). NFU = Normalised fluorescent unit. (b) Repeated applications of glutamate ( $3 \mu\text{M}$ ) revealed a small but significant reduction in neuronal response during the third glutamate application. (d) The neuronal response to glutamate ( $3 \mu\text{M}$ ) application was reversibly inhibited in the presence of glutamatergic antagonists (NBQX  $20 \mu\text{M}$ , DL-AP5  $100 \mu\text{M}$  & (R,S)-MCPG  $500 \mu\text{M}$ ). (f) The neuronal response to glutamate ( $3 \mu\text{M}$ ) application was not significantly affected in the presence of TTX ( $1 \mu\text{M}$ ). Data are presented as mean  $\pm$  S.E.M. with one-way ANOVA with post-hoc Tukey's test performed;  $n \geq 189$  neurons per application, from  $\geq 3$  devices from  $\geq 3$  separate cultures; \*denotes  $P < 0.05$  and \*\*\*denotes  $P < 0.001$ .

of glutamate antagonists, from a baseline of  $0.19 \pm 0.03$  ENM to  $0.42 \pm 0.04$  ENM ( $P < 0.001$ ;  $n = 350$  neurons; Fig. 5c). In contrast, baseline activity in the naive chamber was significantly increased from  $0.10 \pm 0.02$  ENM to  $0.22 \pm 0.03$  ENM ( $P < 0.01$ ; B1 vs B2;  $n = 381$  neurons; Fig. 5d) with the presence of TTX in the directly perfused chamber, whereas glutamate application in the presence of TTX did not induce any further increases in neuronal activity in the naive chamber (Fig. 5d). Finally, in order to confirm that changes in neuronal activity were unidirectional, hippocampal cultures were grown in one chamber only and glutamate perfused in the non-cultured chamber. Repeated application of glutamate ( $3 \mu\text{M}$ ) in the non-cultured chamber resulted in no changes in neuronal activity in the cultured chamber (see Supplementary Fig. S3).

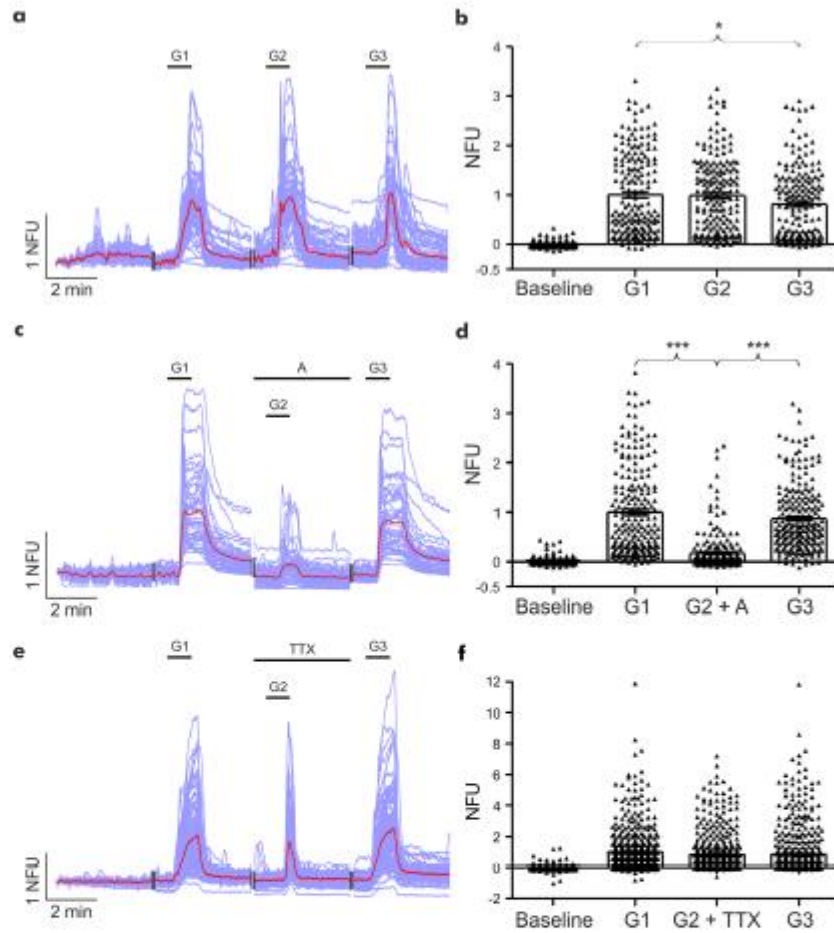


**Figure 4.** Reproducible glutamate responses are inhibited by glutamate antagonists. (a, c + e) Representative Ca<sup>2+</sup> imaging traces of neuronal responses to repeated glutamate applications in the absence or presence of antagonists or TTX (purple trace: individual neuronal responses; red trace: average response). NFU = Normalised fluorescent unit. (b) Repeated applications of glutamate (3 μM) revealed a small but significant reduction in neuronal response during the third glutamate application. (d) The neuronal response to glutamate (3 μM) application was reversibly inhibited in the presence of glutamatergic antagonists (NBQX 20 μM, DL-AP5 100 μM & (R,S)-MCPG 500 μM). (f) The neuronal response to glutamate (3 μM) application was not significantly affected in the presence of TTX (1 μM). Data are presented as mean ± S.E.M. with one-way ANOVA with post-hoc Tukey's test performed; n ≥ 189 neurons per application, from ≥ 3 devices from ≥ 3 separate cultures; \*denotes P < 0.05 and \*\*\*denotes P < 0.001.

of glutamate antagonists, from a baseline of  $0.19 \pm 0.03$  ENM to  $0.42 \pm 0.04$  ENM ( $P < 0.001$ ;  $n = 350$  neurons; Fig. 5c). In contrast, baseline activity in the naive chamber was significantly increased from  $0.10 \pm 0.02$  ENM to  $0.22 \pm 0.03$  ENM ( $P < 0.01$ ; B1 vs B2;  $n = 381$  neurons; Fig. 5d) with the presence of TTX in the directly perfused chamber, whereas glutamate application in the presence of TTX did not induce any further increases in neuronal activity in the naive chamber (Fig. 5d). Finally, in order to confirm that changes in neuronal activity were unidirectional, hippocampal cultures were grown in one chamber only and glutamate perfused in the non-cultured chamber. Repeated application of glutamate (3 μM) in the non-cultured chamber resulted in no changes in neuronal activity in the cultured chamber (see Supplementary Fig. S3).

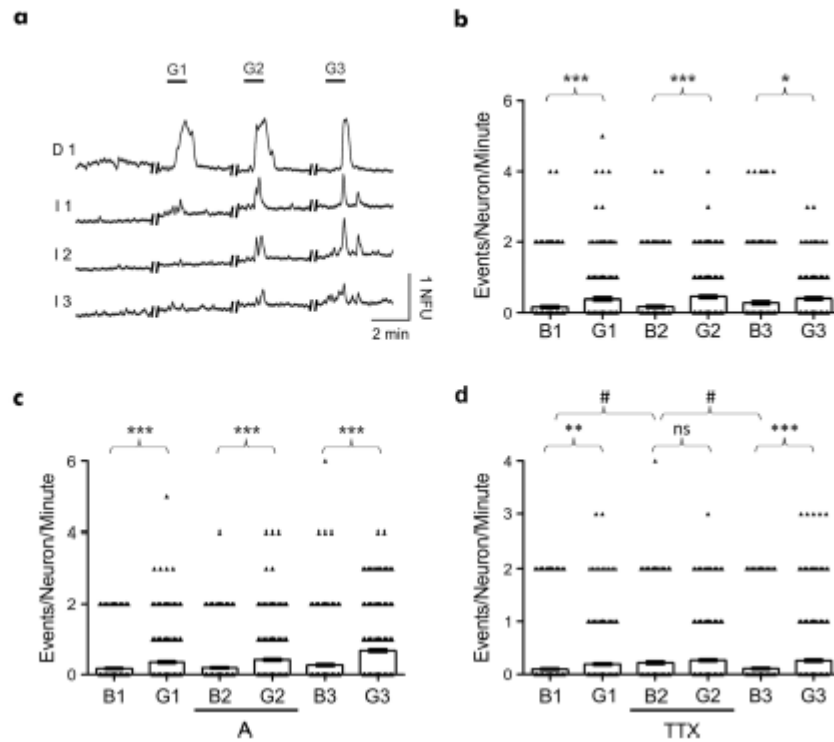


**Figure 5.** Repeated glutamate application induces increased neuronal activity in synaptically connected hippocampal cultures. **(a)**  $\text{Ca}^{2+}$  imaging traces representative of activity obtained from individual neurons in the directly perfused (trace D1) and naive (traces I1–I3) culture chambers, demonstrating functional synaptic communication between independent hippocampal cultures. **(b)** Significant increases in the number of neuronal calcium events were observed in the naive chamber, with respect to the basal (B) activity, in response to the three glutamate (G) applications in the perfused chamber. **(c)** Significant increases in the number of neuronal calcium events were observed in the naive chamber, with respect to the basal (B) activity, in response to glutamate applications (G) in the absence and presence of glutamate antagonists in the perfused chamber. **(d)** Basal activity in the naive chamber was significantly increased in the presence of TTX in the perfused chamber. Further changes in the number of neuronal calcium events were not observed following glutamate (G) application in the presence of TTX. Data are presented as mean  $\pm$  S.E.M. with paired student's *t*-test performed;  $n = \geq 222$  neurons per application,  $\geq 3$  devices from  $\geq 3$  separate cultures; ns denotes  $P > 0.05$ , \*denotes  $P < 0.05$ , \*\*denotes  $P < 0.01$ , \*\*\*denotes  $P < 0.001$  and #denotes  $P < 0.05$ .

## Discussion

This study presents the first successful integration of microfluidic perfusion with  $\text{Ca}^{2+}$  imaging techniques into a platform that allows the pharmacological characterisation of CNS active compounds using primary hippocampal cultures. The novelty of this approach is in examining simultaneously both the direct response to drug application (i.e. neuronal excitability) and the consequent alterations in neuronal activity in synaptically connected but environmentally isolated primary hippocampal cultures (i.e. induced synaptic activity), over customisable and repeatable conditions.

In all the experiments, the diffusive transport of compounds could be neglected with respect to their convective transport in the perfused chamber and microchannel array, as the Péclet number<sup>30</sup> was always  $> 100$  and the Reynolds number was always  $< 1$ . Absence of cross-contamination between chambers was experimentally confirmed using fluorescent imaging and the results were in line with previously established models<sup>30,31–33</sup>. Importantly, interchangeable perfusion of different solutions through a single culture chamber was achieved without disturbance in the flow. This was obtained by rapidly replacing the liquid volume inside the inlet open well of the perfusion chamber, selecting flow rate values that were much greater than that created in the perfused chamber. The open well system, in combination with carefully selected values of the flow rates (equations 1–2), generated a self-adjusting hydrostatic pressure difference between inlet and outlet wells of the perfused chamber that maintained a constant flow rate in the perfused chambers for the duration of the experiment. If the flow rate



assigned to the inlet well had been the same as that of the perfused chamber, then the time taken to completely change perfusates would be significantly longer (~5 minutes), which highlights the need for the faster flow rate at the inlet well. This approach enabled a quick fluid transition without creating a pulsatile flow when exchanging buffer and drug solutions. Further improvements to the platform could be made by replacing the syringe pump setup with a pressure-driven, valve-controlled perfusion system, thus extending the number of drugs that can be tested in the system, as well as reducing the size and number of external instrumentation needed for active flow control.

Microfluidic perfusion has been extensively applied to a variety of cell types and culture conditions, including both brain slices and tissue preparations<sup>18,34–38</sup>. A previous approach has been reported where a single perfusion pump was used to exert a negative pressure across an isolated axonal compartment, consequently withdrawing drug solution (applied *in situ*) from a reservoir to modulate synaptic activity and protein expression<sup>37</sup>. The main limitations of that setup were the requirement for regular, manual drug application throughout the experimental procedure and that the flow of perfusate was not selectively applied to an environmentally isolated culture. Alternatively, a model for perfusion has also been described in which neural networks were continuously perfused with automated pumps for up to 70 days<sup>36</sup>, with the cells grown on a microelectrode array within a microscope on-stage incubator. Whilst constant simultaneous morphological imaging and electrophysiological readout of neuronal activity was monitored over weeks, providing exceptional spatiotemporal resolutions, the protocol is time and resource heavy. Interestingly, these reports have shown that continuous perfusion alters synaptic activity and may be beneficial to the health of primary neuronal cultures<sup>34–36</sup>. Previous reports have shown how 2D vs 3D cultures, co-culture conditions and shear stress may influence gene expression, production/transport/removal of nutrients and molecular secretions<sup>39–42</sup>. Our findings suggest that an optimal steady flow rate confers neuroprotective properties not only to a single perfused primary culture, but also to an adjacent, synaptically connected culture. Recently, we have revealed evidence of neuroprotection against spreading toxicity between neighbouring synaptically connected but environmentally isolated hippocampal cultures<sup>21</sup>, and previous studies have proposed suppression of excitotoxicity via interneurons in response to mechanically-induced astrocytic release of ATP<sup>43–45</sup>. However, the exact mechanisms underlying this observation in the present study remain unclear.

Ca<sup>2+</sup> imaging is a powerful and cost-effective technique that can be used to provide optical readouts of both spontaneous and induced cellular activity<sup>46,47</sup>. When combined with the precise spatial and temporal fluid flow control achieved using microfluidic systems, high-throughput and miniaturised assays can be performed. Whilst neuropharmacological studies have used Ca<sup>2+</sup> imaging to perform high-throughput pharmacological analyses<sup>47–50</sup>, they are either limited in their fine control of stimulus delivery or often require user intervention to perform *in situ* drug delivery. Furthermore, such conventional systems, which integrate Ca<sup>2+</sup> imaging techniques to observe neuronal excitability following compound delivery, lack neighbouring environmentally isolated cultures, thus limiting the understanding of a drug's effect on the synaptic connectivity between cultures.

In the present study, we demonstrate proof-of-concept analysis of both neuronal excitability and consequent synaptic connectivity. First, a concentration response curve was generated by obtaining reproducible responses to a range of glutamate concentrations, revealing an EC<sub>50</sub> of 4.7 μM, which compares well to that reported in the literature<sup>51–53</sup>. Additionally, the neuronal response to glutamate perfusion in the absence or presence of glutamatergic receptor antagonists was examined, revealing reversible inhibition of glutamate-induced transient increases in intracellular Ca<sup>2+</sup>. These assays highlight that the microfluidic perfusion platform described here can be utilised for the pharmacological profiling of CNS active compounds. Furthermore, our miniaturised system shows for the first time, repeatable assessment of induced network synaptic activity in addition to pharmacological profiling of directly applied compounds in a microfluidic format. Indeed, neuronal activity in the naïve hippocampal culture was increased in response to multiple glutamate applications but, strikingly, this led to an increased level of basal neuronal activity prior to the final glutamate application. Whilst the final glutamate application still induced an increase in neuronal activity with respect to baseline, repeated synaptically driven signalling appears to induce an excited state of activity in the naïve culture, which gradually becomes resistant to further stimulation. This observation mimics the increased responsiveness of neurons that undergo synaptic plasticity<sup>54</sup> and in this case, increased responsiveness similar to that observed in long term potentiation (LTP). Whilst we have not probed the underlying mechanisms in the present study, these results are in line with previous studies in which LTP has been investigated in cultured hippocampal neurons using both electrophysiological and Ca<sup>2+</sup> imaging techniques<sup>55–57</sup>. Basal neuronal activity within the naïve chamber was unaltered in the presence of glutamate antagonists whereas increases were observed following glutamate application in their presence. Given that glutamate-induced Ca<sup>2+</sup> responses in the perfused chamber were significantly reduced, but not abolished, in the presence of the antagonists, the increases in the naïve chamber are likely to be induced via the residual responses observed in the perfused chamber. In contrast, basal activity in the naïve chamber was significantly enhanced in the presence of TTX in the perfused chamber. Given that our experiments, in which cultures were grown in one chamber only, revealed that the glutamate-induced increase in neuronal activity is unidirectional, this result indicates that TTX application in the perfused chamber may be impairing an inhibitory tone that controls neuronal activity within the naïve chamber. As primary hippocampal cultures grown under our experimental conditions contain approximately 6% GABAergic neurons<sup>58</sup>, these will exert a strong inhibitory control over excitatory neurotransmission within the cultures. Indeed, application of GABAergic antagonists has been used to mimic epileptiform-like activity in hippocampal cultures<sup>59,60</sup>, hence the inhibition of GABAergic neuronal firing by TTX in the perfused chamber would result in the increased activity in the naïve chamber due to decreased GABAergic tone extending from the perfused to the naïve chamber. Furthermore, glutamate induced increases in neuronal activity were abolished during the co-application of glutamate and TTX, despite increases in intracellular calcium in neurons within the perfused chamber. Collectively, these results demonstrate that changes in neuronal activity within the naïve culture chamber are driven by functional, synaptic communication from neurons in the perfused chamber.

## Conclusions

We have developed a novel platform that integrates microfluidic perfusion and  $\text{Ca}^{2+}$  imaging techniques for studying neuromodulation and synaptic connectivity between primary hippocampal cultures. We show that both direct neuronal excitability and the consequent synaptic communication between synaptically connected but environmentally isolated cultures can be simultaneously monitored, providing hundreds of readouts from each device. In addition, with the recent surge in interest in the use of human stem cell derived neurons to investigate CNS disorders<sup>61,62</sup>, the platform described in the present study may offer new avenues to examine the underlying causes of CNS disease and allow potential novel therapeutics to be tested in a cost-effective, miniaturised manner.

**Data availability.** Access to all data underpinning this publication is restricted to a request only basis. More information and contact details are available from the University of Strathclyde at <http://dx.doi.org/10.15129/5a018c9b-9458-4e3f-8a92-23657abcd44e>.

## References

- World Health Organization. *Neurological Disorders: Public Health Challenges*. <https://doi.org/10.1001/archneur.2007.19> (World Health Organization, 2008).
- EvaluatePharma. *World Preview 2018: Embracing the Patent Cliff* (2012).
- Skripka-Serry, J. *The great neuro-pipeline 'brain drain' (and why Big Pharma hasn't given up on CNS disorders)*. *Drug Discovery World* (2013).
- Hay, M. Clinical development success rates for investigational drugs. *Nat Biotechnol* **32**, (2014).
- Waring, M. J. et al. An analysis of the attrition of pharmaceutical companies. *Nat. Publ. Gr.* **14**, 475–486 (2015).
- Shuler, M. L. & Hickman, J. J. Toward *in vitro* models of brain structure and function. *Proc. Natl. Acad. Sci. USA* **111**, 13682–13683 (2014).
- Tsaiou, K., Bottlaender, M. & Mabondzo, A. ADDME – Avoiding Drug Development Mistakes Early: central nervous system drug discovery perspective. *BMC Neurol* **9**(Suppl 1), S1 (2009).
- Gan, J., Greenwood, S. M., Cobb, S. R. & Bushell, T. J. Indirect modulation of neuronal excitability and synaptic transmission in the hippocampus by activation of proteinase-activated receptor-2. *Br. J. Pharmacol.* **163**, 984–994 (2011).
- Martina, M. et al. Recordings of cultured neurons and synaptic activity using patch-clamp chips. *J. Neural Eng.* **8**, 34002 (2011).
- Dunlop, J., Bowley, M., Peri, R., Vasilyev, D. & Arias, R. High-throughput electrophysiology: an emerging paradigm for ion-channel screening and physiology. *Nat. Rev. Drug Discov.* **7**, 358–368 (2008).
- Gonzalez-Sulser, A. et al. Hippocampal neuron firing and local field potentials in the *in vitro* 4-aminopyridine epilepsy model. *J. Neurophysiol.* **108**, 2568–2580 (2012).
- Spira, M. E. & Hat, A. Multi-electrode array technologies for neuroscience and cardiology. *Nat. Nanotechnol.* **8**, 83–94 (2013).
- Grienberger, C. & Konnerth, A. Imaging Calcium in Neurons. *Neuron* **73**, 862–885 (2012).
- Whitesides, G. M. The origins and the future of microfluidics. *Nature* **442**, 368–73 (2006).
- Park, J. W., Kim, H. J., Kang, M. W. & Jeon, N. L. Advances in microfluidics-based experimental methods for neuroscience research. *Lab Chip* **13**, 509–21 (2013).
- Huang, P. J., Lee, P. J., Sabounchi, P., Lin, R. & Lee, L. P. Continuous perfusion microfluidic cell culture array for high-throughput cell-based assays. *Biotechnol. Bioeng.* **89**, 1–8 (2005).
- McMillan, K. S., Boyd, M. & Zagnoni, M. Transitioning from multi-phase to single-phase microfluidics for long-term culture and treatment of multicellular spheroids. *Lab Chip* **16**, 3548–3555 (2016).
- Kim, L., Toh, Y.-C., Voldman, J. & Yu, H. A practical guide to microfluidic perfusion culture of adherent mammalian cells. *Lab Chip* **7**, 681–694 (2007).
- Young, E. W. K. & Beebe, D. J. Fundamentals of microfluidic cell culture in controlled microenvironments. *Chem Soc Rev* **39**, 1036–1048 (2010).
- Robertson, G., Bushell, T. J. & Zagnoni, M. Chemically induced synaptic activity between mixed primary hippocampal co-cultures in a microfluidic system. *Integr. Biol.* **6**, 636–644 (2014).
- Samson, A. J., Robertson, G., Zagnoni, M. & Connolly, C. N. Neuronal networks provide rapid neuroprotection against spreading toxicity. *Sci. Rep.* **6**, 33746 (2016).
- Kanagasabapathi, T. T., Ciliberti, D., Martinota, S., Wadman, W. J. & Decré, M. M. J. Dual-compartment neurofluidic system for electrophysiological measurements in physically segregated and functionally connected neuronal cell culture. *Front. Neuroeng.* **4**, 13 (2011).
- Taylor, A. M., Rhee, S. W., Tu, C. H., Cribbs, D. H. & Cotman, C. W. Microfluidic Multicompartment Device for Neuroscience Research. *Neurosci. Res.* **19**, 1551–1556 (2010).
- Wevers, N. R. et al. High-throughput compound evaluation on 3D networks of neurons and glia in a microfluidic platform. *Sci. Rep.* **6**, 38856 (2016).
- Park, J. et al. Three-dimensional brain-on-a-chip with an interstitial level of flow and its application as an *in vitro* model of Alzheimer's disease. *Lab Chip* **15**, 141–50 (2014).
- Honegger, T. et al. Microfluidic neurite guidance to study structure-function relationships in topologically-complex population-based neural networks. *Sci. Rep.* **6**, 28384 (2016).
- Takeda, S. et al. Neuronal uptake and propagation of a rare phosphorylated high-molecular-weight tau derived from Alzheimer's disease brain. *Nat. Commun.* **6**, 8490 (2015).
- Ledgerwood, C. J., Greenwood, S. M., Brett, R. R., Pratt, J. A. & Bushell, T. J. Cannabidiol inhibits synaptic transmission in rat hippocampal cultures and slices via multiple receptor pathways. *Br. J. Pharmacol.* **162**, 286–294 (2011).
- Bushell, T. J., Plevin, R., Cobb, S. & Irving, A. J. Characterization of proteinase-activated receptor 2 signalling and expression in rat hippocampal neurons and astrocytes. *Neuropharmacology* **50**, 714–725 (2006).
- Patankar, S. V. *Numerical Heat Transfer and Fluid Flow*. (CRC Press, 1980).
- Kunze, A. et al. Astrocyte-neuron co-culture on microchips based on the model of SOD mutation to mimic ALS. *Integr. Biol. (Camb.)* **5**, 964–75 (2013).
- Taylor, A. M., Menon, S. & Gupton, S. L. Passive microfluidic chamber for long-term imaging of axon guidance in response to soluble gradients. *Lab Chip* **15**, 2781–2789 (2015).
- Taylor, A. M. et al. A microfluidic culture platform for CNS axonal injury, regeneration and transport. **2**, 0–4 (2007).
- Rambani, K., Vukasinovic, J., Glezzer, A. & Potter, S. M. Culturing thick brain slices - An interstitial 3D microperfusion system for enhanced viability. *J. Neurosci. Methods* **180**, 243–254 (2009).
- Cullen, D. K., Vukasinovic, J., Glezzer, A. & Laplaca, M. C. Microfluidic engineered high cell density three-dimensional neural cultures. *J. Neural Eng.* **4**, 159–72 (2007).
- Killian, N. J., Vernekar, V. N., Potter, S. M. & Vukasinovic, J. A device for long-term perfusion, imaging, and electrical interfacing of brain tissue *in vitro*. *Front. Neurosci.* **10**, 135 (2016).
- Taylor, A. M., Dieterich, D. C., Ito, H. T., Kim, S. a. & Erin, M. *Manipulation of Synapses*. **66**, 57–68 (2010).



38. Saalfrank, D. et al. Incubator-independent cell-culture perfusion platform for continuous long-term microelectrode array electrophysiology and time-lapse imaging. *R. Soc. Open Sci.* **2**, 150031 (2015).
39. Dirks, B., Hanke, J., Kriegstein, J., Stock, R. & Winkler, G. Studies on the Linkage of Energy Metabolism and Neuronal Activity in the Isolated Perfused Rat Brain. *J. Neurochem.* **35**, 311–317 (1980).
40. Ivanov, A. & Zilberter, Y. Critical state of energy metabolism in brain slices: The principal role of oxygen delivery and energy substrates in shaping neuronal activity. *Front. Neuroenergetics* **3**, 9 (2011).
41. Miller, L. J. & Gillette, M. U. New perspectives on neuronal development via microfluidic environments. *Trends Neurosci.* **35**, 752–761 (2012).
42. van der Helm, M. W., van der Meer, A. D., Eijkel, J. C. T., van den Berg, A. & Segerink, L. I. Micro fluidic organ-on-chip technology for blood-brain barrier research. *Tissue Barriers* **4**, e1142493 (2016).
43. Guthrie, P. B. et al. ATP Released from Astrocytes Mediates Glial Calcium Waves. *J. Neurosci.* **19**, 520–528 (1999).
44. Zhang, J. M. et al. ATP Released by Astrocytes Mediates Glutamatergic Activity-Dependent Heterosynaptic Suppression. *Neuron* **40**, 971–982 (2003).
45. Bowser, D. N. ATP Excites Interneurons and Astrocytes to Increase Synaptic Inhibition in Neuronal Networks. *J. Neurosci.* **24**, 8606–8620 (2004).
46. Ward, M. W., Kushnareva, Y., Greenwood, S. & Connolly, C. N. Cellular and subcellular calcium accumulation during glutamate-induced injury in cerebellar granule neurons. *J. Neurochem.* **92**, 1081–1090 (2005).
47. Doolen, S., Blake, C. B., Smith, B. N. & Taylor, B. K. Peripheral nerve injury increases glutamate-evoked calcium mobilization in adult spinal cord neurons. *Mol. Pain* **8**, 56 (2012).
48. Tetschert, R. W. et al. Functional profiling of neurons through cellular neuropharmacology. *Proc. Natl. Acad. Sci. USA* **109**, 1388–95 (2012).
49. Larsch, J., Ventimigli, D., Barnmann, C. I. & Albrecht, D. R. High-throughput imaging of neuronal activity in *Caenorhabditis elegans*. *Proc. Natl. Acad. Sci. USA* **110**, E4266–E4273 (2013).
50. Takahashi, N., Takahara, Y., Ishikawa, D., Matsuki, N. & Ikegaya, Y. Functional multineuron calcium imaging for systems pharmacology. *Anal. Bioanal. Chem.* **398**, 211–218 (2010).
51. Haak, L. L. Metabotropic glutamate receptor modulation of glutamate responses in the suprachiasmatic nucleus. *J. Neurophysiol.* **81**, 1308–17 (1999).
52. Yuan, H., Hansen, K. B., Vance, K. M., Ogden, K. K. & Traynelis, S. F. Control of NMDA receptor function by the NR2 subunit amino-terminal domain. *J. Neurosci.* **29**, 12045–58 (2009).
53. Anson, L. C., Chen, P. E., Wyllie, D. I., Colquhoun, D. & Schoepfer, R. Identification of amino acid residues of the NR2A subunit that control glutamate potency in recombinant NR1/NR2A NMDA receptors. *J. Neurosci.* **18**, 581–589 (1998).
54. Bliss, T. V. & Collingridge, G. L. A synaptic model of memory: long-term potentiation in the hippocampus. *Nature* **361**, 31–39 (1993).
55. Frick, A., Magee, J. & Johnston, D. LTP is accompanied by an enhanced local excitability of pyramidal neuron dendrites. *Nat. Neurosci.* **7**, 126–35 (2004).
56. Ivenshitz, M. & Segal, M. Simultaneous NMDA-Dependent Long-Term Potentiation of EPSCs and Long-Term Depression of IPSCs in Cultured Rat Hippocampal Neurons. *J. Neurosci.* **26**, 1199–1210 (2006).
57. Molnár, E. Long-term potentiation in cultured hippocampal neurons. *Semin. Cell Dev. Biol.* **22**, 506–513 (2011).
58. Benson, D. L., Watkins, F. H., Steward, O. & Banker, G. Characterization of GABAergic neurons in hippocampal cell cultures. *J. Neurocytol.* **23**, 279–95 (1994).
59. Colombi, I., Mahajani, S., Frega, M., Gasparini, I. & Chiappalone, M. Effects of antiepileptic drugs on hippocampal neurons coupled to micro-electrode arrays. *Front. Neuroeng.* **6**, 10 (2013).
60. Li, Y., Popko, J., Krogh, K. A. & Thayer, S. A. Epileptiform stimulus increases Homer 1a expression to modulate synapse number and activity in hippocampal cultures. *J. Neurophysiol.* **109**, 1494–504 (2013).
61. Srikanth, P. & Young-Pearse, T. L. Stem cells on the brain: modeling neurodevelopmental and neurodegenerative diseases using human induced pluripotent stem cells. *J. Neurogenet.* **28**, 5–29 (2015).
62. Yu, D. X., Marchetto, M. C. & Gage, F. H. Therapeutic translation of iPSCs for treating neurological disease. *Cell Stem Cell* **12**, 678–688 (2013).

### Acknowledgements

The authors would like to thank the National Centre for The Replacement, Refinement and Reduction of Animals in Research (NC3Rs PhD studentship, NC/L00139X/1) and the University of Strathclyde for financial support.

### Author Contributions


C.M., G.R. and M.Z. designed the microfluidic system and developed the microfluidic perfusion assay; C.M. and T.B. planned the pharmacological assays; C.M. and G.R. performed the experiments and analysed the data; All authors wrote the manuscript.

### Additional Information

**Supplementary information** accompanies this paper at <https://doi.org/10.1038/s41598-017-15950-0>.

**Competing Interests:** The authors declare that they have no competing interests.

**Publisher's note:** Springer Nature remains neutral with regard to jurisdictional claims in published maps and institutional affiliations.

 **Open Access** This article is licensed under a Creative Commons Attribution 4.0 International License, which permits use, sharing, adaptation, distribution and reproduction in any medium or format, as long as you give appropriate credit to the original author(s) and the source, provide a link to the Creative Commons license, and indicate if changes were made. The images or other third party material in this article are included in the article's Creative Commons license, unless indicated otherwise in a credit line to the material. If material is not included in the article's Creative Commons license and your intended use is not permitted by statutory regulation or exceeds the permitted use, you will need to obtain permission directly from the copyright holder. To view a copy of this license, visit <http://creativecommons.org/licenses/by/4.0/>.

© The Author(s) 2017